Development of nulling interferometry devices for the detection and characterization of extrasolar planets

Charles Hanot

To cite this version:

Charles Hanot. Development of nulling interferometry devices for the detection and characterization of extrasolar planets. Astrophysics [astro-ph]. Université de Liège, 2011. English. NNT : . tel-00592081

HAL Id: tel-00592081
https://theses.hal.science/tel-00592081

Submitted on 11 May 2011

Université de Liège

Faculté des Sciences **Département d'Astrophysique, Géophysique et Océanographie**

Development of nulling interferometry devices for the detection and characterization of extrasolar planets

THÈSE

présentée pour l'obtention du diplôme de

Docteur en Sciences

par

Charles Hanot

Soutenue publiquement le 26 avril 2011 devant le Jury composé de :

Président :	Pr. Gregor RAUW
Directeur de thèse :	Pr. Jean SURDEJ
Examinateurs :	Dr. Olivier ABSIL Dr. Bram ACKE Dr. Gaël CHAUVIN Dr. Vincent COUDÉ DU FORESTO Pr. Serge HABRAKEN Pr. Jean-Pierre SWINGS

Institut d'Astrophysique et de Géophysique de l'Université de Liège

Mis en page avec la classe thloria.

Acknowledgments

This thesis is not only the result of a personal work but has been possible thanks to the help and support of many colleagues, friends and to my family. First and foremost, I want to express my deepest gratitude to my academic advisor, Professor Jean Surdej. Thank you Jean for having given me the taste for the fringes during the master course, for welcoming me in your team (I should say family) after a single phone call, a night of January 2007, and for inspiring me with your unconditional support and enthusiasm.

My utmost gratitude also goes to Dr. Malcolm Fridlund and Dr. Roland den Hartog for introducing me to the practical aspects and applications of nulling interferometry during my internship at ESTEC. Your work and passion for the direct imaging of exoplanets have guided me through this work. But all of this would not have been possible without the help of Pr. Jean-Pierre Swings, who introduced me to ESA and to the Darwin team in particular.

I am grateful to Dr. Olivier Absil , Dr. Bram Acke, Dr. Gaël Chauvin, Dr. Vincent Coudé du Foresto, Pr Serge Habraken, Pr. Gregor Rauw, Pr. Jean Surdej and Pr. Jean-Pierre Swings members of my thesis committee, for accepting to read and evaluate my work.

I would like to express my warmest thanks to the wonderful Palomar Fiber Nuller team at the Jet Propulsion Laboratory. I am indebted to Gene Serabyn for giving me the opportunity to work on the project and contribute to the engineering runs. I have particularly enjoyed the fruitful collaboration and discussions with Stefan Martin, Bertrand Mennesson, Kurt Liewer and Frank Loya. I also wish to thank the Palomar Observatory staff for their assistance in installing the PFN and conducting the observations at the Hale telescope.

For preparing and conducting my interferometric surveys on AMBER at VLTI, I had the chance to work with colleagues from IPAG (Grenoble). They provided me numerous hints and information for my program and allowed me to pursue this work on their brand new and efficient visitor instrument at VLTI: PIONIER. In particular, I want to thank Jean-Baptiste LeBouquin, Jean-Philippe Berger, Jean-Charles Augereau and Myriam Benisty for their contributions. Observations at VLT have benefitted from the experience of the entire ESO staff at Paranal, which conducted our observing program.

I am also grateful to both Centre Spatial de Liège for their hard work in the development of the Fresnel rhomb achromatic phase shifters and to Hololab for the logistical and financial support for building the CELINE testbench. My warmest thanks go in particular to Serge Habraken, Jérome Loîcq, Denis Vandormael, Jean-Yves Plesseria and Karl Fleury.

I would like to give a special thanks to all my colleagues and friends at Institut d'Astrophysique et de Géophysique de Liège for all the good time we spent together; this work would never have been possible without your friendship. In particular, I want to thank Dimitri, Olivier, Pierre (aka Poulpy) and Denis for the numerous passionate discussions about interferometry and high-contrast imaging, their unconditional help, support and even tutoring during this thesis. My warmest gratitude also goes to my roommate, Emilie for our four years long, uninterrupted discussion about babies and diapers (and interferometry ... sometimes). Many thanks to Anthony (aka “Le Corse”), Arnaud, Audrey, Davide, Eva, François (aka Paco), Jean-Christophe (aka Mr. Genius Bar), Katerina, Laurent, Méla, Natacha, Thomas and Virgi. Last but not least, all my travels to conferences and foreign laboratories would not have been possible without the hard work of Denise and Sylvia.

I would like to acknowledge my family and my mother in particular for having whipped up my taste of science and my curiosity from the earliest days. Without our trips to Greece, Egypt and our visits to the *Euro-Space Center*, I would certainly have not become so much interested about space and astrophysics.

I also wish to express my gratitude to Diane (aka Poulette), Danilo (aka Dombrovitch) and Michel for supporting me during the past years and having welcomed me in their family.

I want to express my most tender gratitude to my wife, Céline, for supporting and loving me for so many years. Thank you for having stimulated my interest for classes from mathematics at high-school to numerical analysis at the university. Life would have been so much dull without you.

This T is for thesis is D is for dedicated to G is for Gabriel with L is for love from P is for Papa. Thank you for inspiring me every lasting second. I hope that the stars shining in your eyes will never go out. You will soon be a fantastic brother to Margaux, I am sure.

This research was supported by a fellowship from the *Fonds pour la formation à la Recherche dans l'Industrie et dans l'Agriculture de Belgique* ("Boursier F.R.I.A."). During his stay at the *Jet Propulsion Laboratory*, the author was supported by the *Fonds National de la Recherche Scientifique de Belgique* (F.N.R.S), by the *Communauté Francaise de Belgique - Action de Recherche Concertée - Académie Wallonie Europe*, by the *Université de Liège* and by the *Center for Exoplanet Science*.

Contents

Notations and acronyms **1**

Introduction **3**

The quest for exoplanets 3
Evolutionary models 5
Spectroscopy and habitability of exoplanets 6
Direct imaging: Earth-like worlds in the line-of-sight 8
Objectives and outline of this work 10

I Direct imaging of exoplanets with single aperture telescopes **13**

1 An overview of single-aperture high contrast imaging **15**
1.1 Principle of high contrast imaging 16
1.1.1 Wavefront corrections 16
1.1.2 Coronagraphs: getting rid of the starlight 18
1.1.3 Differential imaging: a solution for quasi-static noise 19
1.2 Ground- and space-based coronagraphic facilities 21
1.2.1 Facilities from the 1990s and 2000s 22
1.2.2 Next generation of instruments 22
1.3 Extra-solar planet imaging: ground- vs. space-based coronagraphs 25
1.3.1 Young main sequence stars: the ideal targets for direct imaging 25
1.3.2 Simulated sensitivities of coronagraphic observatories 26
1.3.3 Performance comparison and perspectives 27

2 The Well-Corrected Subaperture: a precursor to future XAO facilities **33**
2.1 Principle and goals of the instrument 33
2.2 Direct imaging of multiple systems at blue wavelengths 34
2.2.1 Observing strategy and data reduction 35
2.2.2 Data analysis 36
2.2.3 Individual star results 39
2.2.4 Error bars on the pixel size and telescope orientation 45

2.3 Reaching high contrasts with phase mask coronagraphs 45

II Multi-aperture imaging: toward other Earths 47

3 An introduction to interferometry and to interferometers 49

3.1 Reaching very high angular resolutions with interferometry 49

3.2 Principles of stellar interferometry 50

3.2.1 Fringe visibilities 53

3.2.2 Phase measurements 55

3.3 Nulling interferometry 56

3.3.1 Null depth 57

3.3.2 Geometric leakage 58

3.3.3 Instrumental leakage 59

3.3.4 Spatial and modal filtering 59

3.4 Current facilities 60

3.4.1 Stellar interferometers 60

3.4.2 Nulling interferometers 63

4 Data reduction challenges 65

4.1 Classical method 65

4.1.1 Photometric corrections 67

4.1.2 Visibility measurement and calibration 67

4.1.3 Influence of noise 68

4.2 Statistical method 70

4.2.1 Paper: **Improving null depth measurements using statistical distributions: theory and first results with the Palomar Fiber Nuller**, *C. Hanot, B. Mennesson, S. Martin, K. Liewer, F. Loya, P. Riaud, O. Absil and E. Serabyn* 70

5 A survey for companions in young stellar moving groups with AMBER 85

5.1 The AMBER instrument at VLTI 86

5.1.1 The VLTI 86

5.1.2 The AMBER instrument 87

5.1.3 FINITO: a fringe tracker for the VLTI 89

5.2 Presentation of the scientific program 89

5.2.1 Why using long baseline interferometry? 89

5.2.2 Observing strategy 91

5.3 Survey status 93

5.3.1 Methodology 95

5.3.2 Results on a sample of early-type stars 96

5.3.3 β Pictoris: a new hope 99

6 CELINE: The ULg nulling testbed 101

6.1 Why develop a nulling testbench? 101

6.2 Beam combiners for nulling interferometry 102

6.3 CELINE instrumental layout 104

6.3.1 Sources and injection 105

6.3.2 Phase control and signal chopping 106

6.3.3 Beam combination and detector 108

6.4 Results 108

6.4.1 Data analysis 108

6.4.2 Nulling results with monochromatic light 109

6.5 Perspectives 111

7 PFN: detecting faint companions inside the diffraction limit of a telescope 113

7.1 Principle of the PFN 114

7.1.1 Instrumental layout 114

7.1.2 Alignment 117

7.2 Laboratory results 118

7.2.1 Broadband nulling 118

7.2.2 Baseline rotation 120

7.3 Observing at high contrasts within the diffraction limit 121

7.3.1 Paper: **High Contrast Stellar Observations within the Diffraction Limit at the Palomar Hale Telescope**, *B. Mennesson, C. Hanot, E. Serabyn, S. Martin, K. Liewer, F. Loya and D. Mawet* 121

7.3.2 Paper: **New Constraints on Hot Dust within a few AU of Vega**, *B. Mennesson, E. Serabyn, C. Hanot, S. Martin, K. Liewer, D. Mawet* 133

7.4 Future upgrades: going deeper and fainter 143

7.4.1 Looking for young exoplanets with the PFN 143

8 Filling the gap: combining interferometry with coronagraphy 145

8.1 Principles 145

8.1.1 Beam combination with a coronagraph 145

8.1.2 Pupil densification 147

8.2 Application to stellar angular diameter measurements 148

8.2.1 Paper: **Combining coronagraphy with interferometry as a tool for measuring stellar diameters**, *P. Riaud and C. Hanot* 149

Conclusions 165

Objectives and results 165

Perspectives 166

Appendix **169**

A Fresnel rhombs as APS for infrared nulling interferometry **171**

Bibliography **189**

Notations and acronyms

Atmospheric windows

J band	from 1.15 to 1.4 μm
H band	from 1.5 to 1.8 μm
K band	from 2.0 to 2.4 μm
L$'$ band	from 3.5 to 4.1 μm
M band	from 4.5 to 5.1 μm
N band	from 8 to 13 μm

Units

arcmin (or $'$)	minute of arc (2.90888×10^{-4} radian)
arcsec (or $''$)	second of arc (4.848137×10^{-6} radian)
mas	milli-arcsec (10^{-3} arcsec)
AU	Astronomical Unit (1.495978×10^{11} m)
pc	parsec (3.085678×10^{17} m)
Myr	Mega-years (one million years)
Gyr	Giga-years (one billion years)

Notations

$M_\odot$	Mass of the Sun (1.98892×10^{30} kg)
$R_\odot$	Radius of the Sun (6.96×10^{8} m)
$L_\odot$	Luminosity of the Sun (3.846×10^{26} W)
$M_{\rm Jup}$	Mass of Jupiter (1.8987×10^{27} kg)
$R_{\rm Jup}$	Radius of Jupiter (7.1492×10^{7} m)
$M_\oplus$	Mass of the Earth (5.97370×10^{24} kg)
$R_\oplus$	Radius of the Earth (6.37814×10^{6} m)
$M_\star$, $T_\star$, $L_\star$	Mass, effective temperature and luminosity of a star
$B_\star$	Photospheric surface brightness of a star
$R_\star$, $\theta_\star$	Linear and angular radius of a star
$\theta_{\rm UD}$, $\theta_{\rm LD}$	Uniform disk and limb-darkened disk stellar angular diameters
b, $b_\perp$	Interferometric baseline length, its projection on the sky plane
a	Semimajor orbital axis for a planet, or diameter for a dust grain

Acronyms

ADI	Angular Differential Imaging
AGPM	Annular Grove Phase Mask Coronagraph
ALADDIN	Antarctic L-band Astrophysics Discovery Demonstrator for Interferometric Nulling
AMBER	Astronomical Multiple Beam Recombiner (at the VLTI)
AO	Adaptive Optics
AT	VLTI Auxiliary Telescope (1.8-m diameter)
BLINC	BracewelL Infrared Nulling Cryostat (for the MMT)
CHARA	Center for High Angular Resolution Astronomy (Georgia State University)
Darwin	Not an acronym—infrared space interferometer (past ESA project)
EGP	Extrasolar Giant Planet
EPICS	Exo-Planet Imaging Camera and Spectrograph
ESA	European Space Agency
ESO	European Southern Observatory
FINITO	Fringe Tracking Instrument of Nice and Torino (at the VLTI)
FLUOR	Fiber Linked Unit for Optical Recombination (at the CHARA Array)
FOV	Field Of View
FQPM	Four Quadrant Phase Mask
GPI	Gemini Planet Imager (for Gemini South)
JPL	Jet Propulsion Laboratory
JWST	James Webb Space Telescope (NASA)
KIN	Keck Interferometer Nuller
LBTI	Large Binocular Telescope Interferometer (for the LBT)
LOCI	Locally Optimized Combination of Images
MIDI	Mid-Infrared Instrument (for the VLTI)
MIRI	Mid InfraRed Instrument (for the JWST)
MMT	Multiple Mirror Telescope
MS	Main Sequence
NASA	National Aeronautic and Space Administrations
NIRCam	Near InfraRed Camera (for the JWST)
OPD	Optical Path Difference
OVC	Optical Vortex Coronagraph
PIONIER	Precision Integrated-Optics Near-Infrared Imaging ExpeRiment
PFN	Palomar Fiber Nuller (at the Palomar observatory)
PSD	Power Spectral Density
SDI	Spectral Differential Imaging
SNR	Signal-to-Noise Ratio
SPHERE	Spectro-Polarimetric High contrast Exoplanet REsearch (ESO)
TPF-I	Terrestrial Planet Finder Interferometer (NASA project)
UT	VLTI Unit Telescope (8-m diameter)
VISA	VLT Interferometer Sub-Array
VLTI	Very Large Telescope Interferometer (ESO)
WCS	Well Corrected Sub-aperture (at the Palomar observatory)
WFS	WaveFront Sensor
XAO	eXtreme Adaptive Optics (also called ExAO)
YSO	Young Stellar Object

Introduction

> *Who are we? We find that we live on an insignificant planet of a humdrum star lost in a galaxy tucked away in some forgotten corner of a universe in which there are far more galaxies than people.*
>
> Dr. Carl Sagan (1934-1996)

Whithin less than 20 years, exoplanet science dramatically changed its status. From a hypothetic subject in between science fiction and astrophysics, it became one of the most popular fields of research of modern astronomy. The reason of this success is twofold. First, finding planets and especially inhabited ones has always been a subject of fascination for researchers but also for the public. Second, answering one of mankind's biggest questions: *"Are we alone in the Universe"* would definitely put an end to the last bastion of helio-centrism left standing.

The quest for exoplanets

The beginning of the 90's has seen the kick-off of exoplanet science with the detection of the first extra-solar planets, first around a pulsar with the radio-telescope of Arecibo (Wolszczan & Frail 1992) and then shortly later around a solar-type main-sequence star (Mayor & Queloz 1995). Since these pioneering discoveries, the number of detections has increased every year to reach today a total of 529 planets detected in 440 different systems (see Figure 1, left). A large majority of these planets have been unveiled by two techniques. First, by radial velocity (RV) measurements showing small Doppler shifts in the stellar lines as the star moves back and forth due to the gravitational pull of its planet. Second, by the photometric measurement of the apparent flux variations due to the transit of the planet in front of the stellar photosphere. These two techniques have the common disadvantage of measuring the effect of the presence of the exoplanet on its environment, and especially its host star, rather than directly collecting its photons. Consequently, they will be hereafter referred as *indirect* methods in opposition to the *direct* ones including for example direct imaging.

Up to now, the detected sample of exoplanets is dominated by massive giant planets orbiting close to their stars, because the signature of their presence is easy to measure by indirect techniques (see Figure 1, right). These planets are referred to as hot Extra-solar Giant Planets (or hot-EGP) because they can be heated up to about 1000 K due to the proximity of their host star. The existence of EGPs at such small orbital distances was rather unexpected according to the classical planet formation theory, which predicted the formation of giant planets to occur further out in proto-planetary disks through core accretion mechanisms of solid particles (Pollack 1984). Indeed, only in these regions, behind the "snow line" (Sasselov & Lecar 2000), can proto-planetary cores find enough gas to accrete and become a gaseous giant planet. This accretion process, while proceeding slowly in the early phases, can eventually run away when the so-called critical mass is reached (at $\sim 10 M_\oplus$). The formation timescale of a gas giant through this mechanism was then estimated around 10 Myr (Pollack et al. 1996). This is dangerously

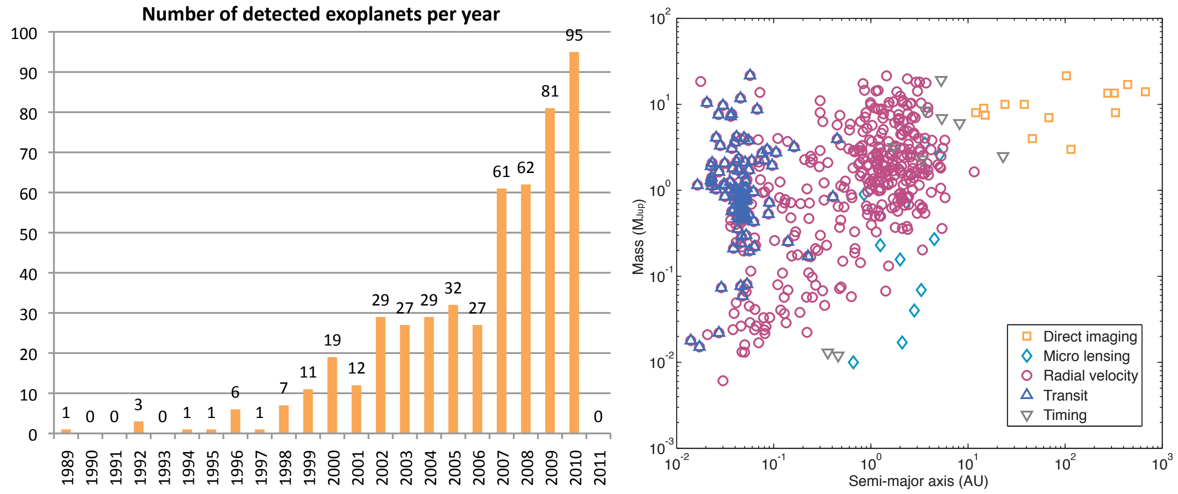

Figure 1: Left: Number of detected exoplanets as a function of the year of detection. Right: Mass of known extra-solar planets (in M_{Jup}) as a function of orbital distance (in AU). The different colors and marks correspond to different observing techniques. Data from the web site of J. Schneider: http://www.exoplanet.eu.

close to the typical lifetime of protoplanetary diks which is believed to be in the 1-10 Myr range (Haisch et al. 2001). Another possible scenario that could explain the formation of EGP within shorter timescales is based on the local gravitational collapse of the protoplanetary disk (Boss 1998). These instabilities lead to the disk fragmentation into a dense core, which then contracts to form an EGP within only hundreds of years. These two mechanisms alone are unfortunately unable to explain the presence of gaseous giant planets at small orbital separations where an insufficient amount of gas is available to form such massive bodies, and the temperature too high to allow the condensation of solid particles. So how can theory and observations be reconciled? The explanation must be found through planetary migration mechanisms. The forming planets are assumed to excite density waves that propagate on both sides of their orbit (Goldreich & Tremaine 1979; Lin et al. 1996). The torque exerted by these waves can cause the planets to migrate inwards in the disk, therefore explaining the distribution of gaseous giant planets at short orbital periods (Mordasini et al. 2009a). Figure 2 illustrates the planetary formation tracks inferred from the simulations. New core accretion models have been recently developed taking into account migration processes as well as disk evolution and gap formation. Much more rapid formations of giant planets has been inferred from these models, which are now compatible with protoplanetary disk lifetimes (Alibert et al. 2005). As a consequence, 90% of the detected planets are now consistent with core-accretion models, the remaining part being explained by disk instabilities (Matsuo et al. 2007). Mordasini et al. (2009b) have further used these models to demonstrate that if EGPs orbit around $\sim$ 7% of the stars, small rocky planets should be widespread. The planets detected so far might even represent only 9% of all existing planets around the stars that have been screened up to date.

The first two decades of exoplanet hunting have lead to many other unexpected discoveries apart from planet migration, such as: (i) the correlation between stellar metallicity and planet occurrence (Boss 2002; Johnson et al. 2010), (ii) high eccentricities of planetary orbits (Marzari & Weidenschilling 2002; Tremaine & Zakamska 2004), (iii) planets with retrograde orbits with respect to the star rotation (Queloz et al. 2010; Winn et al. 2011), (iv) non co-planar planetary systems (Scuderi et al. 2010; Barnes et al. 2011) or even the dearth of bounded brown dwarf companions. These discoveries are leading to further refinements of formation theories based for example on Kozai mechanisms causing a periodic exchange between the inclination and eccentricity of an orbits (Takeda & Rasio 2005; Nagasawa et al. 2008; Libert & Tsiganis 2009; Perets & Naoz 2009; Funk et al. 2011) or planet scattering (Ford et al. 2005).

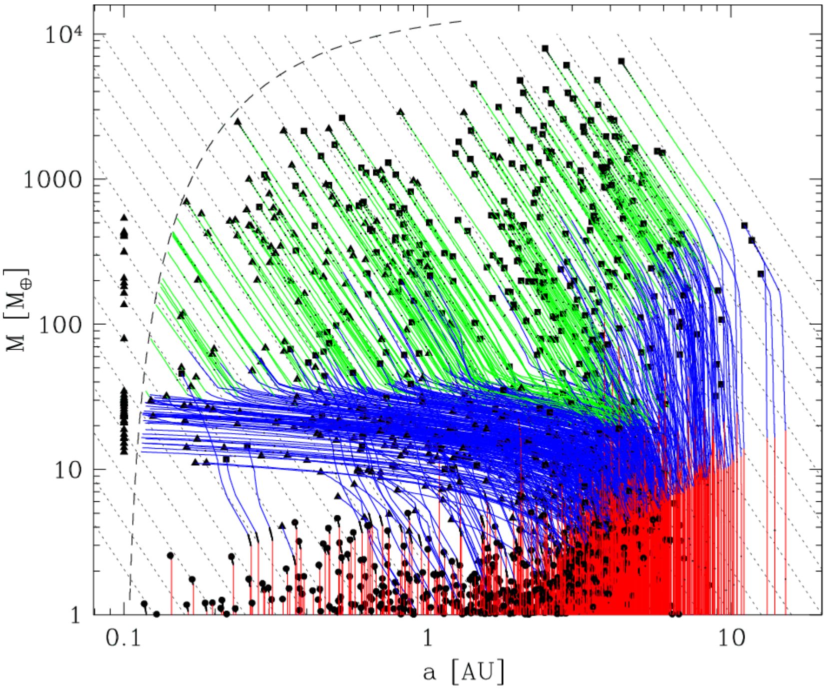

Figure 2: Planetary migration tracks in the mass-semimajor axis phasz space from Mordasini et al. (2009a). The black symbols represent the final position of a planet. Each track is color-coded according to the migration mode: Red for type I migration (Ward 1997), blue for ordinary (disk dominated) type II migration (Goldreich & Tremaine 1980; Lin & Papaloizou 1986) and green for the braking phase (Mordasini et al. 2009a).

This year will undoubtedly represent a milestone for extra-solar planet science with the recent announcement by NASA of the discovery of 1235 exoplanet candidates by the Kepler satellite (Basri et al. 2005). Among them, up to 68 may have a mass similar to that of the Earth and 54 may be potentially habitable (Borucki et al. 2011). Furthermore, 2011 will see the installation of the new generation of ground-based high contrast imagers especially designed for the direct imaging and spectroscopy of exoplanets. While not being as sensitive to low-mass planets as current radial-velocity and transit surveys, imaging techniques will complement indirect methods by probing different orbital distances and providing much needed photometric and spectrometric information on planetary atmospheres.

Evolutionary models

A first step toward the characterization of exoplanets would be the determination of the planets effective temperatures through multi-wavelength photometry, especially at young ages where their cooling history is much uncertain. Indeed, during their life, the properties of extra-solar planets evolve. The modeling of this phenomenon has been studied extensively in the case of stars and consists in solving standard conservation equations written in a spherically symmetric configuration. The rate at which the heat escapes from the planet drastically depends on both the interior and exterior (atmosphere) structures of the planet but also on their interactions (Guillot 2005). On the one hand, the impact of the composition of the planet's interior on the cooling properties and radius is based on the pioneering works of Zapolsky & Salpeter (1969) and Stevenson (1982) who respectively considered various zero-temperature single element compositions and studied H/He, ice and rock planet compositions. The current versions of planet interiors have updated these basic models with recent equations of state and by taking into account the planet irradiation from the parent star. On the other hand, Burrows et al. (1993, 1997), Baraffe et al.

(1995, 1997), and Chabrier & Baraffe (1997) have demonstrated the importance of the use of complex atmospheric codes including wavelength dependent absorptions to realistically model the atmosphere of exoplanets and generate synthetic spectra (the so-called non-grey models). Only a good combination of these two theories can lead to a proper description of the physical and thermal properties of extra-solar planets.

Planet evolution is characterized by the release of gravitational and internal energy from an initial entropy state. The problem is that this state is unknown a priori and strongly influences the modeled radius and luminosity of the planets at their early stages. Two different theories are currently being studied to set the initial conditions of evolutionary models. The first one, similar to the brown dwarf and stellar cases, assumes a high initial entropy state, i.e., a large initial radius and luminosity (Hubbard et al. 2002; Burrows et al. 1997; Baraffe et al. 2003). However, this rather arbitrary assumption of a hot initial state for planets has recently been questioned by Marley et al. (2007) and Fortney et al. (2008), who propose to use initial conditions derived from the core-accretion model. By doing so they find lower initial entropy states than aforementioned. Therefore, Fortney et al. (2008) suggest that young giant planets should be fainter and smaller than predicted by "*hot start*" evolutionary models. Such a model, based on the planitesimals core accretion history could seem to constitute a more robust hypothesis for the initial conditions. However, this approach suffers from another limitation, which is the lack of a proper treatment of the final accretion shock, that determines the nascent planet's initial energy content and radius. More complex theories implying multi-dimensional radiative transfer and hydrodynamical simulations of the accretion process are therefore required to improve the determination of these conditions. Fortunately, the choice of the evolutionary model only impacts the evolution process over relatively short timescales (a few tens of Myr) and does not change the physical properties of more mature planets. This is shown in Figure 3, which illustrates the discrepancies of the two approaches in terms of absolute magnitude as a function of the planet's age. It can be seen that at young ages, the "*hot start*" model is systematically brighter than the "*core-accretion*" one by several magnitudes, no matter the observing wavelength. This difference decreases with time and finally vanishes for ages > 1 Gyr (Fortney et al. 2008). First results obtained on young exoplanetary systems such as HR 8799 and Beta Pic seem to be more compatible with "*hot start*" like models (Janson et al. 2010; Bonnefoy et al. 2011) but results on a wider sample of stars is required and a large amount of work still needs to be done. In the near future, ongoing surveys looking for exoplanets within young moving groups will give us the much needed spectral and photometric information to constrain the initial conditions of evolutionary models.

Spectroscopy and habitability of exoplanets

But the most most exciting goal of exo-planetary science is certainly the spectroscopic characterization of Earth-like rocky planets that may host life. While super-Earth size planets have already been detected (e.g. Gl581e, Mayor et al. 2009), a planet displaying spectral signature of biological activity has not yet been characterized. However, the signature of several molecules has already been identified around hot giant exoplanets and the sensitivity of current methods improves rapidly toward the characterization of smaller and cooler planets which we think are more favorable to the development of life.

But what are the conditions that a planet should fulfill in order to host life? If this question is impossible to answer in an absolute way, considering our geocentric-limited knowledge, the essential elements that are mandatory for the development of life as we know it are relatively well known. First of all, the planet must be located in the so-called *habitable zone* of its parent star. This zone, typically centered around 1 AU for a Sun-like star, is the region within which a planet can sustain liquid water on its surface (Kasting & Catling 2003). But all the planets within a HZ are not necessarily habitable. They also need to be massive enough to accrete and maintain an atmosphere ($> 0.5\,M_\oplus$) but small enough

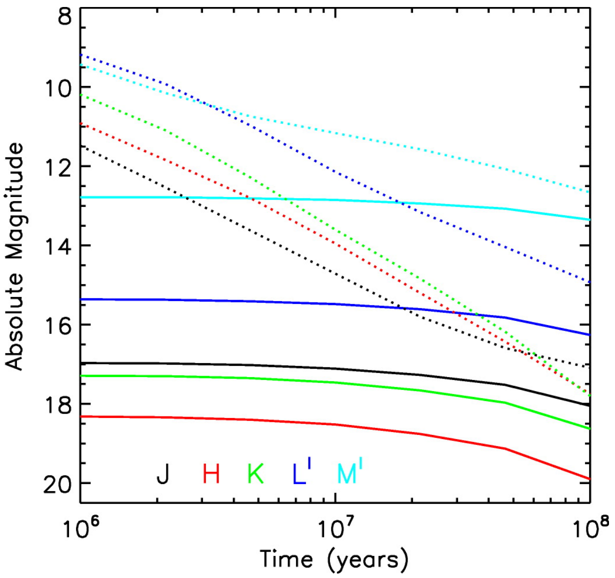

Figure 3: For different wavebands, comparison between the absolute magnitude evolution of a $4M_{\rm Jup}$ planet computed with a "*hot start*" model (Baraffe et al. 1998, 2008) (dashed lines) and a "*core-accretion*" model (Hubickyj et al. 2005; Marley et al. 2007; Fortney et al. 2008) (solid lines). Figure from Fortney et al. (2008).

to avoid the evolution of the planet into a gazeous giant planet ($< 8\,M_\oplus$), on which water cannot be kept liquid. The third requirement is that the planet must contain a certain number of elements which are the building blocks of life. Until recently, it was thought that these elements were only including carbon, hydrogen, nitrogen, oxygen, phosphorus and sulfur but Wolfe-Simon et al. (2010) have milded this statement and demonstrated that under some conditions, phosphorus could be replaced by arsenic. In order to determine if a planet is inhabited, its atmosphere must therefore be probed to search for the spectral features that are specific to biological activities, i.e. biosignatures. Based on the aforementioned conditions, several elements have been identified as potential biosignatures: (i) water vapour (H_2O) is the indicator for the presence of liquid water, (ii) carbon-dioxide (CO_2) is requided for photosynthesis, (iii) methane (CH_4) is more controversy because it can be made by non-biological processes and only suggests the presence of life, and (iv) oxygen (O_2) or ozone (O_3) are probably the best indicators for the presence of an atmosphere modified by biological activities (Léger et al. 1999; Selsis et al. 2002). Detecting a combination of these elements in the atmosphere of an exoplanet and especially O_3 and H_2O would constitute a relatively robust signature of biological activity as no purely abiotic process producing these elements has been identified yet.

Detecting spectral features of extrasolar-planet atmospheres requires the detection of photons from the planet (either transmitted, reflected or emitted). It is a very difficult task because such features are faint and difficult to disentangle from both the parent star emission and the telluric spectral lines (in the case of ground-based observations). Two techniques can be used to measure exoplanet spectra: direct imaging, which is the most promizing but has not reached yet the required sensitivity for exoplanet spectroscopy yet, and photometric measurements of transiting planets. Indeed, when a planet passes in front of its star (primary transit), a fraction of the light is simply blocked by the planet but a part of it is transmitted through its atmosphere. Multi-wavelength observations of the photometric depth during the transit can therefore lead to the detection of atmospheric absorptions. Equivalently, when the planet is occulted by the star (secondary transit), only the flux coming from the star is collected. By comparing this spectroscopic signal to the one obtained just before the transit, it is possible to measure the emitted spectrum of the planet. The first detection of the infrared emission of an exoplanet was accomplished in 2005 with the Spitzer space telescope (Deming et al. 2005; Charbonneau et al. 2005).

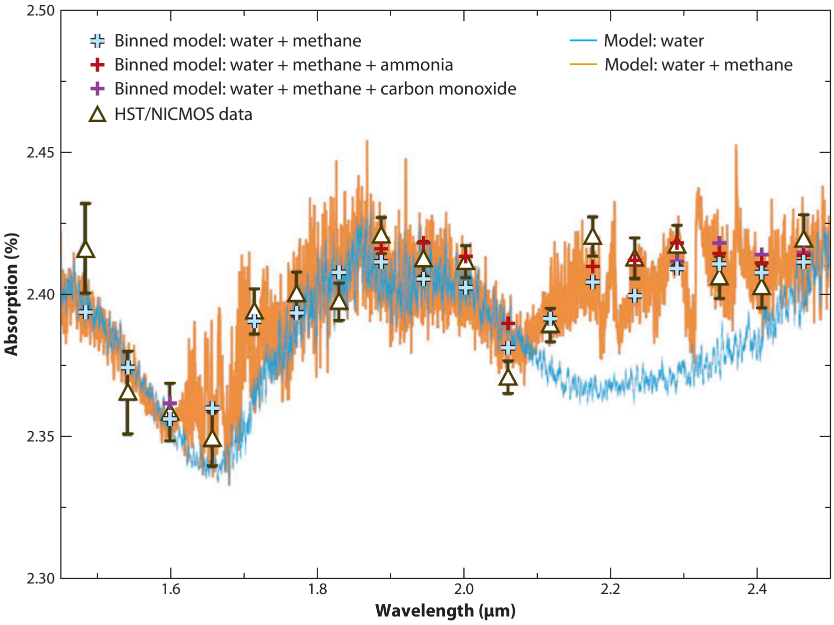

Figure 4: Transmission spectrum of the transiting planet HD 189733. Hubble Space Telescope observations correspond to the white triangles. Two different models highlight the presence of methane in the planetary atmosphere. From Swain et al. (2008).

Since this breakthrough discovery, several tens of planetary spectra have been measured with Spitzer and/or HST both during primary and secondary transits, and many spectroscopic analyses of exoplanet atmospheres are now available. These analyses have lead to the discovery of important elements such as atomic sodium (Na) (Charbonneau et al. 2002; Redfield et al. 2008), methane (CH_4) (Swain et al. 2008), water vapor (H_2O) (Swain et al. 2008), carbon monoxide (CO) and carbon dioxide (CO_2) (Swain et al. 2009a,b; Madhusudhan & Seager 2009) around hot giant exoplanets. This set of molecules has been detected in the two most favorable hot Jupiters for observation (HD 189733b and HD 209458b). Figure 4 shows a comparison between the observed and modeled transmitted spectra of HD 189733b for different simulated compositions (Swain et al. 2008). This striking result must however be mitigated as recent analyses claim that these data do not show significant evidence for molecular features as the uncertainties on the photometry claimed by Swain et al. (2008) are underestimated (Gibson et al. 2010). In the near future, observations of transiting planets with the James Webb Space Telescope or with ECHO/THESIS (a space-based telescope aiming at taking spectra of transiting exoplanets located in the habitable zone of their star, Swain et al. 2010) should allow us to characterize the atmosphere of potentially habitable super-Earth planets orbiting around cool dwarf stars.

Direct imaging: Earth-like worlds in the line-of-sight

Direct imaging of exoplanets gives access to a handful of information on the observed system as it can provide both the orbital position of the planet and its spectrum. It is however a difficult detection to make because of the small angular separation between the star and its planet and the flux ratio between them. For these two reasons, direct imaging of exoplanets has up to now been limited to the most favorable case of (bright) giant exoplanets ($M > 3M_{\mathrm{Jup}}$) orbiting at large distances (> 10 AU) from their host stars (see Figure 1). Indeed, the faint dot representing the image of an Earth-like planet around a solar-type star is $\sim 10^7$ (mid-IR) to $\sim 10^{10}$ (visible) fainter than its parent star. This already challenging task is made even more difficult by the optical imperfections (so-called speckles) corrupting the image of the

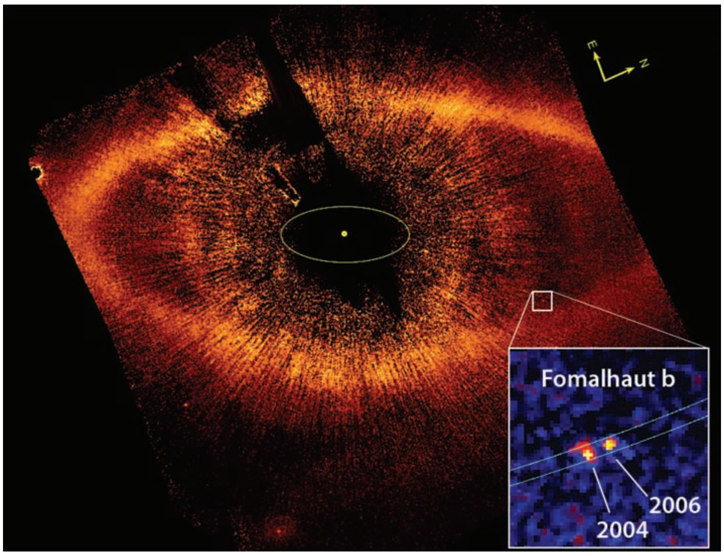

Figure 5: HST coronagraphic image of Fomalhaut at 0.6 μm, showing the location of Fomalhaut b (white square) 12.″7 away from the star and just within the inner boundary of the dust belt. Figure from Kalas et al. (2008).

scene and by the presence of dust belts around the stars which can potentially outshine the planetary signal. The second issue that one has to face to resolve such a system is the small angular separation between the planet-star couple, which is only of 0.″1 for an exoplanet orbiting at 1 AU around its parent star at 10 pc. The image of Kalas et al. (2008) from the Fomalhaut exoplanetary system (Figure 5) is a perfect illustration of the challenge that direct imaging of extra-solar planets has to face and of our current limitations. The system is composed of a ~ 2.5 Jupiter mass planet located 12.″7 (~ 115 AU) away from Fomalhaut, a closeby (7.69 pc) and young (~ 200 Myr) A3V star. The image displays a pale white dot surrounded by a bright circumstellar disk and bright residual speckles. The detection has been made possible by monitoring the trajectory of the dot over the years, which has confirmed the nature of the point-like off-axis source.

To overcome the two aforementioned difficulties and detect habitable planets, it is therefore mandatory to use instruments combining a high resolving power and the capability to dim the light of the central star. Over the years, three technical solutions have emerged:

Coronagraphy: First proposed by Lyot (1939) to observe the Sun's corona. A coronagraph consists in the installation of a sequence of masks in the focal and/or the pupil plane of a telescope to dim the on-axis starlight and reveal faint off-axis structures around the star. Today, several next generation coronagraphic instruments, both from the ground and from space, are especially designed for the direct imaging and spectroscopy of extra-solar planets, such as SPHERE (Beuzit et al. 2008), GPI (Macintosh et al. 2008), P1640 (Hinkley et al. 2010), HiCIAO (Tamura et al. 2006), EPICS (Kasper et al. 2008; Vérinaud et al. 2008), MIRI (Wright et al. 2004) and NIRCam (Rieke et al. 2005b). These facilities should ultimately be able to characterize planets down to a few Earth masses (the so called super-Earths) located in the habitable zone of their stars.

Nulling interferometry: Nulling interferometers combine destructively the light coming from separated apertures to suppress the starlight. Baselines of several hundreds of meters can be used with interferometry allowing extremely high angular resolutions to be reached. This concept, first proposed by Bracewell (1978) is particularly well suited for observing in the mid-infrared where the planet/star contrast ratio is more favorable and the loss of angular resolution due to the use of a longer wavelength requires the use of multiple apertures. Both ESA and NASA have proposed space missions based on nulling interferometry for the characterization of habitable Earth-twins in the mid-IR (i.e., Darwin and TPF-I respectively). Other facilities such as the gound-based Keck Interferometer Nuller (Serabyn et al. 2004) and the Large Binocular Telescope Interferometer (Hinz et al. 2004) are currently being used to characterize circumstellar environments and prepare these ambitious long term projects.

External occulters: Unlike classical coronagraphs which block the starlight inside the optical train of the instrument, the external occulters, or starshades, use an opaque occulting mask located thousands of kilometers away from the telescope to block the starlight before it reaches its primary mirror. The interest is to avoid/minimize the propagation of diffracted and scattered residual starlight within the optics of the telescope. Such an occulter is under study by NASA to be used in combination with the James Webb Space Telescope (Soummer et al. 2010).

Considering the rapid scientific and technical progress that has been achieved within 15 years in the field of exoplanet science, and the huge interest of the public for this topic, we can be confident in the fact that, within the next decade or two, ambitious ground- and space- based instruments inspired from these techniques will give images and spectra of Earth-like exoplanets. Even more interestingly, these exoplanet surveys will possibly report evidences for the presence of life (bio-signatures) on them. The present thesis is dedicated to the study and the development of these techniques in the context of extra-solar planet imaging.

Objectives and outline of this work

Because they have both the required angular resolution to separate an exoplanet from its star and the dynamic range necessary to extract a faint off-axis signal from a bright on axis one, high angular resolution and high dynamic imaging techniques are the best suited to characterize exoplanets dynamically and spectroscopically in order to unambiguously find biosignatures. However, much development still needs to be done to reach this holy grail. The present thesis aims at developing new and existing direct imaging techniques including coronagraphy and nulling interferometry in order to detect and characterize Earth-like worlds.

This manuscript is divided into two main parts dedicated to single- and multi-aperture imaging. For each technique, we will first introduce their principle and discuss the challenges involved. In Chapter 1, we recall the basic principles of single-aperture high contrast imaging including wavefront corrections and coronagraphy, and explain the advanced signal processing methods that have been developed to optimize the sensitivity to exoplanet detections. A brief overview of the current and future coronagraphic facilities is then given. This chapter then compares the sensitivities of ground- and space-based coronagraphic planet imagers and illustrates the results in the case of a survey of low-mass stars within young moving groups. The wavefront corrugations due to the atmosphere turbulence constitute one of the main limitation of high angular resolution imaging. Current state-of-the-art instruments include adaptive optics systems that correct for wavefront perturbations. This correction is however limited by the number of active elements being involved. In Chapter 2, we present a technique that can be used to optimize the correction provided by current AO systems onto a small portion of a telescope in order to get extremely sharp images. Such an instrument anticipates the performance of next-generation AO systems and allows near-infrared diffraction-limited observations to be obtained from the ground. We also present two different ways of using this technique to take images faint-companion.

The second part is then dedicated to multi-aperture imaging, also called interferometry. This technique, which provides much higher angular resolution than single telescopes, may allow the observation of planets in the habitable zone of their stars at longer wavelengths (e.g., in the mid-IR), where the planet emission peaks up. After introducing the theory of stellar and nulling interferometry, we briefly review the various ground-based interferometers being currently operated (Chapter 3). The problem that all interferometers have to face is the difficulty to perform accurate measurements and calibrations, as they are also strongly corrupted by atmospheric turbulence and instrumental drifts. Chapter 4 describes the current limitation of traditional data reduction methods and presents a new method based on statistical distribution aiming at improving the accuracy of interferometric measurements. Despite their current limitations, stellar interferometers can still, in favorable cases, detect sub-stellar companions and even giant exoplanets. In Chapter 5, we describe the survey that we are currently performing with the AMBER instrument at VLTI among late-type stars within young moving groups, for which the star/planet contrast is lower. However, classical stellar interferometers are always limited by the photon noise and systematic biases related to the stellar contribution, and nulling interferometers may bring a significant gain by dimming the starlight. This is why we developed a nulling testbed called CELINE aiming at testing key technologies for future ground or space-based nullers (see Chapter 6). An instrument based on a similar principle, the Palomar Fiber Nuller (PFN), has been developed at the Jet Propulsion Laboratory and is being used at Palomar observatory. In Chapter 7, we briefly describe the principle of this instrument and present the first scientific results obtained so far: (i) the accurate measurement of 8 giant-star diameters and (ii) upper limits on the presence of a debris disk or a companion around Vega.

Even though this manuscript has been divided into two parts, the limit between coronagraphy and (nulling) interferometry is not so clear. The PFN, for example, which recombines two sup-apertures of a single telescope could be seen as a nulling coronagraph. To conclude this manuscript, we introduce a technique that fills even more the gap, by introducing a coronagraph at the combined focus of an interferometer. By combining this principle with the statistical data analysis described in Chapter 4, it is demonstrated that extremely accurate stellar angular diameters can be measured.

Part I

Direct imaging of exoplanets with single aperture telescopes

1

An overview of single-aperture high contrast imaging

Contents

1.1 Principle of high contrast imaging 16
  1.1.1 Wavefront corrections 16
  1.1.2 Coronagraphs: getting rid of the starlight 18
  1.1.3 Differential imaging: a solution for quasi-static noise 19
1.2 Ground- and space-based coronagraphic facilities 21
  1.2.1 Facilities from the 1990s and 2000s 22
  1.2.2 Next generation of instruments 22
1.3 Extra-solar planet imaging: ground- vs. space-based coronagraphs 25
  1.3.1 Young main sequence stars: the ideal targets for direct imaging 25
  1.3.2 Simulated sensitivities of coronagraphic observatories 26
  1.3.3 Performance comparison and perspectives 27

Direct imaging of extra-solar planets is still in its infancy. Until today, only a handful of systems have been imaged thanks to the small values (a few thousands or less) of the flux ratio and the large angular separation between them. These pioneering results have been made possible thanks to the advent of adaptive optics-aided 8-10 meter class telescopes, which are able to correct the atmospheric-induced wavefront corrugations to provide sharp, high angular resolution images. More recently, advanced data reduction methods have been developed to further suppress the stellar scattered light and enhance the sensitivity of current facilities. In this chapter, we first introduce the basic principles of high angular and high contrast imaging. Then, after having introduced the aforementioned data reduction techniques, we assess and compare the sensitivities of upcoming ground- and space-based coronagraphic facilities for exoplanet detection.

1.1 Principle of high contrast imaging

Spatially resolving a planet from its much brighter host star is a very difficult task for two reasons. First, the angular separation between them is small, typically $0.''1$ for a planet with an orbital semi-major axis of 1 AU and located at 10 pc. Second, the flux ratio between them is huge, typically $\sim 10^7$ in the thermal IR and 10^{10} in the visible for an Earth-twin orbiting a solar-type star. In the following sections, we describe different techniques aiming at addressing these issues: adaptive optics on the one side, coronagraphs and differential imaging on the other side.

1.1.1 Wavefront corrections

The image of a point source through an aberration-free optical system is not a point but rather a diffraction pattern. For a telescope composed of a circular primary optics of diameter D, this pattern, also called point spread function (PSF), is ring-shaped and is known as the Airy-pattern. The resolving power of the system, which defines the smallest angular distance between two sources that can be resolved, is given by the half-width of this diffraction pattern and is $1.22\,\lambda/D$ where λ is the wavelength of observation. Over the years, telescopes of increasingly larger diameter have therefore been built, both to improve the angular resolution and increase the collecting area (and therefore the sensitivity). Unfortunately, when the light from an astronomical object enters the Earth's atmosphere, the atmospheric turbulence (induced for example by temperature gradient and wind) strongly distorts the image. If the influence of this phenomenon is minor for small size telescopes (typically < 1 m in diameter when observing in the near-IR), the short exposure images produced by larger telescopes are diffused and composed of bright compact structures (also called speckles) having the same width as the telescope's theoretical PSF. For long exposures observations these fluctuating random speckles average out to create a broad and diffuse PSF (see Figure 1.1). This corrugation of the wavefront has two consequences for high-angular and high-contrast imaging. First, for long exposures, most of the high angular resolution information is lost, which prevents from resolving two closeby objects. For short exposures, Labeyrie (1970, 1995) has demonstrated that short-lived speckles could be used to retrieve the high angular resolution information and take im-

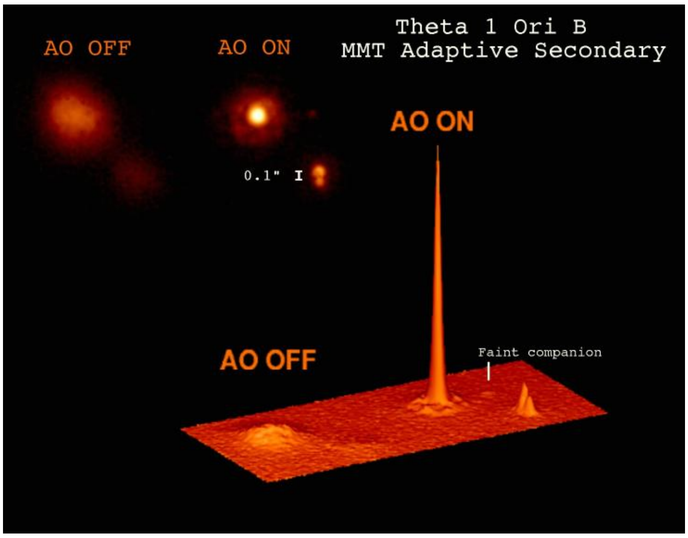

Figure 1.1: Illustration of the wavefront correction provided by a classical AO system. When the AO is turned off, the image seems to be composed of a binary system. Once turned on, two additional stars appear in the image, one of them being a faint companion compared to the primary. Photo Credit: Laird Close, CAAO, Steward Observatory (lclose@as.arizona.edu)

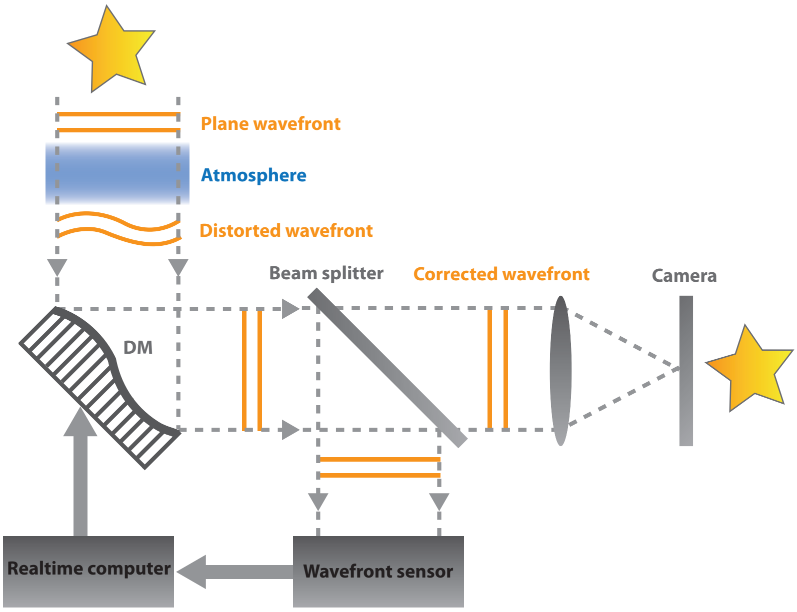

Figure 1.2: Schematic representation of the principle of an adaptive optics system.

ages of exo-planets but at the expense of a limited sensitivity. Second, the diffracted stellar light can outshine the presence of potential faint companions. Moreover, in addition to the fast fluctuating random speckles, optical defects in the optics create quasi-static speckles that can also mimic the signature of an exo-planet.

The solution, envisioned by Babcock (1953) and which has been applied for the first time in astronomy by Rousset (1997) with COME-ON on the 3.6 m telescope of La Silla Observatory (ESO) is called Adaptive Optics (AO). Its principle is the following (see Figure 1.2). The corrugated wavefront coming from the star first hits a deformable mirror (DM). Then a beamsplitter sends a fraction of the light to the scientific camera and the rest of it to the wavefront sensor. The latter measures the residual wavefront errors and transmits the information to a computer which determines the optimal shape to give to the DM for minimizing these residuals. Finally, the commands are sent to the actuators of the DM. In order to leave enough light to the scientific channel while optimizing the sensitivity of the AO system, the wavefront sensors (WFS) generally operates at a different (shorter) wavelength than the science instruments. Several aspects limit the performances of the AO system, such as the latency between the wavefront sensing and the action on the DM or the non common path errors between the technical and scientific beams. But the two major limitations of current AO systems are: (i) their sensitivity. Most AO systems can only track relatively bright stars with $V < 10$. A possible solution consists in the use of a laser guide star (LGS) as a reference star for the wavefront sensor (Primmerman et al. 1991; Wizinowich et al. 2006), (ii) the number of actuators driving the DM. Indeed, the wavefront quality provided by AO systems, usually expressed in terms of Strehl ratios[1], directly depends on the actuator density. For the current generation of adaptive optics, this density is around 4 actuators per square meter of collecting area and leaves residual wavefront errors around 300 nm rms, which corresponds to Strehls around 40% in the near IR (H and K bands). Such an image quality, even though sufficient to retrieve most of the high spatial frequency information, is a big limitation for high contrast imaging as 60% of the stellar light is still diffracted into off-axis speckles (short exposure) or into a halo (long exposure), potentially hiding the presence of faint companions in the star's vicinity. With the evolution of the technologies over the

---

[1] The Strehl ratio is the ratio of peak diffraction intensities of an aberrated vs. a perfect wavefront and can also be computed from the measured rms wavefront error (here-after σ) using the expression $S = e^{(-2\pi\sigma/\lambda)^2}$, where λ is the wavelength. The approximation is accurate to a couple of percent for RMS errors of $\sim \lambda/10$. From this definition, an image is conventionally considered as being diffraction limited when the Strehl is above 80%.

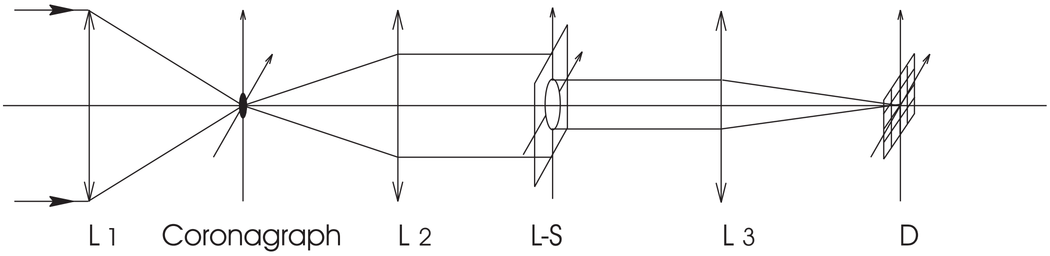

Figure 1.3: Classical coronagraphic bench layout. L1, L2 and L3 correspond to converging optics, L-S is the Lyot-stop (a pupil mask) and D is the detector array.

years and the power of computers in particular, adaptive optics systems disposing of much higher actuator density are being developed (Dekany et al. 2006; Bouchez et al. 2010; Beuzit et al. 2008; Macintosh et al. 2008). These facilities, also called extreme adaptive optics or XAO, will provide in the near future diffraction limited images of tremendous quality with Strehl ratios of 90% (Beuzit et al. 2008; Macintosh et al. 2008).

1.1.2 Coronagraphs: getting rid of the starlight

Space-based telescopes alone or ground-based ones aided by AO systems are great because they provide images of extremely good quality, enabling high-angular resolution studies. However, a perfect wavefront alone is not sufficient for detecting telluric extra-solar planets: due to the huge contrast, the stellar light must be dimmed. Indeed, the stellar signal largely outshines the million times fainter planets orbiting around it. The coronagraph, first introduced by Bernard Lyot in the 30's (Lyot 1939) was originally designed to block light coming from the Sun's photosphere and observe its corona without having to wait for a total eclipse. It consists in blocking the on-axis light of a telescope beam while permitting the light from surrounding sources to pass through the optical system. The basic principle of coronagraphy is relatively simple (see Figure 1.3). The light enters the telescope aperture and illuminates the primary uniformly. A converging optics (L1) images the light, and here where a camera or detector would usually record the image, an occulting spot, or focal plane mask, is placed instead. L1 must ideally be chosen with a large F/d ratio (where F is the focal length and d the diameter of the beam) in order to minimize spatial defects. The mask absorbs most of the light from the center of the field of view (FOV),. When the pupil is re-imaged by another lens (L2), any remaining light from the central source is concentrated around the edges of the telescope pupil. Next, the Lyot-Stop (L-S) blocks out the stellar light diffracted on the pupil edges while allowing most of the light of surrounding sources to pass through the system. Finally a converging optics (L3) forms the coronagraphic image on the detector.

There are two different families of coronagraphs. The first kind includes opaque masks physically blocking the starlight. They are called amplitude coronagraphs and include standard and apodized Lyot coronagraphs (Soummer 2005) and band-limited coronagraphs (Kuchner & Traub 2002). The second one makes use of the phase to create destructive interferences for the on axis light: they are phase mask coronagraphs. The Four Quadrant Phase Mask (FQPM, Rouan et al. 2000; Riaud et al. 2001, 2003; Boccaletti et al. 2004), the Annular Groove Phase Mask (AGPM, Mawet et al. 2005b) and the Optical Vectorial Vortex Coronagraph (OVVC, Mawet et al. 2009) are some examples of phase mask coronagraphs. Between these two antagonistic families are the hybrid masks, taking advantage of the two principles to enhance the rejection (Baudoz et al. 2000).

The main characteristics of a coronagraph are its rejection and its Inner Working Angle (IWA). Whereas the latter, expressed in terms of λ/D, only depends on the design of the coronagraph, the total rejection provided by a coronagraphic instrument strongly depends on the wavefront quality feeding the instrument. Indeed, as already mentioned in Section 1.1.1, when a corrugated wavefront is collected by a telescope, the image being formed is blurred and only a small fraction of the energy is located in the central peak of the PSF, which substantially degrades the coronagraph's ability to remove the starlight. For this reason, the use of adaptive optics is mandatory for the detection of faint off-axis objects with ground-based coronagraphs. As an example, the performance of the current generation of AO systems limits the raw peak rejection of coronagraphs to a couple of hundreds. In the upcoming years XAO systems will dramatically improve the performance of ground-based coronagraphs, making them much more efficient for imaging surveys of extra-solar planets.

1.1.3 Differential imaging: a solution for quasi-static noise

Noise is always present in an observation, no matter the instrument being used. For ground-based imaging, short-lived speckles produced by the atmospheric turbulence add to the classical Poisson noise and mask faint companions. If these two noises were the only ones, increasing the integration time (t_i) would average out these random noises and the gain in SNR would be proportional to $\sqrt{t_i}$. Unfortunately, it has been shown that the PSF noise does not fluctuate randomly over the time but,x instead, converges into quasi-static noise patterns, thus preventing a gain with increasing integration time (Marois et al. 2003, 2005; Masciadri et al. 2005). To suppress the PSF noise and improve the detection limit, it is necessary to subtract the quasi-static noise using a reference PSF. In this section, we present different differential imaging methods that have been developed for this purpose.

Spectral differential imaging (SDI) is a PSF subtraction technique that can be efficient over the whole field of view. It consists in the simultaneous acquisition of images in adjacent narrow spectral bands within a spectral range where the star and planet spectra differ (Smith 1987; Racine et al. 1999; Marois et al. 2000; Lafrenière et al. 2007a). By computing the difference of two images, the signature of the companion can be easier to retrieve. Indeed, quasi-static speckles result from the diffraction of the stellar light and have therefore the same spectral signature. Moreover, main sequence stars have rather smooth spectra while Jovian planets for example exhibit very strong CH_4 absorption bands lying in the near IR (see Figure 1.4, left). By subtracting the image recorded in different narrow bands, it is therefore possible to strongly attenuate the stellar PSF and their speckles while leaving the planetary signal intact. For an optimal result, a number of precautions must be taken. First, the geometry of the frames taken at different wavelengths must be rescaled as the dimension of the speckle pattern is proportional to the wavelength. Second, the fractional difference between filter wavelengths must be small to minimize the residuals caused by the evolution diffraction pattern with wavelength. Third, the fractional bandpass of the filters must be similar in order to minimize the difference of speckle chromaticity dispersion between the frames. Another limitation of such a technique is the dependency of spectral features on the temperature of the planet. Figure 1.4, shows a comparison between the spectrum of a *"cold"* ($T_{\rm eff} \sim 130\,$K) and a *"hot"* ($T_{\rm eff} \sim 1000\,$K) exoplanet. If the contrast between the flux in the H_2 (1.5953 μm) and H_3 (1.667 μm) bands is high for cold planets (1 : 100), it is not the case for planets having a high effective temperature ($T_{\rm eff} > 500\,$K). For those planets, SDI can still be used to subtract the speckle but the discovery space is restricted to large angular separations. Indeed, before subtraction, the images taken in the two filters must be rescaled in order to super-impose the wavelength-dependent diffraction pattern. However, the image of the planet is always located at the same separation. When rescaling the frames, the position of the planet is therefore modified by $\theta\,\Delta\lambda/\lambda$, where θ is the angular separation between the planet and the star, λ is the observation wavelength and $\Delta\lambda$ is the difference between the filter wavelengths. When this quantity is larger than the PSF FWHM, the rescaled images of the planets taken in the different filters are no longer superimposed and are therefore not subtracted in the difference image.

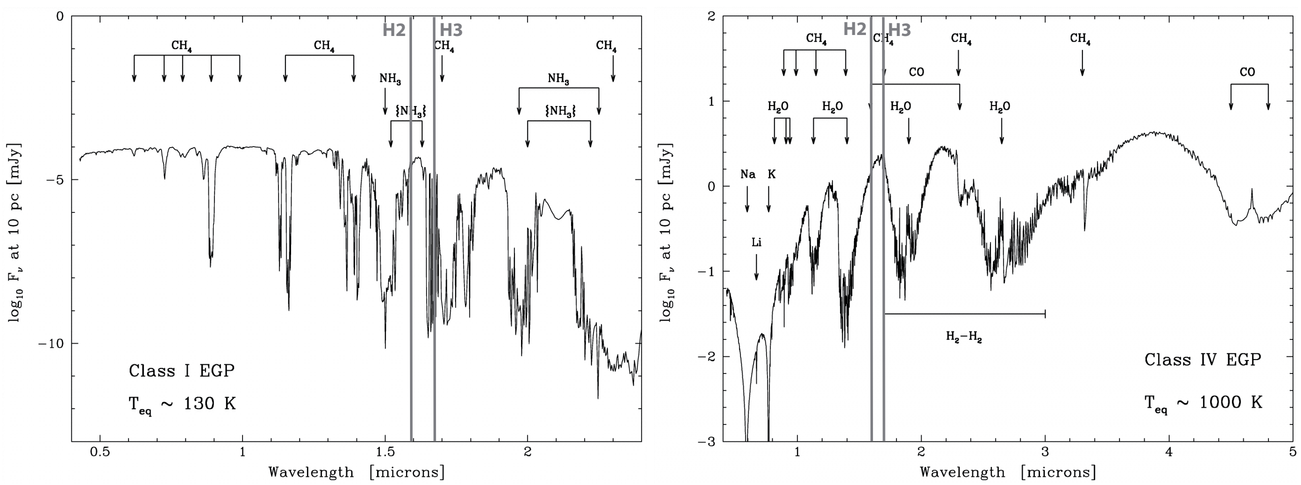

Figure 1.4: *Left:* Emergent spectrum of a class I (*"Jovian"*; ~5 AU) extrasolar giant planet (EGP). *Right:* Emergent spectrum of a class IV EGP orbiting at ~0.1 AU. While the first one displays deep narrow absorption lines which makes it an ideal candidate for SDI, the second one has much broader features. The flux ratio between the H_2 and H_3 bands, commonly used for SDI is weak in this case and the technique is not efficient. Figures from Sudarsky et al. (2003).

A second speckle subtraction technique is the Angular Differential Imaging (ADI, Marois et al. 2006). In this method, a sequence of observations are taken with a telescope mounted on an Alt-Azimuthal mount whose field derotator is switched off. By doing so, the telescope and its instrument remain aligned and the field-of-view rotates with respect to the instrument while keeping the quasi-speckles at the same place. For each image, a reference PSF is constructed from other images of the same sequence and subtracted to remove quasi-static structures. All residual images are then rotated to align the field and are summed. On-sky results have shown that PSF speckles can be reduced by a factor of 5 using this technique (Marois et al. 2006). While being immune to the planet spectrum (unlike SDI), ADI performs better at large angular separations and/or larger field rotation as the displacement of planet on the detector must be sufficient to separate it from the speckles.

While the light emitted by a star, and therefore its speckles, is not polarized, the one scattered by dust grains in circumstellar disks or by a planet can be significantly polarized. A third solution for efficient PSF subtraction is therefore to divide the collected light into its two linear polarization components and to subtract them. This solution, described by Kuhn et al. (2001) is capable of tracing scattered light very close to the central star.

Last, Lafrenière et al. (2007b) recently developed an algorithm for PSF subtraction in high-contrast imaging. The principle of this algorithm, called LOCI (Locally Optimized Combination of Images) is to generate an optimal artificial PSF from a set of reference images and then to subtract this PSF from the scientific image. The building process of this PSF is the following. First a set of reference images are taken in an instrumental and observational configuration that is as close as possible from the scientific observation. The use of ADI, if available, is an ideal solution but the technique can also be applied to SDI or to different discrete FOV orientations. The images are then divided into multiple sub-sections of rings (see Figure 1.5). For each of them, an artificial portion of the PSF is built independently as a linear combination of the reference images available for minimizing the residual difference with the target image into a larger *"optimization"* subsection. The application of LOCI to ADI brings a factor of up to 3 improvements over the algorithm proposed by Marois et al. (2006) at small angular separations where ADI is the least efficient (Lafrenière et al. 2007b). The technique is now being widely used in exoplanet AO surveys and has led to the imaging of several exo-planetary systems, among which the famous HR8799 hosting at least 4 planets (Marois et al. 2008; Serabyn et al. 2010).

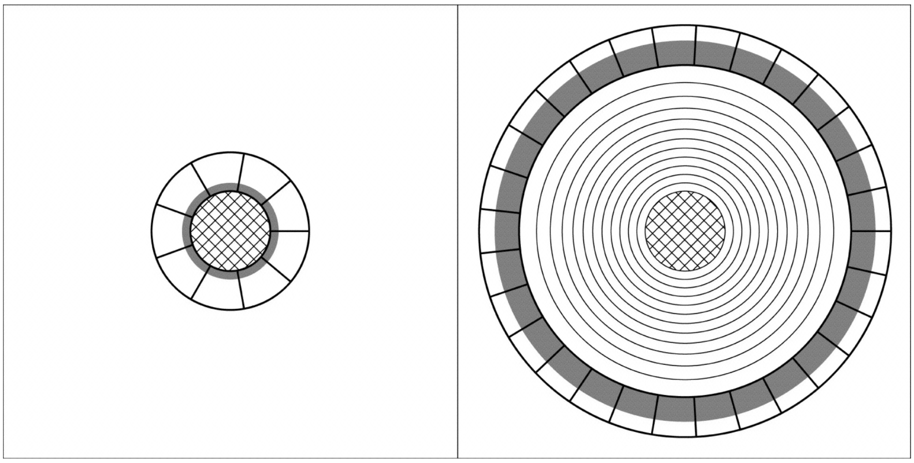

Figure 1.5: Illustration of the principle of the LOCI PSF construction process. The set of reference images are linearly combined to minimize residuals with the scientific image inside the optimization subsection (delimited by thick lines). This linear combination is then used to build the reference PSF inside the subsection delimited by the gray shaded area. The left and right panels show the subtraction and optimization subsections for the 1st and 13th subtraction annuli, respectively. Image taken from Lafrenière et al. (2007b).

1.2 Ground- and space-based coronagraphic facilities

Ground- and space-based instruments aimed at achieving high-angular resolution imaging with a high-dynamic range have to face very different issues. On the one hand, ground-based telescopes of large sizes (see Table 1.1) are being built since the second half of the twentieth century but are limited by the presence of the Earth atmosphere. The latter strongly corrupts the formation of sharp images for these optical telescopes but also restricts the range of observing wavelengths to the visible and near infrared. At longer infrared wavelengths, (typically $> 4\,\mu$m), water absorption and thermal background emission strongly reduce the sensitivity of ground-based observatories. On the other hand, space-based observatories are intrinsically limited in terms of size by the rocket fairing they must fit in, but are neither limited in wavelengths nor by atmospheric perturbations. As a result, stable diffraction-limited observations can be performed from the visible to the thermal IR where the emission of extra-solar planets peaks.

However, since the mid 90's and the installation of the first AO on a scientific telescope (Rousset 1997), astronomers are able to collect high-angular resolution images from ground-based telescopes. Thanks to this breakthrough progress, coronagraphic instruments have been developed and installed on most of the large telescopes to take advantage of the sharpness of the collected images to dim the bright central object and observe its immediate environment with an unprecedented sensitivity. Until today, this technology was limited by the computation speed of computers that restricted the number of active actuators of adaptive optics systems. Because the quality of wavefront correction strongly depends on this number, the Strehl ratios of ground-based telescopes were limited to 40-50 % in the near-IR. This level of wavefront correction, even though being an important improvement, significantly limits the performance of coronagraphs, as a fraction of the stellar light is diffracted into bright speckles. With the increasing power of modern computers, a new generation of AO (so called Extreme-AO system or XAO) with a much higher density of actuators is coming with expected Strehl ratios $> 90\%$. XAO equipping large telescopes with apertures of 8 m or more now makes ground-based facilities competitive with space-based ones. In this section, we briefly introduce the main current and future coronagraphic facilities.

Table 1.1: List of all optical ground-based telescopes with a primary mirror larger than 5 m in diameter. Note that unlike classical telescopes, the Hobby-Eberly and Salt telescopes do not move themselves to track the night sky; instead, the instruments at the focus are moved across the face of the unmoving mirror, allowing a single target to be tracked for up to two hours.

Name	Location	Diameter (m)	Latitude	Altitude (m)	Year
LOMO	Zelentchuk (Caucasus)	6	47° N	2070	1972
Hale	Mt. Palomar (California)	5	34° N	1706	1948
LBT	Mt. Graham (Arizona)	2 × 8.2	32° N	3266	2007
Hobby-Eberly	Mt. Locke (Texas)	9.2	30° N	2076	1997
GranTeCan	La Palma (Canaria)	10.4	28° N	2370	2008
Keck	Mauna Kea (Hawaii)	2 × 10	19° N	4200	1994
Subaru	Mauna Kea (Hawaii)	8.4	19° N	4200	1999
Gemini N.	Mauna Kea (Hawaii)	8	19° N	4200	1994
VLT	C. Paranal (Chile)	4 × 8.2	23° S	2650	1998
Magellan	Las Campanas(Chile)	2 × 6	29° S	2280	2002
Gemini S.	C. Pachon (Chile)	8.1	30° S	2738	2001
Salt	Sutherland (South Africa)	11.1	32° S	1783	2005

1.2.1 Facilities from the 1990s and 2000s

Since the implementation of the first AO system on a scientific telescope, many observatories have taken advantage of the improved wavefront quality to block the starlight by means of coronagraphs. Among the largest telescopes, we can for example cite the CIAO instrument on Subaru (Murakawa et al. 2004), NACO at VLT (Rousset et al. 2003; Lenzen et al. 2003), NICI at Gemini South (Ftaclas et al. 2003), NIRC-2 at Keck (McLean & Adkins 2004) and PHARO at Palomar (Hayward et al. 2001). On the other hand, space-based observatories have been equipped for many years with a coronagraphic facilities: an example is the NICMOS instrument onboard HST (Schultz et al. 2000). Thanks to these state-of-the-art high-contrast imagers, the first pictures of extra-solar planetary systems have been taken (Chauvin et al. 2005; Lagrange et al. 2009b,c, 2010; Marois et al. 2008; Kalas et al. 2008), providing a unique scientific return. Indeed, direct imaging techniques do not only ollow to detect the presence of exoplanets but are also able to image the circumstellar material orbiting the stars (Absil & Mawet 2010). More than the spectroscopic or dynamical information that can be retrieved, high-angular resolution techniques can therefore give a direct insight on the mechanisms governing the formation and evolution of planetary systems (Riaud et al. 2006). Unfortunately, the performance of current AO systems only allows to detect planets in a few cases for which the planet/star flux ratio is favorable and the angular distance between them is sufficiently large. HST, with NICMOS, is also disadvantaged by its aperture size and the large IWA of its coronagraphs. In the next section, we present the next generation of ground- and space- based coronagraphic facilities that have been designed to correct for these limitations.

1.2.2 Next generation of instruments

Recent progresses in technologies make possible the development of very efficient adaptive optics, the construction of huge telescopes composed of hundreds of segmented mirrors and even deployable mirrors that are being used for future space-borne missions. In this section, we briefly describe the future generation of planet imagers.

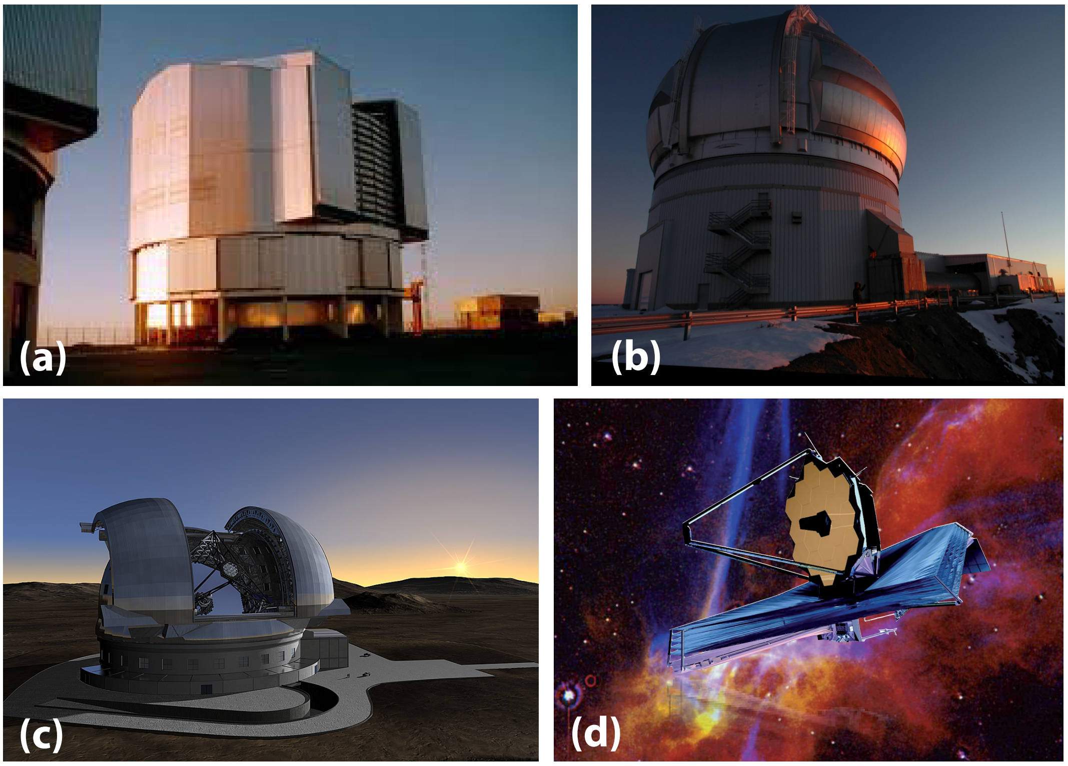

Figure 1.6: (a) Picture of one of the four 8.2 m VLT telescopes that will host the SPHERE instrument (courtesy of John Davies), (b) Gemini South telescope for the Gemini Planet Imager (image from the National Science Foundation), (c) Representation of the future 42 m E-ELT (image from ESO website), and (d) Artist view of the JWST (NASA-ESA).

Project-1640 (Palomar)

The Project-1640 (Roberts et al. 2009; Hinkley et al. 2010) is the next generation of near-infrared coronagraph for the 5.08 m Hale telescope of Palomar observatory. This instrument will take advantage of the upcoming PALM-3000 XAO system (Dekany et al. 2006; Bouchez et al. 2010) to efficiently dim the starlight, using a three step process. First, an apodized coronagraph will suppress the on-axis starlight subsequent to AO correction. Next, a coronagraphic stop will measure the quasi-static speckles and feed this information to the AO control loop to minimize these residuals. Last, a low resolution integral-field spectrograph ($R = 50$) will be used to differentiate the chromatic signature of planetary companions from residual speckles. The Project-1640 is being commissioned since 2008 with the current generation of AO system (PALAO) and is currently being tested with PALM-3000. First scientific observations are planned for 2011.

SPHERE (VLT)

SPHERE, which stands for Spectro-Polarimetric High contrast Exoplanet REsearch (Beuzit et al. 2008) is a second generation instrument for the Very Large Telescope (ESO, Chile). Mainly designed for the detection and characterization of extra-solar planets in the near-IR (H- and K- bands), this instrument will combine XAO and coronagraphy together with spectral, polarimetric and angular differential imaging in order to reach contrasts of ~15 magnitudes with respect to the central star over a field of view comprised between $0\farcs1$ and $3''$. For this purpose, SPHERE will be equipped with different amplitude and phase coronagraphs especially designed to optimize the rejection at small angular separations from the star over a large bandwidth (Boccaletti et al. 2008). After integration of the different devices in the instrument at

IPAG (Grenoble), its commissioning should start in 2011.

GPI (Gemini S.)

GPI, for Gemini Planet Imager, is the American counterpart of SPHERE (Macintosh et al. 2008). It is built and developed by a consortium of U.S. and Canadian institutes and is planned to be delivered to the Gemini South observatory in Spring 2012. Similarly to SPHERE, GPI is a high contrast, near-IR (Y, J, H and K bands) imaging spectrograph with a selective dual channel polarimetry mode. It operates only with on-axis, natural guide stars and is equipped with an apodized pupil Lyot coronagraph that employs three optical masks to control diffraction: successively a pupil apodizer, a hard- edged occulting spot, and a final pupil stop. The light diffracted on the coronagraph spot is monitored in real time to optimize the AO correction. Lastly, an atmospheric dispersion corrector can be deployed for operation away from the zenith.

EPICS (E-ELT)

The Exo-Planet Imaging Camera and Spectrograph (EPICS) is one of the instrumental projects that is under study for implementation on the European Extremely Large Telescope (E-ELT) (Kasper et al. 2008; Vérinaud et al. 2008). Like the three aforementioned instruments, EPICS is designed for the detection and characterization of extra-solar planets in the near infrared ($0.6-1.65\,\mu$m). However, thanks to the extremely high sensitivity and angular resolution provided by the 42 m wide primary mirror of the E-ELT, EPICS should be able to detect Earth mass planets in the habitable zone of their host stars (Kasper et al. 2008). Unlike the other planet imager facilities, the conceptual design of EPICS does not plan on using coronagraphs to dim the starlight but will instead rely entirely on angular, spectral and polarimetric differential imaging.

MIRI and NIRCam (JWST)

MIRI (Wright et al. 2004) and NIRCam (Rieke et al. 2005b) are two of the three instruments that will fly onboard the James Webb Space Telescope (JWST). The MIRI instrument will provide imaging, spectroscopy and coronagraphy in the mid-IR (5 to $28\,\mu$m) and will propose 4 different wavebands for its coronagraphic mode, respectively centered on 10.65, 11.4, 15.5 and 23μm. While the latter channel will be equipped with a standard Lyot coronagraph, the other three will use FQPM coronagraphs (Boccaletti et al. 2005; Baudoz et al. 2006). Compared to amplitude mask coronagraphs, these masks have the advantage to compensate for the lack of angular resolution compared to ground-based facilities by providing a small IWA. For the three "short" wavelength channels, the discovery space will therefore be comprised between ~0.2" and ~13". The main advantage of MIRI is its sensitivity to low-mass companions as it operates at thermal infrared wavelengths with low background levels, where planetary emission is high. NIRCam on the other hand will focus on the near-IR wavelengths (0.6 to $5\,\mu$m) and will include a coronagraph with 5 focal plane masks, all based on the quasi-band limited design (Kuchner & Traub 2002). It will provide contrasts of 12-18 magnitudes at angular separations between 1" and 4" in order to unveil the presence of giant planets around nearby stars (Beichman et al. 2010).

1.3 Extra-solar planet imaging: ground- vs. space-based coronagraphs

In the last few paragraphs, we have presented the future ground- and space-based coronagraphic facilities that will come online in the upcoming years. With the development of XAO and the construction of extremely large telescopes, ground-based facilities will be able to compete with space-based observatories in terms of sensitivity, angular resolution and stability. This section aims at comparing the performances of some of these instruments (i.e., SPHERE, EPICS and MIRI) in terms of sensitivity to extra-solar planet detection. For this purpose, we will particularly focus on the more favorable case of planet detection around young-main sequence stars located in nearby moving groups. After explaining the hypotheses and the methodology used for performing this comparison, we will present the results of our study and show the complementarity between ground- and space-based observatories.

1.3.1 Young main sequence stars: the ideal targets for direct imaging

Direct imaging of exoplanets has to face two major difficulties that are the required resolving power to spatially separate the planet from its star and the huge flux ratio between them. For these reasons, young main sequence stars hold a key place in the study of planetary systems with direct imaging. With ages typically between 10 and 100 Myr, the optically thick protoplanetary discs originally surrounding these stars have been cleared out by various physical processes and only optically thin disks are still present. Therefore, providing an easier access to the planetary emission. Furthermore, at such ages, giant planets have just formed and have not yet had the time to cool down to their final equilibrium temperature. They are thus significantly brighter than their old counterparts (Baraffe et al. 2003; Marley et al. 2007). Theoretical models for the early cooling and contraction of giant planets are however poorly constrained, and large uncertainties are affecting the first tens of Myr in their cooling history. In particular, the sensitivity to initial conditions is strongly affecting the cooling models during the first 10-100 Myr for planets with masses larger than that of Jupiter (see Figure 3). The direct detection and characterization of extrasolar planets with well-defined ages below 100 Myr therefore represents a much-needed observational constraint for these models.

During the past decade, a series of young stellar kinematic groups have been identified in the solar neighbourhood (< 100 pc), with ages ranging from about 8 to 200 Myr (Zuckerman & Song 2004). SInce then, searching for planets around stars in such groups has become a very active topic in extrasolar planet studies. Dedicated observing campaigns have been undertaken in all major observatories (especially with 10-m class telescopes), and the forthcoming advent of 2nd generation planet imaging instruments equipped with extreme adaptive optics (such as VLTI/SPHERE, Gemini/GPI and Subaru/HiCIAO) will further improve the sensitivity of ground-based telescopes to giant planet detection in nearby young associations, especially for semi-major axes in the 5-100 AU range (where most giant planets are supposed to be found). However, such instruments will achieve their ultimate performance only on relatively bright stars ($V \leq 10$). For fainter stars, the AO systems will generally fail to provide high-quality wave front correction due to the limited sensitivity of the wave front sensors. Consequently, ground- and space-based imaging instruments will be complimentary as they will have optimal performances for different types of stars. MIRI/JWST will provide tremendous sensitivities to giant planets around M dwarfs in nearby associations, which have $V > 10$ in almost all cases while ground-based facilities will give the full potential of their high angular resolutions around young and bright stars.

Direct imaging surveys around young stars are also complementary with RV surveys for two main reasons. First, current RV and transit surveys are detecting planets with orbital distances below 5 AU, and larger separations (5-100 AU) are still to be explored. Improving our understanding of planetary

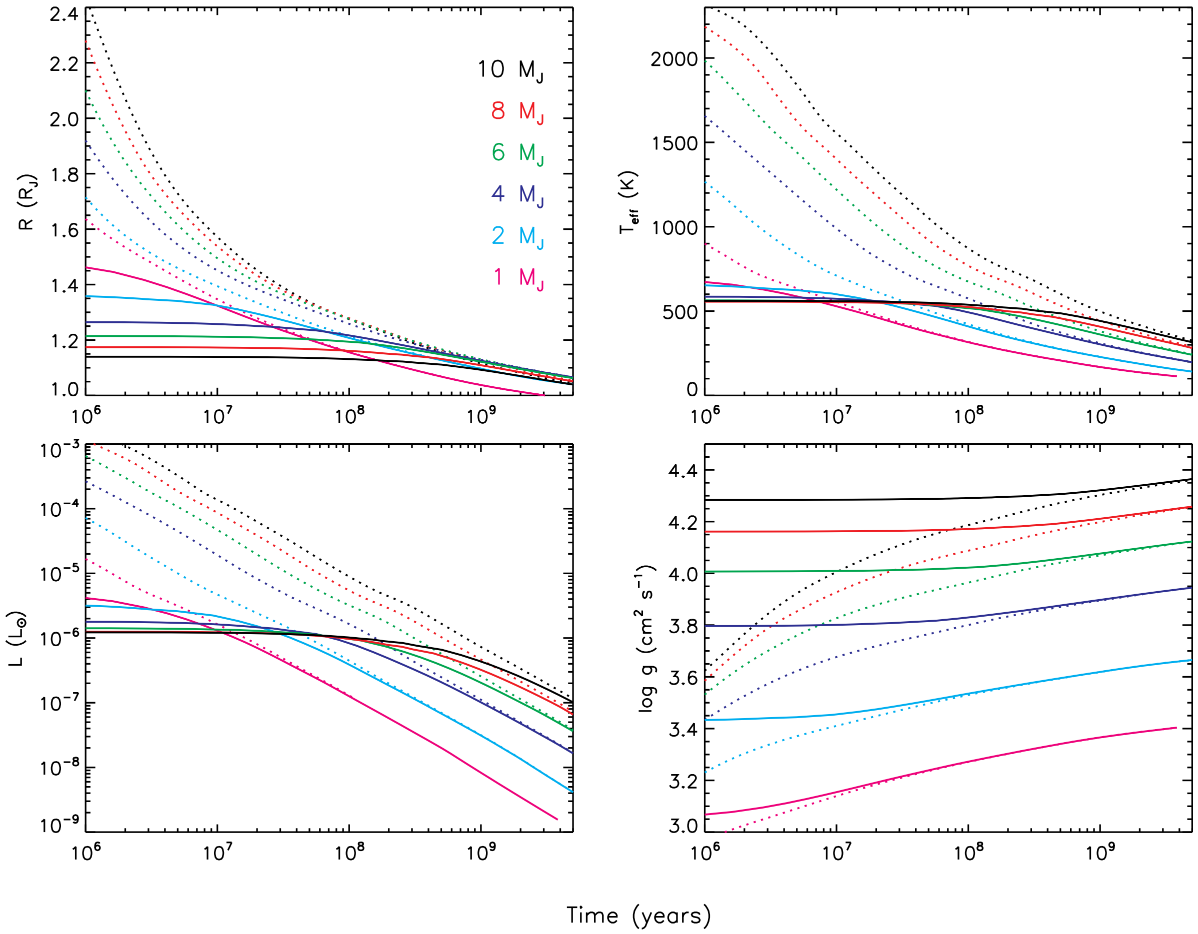

Figure 1.7: Comparison between the planetary evolution models obtained respectively with “hot start” planets with arbitrary initial conditions (dotted lines, Baraffe et al. 1998, 2003) and planets with an initial model from the Hubickyj et al. (2005) core accretion formation mode (solid lines). The model atmosphere grid is 1× solar and includes the opacity of refractory cloud species. As in Marley et al. (2007), times along the x-axis correspond to a duration in years since formation, which takes no time (by definition) for hot start planets, and $\sim 2.3 - 3.0$ Myr for core accretion planets.

formation at such distances will also bring much-needed constraints on the formation of planetary systems in general. Second, young stars are not the best suited for RV surveys because their high stellar activity can mimic the signature of a planet (e.g. TW Hya Setiawan et al. 2008; Huélamo et al. 2008). A few programs, for e.g. led by Setiawan with FEROS, Joergens (UVES) and Guenter (HARPS) in the visible have led to precisions of $\sim 50 - 100$ m/s (Paulson & Yelda 2006). The latter can however be slightly improved down to about 5-20 m/s by observing in the infrared (Kaeufl et al. 2004; Seifahrt & Käufl 2008; Bean et al. 2010) and some relevant surveys have recently been initiated (e.g. Di Folco and Bean with CRIRES). Such precisions translate into sensitivities of a couple of Jupiter masses for very short period orbits (a couple of days) but significantly decrease for longer orbital periods.

1.3.2 Simulated sensitivities of coronagraphic observatories

This section briefly describes the basic principles and hypotheses used for simulating the performance of the different instruments. These simulations are based on a three step process. First, a selection is made among the young stars with known ages in the nearest young moving groups. Then, using the coronagraphic profiles provided by the instruments consortia and giving the contrast achievable by the different instruments as a function of the angular separation and of the brightness of the source, we derive the sensitivities that can be achieved for each selected target. Finally, knowing the age and brightness of the sources as well as the achievable contrasts, we derive the corresponding masses of the companions using evolutionary models.

The goal of this assessment is not to predict accurately what will be achieved with the upcoming facilities but rather to compare the three instrumental performances under simple conditions and assumptions. These assumptions must be chosen to obtain a fair comparison between the three chosen instruments (MIRI, SPHERE and EPICS), even though they do not use the same technologies. As for the integration time, we adopt a generic value of 1h even though in reality, this can be modulated depending on the instrument and the star magnitude. Longer integrations will be needed for fainter stars and/or to reach larger contrasts (provided that the systematics remain negligible). However, for surveys on such instruments under high scientific pressure, it is probably not realistic to consider much longer observation times for surveys on dozens of stars. The other assumptions are the following:

- For MIRI, we use for the coronagraphic profile, the achievable contrasts corresponding to the FQPM at 11.4 μm and a simple reference subtraction. The reason for choosing this wavelength is because there is less chance to see the planetary signal being dimmed by an absorption line (cf. ammonia at 10.65 μm) and the angular resolution is significantly better than at 15.5 μm. These profiles have been provided by A. Boccaletti (LESIA).
- For SPHERE, we use two different hypotheses: (i) the use of a FQPM in H band (1.68 μm) and a simple reference subtraction, and (ii) on top of the reference subtraction we use Spectral Differential Imaging (Lenzen et al. 2005) between the H2 (1.593 μm) and H3 (1.667 μm) spectral bands (Carbillet et al. 2008). The simulations of the coronagraphic performances have also been provided by A. Boccaletti.
- EPICS has unfortunately relatively different hypotheses from the two other instruments. It is due to the way the instrument is conceived and simulated. Indeed, by default, EPICS uses more advanced subtraction methods such as SDI, Angular Differential Imaging (ADI) and differential polarimetry. The simulations of EPICS performances given by C. Vérinaud (LAOG) naturally also include the gain provided by all these differential imaging techniques. The instrument uses wavelengths between 0.95 and 1.65 μm. Note that an optical bench is being built in Grenoble to confirm experimentally the contrast expected from the simulations.

Finally, the instrumental simulations are not the only component of our study. Indeed, in order to calculate the masses corresponding to a given magnitude at a given age, we used planetary evolutionary models. Two categories of models are currently available (i) the so called *"hot start"* cooling models (Baraffe et al. 2003, 2008) and (ii) the *"core accretion"* evolutionary models (Fortney et al. 2008). These two types of models show discrepancies up to a few magnitudes during the first 10-100 Myr after the formation of the planets (see Figure 1.7). In our simulations, we choose the *"hot start"* cooling models (Baraffe et al. 2003, 2008) as these are available for planet masses $< 1\,M_{\rm Jup}$. In order to account for a realistic planetary composition, we use the Z=0.1 models (where Z is the metal fraction) for masses above 0.1 $M_{\rm Jup}$ and the Z=0.5 models for masses below 0.1 $M_{\rm Jup}$.

1.3.3 Performance comparison and perspectives

Based on the aforementioned hypotheses, Figure 1.8 compares the instrumental sensitivities in terms of detectable companion mass for three different stellar types (G0, K0 and M0) as a function of their age. The left-hand side plot corresponds to the detection of planets at an angular separation of 0.2" while the right-hand side one corresponds to an angular separation of 2". At 0.2", EPICS exploits at best the field of view of its 42 m telescope aperture while at the other end, MIRI is working at its very inner working

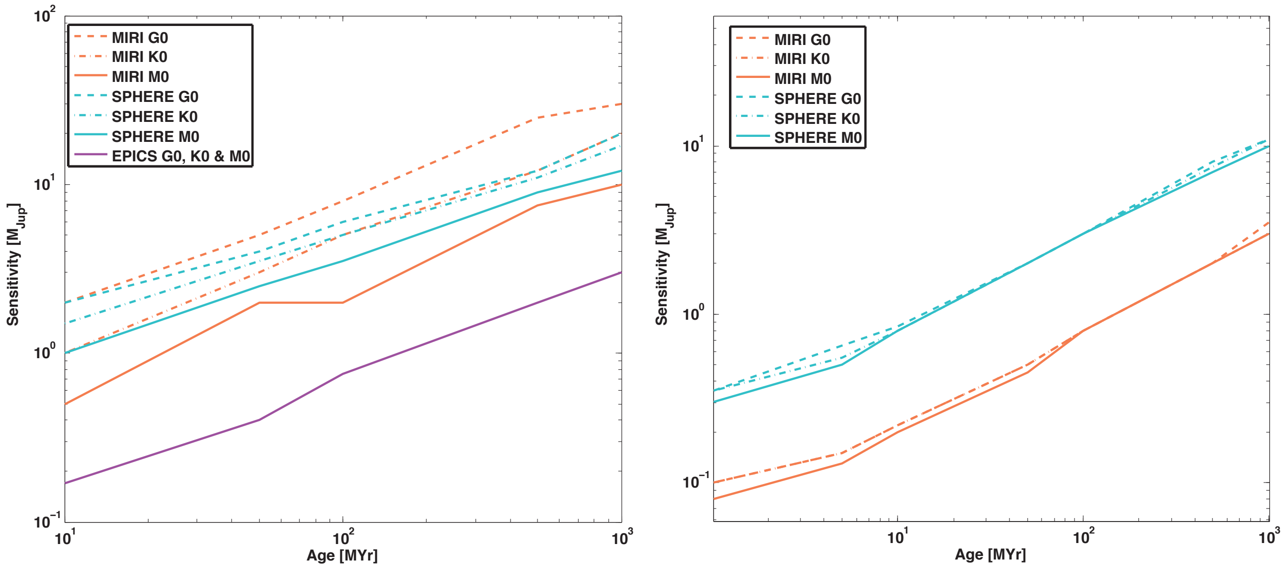

Figure 1.8: Left: Comparison of the instrumental sensitivities of SPHERE (with SDI), EPICS and MIRI at an angular separation of 0.2” around G0, K0 and M0 stars as a function of the stellar age. Right: Same comparison for an angular separation of 2”. Note that in this case, one is outside the EPICS field of view that cuts off at 0.4”.

angle. Logically, EPICS is therefore the most sensitive instrument for the smallest separation, no matter the age or stellar type. Because of the relatively short integration time, the results obtained with EPICS are background limited. This is why the sensitivities are the same for the three stellar types. Between MIRI and SPHERE, MIRI is slightly better for the dimmest objects (M0 stars) but SPHERE is more efficient for G0 stars. As expected, these simulations confirm that the fainter and younger the star, the better the sensitivity in terms of companion mass for all three instruments.

At 2” the situation is very different. First of all, we are well outside the EPICS field of view so that only SPHERE and MIRI can be used. Second, as we are at large angular separations from the star, none of the imagers is limited by the off-axis stellar residuals any longer but rather by the background level. Therefore, because MIRI is a space based telescope and because it operates at wavelengths where the star/planet contrast is more favorable, it performs best with sensitivities down to $0.1\mathrm{M}_{\mathrm{Jup}}$ for 10Myr old stars.

Figure 1.8 clearly illustrates the interest of observing young M stars rather than old stars with an earlier stellar type. Indeed, for MIRI at 0.2”, the detection limit goes from $0.5\,\mathrm{M}_{\mathrm{Jup}}$ around a 10Myr old M0 star to $3\,\mathrm{M}_{\mathrm{Jup}}$ planets around 1 Gyr old G0 stars. Therefore, we decided to explore the potential of a survey on a real sample of M type stars among the closest and youngest moving groups. For all these targets, we compare the sensitivity of the three instruments. Figure 1.9 shows this comparison for the best targets in our sample. The number of observable stars with the two ground based facilities is low because most young and nearby M stars are either too faint to be tracked by the AO systems ($V \leq 10$) or not observable from these observatories. On this graph, two different sensitivities have been plotted for SPHERE: one with and one without SDI. The use of SDI techniques obviously brings a significant gain in sensitivity but this result must be taken with care. Indeed, one must note that the SPHERE simulations with SDI implicitly assume that the planetary spectrum shows large variations within (at least one) of the observed spectral band(s). With SPHERE these bands are centered on $1.593\,\mu$m (so-called H2 band) and $1.667\,\mu$m (H3) and correspond to a strong CH_4 absorption line. If the magnitudes of the cold planets change significantly between these two spectral bands, it is not the case anymore for planets warmer than $\sim 500\,$K. Therefore, some planets around $1\,\mathrm{M}_{\mathrm{Jup}}$ that should in principle be detectable with the SDI

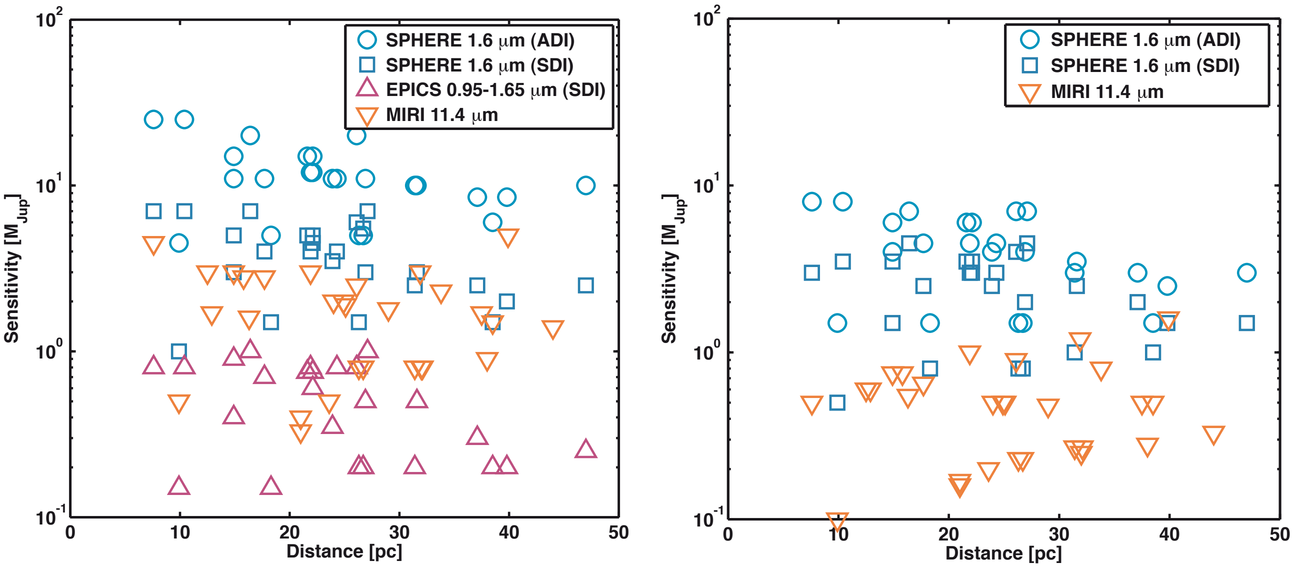

Figure 1.9: Left: Comparison of the instrumental sensitivities of SPHERE, EPICS and MIRI for an angular separation of 0.2" around the closest M stars in young moving groups/associations as a function of the stellar distance. Right: Same comparison at an angular separation of 2". Note that in this case, one is outside the EPICS field of view that cuts off at 0.4".

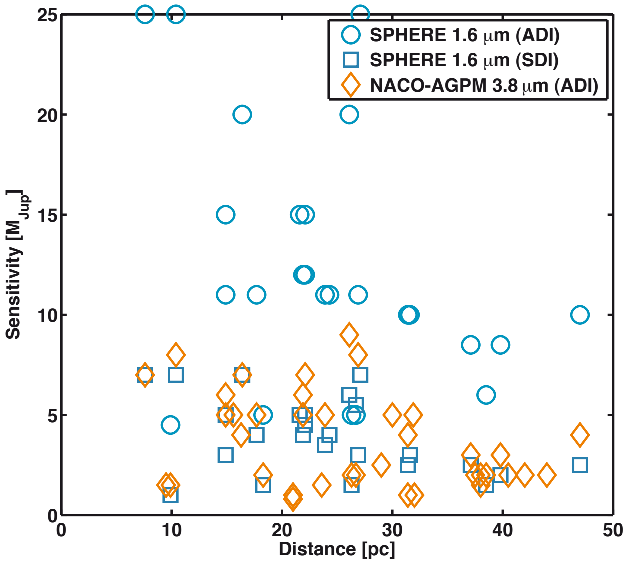

Figure 1.10: Comparison of the instrumental sensitivities of SPHERE and NACO used in L band with an Annular Groove Phase Mask (AGPM) coronagraph.

mode of SPHERE could in fact stand below the detection limit due to their weak spectral signature.

L band coronagraphy: an efficient upgrade for current facilities

The expected performance of the next generation of high contrast imagers using XAO is very promising. However, such expensive instruments are not the only solution for upgrading current facilities, and simpler, cheaper solutions exist. The first one, which consists in the optimization of the AO correction on a sub-aperture of a telescope will be the subject of Chapter 2. Another possibility is to observe at longer wavelengths, in L band in particular. Indeed, around 3.8 μm, the thermal emission of extra-solar planets increases significantly with respect to J, H and K bands and the contrast ratio with the star decreases

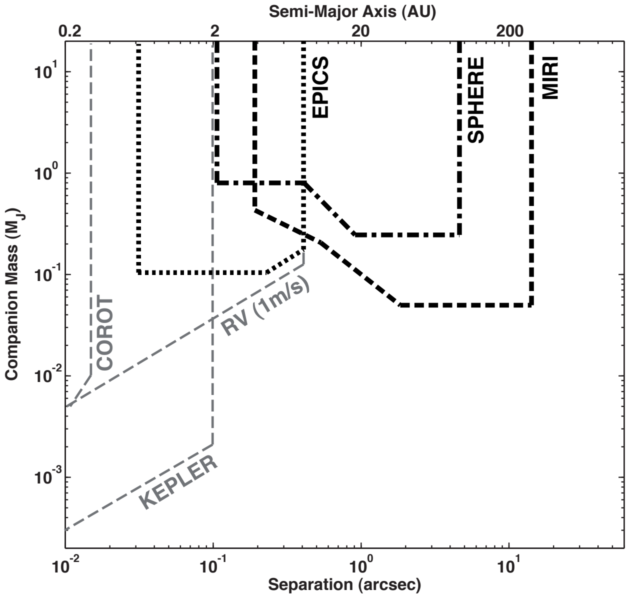

Figure 1.11: This graph compares the sensitivity of different instruments for exoplanet detection as a function of the celestial angular separation. For MIRI, SPHERE and EPICS, the results correspond to 1 hour observations among young (10 Myr) closeby stars (20 pc). For the three other curves (COROT, KEPLER and Radial Velocities), the sensitivities correspond to observations of exoplanets around main sequence stars.

while the background emission is still at reasonable levels (the magnitude limits after 1h of exposure is $L = 17$, Kasper et al. 2007). Moreover, in this waveband, Strehls of $\sim$ 80% can be obtained with the current generation of AO (compared to $\sim$ 40% in the near-IR) leading to efficient starlight suppression with coronagraphs. However, the price to pay is a loss in resolving power. To circumvent this issue, coronagraphs with small inner working angles such as phase mask coronagraphs can be used. Figure 1.10 illustrates the simulated performances of NACO in L band if used with an AGPM coronagraph (Mawet et al. 2005c,b). The results show that sub-Jupiter mass planets can be imaged around young stars and that sensitivities comparable to SPHERE can be obtained. Moreover, when scientific observations are made in the L band, the near-infrared light (otherwise sent to the scientific camera) can be used for the wavefront sensors. As late type stars are more luminous at infrared-wavelengths than in the visible, it can lead to a significant improvement of the AO sensitivity.

Perspectives

Direct imaging of planetary systems contributes to the understanding of planet formation by confronting the observed photometry with evolutionary models for instance. By detecting planets around young M stars, it is possible to constrain theoretical models for the cooling of gas giants, especially at a few tens of Myr where the uncertainties and discrepancies between models are still large. To this aim, any detection of a planetary system should be confirmed with observations at other wavelengths in order to have a model-independent estimation of the planet's effective temperature. Such a result would provide a direct distinction between the so-called *"hot start"* cooling models (Baraffe et al. 2003) and the *"core accretion"* cooling models (Fortney et al. 2008), as they show discrepancies up to a few magnitudes during the first 10-100 Myr after their formation (see Figure 3). To do so, one could for example make use of the MIRI FQPM modes at 10.65 and 15.5 μm or SPHERE observations in H or K bands. Moreover, because they will directly detect the photons from the planet, planet imager will enable the possibility to detect the presence of chemical elements within the planet's atmosphere. For example, MIRI observations at 10.65 μm will allow to detect the presence of ammonia through its absorption band at that particular wavelength. This information could also be used to further constrain the planetary temperature. Follow-up observations with SPHERE in H and K bands (for planets “closer” than 5”) or EPICS between 0.95 and 1.65 μm (for planets within 0.4”) would also greatly help in constraining theoretical emergent spectra predicted by various atmospheric models. Finally, for planets having a short enough orbital period, it will also be possible to constrain the planetary orbit as well as the dynamical mass of the planets by taking images of the systems at two (or more) different orbital locations (Lagrange et al. 2010). To summarize, Figure 1.11 illustrate and compares the discovery space of these future high contrast imagers with current planet hunter instruments such as COROT, KEPLER and HARPS.

2

The Well-Corrected Subaperture: a precursor to future XAO facilities

Contents

2.1 Principle and goals of the instrument **33**
2.2 Direct imaging of multiple systems at blue wavelengths **34**
2.2.1 Observing strategy and data reduction 35
2.2.2 Data analysis 36
2.2.3 Individual star results 39
2.2.4 Error bars on the pixel size and telescope orientation 45
2.3 Reaching high contrasts with phase mask coronagraphs **45**

Efficient AO systems are mandatory to correct for the atmospheric-induced wavefront corrugations. The quality of correction provided by an AO system is proportional to both the actuator density and the observing wavelength. In the coming years, a new generation of AO systems having a much larger number of actuators will come online, providing diffraction limited images on 10-m class telescopes in the near-IR. In the previous chapter, we have presented an alternative solution to XAO systems, which consists in observing at longer wavelengths. Here we present another solution which consists in increasing the actuator density by optimizing the AO correction over a small portion of the telescope pupil. After explaining the basic principle of this instrument, we will show how it can be used to perform high angular resolution imaging of nearby companions and exoplanets from blue wavelengths to the near-IR.

2.1 Principle and goals of the instrument

The principle of the Well-Corrected Subaperture (WCS) has been presented in detail by Serabyn et al. (2007) and its performance has been demonstrated on the 5.08 m Hale telescope at the Palomar observatory (Serabyn et al. 2007, 2010). It consists in improving the level of wavefront correction by using available wavefront sensors and deformable mirrors to correct more accurately a smaller off-axis section of the full telescope pupil. In practice, a simple set of relay optics is inserted prior to the AO system in order to re-image a sub-aperture onto the deformable mirror (DM) (Haguenauer et al. 2005; Haguenauer & Serabyn 2006; Serabyn et al. 2006) (see Figure 2.1). Despite a lower sensitivity of the system due to a lower flux on each wavefront sensor (WFS) element, a significantly better wavefront quality is obtained

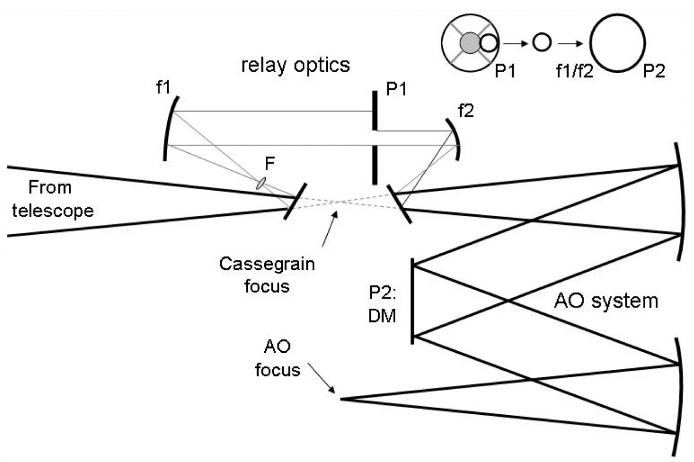

Figure 2.1: Schematic representation of the relay optics of the WCS. A flat mirror first intercepts the light before the Cassegrain focus. A pair of paraboloids (f_1 and f_2) then magnifies the pupil and a mask (P_1) re-defines a portion of it as being the new telescope pupil. This sub-aperture is then reflected onto the DM as if it was the initial pupil and is finally imaged onto the camera. Image from Serabyn et al. (2007).

thanks to the smaller effective spacing of the actuators on the DM. Moreover, the use of an unobscured sub-aperture of the telescope further improves the image quality as it reduces the amount of scattered light due to vignetting elements. Under standard observing conditions at Palomar, the WCS can reduce the wavefront errors from 200-250 nm to 80-100 nm, therefore providing Strehl rations of 88-95 % in the near infrared (1.6 to 2.4 μm). This level of wavefront correction is ideal for coronagraphic observations in the near-IR as only a very small amount of the stellar light is diffracted into a halo of speckles, leaving an almost aberration-free PSF (see Section 2.3). However, such a concept can also be used to observe at shorter wavelengths. Indeed, whereas current AO systems are unable to correct the wavefront aberrations at wavelengths shorter than typically 1 μm, the WCS can improve these performances and provide good Strehl ratios down to optical wavelengths (see Figure 2.2). However such a system also suffers from drawbacks. First, each wave front sensor element receives the light collected by smaller apertures. The overall sensitivity of the WCS is therefore limited to stars brighter than $V \simeq 5$. Second, at a given λ, the resolving power of the WCS is worse than that obtained with the full telescope pupil. This latter effect can partially be compensated either by observing at shorter wavelengths or, in coronagraphic mode, by using coronagraphs having a small inner working angle (IWA) such as the phase masks. These two applications will be the subject of the two following sections.

2.2 Direct imaging of multiple systems at blue wavelengths

Multiple systems with angular separations shorter than $\sim 0\farcs5$ are difficult targets to image. Indeed, to achieve the mandatory angular resolution, they require the use of large (5-10 m) ground based telescopes equipped of AO systems. Unfortunately, the wavefront correction of current adaptive optics systems does not work efficiently at wavelengths shorter than the near-IR (see Figure 2.2). At these wavelengths however, the luminosity binary systems composed of red giant primary peaks up and the contrast between the primary and its companions is large. A good example is Mira, a well known variable star which has a typical (B-V)$\simeq$ 7 (depending on the period of observation) and having a stellar companion. In such conditions, coronagraphic devices are mandatory to dim the starlight and reveal the companion. The use of a well corrected subaperture can allow high angular resolution imaging down to optical wavelengths where the contrast of such systems is lower, and the use of a coronagraph is no longer necessary. Unfortunately, the AO system uses most of the visible light for its WFS. Therefore, we

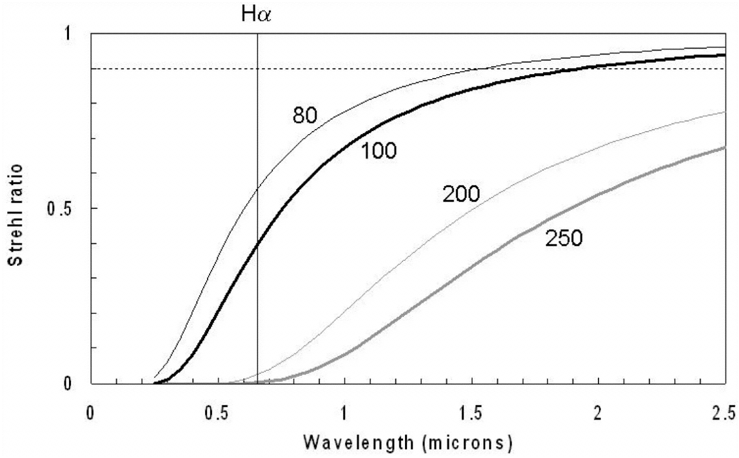

Figure 2.2: As a function of the wavelength, expected Strehl ratios provided by AO systems leaving 250, 200, 100 and 80 nm rms residual wavefront errors. While the two lower curves represent the performances of current AO systems, the two upper ones correspond to the performances of future XAO and of the WCS. Image from Serabyn et al. (2007).

decided to use the blue wavelengths are transmitted to the scientific camera to observe multiple stellar systems. In the B band (~ 425 nm), the WCS provides Strehls ratios around 12% and the measured FWHM for the 1.5 m off-axis and unobscured subaperture at Palomar observatory is on average $\simeq 0\farcs120$ (about $2\lambda/D$).

Here, we use this capability to image several known spectral and visual multiple systems with an angular separation down to $0\farcs15$, providing new orbital and photometric data in a few cases. For that, a total of 9 multiple systems have been chosen for observation during a total of two nights (April 29 and August 11, 2007) with the WCS at Palomar observatory. These targets have been chosen among known visual multiple systems featuring a red giant primary, that are several magnitudes fainter in the blue than in the infrared. The flux ratio of each observed system with respect to their companion was therefore reasonable with $\Delta B \in [0.9; 2.6]$. Table 2.1 summarizes the set of targets that have been selected for the two observing nights.

2.2.1 Observing strategy and data reduction

For each targets, between 5 and 15 images are acquired with integration times ranging between 1 sec and 250 sec depending on the magnitude of the star. Each observation of a scientific star is then followed by the acquisition of several images on a calibrator star of similar magnitude. Finally, for each observing night, a well known wide binary system is observed in order to calibrate both the pixel size and instrument orientation (see Section 2.2.2 for more details)[2]. The individual images obtained on each target are co-aligned and added to each other with a sub-pixel precision by fitting a two dimensional Gaussian profile on the central PSF. The background level is then subtracted. Because the Strehl ratio is relatively low (typically ~ 12%), the instrumental response of the telescope changes rapidly and the subtraction of the central PSF by a reference star is not efficient. Instead, we decided to subtract it by MOFFAT profiles (Markwardt 2009) which are designed to realistically represent point spread functions affected by atmospheric turbulences. Then, to enhance even more the sensitivity to off-axis point sources, we remove the low spatial frequency content from the image. This step is done by applying a high pass

---

[2] For other instruments, this step is usually done by observing a stellar cluster rather than a single binary star because it provides a larger amount of information to calibrate the instrument. However, this method cannot be applied to the WCS because of its limited sensitivity.

Table 2.1: Summary of the results obtained with the WCS of the Hale telescope at Palomar observatory. The results on α Her are used as calibrators for the pixel size and telescope orientation and have therefore been written in bold.

Name	Epoch MJD	V	B	$\rho_{\text{obs.}}$ ″	$\theta_{\text{obs.}}$ °	$\Delta m_{\text{obs.}}$	$\rho_{\text{cat.}}$ ″	$\theta_{\text{cat.}}$ °	$\Delta m_{\text{cat.}}$
47 Cyg	54219	4.61	6.21	0.244	274.7	1.8	0.230	NA	1.6
49 Cyg	54219	5.51	6.39	2.681	44.3	2.13	2.753	45.5	2.15
62 Cyg	54219	3.72	5.37	0.162	256.0	2.5	SB	SB	4.0
β Cyg	54219	3.18	4.17	0.344	106.4	0.9	0.240	97.3	0.9
α Her	**54219**	**3.06**	**4.51**	**4.651**	**103.8**	**3.1**	**4.650**	**103.8**	**2.59**
ϵ Hya $_{\text{ab}}$	54219	3.49	4.06	0.142	109.0	1.19	0.160	110.9	0.44 (vis)
ϵ Hya $_{\text{ac}}$	54219	3.49	4.06	2.703	302.2	3.8	2.880	303.0	4.2
HD 90537	54219	4.21	5.11	0.448	219.6	1.1	0.450	220.7	0.4 (vis)
HD 95689	54219	1.79	2.86	0.464	42.9	1.9	0.470	58.5	1 (vis)
α Her	**54323**	**3.06**	**4.51**	**4.651**	**103.8**	**2.1**	**4.650**	**103.8**	**2.59**
β Cyg	54323	3.18	4.17	0.358	103.7	1.8	0.240	97.3	0.9
Mira $_{\text{ab}}$	54323	~ 9	~ 10.42	0.504	104.6	1.4	0.520	103.0	NA
Mira $_{\text{ac}}$	54323	~ 9	~ 10.42	0.201	348.4	1.2	NA	NA	NA
NS Vul	54323	8.57	10.37	0.721	272.1	-1.25	0.750	276.4	-1.44

filter whose cutoff frequency corresponds to about twice the instrumental FWHM. Finally, the pixel size and telescope orientation must be determined for each observing run. This step is further described in Section 2.2.2.

2.2.2 Data analysis

We hereby summarize the results of our instrumental calibration and the individual results obtained on each star.

Calibration of the pixel size and telescope orientation

The WCS is a visitor instrument, and must be re-installed at the Cassegrain focus of the telescope at each observing run. Therefore, its alignment changes from run to run and the observation of a reference binary star having a large and well known angular separation is mandatory in order to determine both the pixel size and the telescope orientation. For our observations, we decided to choose α Herculis which is composed of an M5Iab red supergiant primary (V=3.06, B=7.1) and a G5III secondary (V=5.39, B=7.1) separated by 4″.650. Once computed, the separation of the binary in pixel units, and its orientation are compared to the orbital parameters that are available. Using α Her on the two observing nights (April 29 and August 11, 2007) we measured respective pixel sizes of 24.3 mas and 23.7 mas. From the orientation of the binary on the image, we also measured the telescope orientation. This orientation is measured from North to East counter-clockwise (see Figure 2.3). The orientation for the two observing nights are respectively 89° for the April 29 run and 109.4° for the August 11 run. The stability of this calibration will be discussed in Section 2.2.4.

Note that α Her A and B are both known to have a stellar companion at short angular separations. We tried to resolve these two tight binaries by subtracting Moffat profiles from their respective primaries. Unfortunately, no companion was found in the direct vicinity of these two stars, mainly because of limited resolving power of the telescope but also because of the presence of bright residual speckles in

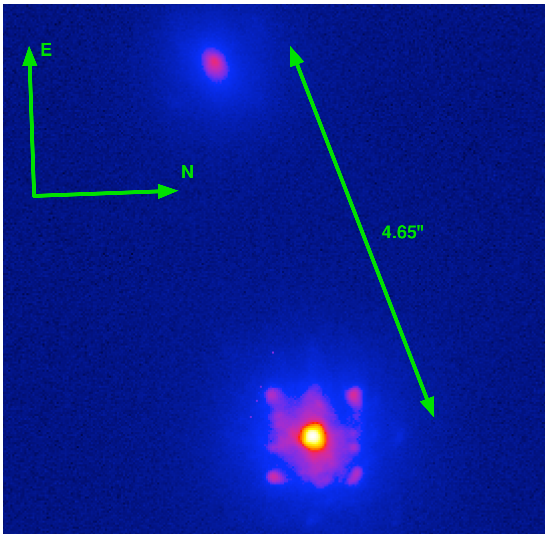

Figure 2.3: Image of α Her taken on April 29 and resulting from the addition of 15 frames for a total exposure time of 348 sec.

the subtracted images. However, this non detection does not affect the pixel scale measurement.

Calculation of orbital parameters

The relative motion of the two bodies composing a binary system is represented by the second-order differential equation

$$\frac{d^2\mathbf{r}}{dt^2} = -k^2(M_1 + M_2)\frac{\mathbf{r}}{|\mathbf{r}|}^{3} \tag{2.1}$$

where $\mathbf{r} = (r, \theta)$ is the vector defining the relative position of the two bodies at any time t (assuming the primary to be at the origin of the axes), and M_1 and M_2 are the masses of the primary and secondary, respectively. The Kepler laws describe the solution of this equation. First, the orbital motion corresponds to a conic section (i.e. an ellipse for a bound system) with the primary star at the focus. Second, the area swept by the radius vector **r** joining the primary with the secondary star is constant per unit of time. The third law, described by the relation $P^2 = 4\pi^2/G(M_1 + M_2)a^3$, where G is the gravitational constant, can however only be used once the orbit semi-major axis and the total mass of the system are known. Four fundamental parameters describe the properties of the orbit and of the motion on it:

P is the revolution period in years.

T is the passage through periastron, given in years.

a is the semi major axis of the true orbit in arc-seconds.

e is the eccentricity.

However, except in very exceptional cases, the orbital plane is not perpendicular to the observer line-of-sight. As a consequence, the observed orbit is not identical to the true orbital ellipse but is one of its parallel projections onto the celestial plane. Three more elements must therefore be used to describe this projection.

Ω , the longitude of node, is the position angle with respect to the North, of the intersection line between the celestial plane and the true orbital plane. The ascending and descending nodes differ from 180° and correspond to the node where the orbital motion is directed away and toward the observer's direction respectively.

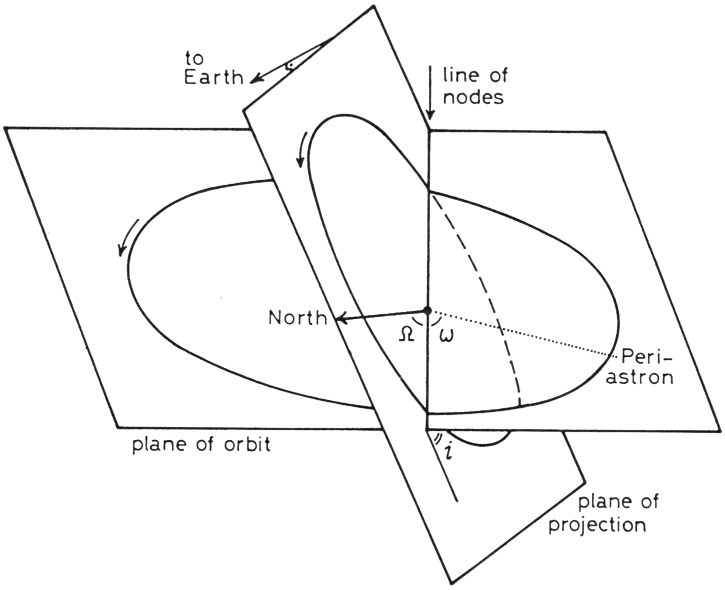

Figure 2.4: Schematic representation of an orbit, its projection into the celestial plane (or plane of projection) and the various geometrical elements. Image from Heintz (1978).

- ω , the longitude of periastron, is the angle in the orbital plane between the ascending node and the position of the periastron. It is ranging from 0° to 360°.
- i is the inclination angle between the orbital plane and the celestial plane, and it ranges between 0° and 180°. The motion is said to be direct (indirect) when the position angle increases (decreases) over time and the inclination is then $i < 90°$ ($i > 90°$).

The four classical elements a, ω, Ω and i can be replaced by equivalent parameters (called Thiele-Innes elements) which are better suited to calculation in rectangular coordinates:

$$\begin{aligned} A &= a(\cos\omega\ \cos\Omega - \sin\omega\ \sin\Omega\ \cos i) \\ B &= a(\cos\omega\ \sin\Omega + \sin\omega\ \cos\Omega\ \cos i) \\ F &= a(-\sin\omega\ \cos\Omega - \cos\omega\ \sin\Omega\ \cos i) \\ G &= a(-\sin\omega\ \sin\Omega + \cos\omega\ \cos\Omega\ \cos i) \end{aligned} \tag{2.2}$$

When the three elements P, T and e are known, the four Thieles-Innes elements and the corresponding orbital elements can be easily determined by means of a least squares method (Hartkopf et al. 1989). First, let us consider a set of observations (t_i, x_i, y_i) where t_i, x_i and y_i are the time and the coordinates of the binary relative to the primary for the i$^{\text{th}}$ observations. Assuming that (P, T, e) are known, it is possible to find the eccentric anomalies E_i (angular parameter defining the position of a body moving on an elliptic Keplerian orbit) using the equation:

$$u\,(t_i - T) = E_i - e\ \sin E_i \tag{2.3}$$

where $u = 2\pi/P$. The normalized rectangular coordinates can then be computed as follows:

$$X_i = \cos E_i - e \tag{2.4}$$
$$Y_i = \sqrt{1 - e^2}\ \sin E_i \tag{2.5}$$

The Thiele-Innes elements can then be found by minimizing the residuals of the following equations (Heintz 1978)

$$x_i = AX_i + FY_i \tag{2.6}$$

$$y_i = BX_i + GY_i \tag{2.7}$$

In practice, P, T and e are not known but are part of the elements that one wants to determine. The way to proceed is therefore to test different values in the (P, T, e) phase space and measure the best least square residual of Equations 2.6 and 2.7 for each of them. To minimize the computing time, the step size in this grid is first chosen relatively large and is then refined gradually as the search space is decreased, finally leading to the best solution given the desired accuracy. Finally, a Bayesian analysis is performed in order to check the robustness of the solution found for the optimal orbital parameters and evaluate the error bar for each of them (Press et al. 2007).

2.2.3 Individual star results

47 Cyg

47 Cyg is a system composed of a spectroscopic binary system (SB1) HD 196093-94 that has been resolved several times by speckle interferometry. According to Parsons & Ake (1998), HD 196093 (47 Cyg A) is probably an M1 with $V = 4.61$ and $B = 6.21$ and HD 196094 (47 Cyg B) a B4 with $V = 7.91$ and $B = 7.71$. The magnitude difference in the B band is therefore $\Delta B = 1.5$. This binary has been imaged several times by speckle interferometry (McAlister & Fekel 1980; McAlister & Hendry 1982b; McAlister et al. 1983, 1984, 1987, 1989, 1990). All these observations have lead to similar angular separations and orientation, respectively around $0\farcs280$ and 98°. However, these speckle interferometry observations suffer from a 180° ambiguity on the determination of the position angle. Therefore, the real position angle of the companion can either be 98° or 278°. Assuming an approximate distance of $\sim$ 500 pc, the projected orbital distance of this binary is a $\sim$ 140 AU. Further assuming a circular orbit and a system seen face-on, Griffin (1992) has suggested that the orbital period should be around 500 years. Our observations being temporally separated from the one performed by McAlister et. al by roughly 20 years, we can expect to measure a rotation of the binary of about 14.4°, which is large enough to be detected with the WCS.

The image obtained on 47 Cyg is the result of three frames for a total integration time of 50 sec. After subtraction of the primary by a Moffat profile, a companion is revealed at $0\farcs244$ at an orientation of 274.7° with a $\Delta B = 1.8$ (see Figure 2.5, (a)). This result is perfectly consistent in terms of both angular separation and orientation of the binary with the aforementioned speckle interferometry observations and lefts up the 180° ambiguity. However, the angular movement of the binary system is smaller than expected with less than 4° rotation within 20 years while we were expecting $\sim$ 14.4°. A refinement of the orbit might therefore be necessary.

49 Cyg

49 Cyg (HD 197177) is composed of a G7-8II-type primary ($V = 5.51$ and $B = 6.39$) separated from a secondary of probable type A or B by $2\farcs75$ (Parsons 2004). The measured magnitude difference in the visible between these two components is $\Delta V \simeq 2.5$, which, based on the estimated spectral types, should give a $\Delta B \simeq 1.6$. The position angle of this wide binary obtained by direct imaging is 45.5° . In addition, each of the two components is suspected to have another companion orbiting closer in. While the second component around 49 Cyg B has recently been unveiled by SED fitting (Parsons 2004), the SB around

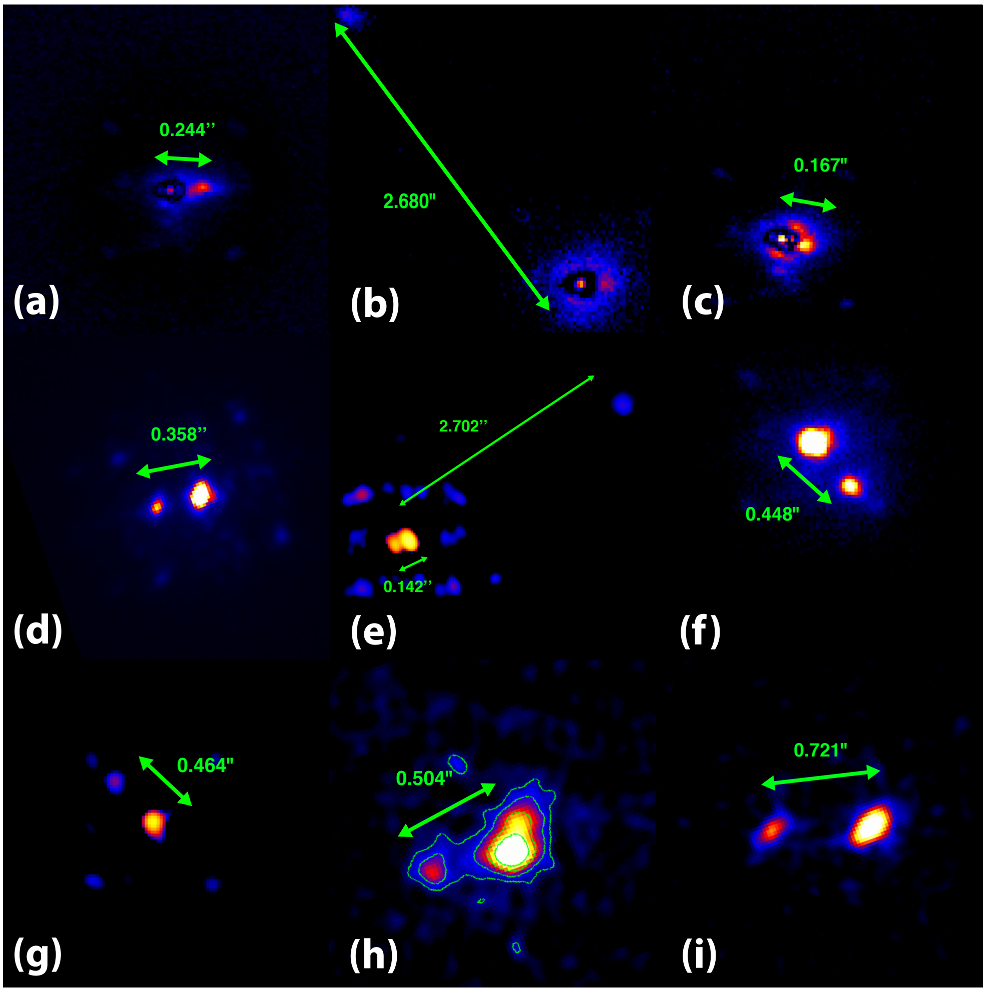

Figure 2.5: Summary of the observations taken during the two observing nights on the 9 scientific targets. For some of them (a, b and c), the primary target has been subtracted using a Moffat profile in order to reveal the companion. The different images respectively correspond to: (a) 42 Cyg, (b) 49 Cyg, (c) 62 Cyg, (d) β Cyg, (e) ϵ Hya, (f) HD 90537, (g) HD 95689, (h) Omi Cet, and (i) NS Vul. All these images have been taken on April 29 except for : Beta Cyg (d), Omi Cet (h) and NS Vul (i) that are from the August 11 run. In these images, North is up and East to the left.

49 Cyg A was discovered in 1979 (WDS catalogue[3]) but has never been confirmed since then by speckle interferometry. It is however listed with an expected separation $\sim 0.''200$. Considering that the star is located at a distance of $\sim 250\,\mathrm{pc}$ and assuming circular orbit seen face-on, this gives a semi-major axis of 50 AU and therefore, a long orbital periods ($\sim$ 200 years) depending on the mass of the secondary component.

Our image of 49 Cyg, after subtraction of the primary PSF using a Moffat profile (see Figure 2.5, (b)) shows an obvious secondary at $2.''680$ with an orientation of 44.3°. The measured magnitude difference is $\Delta B = 2.1$. The measured position is in very good agreement with what has been found up to now on this system. However the measured contrast in the blue seems higher than expected. This discrepency is probably due to photometric uncertainties in our images, so that we cannot further constrain the spectral type of this binary based on our result alone.

More interesting is the residual feature in the subtraction of the primary's PSF. This residual feature located at $0.''172$ West from the primary and having a contrast $\Delta B \simeq 2.5$ could be the companion orbit-

---

[3] `http://ad.usno.navy.mil/wds/`

Table 2.2: New orbital elements of β Cyg and α UMa.

Name	HD	P	a	i	Ω	T_0	e	ω
		(yr)	(arcsec)	(deg)	(deg)	(yr)		(deg)
β Cyg	183912	146.1	0.447	151.8	108.3	1869.5	0.25	46.1
		±0.3	±0.004	±1.43	±2.43	±0.1	±0.01	±1.49
α UMa	95689	41.0	0.576	167.4	99.49	2001.8	0.41	−32.02
		±0.3	±0.003	±3.04	±11.99	±0.1	±0.01	±12.75

ing close to 49 Cyg A and reported in 1979 (WDS). If the result is in good agreement with the 1979 observations, the detection is too marginal to be confirmed (see Figure 2.5, (b)).

62 Cyg

62 Cyg is a spectroscopic binary of type SB1 that has been discovered in the far and mid-UV by Parsons & Ake (1998). This multiple system is poorly constrained but the latest studies devoted to this star suggest that it is composed of a K5 primary with an A1 secondary. The visual magnitude difference $\Delta V = 5.6$ and the primary $(B-V) = 1.65$ should theoretically give a contrast in the B band $\Delta B = 3.95$. Finally, Parsons & Ake (1998) give an orbital period of 18.5 years and report that the latest prime conjunction occured in January 2004. Considering that 62 Cyg is about 361 pc away from us, this relatively short orbit should not be detectable with the WCS. However, our images reveal a marginal detection at an angular separation of $0\farcs167$, an orientation of 256° and a contrast of $\Delta B \simeq 2.5$. The distance of this feature from the central star correspond to about 60 AU is not compatible with the aforementioned orbital period.

β Cyg

β Cyg is a multiple system composed of a wide binary (HD 183912 and HD 183914) separated by $34\farcs51$ with an additional component orbiting close to HD 183912. This pair, whose orbital parameters are not well known (grade 4/5 on WDS), is composed of a bright K3II giant star ($V = 3.18$) plus a B0V component ($V = 5.82$) (ten Brummelaar et al. 2000). Based on these spectral types, the expected magnitude difference in the B band is $\Delta B = 0.95$. Even though very few observations of this close binary have been obtained so far, an orbital solution has been computed and gives an estimated semi-major axis of $0\farcs586$, an inclination of 118° and a period of 96.84 years (McAlister & Hendry 1982a; Hartkopf 1999; Hartkopf et al. 2000). Knowing that, the expected separation and position angle of the companion in April 2007 should be respectively $0\farcs240$ and 97.5°.

Our two observations of April and August 2007 show consistent results with respective separations of $0\farcs344$ and $0\farcs358$ and a measured orientation of 106.4° and 103.7° (see Figure 2.5 (d)). Finally, the contrasts measured between the two components is $\Delta B = 0.91$ for the April run and $\Delta B = 1.34$ for the August one. If the measured contrast is in good agreement with the available information about this binary, the measured separation and orientation are far from what we were expecting. However, the poor confidence that the WDS catalogue gives on this orbit and the good consistency of our results between the two observing runs make us confident in our measurements. Based on our two images and the previous measurement of the separation and angular position of the binary (McAlister & Hendry 1982a; Hartkopf 1999; Roberts et al. 2007) (see Table 2.3), we derive a low inclination orbit ($i = 151.8°$) having a semi major axis of $0\farcs447 \simeq 53$ AU (based on the Hypparcos parallax), an excentricity $e = 0.25$ and a period of $\sim$ 146.1 years. The summary of these new orbital elements can be found in Table 2.2 and a comparison between the various observations of β Cyg with the new ephemeris can be found in Table 2.3. Figure 2.6

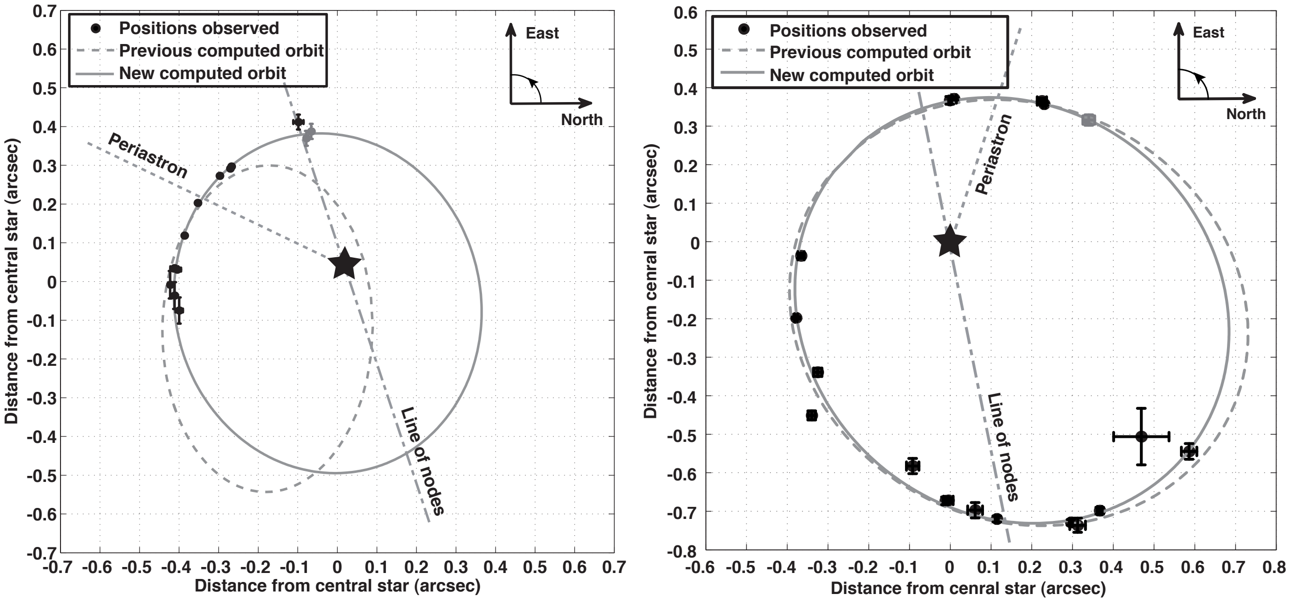

Figure 2.6: Comparison between the orbit found with previous observations (dashed line) and the one we find by combining those observations with ours (plain line) for β Cyg (left panel) and HD 95689 (right), respectively. All the visual observations of the binary system obtained with other instruments are represented by the black dots, while WCS measurements are in grey.

illustrates this orbital solution and compares it to the observations and to the previous calculated orbit (dashed line).

ϵ Hya

ϵ Hya is a system composed of multiple visible components among which three are within less than $3''$ from each other. The central pair consists in an F8V primary (ϵ Hya A, $V = 3.49$) and its companion (ϵ Hya B,$V = 5$) located at $0\farcs160$ with a position angle of 110.6° at the time of observation. Further away, the third component (ϵ Hya C, $V = 6.66$) is separated from the primary by $2\farcs88$ with an orientation of 303°.

Our image (see Figure 2.5, (e)) shows a good consistency with these positions for both companions. The respective separations and position angles measured for the two companions are $0\farcs142$ and 108.9° for the ϵ Hya B and $2\farcs703$ and 302.2° for ϵ Hya C. The fact that ϵ Hya B is well resolved at a separation that corresponds to only twice the diffraction limit of the telescope at our observing wavelength demonstrates the efficiency of the WCS to compensate for wavefront errors down to blue wavelengths. Note that discrepancy between the measured separation of ϵ Hya B with the primary and the one reported in reference papers is somewhat high considering its large angular separation. However, the distance measured in previous observations might have been measured from the centroid of the close binaries, which would explain part of the difference.

HD 90537

HD 90537 is a G8III star and is known to have a companion at a separation of $\sim 0\farcs5$ with a $\Delta V = 1.43$. The orbital parameter being well constrained, the expected separation and orientation of the pair at the time of observation is $0\farcs450$ and 220.7°. Our image (see Figure 2.5, (f)) shows excellent agreement with previous observations as the measured separation is $0\farcs448$ and the position angle 219.6°. The magnitude

Table 2.3: Summary of the results obtained on β Cyg and HD 95689 by different surveys and comparison with the new orbital solutions calculated in this Section.

Name	Date (BY)	θ (deg)	ρ (arcsec)	σ_θ (deg)	σ_ρ (arcsec)	$\Delta\theta_{\mathrm{o-c}}$ (deg)	$\Delta\rho_{\mathrm{o-c}}$ (arcsec)	*References*
β Cyg	1976.3676	186.2	0.444	4.6	0.005	-2.09	0.0075	McAlister & Hendry (1982a)
	1976.6133	195.3	0.434	4.6	0.005	7.01	-0.0025	McAlister & Hendry (1982a)
	1976.6217	190.0	0.437	4.6	0.005	1.71	0.0005	McAlister & Hendry (1982a)
	1979.5295	181.2	0.424	0.5	0.01	-0.25	-0.0040	McAlister & Hendry (1982b)
	1979.7699	180.7	0.431	0.5	0.01	-0.17	0.0036	McAlister & Hendry (1982b)
	1984.7010	169.0	0.413	0.3	0.0025	-0.30	-0.0018	Hartkopf et al. (2000)
	1984.7112	156.3	0.406	0.3	0.0025	-0.17	0.0033	Hartkopf et al. (2000)
	1994.7080	143.6	0.393	0.3	0.0025	-0.02	0.0015	Hartkopf et al. (2000)
	1996.4227	139.0	0.384	0.4	0.003	-0.05	-0.0033	Hartkopf et al. (2000)
	1996.6984	138.1	0.385	0.4	0.003	0.32	-0.0013	Hartkopf et al. (2000)
	2002.6800	107.5	0.390	2	0.02	-12.62	0.0205	Roberts et al. (2007)
	2007.3260	106.4	0.344	0.75	0.02	0.79	-0.0101	Our blue AO results
	2007.6190	103.7	0.358	0.75	0.02	-0.67	0.0052	Our blue AO results
HD 95689	1980.0000	317.1	0.800	2	0.02	-0.69	-0.0011	Comellas, J.L.
	1983.1500	312.8	0.690	6	0.1	7.49	-0.1155	Heintz, W.D.
	1985.0030	297.7	0.789	0.5	0.01	-0.24	-0.0058	McAlister et al. (1987)
	1986.2490	293.0	0.800	1.5	0.02	0.29	0.0183	Tobal, T.
	1986.4039	292.1	0.787	0.3	0.008	-0.23	0.0064	Hartkopf et al. (2000)
	1989.2378	279	0.729	0.3	0.008	-0.53	-0.0035	Hartkopf et al. (2000)
	1990.0460	275.0	0.700	1.5	0.02	-0.47	-0.0140	Tobal, T.
	1991.2500	269.6	0.672	1	0.006	0.44	-0.0113	Hipparcos cat.
	1991.3240	269.0	0.673	0.5	0.01	0.27	-0.0081	Hartkopf et al. (1994)
	1993.3340	261.0	0.590	1.5	0.02	4.51	-0.0291	Miura et al. (1995)
	1995.9400	233.0	0.565	1	0.015	-3.24	0.0412	Aristidi et al. (1997b)
	1997.0740	226.2	0.470	1	0.015	1.89	-0.0069	Aristidi et al. (1997a)
	1998.4300	207.6	0.427	0.4	0.004	-0.03	0.0027	Prieur et al. (2001)
	1999.8890	185.7	0.368	1	0.008	2.37	-0.0046	Horch et al. (2002)
	2004.2130	90.2	0.367	0.4	0.01	-1.47	0.0015	Scardia et al. (2005)
	2004.3970	88.6	0.371	0.9	0.003	0.13	0.0012	Scardia et al. (2005)
	2006.2700	58.4	0.429	1.8	0.005	0.50	0.0005	Prieur et al. (2008)
	2006.3100	57.2	0.425	0.6	0.004	-0.01	-0.0052	Prieur et al. (2008)
	2007.3260	42.9	0.464	0.75	0.02	-1.01	-0.0036	Our blue AO results

difference in blue is somewhat smaller than in the visible with $\Delta B = 1.08$ suggesting a companion with an earlier stellar type than the primary (i.e. G0V).

HD 95689

HD 95689 whose primary is a G9III star with $V = 2.02$ is a triple system with a wide companion and a closer one having a separation and orientation at the time of observation (published orbital solution) of about $0\farcs470$ and 58.4° (Scardia et al. 2005; Prieur et al. 2008). However, the orbit is still uncertain as explained in Prieur et al. (2008), who measure an angular position difference between their observations and the theoretical orbit of 2.2° to 2.9°. Moreover, the WDS catalogue reports an observation of this binary in 2007 that measures the orientation of the companion at 44.0°. This orientation is far from the 58.5° predicted by the orbital elements currently available for this system.

Our observations (see Table 2.1), while consistent with current orbital solutions in terms of separation ($\rho = 0\farcs464$), also reveal a significant difference between the measured and expected orientation of the companion ($\theta = 42.9°$). This orientation is very close to the last observation of 2007 reported in WDS. The result of our calculation of a new orbital solution including the most recent observations of

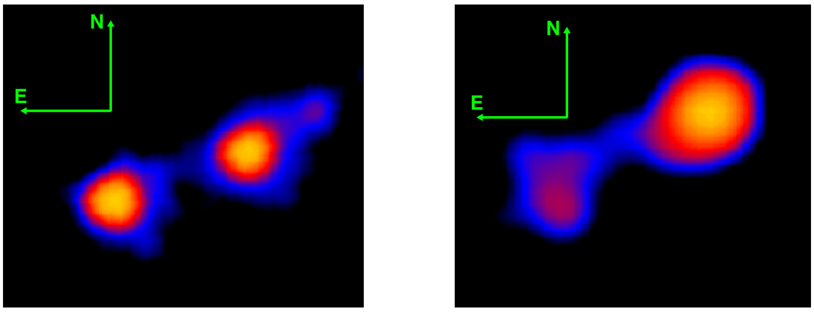

Figure 2.7: Left: The Mira system as seen in the UV by the HST. Mira A is losing gas rapidly from its upper atmosphere via a stellar wind. Mira B exerts a gravitational tug that creates a gaseous bridge between the two stars. Gas from the wind and bridge accumulates in an accretion disk around Mira B. Right: X-ray image of the Mira binary system obtained with Chandra. The collisions between rapidly moving particles in the disk produce X-rays.

HD 95689 by Prieur et al. (2008) and with the WCS at Palomar in 2007 is summarized in Table 2.2. The most significant change from the previous orbit found by Scardia et al. (2005) is the period, which is decreased from 44.5 yrs to 41 yrs, leading to a much better correspondance between the predicted ephemeris and the latest observations (see Figure 2.6, and Table 2.3).

o Cet (Mira)

Mira AB, is an interacting binary with an ageing cool M7III giant primary ($V = 6.8$) losing mass and an accreting white dwarf secondary ($V = 10.4$). The separation and orientation of Mira B predicted for our observation is $\rho = 0\farcs520$ and $\theta = 103°$. This pair has been imaged at various wavelengths in the past ten years. Both an X-Ray Chandra image (Karovska et al. 2005) and a Hubble UV image have revealed an extended structure filling the gap between the two stars which corresponds to accreting matter transiting between the giant primary and the white dwarf secondary.

Our image of the system (see Figure 2.5, (h)) shows a good agreement with the expected positions of the two components. Indeed we measure a separation of $0\farcs505$ and a position angle of 104.6°. An extended source bridging the gap between the two stars is also detected in the blue with a $\sim 15\,\sigma$ confidence level. This source is perfectly consistent with the previous HST observations (see Figure 2.7). Finally, as it can be seen on Figure 2.5, the image of Mira A is highly elongated toward the North. This extension detected to the North of the primary, resembles to a point like source but does not appear on any high angular resolution image of the system taken from the X-rays to the visible.

NS Vul

NS Vul is an visual binary composed of a red supergiant M5I primary ($V = 8.57$) and a A2 secondary ($V = 8.9$). The primary being a red supergiant, its luminosity drops rapidly in the blue ($B - V = +1.8$) while the magnitude of the secondary is similar in the blue and in the visible ($B - V = +0.03$). Therefore, the secondary will be brighter in our blue image with a magnitude difference $\Delta B = -1.44$. Its orbital parameters – mostly determined by speckle interferometry – are well known and the expected separation and position angle at the time of observation are respectively $\rho = 0\farcs750$ and $\theta = 276.4°$ (Proust et al. 1981; Jura et al. 1997; Worley & Mason 1998; Germain et al. 1999).

On the image taken during our run (see Figure 2.5, (i)) , we measure a separation of $0\farcs721$ and a position angle of 272.1° between the primary (fainter on our image) and the secondary. The contrast

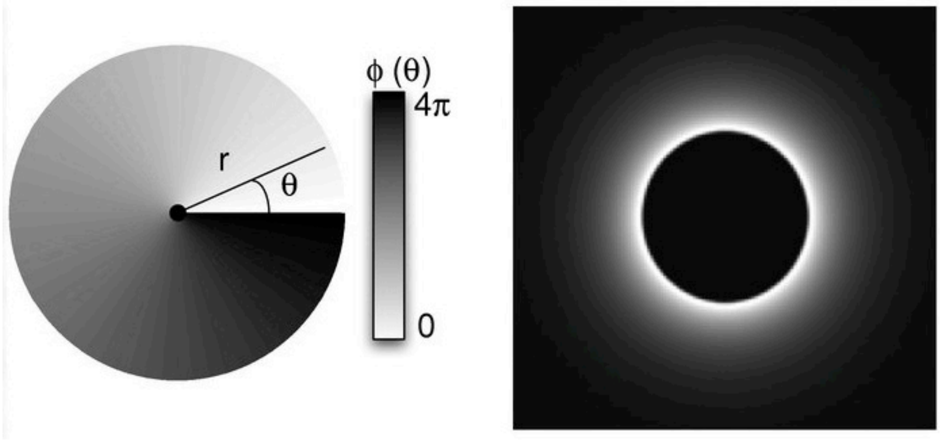

Figure 2.8: *Left:* Phase ramp produced by an optical vortex of topological charge 2. *Right:* Focal plane image of the coronagraphic pupil. The Fourier transform of the product of the PSF by the azimuthal phase ramp sends the light outside the original pupil area. Image from Mawet et al. (2010).

measured between the two components of the system is $\Delta B = -1.25$, in good agreements with their spectral types.

2.2.4 Error bars on the pixel size and telescope orientation

The separations and orientations that we measure in our images strongly depend on the accuracy to which the pixel size and telescope orientation have been determined on the reference binary (α Her). By comparing our measurements of the companions separation and angular position with their expected positions, it is possible to derive a mean value of the error on the pixel size and on the telescope orientation. By doing so, a conservative error of 4% on the pixel size is measured on average for the run of April and 3.5% for the run of August. These values are however pessimistic as they include the two binaries for which a new orbital solution has been found. Moreover, the wide pair of ϵ Hya for which the error on the pixel size is $\sim$ 6% is also included despite the fact that most of the error can probably be explained by the poor determination of the primary's centroid obtained with previous observations. If this hypothesis is verified, the measured separation would be more consistent with the other observations. Taking the new orbital solution into account, a more realistic value can be obtained for the error bar on the pixel size at the 2.5% level over the two nights. As for the orientation, the mean error observed is also rather small: 1.3° for April and 2.8° for August. Again, two outliers are observed: β Cyg and HD 95689. If the new orbital solutions of these two stars can be trusted, the error on the position angle can be pushed down to 1.1° for April and 2.2° for August.

2.3 Reaching high contrasts with phase mask coronagraphs

The previous section has demonstrated that Extreme AO systems can be used to observe close binaries in the blue. This technique has the advantage of partially compensating for the loss of resolving power when optimizing the wavefront correction on a small sub-aperture of a large telescope, but does not provide high Strehl ratios; it is therefore not suited for coronagraphic observations. On the other hand, when used in the infrared, the WCS can provide diffraction limited images (Strehl $>$ 85%) from a clear, unobscured aperture. It is therefore well optimized for coronagraphy and high-contrast imaging in general, but suffers from a lack of angular resolution. A solution to this drawback is the use of optical

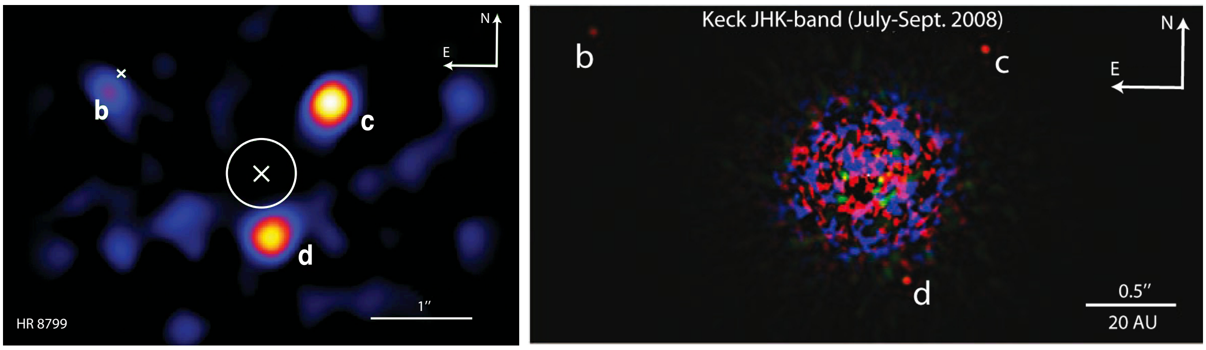

Figure 2.9: *Left:* Final calibrated image of HR 8799 obtained with the OVVC on the WCS. *Right:* Color image of HR 8799 produced by combining J-, H- and K_s- images collected by the Keck telescope. For both results, PSF subtraction has been performed using the LOCI algorithm (Lafrenière et al. 2007b). Images from Serabyn et al. (2010) and Marois et al. (2008), respectively.

vortex phase-mask coronagraphs (Mawet et al. 2005b; Foo et al. 2005; Jenkins 2008; Swartzlander et al. 2008) which have been identified by Guyon et al. (2006) as one of two masks being nearly perfect in terms of useful throughput because they feature a small IWA ($< 1.5\lambda/D$), a high throughput ($> 90\%$) and a 360° off-axis discovery space (Mawet et al. 2009). An optical vortex is a phase singularity in an optical field resulting from a phase ramp dislocation of the form $e^{il\theta}$, with l and θ being the topological charge and the azimuthal coordinate, respectively. Because of this ramp, the light waves at the axis itself cancel each other out, creating a so called dark-hole (see Figure 2.8).

First equipped with a Four Quadrant Phase Mask coronagraph (Rouan et al. 2000; Riaud et al. 2001, 2003), which can be seen as a discretized version of an optical vortex, the WCS is now equipped with an optical vectorial vortex coronagraph (OVVC) made of liquid crystal polymers (Mawet et al. 2009). This unique facility allows operation in the XAO regime in the near infrared (H and K bands) and provides a raw attenuation of $\sim 2 \times 10^{-2}$ on the peak (on-axis), which goes down to $\sim 4 \times 10^{-4}$ at angular distances as small as $3\lambda/D$, with 15% bandwidth. Furthermore, thanks to the extreme stability of the PSF (which results in only quasi-static speckles), differential imaging techniques can be efficiently used to push the detection limit of the instrument down to $\sim 3 \times 10^{-5}$ from λ/D ($0\farcs5$ in the $\mathrm{K_s}$ band) to the outer field of view. This sensitivity, even at small angular separations, makes it competitive with both 8 m- class telescopes, and with NICMOS on the HST for the direct imaging of extra-solar planets and circumstellar disks around relatively bright stars. Since the first commissioning run in 2007, the WCS has lead to the imaging of several known and unknown brown dwarf companions around HD 130948, HD 49197, HR 7672 and HD 171488 (Serabyn et al. 2009) and of a circumstellar disk around HR 7672b having a fractional luminosity of 0.3% (Mawet et al. 2009). But the most striking result of the WCS+OVVC is certainly the picture of the famous exoplanetary system HR 8799 hosting 4 planets, three of which are clearly detected (Serabyn et al. 2010). Figure 2.9 shows a comparison between the image of the system obtained with the WCS at Palomar (left) and the first observation of Marois et al. (2008) with the Keck telescope. Despite an obvious difference in terms of angular resolution, the two images are similar, proving the interest of optimizing the wavefront correction on a small sub-aperture of a telescope to reach the XAO regime. This pioneering result, obtained with an 1.5 m aperture, is a very promising example of what will be achieved in the near future when such a level of AO correction will be available on 10-m class telescopes and later, on the Extremely Large Telescopes.

Part II

Multi-aperture imaging: toward other Earths

3

An introduction to interferometry and to interferometers

Contents

3.1 Reaching very high angular resolutions with interferometry 49

3.2 Principles of stellar interferometry 50

3.2.1 Fringe visibilities 53

3.2.2 Phase measurements 55

3.3 Nulling interferometry 56

3.3.1 Null depth 57

3.3.2 Geometric leakage 58

3.3.3 Instrumental leakage 59

3.3.4 Spatial and modal filtering 59

3.4 Current facilities 60

3.4.1 Stellar interferometers 60

3.4.2 Nulling interferometers 63

The resolving power of a telescope is proportional to the diameter of its mirror and inversely proportional to the observing wavelength. Considering that the wavelength is generally determined by the astrophysical phenomena under study (especially on the ground), the ultimate resolution is therefore set by the aperture diameter. Projects for building extremely large ground-based telescopes are being pursued but their sizes are still limited to a few tens of meters. The size of space-based telescopes is even more restricted because they must fit in their launcher fairing. A possible solution consists in discretizing the aperture by recombining coherently the light collected from various telescopes. In doing so, it is theoretically possible to increase indefinitely the resolving power by increasing the separation between the individual apertures. In this chapter, we review the principles of this technique called interferometry and introduce the required concepts for the next chapters, as well as some technical aspects. We then present the main interferometric facilities as well as their major scientific discoveries.

3.1 Reaching very high angular resolutions with interferometry

Since the first telescope imagined by Galileo to observe the sky, astronomers have always wished to build more and more advanced devices in order to probe very small details in the sky. However the capability to distinguish small details in an image directly depends on the resolving power of the optical system being used. This angular resolution (the inverse of the resolving power) is given by $\theta = 1.22\lambda/D$ where λ is the wavelength of observation and D the telescope diameter. With the evolution of the technology, telescopes with increasing sizes have been built over the years. Today, projects such as the Thirty Meter Telescope (TMT) (Nelson & Sanders 2006; Szeto et al. 2008; Crampton et al. 2009; Simard et al. 2010), the Giant Magellan Telescope (GMT) (Johns 2008; Shectman & Johns 2010) and the European Extremely Large Telescope (E-ELT) (Cuby 2010; Markus 2010) are even planing to construct telescopes with diameters up to 42 m. However, another solution exists to reach a similar or even still better resolving powers but with much smaller apertures: interferometry.

The idea behind optical interferometry is to coherently recombine the light coming from different telescopes in order to reach an angular resolution which is not limited by the size of the individual apertures anymore but by the distance between them. In 1868, Fizeau discovered that when a source was observed through two separated apertures, the contrast of the resulting fringe pattern in the image plane was inversely proportional to the size of the source. He proposed to apply this technique to measure the angular diameter of stars. For that, he suggested to install an opaque mask containing two holes in front of the mirror of a telescope and measure the fringe contrast resulting from the observation of stars. In 1873, Stéphan used the 80 cm-wide telescope of the Observatoire de Marseille, and observed the brightest stars in the sky looking for any variation of the fringe contrast. Unfortunately, because of the rather short available baseline on this telescope ($\sim$ 65 cm) he was unable to resolve any of them. Twenty years later, Michelson was the first to successfully measure angular diameters with interferometry while observing the four satellites of Jupiter. He then proposed to increase the available baseline length by installing a 7 m long beam on the 60 inches telescope of Mt. Wilson (Michelson 1920; Michelson & Pease 1921). Thanks to this ingenious setup, Michelson and Pease measured for the first time the diameter of a star: α Ori ($\sim 0\farcs47$, Michelson & Pease 1921). The instrument was then used for resolving narrow spectroscopic binaries. After a long hibernation, Brown and Twiss resurrect interferometry in 1956 using a principle somewhat different from that of Fizeau, called intensity interferometry. Thanks to their instrument they measured the stellar diameters of 32 stars with an unprecedented resolution ($\theta = \lambda/2b \sim 0.5$ mas, b being the baseline). Twenty years later, in 1975, Labeyrie was the first to construct a Fizeau interferometer composed of two separate telescopes (Labeyrie 1975). Using a baseline of 12 m, he reached an angular resolution of 5 mas. Since then, many interferometers around the world have been built with operational wavelengths from the visible to the mid-infrared and baselines up to 331 m and many fields in astrophysics now benefit from their incredible angular resolution. A summary of current interferometric facilities will be presented in Section 3.4.

3.2 Principles of stellar interferometry

The principle of interferometry is to recombine the light collected by different telescopes that observe a common astrophysical source (see Figure 3.1). By doing so, one gets a spatial information on the source with an angular resolution that is inversely proportional to the distance between the observing apertures. It is therefore possible to get information at very high angular resolution without requiring the use of extremely large apertures.

The expression of a monochromatic plane wave collected by a telescope i of an interferometer and emitted by an unresolved source is given at any point $\mathbf{r}$ of the pupil by:

$$\mathbf{E_i}(\boldsymbol{\theta}, \mathbf{r}) = \Pi(r/R)\, \mathbf{E_i}(\boldsymbol{\theta}) e^{i\phi_i} \tag{3.1}$$

where $\boldsymbol{\theta} = (\theta, \alpha)$ are the coordinates of the source in the sky plane, $\mathbf{E_i}(\boldsymbol{\theta})$ is the complex amplitude of the light collected by this telescope, ϕ_i an instrumental phase added to the beam collected by telescope

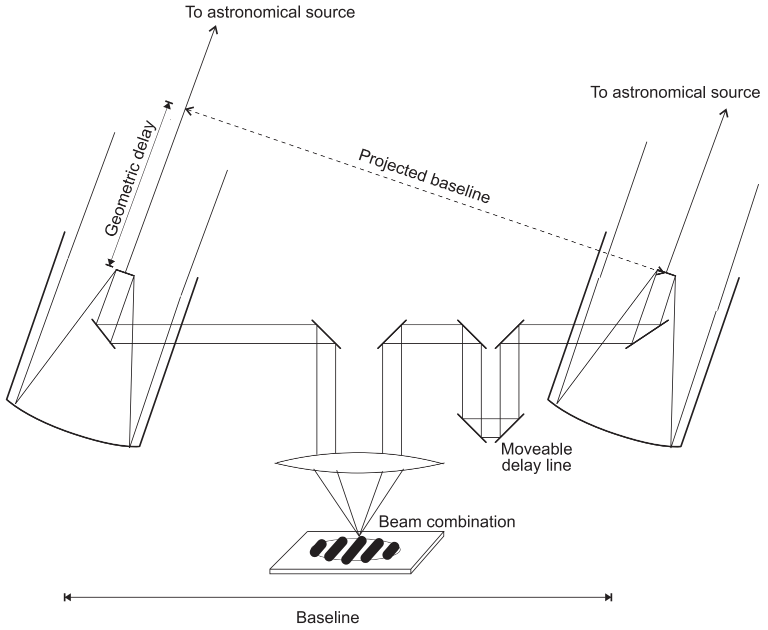

Figure 3.1: Schematic representation of a Fizeau type interferometer. The optical paths of light beams coming from the telescopes are first matched using a delay line. The two beams are then focused onto a detector to produce an interference pattern. Image from Absil (2006).

i and $\Pi(r/R)$ is the pupil response of this telescope of diameter $D = 2R$. The complex amplitude of the electromagnetic fields, once recombined at the pupil plane is simply obtained by adding the individual contribution of the telescopes. For the simplest case of a two telescope interferometer, this amplitude is:

$$\mathbf{E}(\boldsymbol{\theta}, \mathbf{r}) = \Pi(r/R)\left(\mathbf{E_1}(\boldsymbol{\theta})e^{i\phi_1} + \mathbf{E_2}(\boldsymbol{\theta})e^{i\phi_2}\right) \tag{3.2}$$

The expression of the complex electromagnetic field $\mathbf{E_i}(\boldsymbol{\theta})$ can be further decomposed into its modulus E_i and a phase term. Let us denote the phase difference introduced between the two beams for a source on the optical axis as $\Delta\phi = \phi_2 - \phi_1$. The additional phase associated with a slightly off-axis source due to its differential external path ΔOPD is $\pm\pi\frac{b\theta}{\lambda}\cos\alpha$ (see Figure 3.2) and the recombined electromagnetic fields thus writes:

$$\mathbf{E}(\boldsymbol{\theta}, \mathbf{r}) = \Pi(r/R)\left(E_1 e^{i\pi(b\theta/\lambda)\cos\alpha} + E_2 e^{-i\pi(b\theta/\lambda)\cos\alpha + i\Delta\phi}\right) \tag{3.3}$$

The intensity distribution in the pupil plane $I(\boldsymbol{\theta}, \mathbf{r})$ is then obtained by multiplying the amplitude of the resulting electromagnetic field $\mathbf{E}(\boldsymbol{\theta}, \mathbf{r})$ by its complex conjugate $\mathbf{E}^*(\boldsymbol{\theta}, \mathbf{r})$:

$$\begin{aligned} I(\boldsymbol{\theta}, \mathbf{r}) &= \Pi^2(r/R)\ (\mathbf{E}(\boldsymbol{\theta}, \mathbf{r})\,\mathbf{E}^*(\boldsymbol{\theta}, \mathbf{r})) && (3.4) \\ &= \Pi^2(r/R)\ \left[E_1^2 + E_2^2 + 2E_1E_2\,\Re\left[e^{i(2\pi(b\theta/\lambda)\cos\alpha + \Delta\phi)}\right]\right] && (3.5) \end{aligned}$$

Considering the case of two identical telescopes and a perfectly symmetric transmission of the two beams through the optical system, we have $E_1^2 = E_2^2 = I$ and the above equation can be simplified as:

$$\begin{aligned} I(\boldsymbol{\theta}, \mathbf{r}) &= \Pi^2(r/R)\,2I\left(1 + \cos\left(2\pi\frac{b\theta}{\lambda}\cos\alpha + \Delta\phi\right)\right) && (3.6) \\ &= \Pi^2(r/R)\,4I\cos^2\left(\pi\frac{b\theta}{\lambda}\cos\alpha + \Delta\phi\right) && (3.7) \end{aligned}$$

In this simple case, the intensity distribution is a square cosine function depending on the angular distance of the source from the optical axis (or equivalently on an artificial phase shift introduced between

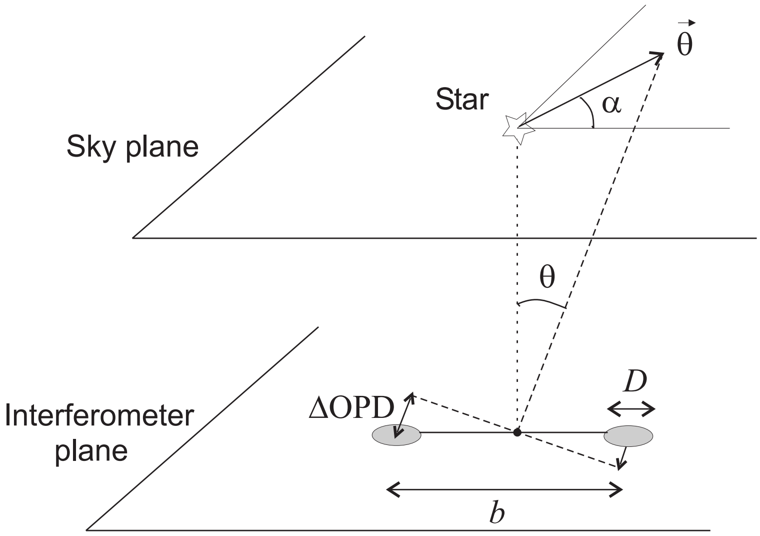

Figure 3.2: Illustration of the two angular coordinates (θ, α) giving the position of a point-source in the sky plane. The OPD between the arms is also represented for a two telescope interferometer having a baseline b. In this figure, it is assumed that the line-of-sight is perpendicular to the plane of the interferometer. Image from Absil (2006).

the two beams) and vary between zero and $4I$. The angular resolution of the interferometer is defined by the distance between a light intensity minimum and a maximum in this diffraction pattern and is equal to $\lambda/2b$. This value should be compared with the angular resolution of a single telescope of diameter D which is $1.22\lambda/D$.

Interferometers with finite bandwidth

The interference pattern described by Equation 3.7 corresponds to a monochromatic observation at a certain wavelength λ. In this particular case, interferences between two beams can be obtained regardless of the optical path difference (OPD) between them. From a realistic point of view, astronomical observations are always performed on polychromatic sources with an instrument characterized by a finite bandwidth. Let's see now how Equation 3.7 evolves in this case.

We consider that the interferometer has a spectral transmission $\eta(\lambda)$ and that the intensity of the source collected by each telescope has a spectral intensity $I(\lambda)$. The astronomical sources provide individual frequencies that are mutually incoherent. Therefore, the polychromatic interference fringe pattern can simply be computed by summing the individual monochromatic contributions over the instrumental passband. For simplicity, we take both the source spectral intensity and the instrumental throughput as being constant over a wavelength band $\Delta\lambda$ centered around λ_0. The intensity response of the interferometer becomes:

$$\begin{aligned} I(\boldsymbol{\theta}, \mathbf{r}) &= \Pi^2(r/R) \int_{\lambda_0-\Delta\lambda}^{\lambda_0+\Delta\lambda} 2I(\lambda)\eta(\lambda)\left(1+\cos\left(2\pi\frac{b\theta}{\lambda}\cos\alpha+\Delta\phi\right)\right)d\lambda \qquad (3.8)\\ &= \Pi^2(r/R)\, 2I_{\lambda_0}\eta_{\lambda_0}\Delta\lambda\left[1+\mathrm{sinc}\left(2\pi\frac{b\theta\Delta\lambda}{\lambda_0^2}\cos\alpha+\Delta\phi\right)\cos\left(2\pi\frac{b\theta}{\lambda_0}\cos\alpha+\Delta\phi\right)\right] \qquad (3.9)\\ &= \Pi^2(r/R)\, 2I_\lambda\left[1+M(\Lambda_{\mathrm{coh}}, \boldsymbol{\theta}, \Delta\phi)\cos\left(2\pi\frac{b\theta}{\lambda_0}\cos\alpha+\Delta\phi\right)\right] \qquad (3.10) \end{aligned}$$

where I_λ is the overall source intensity arriving at the detector and collected by each telescope over the instrument passband, $M(\Lambda_{\mathrm{coh}}, \boldsymbol{\theta}, \Delta\phi)$ is the fringe envelope modulation function and $\Lambda_{\mathrm{coh}} \equiv \lambda_0^2/\Delta\lambda$ is the coherence length. A fringe pattern similar to the monochromatic case is still present with a spacing between two constructive interferences of λ/b but the amplitude of the fringes is now modulated by a sinc function. The amplitude of the fringes cancels out when $|2\pi b\theta/\Lambda_{\mathrm{coh}} + \Delta\phi| = 1$ and stays small while being > 1. The dark plain line in Figure 3.3 is the fringe pattern of a 100 m baseline interferometer with 0.2 μm bandwidth and centered at 2.2 μm.

Observation of extended sources

Now that the response of an interferometer to an unresolved source has been described, it is time to see how the intensity distribution of the interferences evolves when a partially resolved source is observed. The source intensity collected by each telescope $I_\lambda(\boldsymbol{\theta})$ must now be described as a function of the position $\boldsymbol{\theta}$ in the sky plane. This intensity distribution does not only reflect the target physical brightness distribution but it also takes into account the throughput or collection efficiency of the interferometer telescopes as a function of the position in the sky. It is generally considered that a source of finite extent can be modeled as the sum of incoherent infinitesimal sources. The intensity distribution can then be re-written as follows:

$$\begin{aligned} I(\mathbf{r}) &= \Pi^2(r/R)\,2\left(\int_{\boldsymbol{\theta}_{\mathrm{src}}} I_\lambda(\boldsymbol{\theta})d\boldsymbol{\theta} + \int_{\boldsymbol{\theta}_{\mathrm{src}}} I_\lambda(\boldsymbol{\theta})M(\Lambda_{\mathrm{coh}},\boldsymbol{\theta},\Delta\phi)\cos\left(2\pi\frac{b\theta}{\lambda_0}\cos\alpha + \Delta\phi\right)d\boldsymbol{\theta}\right) && (3.11)\\ &= \Pi^2(r/R)\,2I_{\lambda,\mathrm{tot}}\left(1 + \Re\left\{\mathcal{V}e^{i(\Delta\phi)}\right\}\right) && (3.12)\end{aligned}$$

where $\mathcal{V}$ is called the complex visibility (or the complex degree of coherence) and is defined by:

$$\mathcal{V}(b,\lambda) = \frac{\int_{\boldsymbol{\theta}_{\mathrm{src}}} I_\lambda(\boldsymbol{\theta})M(\Lambda_{\mathrm{coh}},\boldsymbol{\theta},\Delta\phi)e^{i\,2\pi\frac{b\theta}{\lambda_0}\cos\alpha}d\boldsymbol{\theta}}{\int_{\boldsymbol{\theta}_{\mathrm{src}}} I_\lambda(\boldsymbol{\theta})d\boldsymbol{\theta}} \tag{3.13}$$

Compared to the intensity distribution of an unresolved source (Equation 3.12), the fringe modulation (or amplitude) of an extended object (Equation 3.12) is now proportional to $\Re\left\{\mathcal{V}e^{i(\Delta\phi)}\right\}$, which directly depends on the source intensity distribution $I_\lambda(\boldsymbol{\theta})$ (Equation 3.13). This intensity modulation, also called fringe contrast, is therefore directly related to the source distribution and is maximum for an unresolved source. The amplitude and phase of $\mathcal{V}$ carry the high angular resolution information of the source. Figure 3.3 shows a comparison between the interferogram resulting from the observation of an unresolved source (black curve) with that corresponding to the observation of a resolved binary system with a contrast of 1:5 (grey curve). Two things can be observed from this comparison. First, the contrast of the fringes measured on the binary system is lower than for the unresolved single star. This contrast is proportional to the visibility's modulus and gives an indication of how spatially extended the source is. Second, the grey interferogram is not symmetric with respect to the optical axis ($\theta = 0$). This asymmetry is related to the phase of the visibility and measures the observed source asymmetry in the direction of the interferometer's baseline. In Sections 3.2.1 and 3.2.2 we further explain how to extract and exploit these two quantities related to the source complex visibility.

3.2.1 Fringe visibilities

In stellar interferometry, the basic observable is the contrast of the fringes produced by the combination of the various light beams. For a two telescope interferometer, it is given by the amplitude of the complex degree of coherence $\mathcal{V}$ defined by Equation 3.13 and can be found by measuring the ratio between the fringe amplitude and the average intensity:

$$|\mathcal{V}| = \frac{I_{\mathrm{max}} - I_{\mathrm{min}}}{I_{\mathrm{max}} + I_{\mathrm{min}}} \tag{3.14}$$

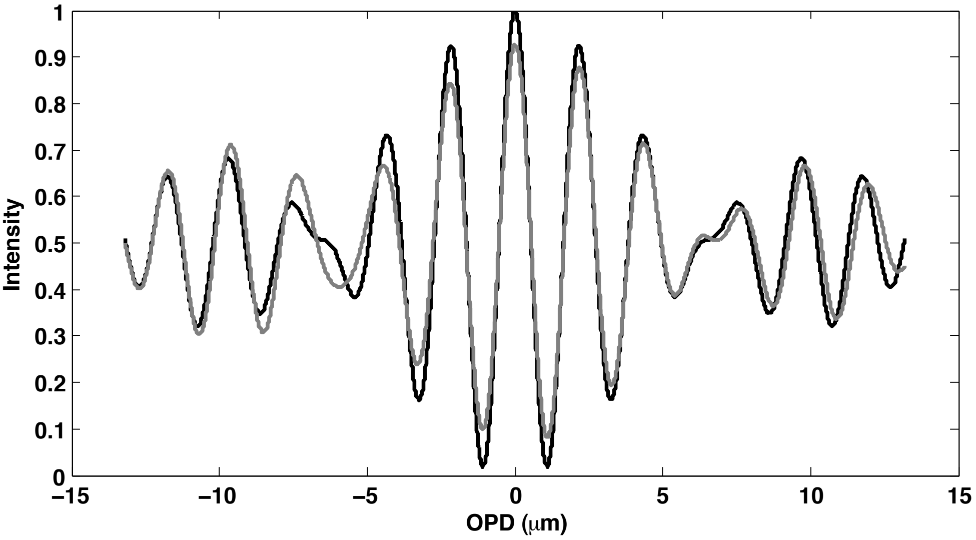

Figure 3.3: The plain black line is a fringe pattern corresponding to the observation of a single star at 2.2 μm with projected interferometric baseline of 100 m. The grey line is the same interferogram but for a binary system with a separation of 15 mas and having a contrast ratio of 5:1.

where $I_{\max}$ and $I_{\min}$ denote the maximum and minimum intensites of the fringes and $|\mathcal{V}| \in [0, 1]$. This quantity, first used by Michelson and Pease at Mt. Wilson to measure stellar angular diameters (Michelson 1920; Michelson & Pease 1921) is directly related to the unique Fourier component of the source's brightness distribution corresponding to the spatial frequency $u = b/\lambda$ (Thompson et al. 2001). For example, the fringe contrast measured on a single star is directly related to its physical size. Approximating a single star by a uniform disk of diameter $\theta_\star$, the visibility measured by a two-telescope interferometer is obtained by computing the integral in Equation 3.13:

$$|\mathcal{V}(b_\perp, \lambda, \theta_\star)| = \left(\frac{2J_1(\pi\theta_\star b_\perp/\lambda)}{\pi\theta_\star b_\perp/\lambda}\right) \tag{3.15}$$

where $b_\perp$ is the length of the baseline vector projected onto the sky plane. For an unresolved star ($\theta_\star \ll \lambda/b_\perp$), the above expression can be approximated by

$$|\mathcal{V}(b_\perp, \lambda, \theta_\star)| = \left(1 - \frac{(\pi\theta_\star b_\perp/\lambda)^2}{8}\right) \tag{3.16}$$

In practice, the observed fringe system is not perfect, but is corrupted by fast fluctuations of phase and intensities that are introduced either by the atmosphere or by the instrumental setup. Instead of considering the visibility, Perrin (2003) has demonstrated that it is better to work with its square modulus because estimators can be constructed to properly take into account the noise bias. The measured visibility on the target is however always affected by atmospheric and instrumental effects and it is important to combine the observation of a scientific star with that of a reference star which is not resolved by the interferometer. The actual visibility of the target is then simply given by the ratio of its observed visibility divided by that of the calibrator star's. Unfortunately, the observing conditions inevitably change between the visibility measurement taken on the science star and the reference one. Therefore, the accuracy of current interferometric data reduction methods based upon visibility measurements is limited to $\sim 1\%$. We will show in Section 4.2 that it is possible to increase this accuracy by an order of magnitude or more by using an advanced statistical analysis of the fluctuating visibility measurements.

3.2.2 Phase measurements

The second observable that one can extract from an interferometer is the phase of the complex visibility. However, for ground based interferometry, this information is largely corrupted by atmospheric-induced phase errors. The random OPD between the interferometric beams is due to the fact that the atmospheric layers above each telescope composing the array are different. Moreover, the OPD error fluctuates rapidly as turbulent cells cross the apertures. If we denote by ϕ_i the random phase error introduced by the atmosphere at each telescope i, the phase measured for each baseline of an interferometer $\Phi(i-j)$ is:

$$\Phi(i-j) = \Phi_0(i-j) + [\phi_i - \phi_j] \tag{3.17}$$

where $\Phi_0(i-j)$ is the intrinsic phase of the source as seen by the baseline $i-j$. Compensating for these random perturbations is one of interferometry's biggest challenge. Indeed, phase fluctuations distort the recorded interference pattern at relatively high frequency (typically $0.1 - 1\,\mathrm{kHz}$ in the near infrared). One can consider the problem as being a discretized version of the wavefront errors introduced by the same turbulent cells over large single-aperture telescopes. In order to avoid the blurring of the fringes, one must therefore either record them very rapidly ($> 1\,\mathrm{kHz}$) or monitor the target's phase to correct for the wavefront corrugation in real time.

Phase referencing

The two aforementioned solutions, even though efficient, are limited to relatively bright sources ($m_K \simeq 5$ with the ATs on the VLTI), which limits the number of observable targets. The phase referencing technique (Shao & Colavita 1992a; Quirrenbach et al. 1994) proposes to use a bright reference star to determine the atmospheric phase and to either correct in real-time (Delplancke et al. 2000) or by post-processing the fringe phase on the faint scientific star. The main limitation of this method is that the angular separation between both stars must be small enough to be affected by the same atmospheric turbulence. This maximum separation is given by the isoplanetic angle θ_i, which is the angle on the sky over which the atmospherically induced phase is correlated. It can be approximated by $\theta_i \propto r_0/h^*$, where r_0 is the atmospheric coherence diameter and h^* is the effective height of the turbulence profile, and is usually $\sim 20''$ in the K band. This technique has been applied to narrow-angle astrometry (Shao & Colavita 1992b; Colavita 1994) where the fringe phase of two stars is measured simultaneously. Astrometric accuracies down to a couple of micro-arcseconds can then potentially be reliably measured (Shao & Colavita 1992a; Muterspaugh et al. 2006; van Belle 2011).

Closure phases

First used in radio-astronomy, the closure phase technique consists in combining the phase information measured by three different interferometric baselines to get rid of the phase error and obtain an absolute measurement of the target's phase (Jennison 1958). Indeed, when more than two telescopes are combined pair-wise, the sum of the phases measured on three different baselines is a quantity, called the bispectrum, which is independent of the atmospherical phase and only depends on the brightness distribution of the source:

$$\Phi(i-j-k) = \Phi_0(i-j) + \Phi_0(j-k) + \Phi_0(k-i) \tag{3.18}$$

Unfortunately, only partial phase information can be retrieved as the phase measurements on three baselines must be added to get one closure phase. However, when a larger number of telescopes (N) are used simultaneously, the number of closure phases measured on triplets of telescopes is $(N-1)(N-2)/2$

while the number of independent Fourier phases is $N(N-1)/2$. The proportion of phase information that can be retrieved using closure phases is therefore given by $(N-2)/N$. This completeness, while being low (33%) for a three telescope array, rapidly increases to exceed 90% for $N > 20$ (if baselines are not redundant). This technique, now widely used at near-infrared wavelengths, can currently lead to accuracies on the phase measurement of about 0.2° (Zhao et al. 2008; Absil et al. 2010).

3.3 Nulling interferometry

In the previous sections, we introduced stellar interferometry and its fundamental observable which is the complex visibility. Figure 3.3 illustrates the comparison between fringes obtained on a single unresolved star and a resolved binary star having a contrast ratio of 5:1. If the loss of contrast is easily detected at moderate contrasts, the accuracy on visibility measurement is currently limited to about 1% which is not enough to detect extra-solar planets for which the contrast is substantially above 100:1. Moreover, even for a perfectly calibrated observation, the shot noise associated with the light of the much brighter central star remains, hiding the presence of any faint off-axis source. To circumvent this issue and the limitation of indirect techniques (radial velocity, astrometry) to detect exoplanets, Bracewell (1978) proposed a novel technique called nulling interferometry. The principle of a two-telescope nulling interferometer is to recombine destructively the collected on-axis stellar light by introducing an artificial half-wave phase shift between the beams, i.e. $\Delta\phi = \pi$. Unlike classical interferometry for which the interferograms are recorded either by temporally modulating the OPD or by spatially imaging the fringe pattern onto a detector, nulling interferometers maintain a fixed π phase shift. The detected flux is therefore the sum of all transmitted sources in the field of view. By doing so, the star located at $\theta = 0$ is cancelled while faint off-axis sources can be revealed.

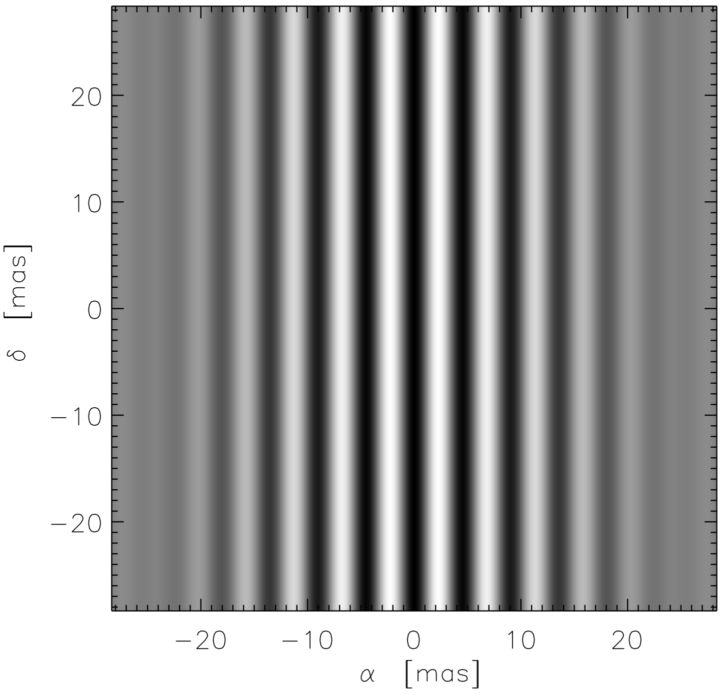

Figure 3.4: Polychromatic transmission map at 2.2 ± 0.2 μm for a 100 m Bracewell interferometer composed of two 8 m telescopes. The field of view has been limited to the diffraction-limit of the individual apertures (λ/D).

Such an interferometer is characterized by its intensity response projected onto the plane of the sky, also called *transmission map*. This map defines (in a focal plane) the transmission of the interferometer $R_\lambda(\boldsymbol{\theta})$ for every single point $\boldsymbol{\theta}$ within the field of view. Its expression is simply obtained by computing the Fourier transform of Equation 3.10 where $I_\lambda = 1$ and $\Delta\phi = \pi$:

$$R_\lambda(\boldsymbol{\theta}, \boldsymbol{\theta}_f) = \left(\frac{2J_1(\pi D\theta/\lambda)}{\pi D\theta/\lambda} \otimes \delta(|\boldsymbol{\theta}_f - \boldsymbol{\theta}|)\right) \left[1 - M(\Lambda_{\mathrm{coh}}, \boldsymbol{\theta}) \cos\left(2\pi \frac{b\theta}{\lambda_0} \cos\alpha\right)\right] \tag{3.19}$$

where $\boldsymbol{\theta}_f$ is the angular coordinate in the focal plane and $\otimes$ the convolution sign. In this equation, the first term (between brackets) represents the classical response of a single aperture centered at the position $\boldsymbol{\theta}$ of any point-like object. Because it is constant over the whole field of view, this term can be supressed from the expression of the transmission map and only the last term corresponding to the interference process remains:

$$R_\lambda(\boldsymbol{\theta}) = 1 - M(\Lambda_{\mathrm{coh}}, \boldsymbol{\theta}) \cos\left(2\pi \frac{b\theta}{\lambda_0} \cos\alpha\right) \tag{3.20}$$

An example of polychromatic transmission map is represented in Figure 3.4 for a 100 m interferometer working at 2.2 ± 0.2 μm. The FOV of the transmission map has been limited to the diffraction limit of a single 8 m telescope ($\lambda/D \simeq 57$ mas). In practice the FOV of an interferometer can be extended to much larger angular separations (e.g. $\sim 40''$ for the LBTI, Hinz et al. (2004)) but the high angular resolution information is limited by the coherence length ($\lambda_0^2/\Delta\lambda$). For larger angular separations ($\theta > 25$ mas in Figure 3.4), the fringe pattern washes out and only the lower spatial resolutions (the ones limited by the individual telescopes point spread functions) remain. For this reason, the FOV of most interferometers is limited to the size of an Airy pattern by means of spatial or modal filters. The spatial (or modal) filtering, has the further advantage to clean the wavefront from its aberrations induced by the atmosphere and the instrument optics, and which can strongly limit the dynamic of the nulling interferometer (see Section 3.3.4).

The final detection can be performed either in a pupil or an image plane. In the first case, a single-pixel detector is sufficient to record the total flux in the output pupil, emanating from all the sources in the diffraction-limited field-of-view. In the latter, an image similar to that of a single telescope is formed, except that the relative contribution of each source is affected by the interferometer's intensity response at its location. Unlike for stellar interferometry, no fringe is formed nor recorded and the final output at time t generally consists in a single value corresponding to the total intensity within the diffraction limit of an individual aperture [4]:

$$F_\lambda(t) = \int_\theta \int_\alpha R_\lambda(\theta, \alpha, t) B_\lambda(\theta, \alpha)\, \theta\, d\theta\, d\alpha \tag{3.21}$$

where $R_\lambda(\theta, \alpha, t)$ is the polychromatic time-dependent transmission map defined by Equation 3.20 in a static case and $B_\lambda(\theta, \alpha)$ is the brightness distribution of all coherent sources within the field-of-view and emitting in the wavelength range $[\lambda_0 - \Delta\lambda\,; \lambda_0 + \Delta\lambda]$.

3.3.1 Null depth

The only observable of a nulling interferometer is the null depth, which is defined as the ratio of the total intensity within the field-of view and measured by the detector divided by the total brightness of

---

[4] For simplicity and in order to be consistent with the demonstration leading to the definition of the visibility (see Section 3.2), we consider here that the background can be neglected. In Section 4.2 we will introduce the effect that the main noise sources and incoherent sources such as the background can have on the null depth estimation.

the coherent sources collected by the array.

$$N_\lambda(t) = \frac{F_\lambda(t)}{\int_\theta \int_\alpha B_\lambda(\theta, \alpha)\, \theta \, d\theta \, d\alpha} \tag{3.22}$$

The null depth can equivalently be expressed from Equation 3.12. Indeed, the fringe response of a nulling interferometer to a resolved source is the same as for a classical interferometer for which an optical path difference of $\lambda/2$ is maintained between the beams for an on axis source. Equation 3.12 then becomes $I(\boldsymbol{\theta}, \mathbf{r}) = \Pi^2(r/R)\, 2I_{\lambda,\mathrm{tot}}(1 - \Re\{\mathcal{V} e^{i(\Delta\phi)}\})$ and the null depth can be defined as:

$$N = \frac{I_{\min}}{I_{\max} + I_{\min}} \tag{3.23}$$

N is therefore comprised between 0 and 0.5. Inserting this expression into the definition of the visibility's amplitude given by Equation 3.14, a simple relation can be found between the latter quantity and the null depth:

$$|\mathcal{V}| = 1 - 2N \tag{3.24}$$

with $|\mathcal{V}| \in [0, 1]$.

3.3.2 Geometric leakage

In the case of a point source located on the optical axis of a nulling interferometer ($\theta = 0$), its light is perfectly cancelled and one has $N = 0$. However, interferometers can resolve astrophysical sources as small as a couple of milli-arcsec and many stars have to be considered as extended sources. As soon as a target is even partially resolved by a nulling interferometer, the off-axis regions of the sources are not perfectly cancelled by the instrument and a stellar leakage is measured. This leakage represents an important limitation as it can prevent a faint companion from being detected.

As long as the off-axis angle is small compared to the fringe spacing ($\theta \ll \lambda/b$), the expression of the transmission map of a two-beam interferometer can be simplified as follows:

$$R_\lambda(\boldsymbol{\theta}) \simeq 2\left(\pi \frac{b\theta}{\lambda} \cos\alpha\right) \tag{3.25}$$

If we consider a star of finite size with a uniform brightness distribution, the part of the stellar light that will leak through the transmission map is given by:

$$F_\lambda = B_\lambda \int_0^{2\pi} \int_0^{\frac{\theta_\star}{2}} R_\lambda(\theta, \alpha)\, \theta \, d\theta \, d\alpha \tag{3.26}$$

where $\theta_\star$ is the stellar angular diameter. The nulling ratio being defined as the ratio between the transmitted flux and the flux collected by both telescopes and arriving at the input of the beam combiner, the null depth astrophysical leakage N_a is:

$$N_a = \frac{F_\lambda}{2\pi\theta_\star^2 B_\lambda} = \frac{\pi^2}{16}\left(\frac{b\theta_\star}{\lambda}\right)^2 \tag{3.27}$$

Note that by comparing Equation 3.27 with Equation 3.16 which gives the relation of the visibility of a partially resolved star as a function of its angular diameter, one can verify the simple relation that exists between visibility and null depth (i.e. $N = 1 - 2|\mathcal{V}|$).

3.3.3 Instrumental leakage

The previous sections presented the theoretical intensity response of a perfect interferometer. However, during interferometric observations, quasi-static and fluctuating perturbations influence the interferometric response of the instrument. In this section, the impact of intensity, phase and polarization errors are assessed.

Let us consider the case of an imperfect monochromatic two-telescope interferometer operating at a wavelength λ. The collected intensities in each beam are denoted as $I_1(\lambda)$ and $I_2(\lambda)$ and we introduce the relative intensity mismatch as being $\delta I(\lambda) = 2(I_1(\lambda) - I_2(\lambda))/(I_1(\lambda) + I_2(\lambda))$. The phase error, measuring the OPD departure from its optimal value is $\Delta\phi(\lambda)$. The last error source we consider in this section is due to the polarization. Different types of polarization error exist: (i) the differential phase shift between two polarization states s and p ($\Delta\phi_{s-p}$) can be simply included in the phase error that we just introduced, and (ii) the differential rotation of the polarization between the two beams is denoted as α_{rot} and can be seen as an intensity error when projecting the rotated polarization components onto the initial direction of the s and p vectors. Inserting these perturbations into Equation 3.5, the combined intensity at the constructive interference (+) and destructive interference (−) is given by (Serabyn 2000):

$$\begin{aligned} I_{\pm}(\lambda) &= \left[I_1(\lambda) + I_2(\lambda) \pm 2\sqrt{I_1(\lambda)I_2(\lambda)}\cos\Delta\phi\cos\alpha_{rot}\right] && (3.28)\\ &= 2\langle I(\lambda)\rangle\left[1 \pm \sqrt{1 - \frac{\delta I(\lambda)^2}{4}}\cos\Delta\phi\cos\alpha_{rot}\right] && (3.29)\end{aligned}$$

where $\langle I(\lambda)\rangle = (I_1(\lambda) + I_2(\lambda))/2$ is the average input beam intensity, and where the pupil response has been considered as equal to unity. If the intensity, phase and polarization errors are all $\ll 1$, the null depth for a point source in absence of the background can be approximated by:

$$N(\lambda) \simeq \frac{\delta I(\lambda)^2}{16} + \frac{\Delta\phi(\lambda)^2}{4} + \frac{\alpha_{rot}(\lambda)^2}{4} \qquad (3.30)$$

For a source of finite extent, the observed null depth also depends on the astrophysical null depth N_a, determined by the leakage of the source spatial brightness distribution through the null fringe pattern. For small values of N_a, the observed null depth can be expressed as the sum of an instrumental term given by Equation 3.30 and the astrophysical null (Serabyn 2000).

$$N(\lambda) = N_a(\lambda) + \frac{\delta I(\lambda)^2}{16} + \frac{\Delta\phi(\lambda)^2}{4} + \frac{\alpha_{rot}(\lambda)^2}{4} \qquad (3.31)$$

3.3.4 Spatial and modal filtering

In addition to the residual piston (or OPD) error between the two optical beams of an interferometer, the corrugation of wavefronts is one of the main contributors to instrumental leakage. These phase defects include low-order optical aberrations of the mirrors and higher spatial frequency wavefront errors due to polishing imperfections or, in the case of ground-based observations, atmospheric turbulence. If $\sigma^2_{\phi_{1,2}}$ designates the phase variance over each pupil, the mean leak coming from the on-axis transmission corresponds to (Mennesson et al. 2002)

$$N_{\mathrm{instr}}(\lambda) = \frac{\sigma^2_{\phi_1} + \sigma^2_{\phi_2}}{4} \qquad (3.32)$$

Even when measuring modest null depths such as 10^{-2}, this instrumental bias requires the wavefront error to be lower than $\lambda/44$ RMS. This wavefront quality corresponds to Strehl ratios of 98%. If standard mirrors can reach this level of surface accuracy, atmospheric induced wavefront corrugation strongly degrades the Strehl ratio in the case of ground-based observations. AO systems reduce the impact of the atmosphere but we will have to wait for the installation of XAO systems on interferometers to reach the required correction level.

It has been demonstrated by Ollivier & Mariotti (1997) that defects of the incoming wavefronts of an interferometer can be efficiently corrected by spatial filtering. The use of simple pinholes for example is very effective for eliminating the high spatial-frequency corrugations (effect of dust scattering, high-spatical frequency polishing residuals, etc...) but its influence is less dramatic on large scale defects. The pinhole size can be optimized to correct for low order aberrations but at the expense of the overall throughput.

To compensate for the drawbacks of pinholes, Mennesson et al. (2002) proposed to replace pinholes by single-mode fibers. Indeed, when a light beam is injected into such fibers, only the fundamental mode of the electric field is propagated. The shape of the initial wavefront simply affects the amount of energy coupled into the guide. In other words, the phase effects are traded against intensity mismatch and all phase errors besides the residual piston are corrected. Quantitatively, the injection efficiency of a weakly aberrated incoming wavefront into a single-mode fiber is proportional to its Strehl ratio ($S = \exp(-\sigma^2_{\phi})$). For small aberrations, the photometric relative unbalanced x is given by $x = \sigma^2_{\phi_1} - \sigma^2_{\phi_2}$ and its influence on the stellar leaks becomes

$$N_{\text{instr}}(\lambda) = \frac{(\sigma^2_{\phi_1} - \sigma^2_{\phi_2})^2}{16} \tag{3.33}$$

Compared to the case where no spatial filtering is applied, the use of a single mode fiber can allow to dramatically relax the constraints on the wavefront error. Null depth ratios of 10^{-2} can be obtained with $\lambda/5$ RMS wavefront quality (i.e. Strehl ratio of 20%), which is easily achievable with ground based facilities down to near-infrared wavelengths. The throughput efficiency of single mode waveguide injection is relatively high: up to 81% in the case of a pupil without central obscuration. In this case, the $1/e$ width field-of-view is limited by the acceptance cone of the fiber and is equal to $0.71\lambda/D$ (Ruilier & Cassaing 2001).

3.4 Current facilities

Since the first successful application of optical interferometry to separate telescopes by A. Labeyrie in 1975 with the I2T (Labeyrie 1975), several interferometers have been built around the world. In this section, we give a brief summary of the main interferometric facilities that are currently operational or that will soon be. For convenience, we divide them into two natural sub-categories which are *stellar interferometers* and *nulling interferometers*.

3.4.1 Stellar interferometers

It is Michelson, who in 1890, made the first successful application of stellar interferometry to measure the angular diameters of the four satellites of Jupiter. Since this breakthrough observation, interferometry has been extensively used to measure stellar diameters. Over the years, astronomers have started to realize how this technique could be providential for different research themes in astrophysics. A non exhaustive list of the major results obtained with "visibility" interferometers include the detection and characterization of binary systems (e.g. Boden (2000); Boden et al. (2005); Muterspaugh et al. (2005, 2006); Tango et al. (2009)), the detection of circumstellar dust around stars (Absil et al. 2006b), the imaging of stellar surfaces (Monnier et al. 2007; Le Bouquin et al. 2009b; Kloppenborg et al. 2010), the characterization of the diameter and pulsation of Cepheid stars (Kervella et al. 2004a; Mérand 2008) and the discovery that the emission of AGNs mainly originates from the central accretion disc (Swain et al. 2003). We describe hereafter the five main interferometric facilities which have contributed or will contribute to these breakthrough discoveries: the VLTI, KI, CHARA, LBTI and MROI.

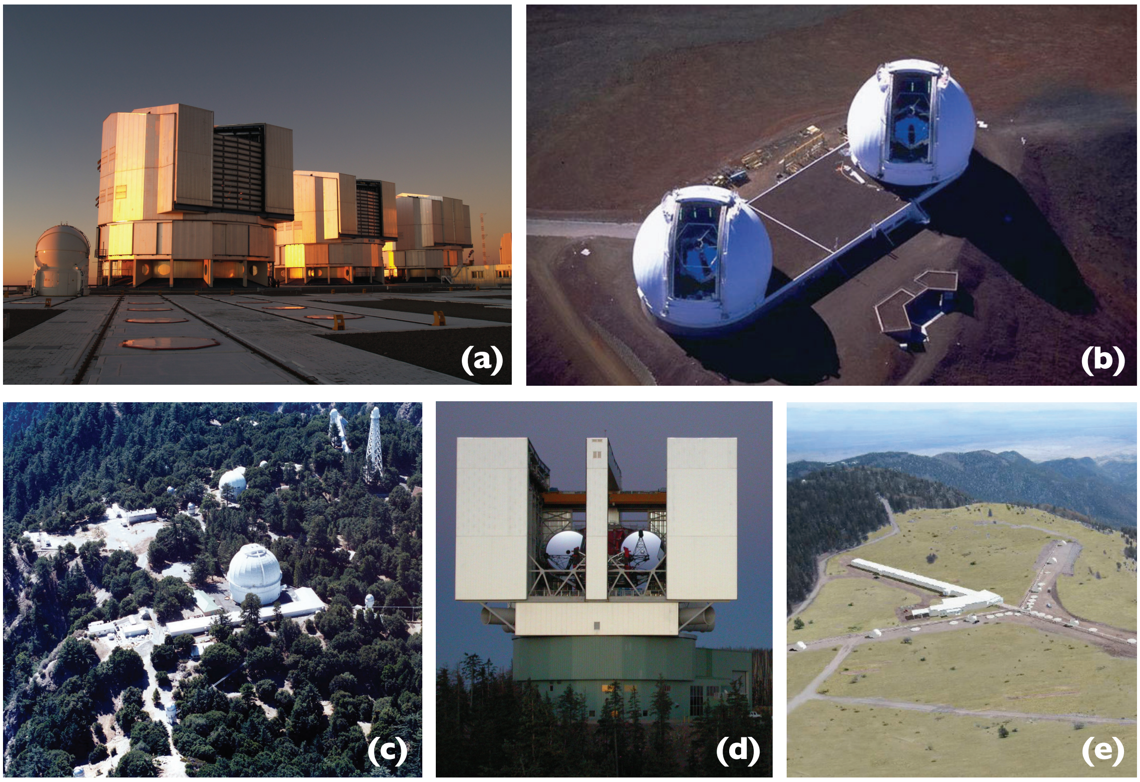

Figure 3.5: Pictures of the main stellar interferometric facilities around the world. From top left to bottom right we have respectively: (a) VLTI (b) KI (c) CHARA (d) LBTI and (e) MROI.

Very Large Telescope Interferometer (VLTI)

The VLTI (see Figure 3.5, (a)) is the largest infrared interferometer in the world. Installed on top of Cerro Paranal in the Atacama desert (Chile) and operated by ESO, it is composed of four 8 m telescopes (called UTs) and four mobile 1.8 m telescopes. Up to four of these telescopes can be recombined simultaneously (either the four UTs or the four ATs) with baselines up to 130 m. The main interferometric instruments at VLTI are: (i) AMBER, a near-infrared (J, H and K bands) spectro-interferometer which is able to recombine up to three telescopes, (ii) MIDI, which is a two beam mid-infrared interferometer working in the N band, (iii) PIONIER, is a visitor instrument and is able to combine four UTs or ATs using integrated optics beam combiners, and (iv) PRIMA is a system designed to enable simultaneous interferometric observations of two nearby objects. This particular facility will be either used for doing precision astrometry or to produce images of the fainter of the two objects. The description of the VLTI in general and of the AMBER instrument in particular will be further detailed in Section 5.1.

Keck Interferometer (KI)

The Keck interferometer (see Figure 3.5, (b)) is located at an altitude of 4150 m atop of Mauna Kea Volcano on Big Island (Hawaii). It has been built by NASA to fulfill one of the main agency's Origin

Program objective: to find planets and ultimately life beyond the solar system. It has been therefore designed accordingly to combine the twin 10 m Keck telescopes to measure the emission from dust orbiting nearby stars. Operational since 2001, it offers today both an H and K band visibility measurement mode and a 10 μm (N band) nulling mode (see Section 3.4.2 for more details on this mode). The distance between the twin telescopes being 85 m, the KI provides maximum angular resolutions of 4 mas at 1.65 μm, 5 mas at 2.2 μm and 24 mas at 10 μm.

Center for High Angular Resolution Astronomy (CHARA)

The first stones of the CHARA array (see Figure 3.5, (c)) have been put together in 1996 on the historic site of Mt. Wilson Observatory (California). After having obtained its first fringes in 2001, the interferometer is now fully operational since 2004 and offers six 1 m telescopes organized along a Y-shaped array configurations. 15 different baselines are available ranging from 31 m up to 331 m (world's longest operational IR baseline). The main particularity of the CHARA array compared to the other long baseline interferometers is that the interferometric beams collected by the telescopes are transported to the interferometric lab through vacuum pipes, which strongly reduces the effect of local turbulence on the beams wavefronts. This interferometer is equipped with 4 main instruments which are: (i) FLUOR, a two beam combiner at 2.2 μm, (ii) VEGA, a visible spectro-polarimetric interferometer recombining 3 beams (4 once fully operational) (iii) PAVO, which is an integral-field-unit for measuring spatially-modulated pupil-plane fringes (3 telescopes) and (iv) MIRC, the Michigan infraRed (1.5 to 2.4 μm) Combiner, which is designed for imaging and will combine up to 6 telescopes once fully operational.

Large Binocular Telescope Interferometer (LBTI)

The LBTI is a ground-based interferometer and consists in the recombination of two 8-meter class telescopes separated by 14.4 m and mounted on a common alt-azimuthal mount (see Figure 3.5, (d)). This instrument was delivered in July 2008 and the scientific operations will start in 2011. The two unique features of the LBTI are (i) that the secondary of each telescope is the actual deformable mirror and delivers a high wavefront quality to the interferometer ($>$ 80% in the near-infrared), (ii) that because both telescopes are on a common mount, no delay lines are needed, which significantly reduces the number of relay optics. The LBTI is equipped with two different interferometric instruments. The first one, caIled LINC-NIRVANA, is a near-infrared (J, H and K bands) image-plane beam combiner with Multi-Conjugate Adaptive Optics (MCAO). Thanks to the Fizeau beam recombination scheme, this interferometer has the particularity of producing interference fringes over a wide field of view (2 arcmin). The key science program of this instrument includes pushing supernova cosmology studies beyond redshift 3, following the evolution of complex structures in star forming regions and detecting Jupiter-mass planets thanks to their astrometric signature on their host star. In addition to its Fizeau mode, the LBTI will also host a nulling beam combiner (see Section 3.4.2 for more details).

Magdalena Ridge Observatory Interferometer (MROI)

The MRO interferometer (New Mexico), is an ambitious project consisting in the development of an array of up to ten 1.4 m telescopes with baselines ranging from 7.5 to 340 m (see Figure 3.5, (e)). The initial design plans to recombine all 10 beams simultaneously at wavelengths between 0.6 and 2.4 μm, providing a unique imaging capability with a sub-milli-arcsec resolution. The key science program includes three different areas which are star and planet formation, stellar accretion and mass loss, and active galactic nuclei. Most of the design work is done and the major subsystems are being built. The beam combining facility has been constructed in 2008 and the first telescope has been manufactered by AMOS (Belgium).

3.4.2 Nulling interferometers

Some scientific topics such as the observation of circumstellar disks or extra-solar planets require both a high angular resolution and a high dynamic. Nulling interferometers have been developed to meet these two requirements. In this section, we present the nulling facilities that have been installed around the world since a decade.

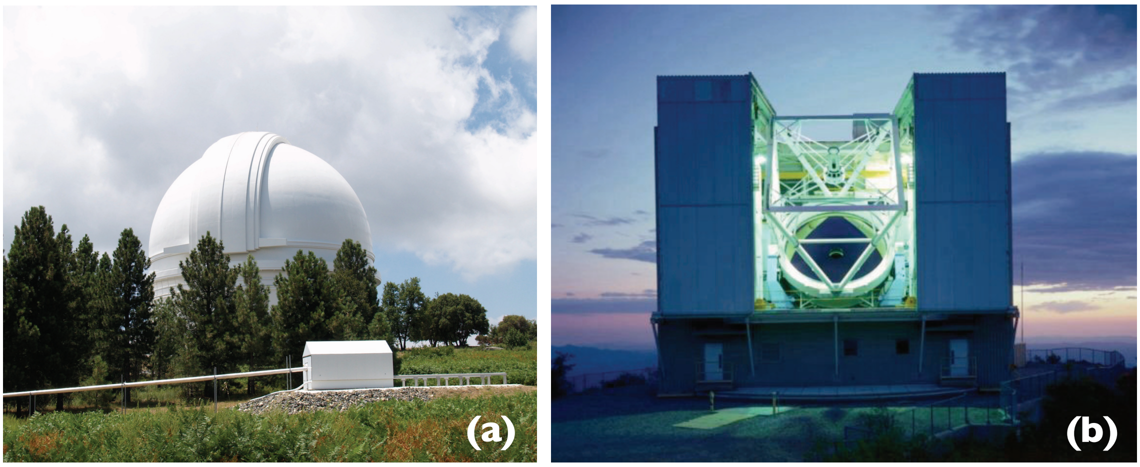

Figure 3.6: (a) Picture of the 5.08 m Hale telescope (Palomar observatory) hosting the PFN. (b) 6.5 m Multiple Mirror Telescope (MMT) used for the BLINC instrument (Mt. Hopkins).

Keck Interferometer Nuller (KIN)

The Keck Interferometer - which is part of the KI project described in the previous section - is the world's largest nulling interferometer. Operating at a wavelength of $10\,\mu$m, it is a four-beam nulling interferometer recombining two sub-apertures of each Keck telescopes together. The principle is based on two modified Mach-Zehnder nullers combining the light from the left halves and right halves of the telescopes on the 85 m long baseline. The outputs of these two long baseline nullers are then combined with a Michelson combiner with a short 4 m effective baseline. On top of the scientific mid-IR camera recording the nulled output, the KIN is equipped with two fringe trackers working at $2\,\mu$m and angle trackers operating either at 1.2 or $1.6\,\mu$m. It is operational since 2005 and its main scientific objective is to detect exozodiacal disks with sensitivities down to the 30-zodi level[5] around G2V stars at 10 pc.

Palomar Fiber Nuller (PFN)

The Palomar Fiber Nuller is a so called *nulling coronagraph* developed at the Jet Propulsion Laboratory. Instead of recombining the light from distant telescopes, it recombines two elliptical subapertures (1.5 m $\times$3 m) of the 5.08 m wide Hale telescope (see Figure 3.6, left) that are separated by 3.5 m (Martin et al. 2008). Working in the K band, this nuller has a resolution of 130 mas for a field of view of 600 mas in diameter. Thanks to the contrast it can achieve ($> 10^3$) the PFN is able to detect faint structures well within the diffraction limit of the interferometer (< 50 mas). A more thorough description of this

---

[5] 1-zodi corresponds to the density of an exozodiacal disk similar to the one of our local zodiacal disk.

instrument is presented in Chapter 7 together with the first results that we have obtained during the engineering runs.

BracewelL Infrared Nulling Cryostat (BLINC)

BLINC is an instrument using two parts of the 6.5 m refurbished Multiple Mirror Telescope (MMT) in Arizona (see Figure 3.6, right) to create a nulling interferometer with apertures of 2.7 m in diameter and a baseline of 4 m (Hinz et al. 2000). Just like the PFN, the telescope AO helps in stabilizing the fringes and maintaining the cancellation of starlight. Working in K band, the goal of BLINC is to reach contrasts up to 10000:1 in order to detect zodiacal dust around nearby stars (Hinz et al. 2001a,b) and young giant exoplanets. It also serves as a demonstrator to the LBT which will come online in the upcoming year.

Large Binocular Telescope Interferometer (LBTI)

Together with the LINC-NIRVANA Fizeau interferometer (see Section. 3.4.1), the LBTI is also composed of a nulling instrument. The main component of this instrument is the Nulling Infrared Camera (NIC) which has two science channels: an 8-13 μm wavelength Nulling Optimized Mid-Infrared Camera (NOMIC) and a 3-5 μm imaging camera (LMIRCam). The components of NIC are housed within a single cryostat. This feature together with the low number of optical elements prior to the cryostat compared to other mid-IR interferometers is the main advantage of NIC. It minimizes the thermal radiation arising in the delay lines and transfer optics which usually dominates the background at 10 μm. The NIC cryostat also houses a K band fast readout camera (Phasecam) to sense phase variations between the LBT apertures and carry out closed loop correction.

The main scientific objective of the LBTI nuller is to perform a survey within the nearest targets looking for exo-zodiacal emissions around these stars. It will also be sensitive enough to detect young (1< Gyr) giant planets in the range 5-10 M_{Jup}.

4

Data reduction challenges

Contents

4.1 Classical method **65**

4.1.1 Photometric corrections 67

4.1.2 Visibility measurement and calibration 67

4.1.3 Influence of noise 68

4.2 Statistical method **70**

4.2.1 Paper: **Improving null depth measurements using statistical distributions: theory and first results with the Palomar Fiber Nuller**, *C. Hanot, B. Mennesson, S. Martin, K. Liewer, F. Loya, P. Riaud, O. Absil and E. Serabyn* 70

In the previous chapter, we have introduced the basic theory of both stellar and nulling interferometry. Their main observable quantity, the visibility and the null depth respectively, measures the contrast of the fringes and gives a direct information on the spatial intensity distribution of the source. If these quantities are in principle easy to measure, they are unfortunately strongly corrupted by the instrumental response of the interferometer and by the atmospheric-induced wavefront corrugations. In this chapter, we first present the method that has been used for analyzing interferometric data for more than a decade. After explaining its limitations, we then introduce a new method based on statistical distributions that can improve the accuracy of the measurements by an order of magnitude or more, depending on the instrument being used.

4.1 Classical method

As we have introduced in Chapter 3, the visibility (or the null depth) is the main observable of stellar interferometers (or nulling interferometers) and is related to the spatial intensity distribution of the observed source. Unfortunately, through the observations, we do not have a direct access to $\mathcal{V}$ but rather to a corrupted version of it, denoted μ, which depends on both instrumental and atmospheric effects. The relation between μ and $\mathcal{V}$ is

$$\mu = T_i \, T_a \, \mathcal{V} \tag{4.1}$$

where T_i and T_a are respectively the instrumental and atmospheric transfer functions. Whereas the instrumental response of interferometers can be corrected by calibration when it varies over sufficiently

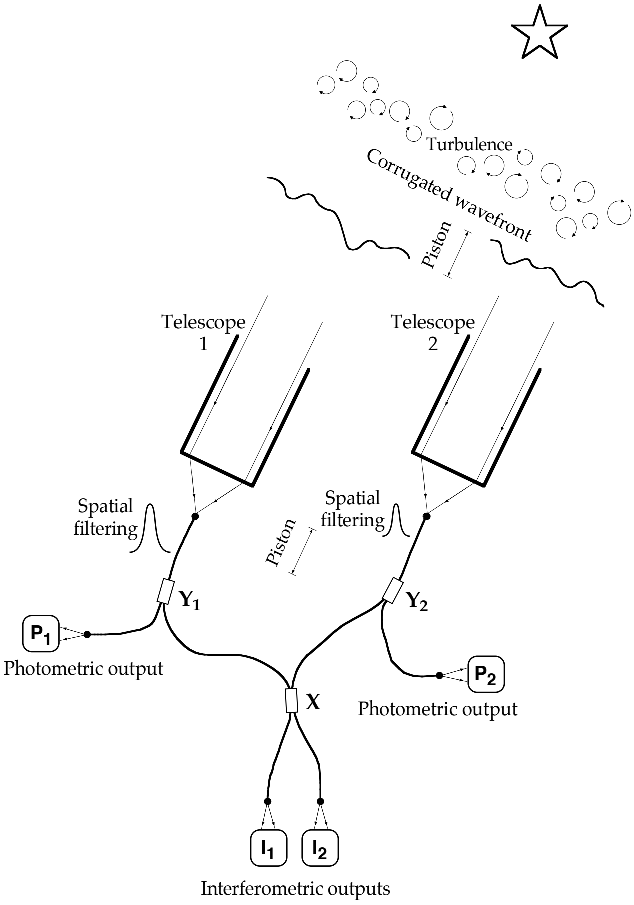

Figure 4.1: Conceptual design of a fibered interferometer. Image from Coudé du Foresto et al. (1997).

long timescales ($>$ 10 min), this is not the case for the atmospheric perturbations which fluctuate randomly over very short timescales. The latter, also called the atmosphere coherence time, is inversely proportional to the wavelength and is typically of the order of 10 ms in the near-infrared under average seeing conditions on a good observing site. In a classical, non-fibered interferometer, there is no way to directly measure T_a as it would require a real time sensing of the wavefront corrugations above the array. Therefore, the only possible option consists in a statistical calibration of a series of measurements. With such a technique (non-fibered interferometer, classical reduction method) the relative accuracies on visibility (or null depth) measurements are about 10%, which is clearly not sufficient for most astrophysical applications (Coudé du Foresto et al. 1997).

As we have introduced in Section 3.3.4, this problem can be partially solved using single-mode fibers to spatially filter the incoming beams. By doing so, the wavefront corrugations are converted into an intensity error (which are less detrimental to the measurement quality) plus a differential piston error between the beams. Accuracies around the 1% level can then be achieved on the visibilities (or on the null depth) as demonstrated for e.g. on VINCI (VLTI) by Kervella et al. (2004b) and on FLUOR (CHARA) by Absil et al. (2006b). In the following sections, we describe the successive steps used to properly reduce interferometric data from fibered interferometers. Applying this method to non-fibered interferometers is possible and detailed by Coudé du Foresto et al. (1997) but is out of the scope of this chapter.

4.1.1 Photometric corrections

The principle of a two beam fibered stellar interferometer is presented in Figure 4.1. The wavefronts corrugated by atmospheric turbulence and collected by the two telescopes are first injected into separate single-mode fibers. The electromagnetic fields are then guided through the fibers to single-mode couplers (denoted Y_1 and Y_2). At this stage, part of the light is sent to photometers to monitor the photometric signals P_1 and P_2 while the rest is sent to a directional coupler (X). At this coupler, the signal from the two beams are combined and the two complementary interferometric outputs I_1 and I_2 are monitored by additional photometers. With this kind of design, the interferogram is recorded by scanning the OPD. This scan has to be fast enough to freeze the atmosphere-induced OPD perturbations during each individual measurement along the scan. From this set of four photometric signals, the expression of the interferogram introduced in Section 3.2 can be written as follows:

$$I(t) = P_1(t) + P_2(t) + 2\sqrt{P_1(t)P_2(t)}\,\mu\cos\left(\frac{2\pi b x(t)}{\lambda} + \Delta\phi\right) \tag{4.2}$$

where $x(t)$ is the time-dependent optical path difference introduced between the beams and μ the modulus of the complex coherence factor. As both $P_1(t)$ and $P_2(t)$ are monitored in real time, it is possible to correct the interferogram from the intensity fluctuations and measure μ more accurately:

$$\begin{aligned} I_{\mathrm{corr}}(t) &= \frac{I(t) - P_1(t) - P_2(t)}{2\sqrt{P_1(t)P_2(t)}} && (4.3) \\ &= \mu\cos\left(\frac{2\pi b x(t)}{\lambda} + \Delta\phi\right) && (4.4) \end{aligned}$$

The quantity $1 + I_{\mathrm{corr}}$ corresponds to the interferogram that would be observed if $P_1(x)$ and $P_2(x)$ had been equal and constant.

4.1.2 Visibility measurement and calibration

As explained in the previous paragraph, it is hereby considered that the interferogram is recorded by scanning the OPD at a certain speed v. The speed of the scan is chosen such that the fluctuating atmospheric phase can be considered as constant for each sample along the scan while providing an appropriate fringe sampling. In such a case, the differential piston introduced between the beams is equivalent to the addition of a small random delay $\Delta\phi$ in the OPD and there is a linear relationship between the time variable t and the global OPD x. If the signal is recorded at fixed time intervals δt, they also correspond to differential piston values $\delta x = v\,\delta t$ in Equation 4.3. When v is high enough, the interferogram is only composed of two distinct components in the frequency space (Coudé du Foresto et al. 1997):

- a low frequency scintillation noise
- an interferometric signal at a higher frequency.

While the first one is the spectrum of the coupling fluctuations into the fiber, the latter corresponds to the spectral intensity of the source multiplied by the coherence factor between the two beams and convolved with the Fourier transform (FT) of the coupling fluctuations (see Figure 4.2). Using the FT of the signal, the interferometric signal is first isolated from the scintillation noise by separating the low- from the high- frequency components. This step is usually performed by correcting the interferogram from the intensity fluctuations according to Equation 4.3. Assuming that the instrument is stable enough, the energy contained in the high frequency peak of the PSD of the interferometric signal is directly related to the coherence factor $\mu = T_i\mathcal{V}$. By observing a reference object whose complex visibility is well

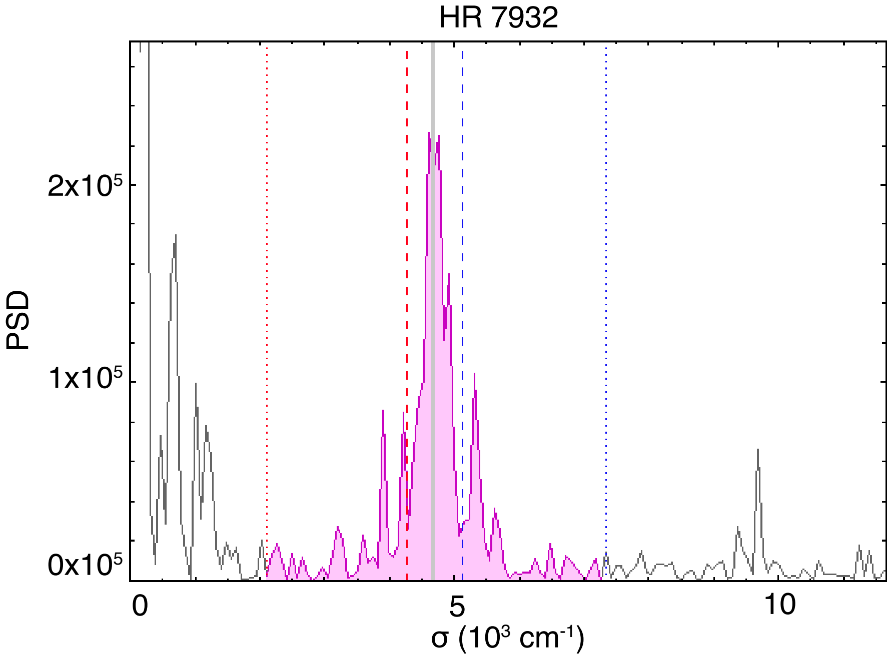

Figure 4.2: Modulus of the FT of the interferogram $I(t)$. Courtesy of Benjamin Mollier.

known, the instrumental transfer function can then be calibrated:

$$T_i = \frac{\mu^{(\mathrm{ref})}}{\mathcal{V}^{(\mathrm{ref})}} \tag{4.5}$$

From this expression, the modulus of the object visibility is given by:

$$\mathcal{V}^{(\star)} = \mathcal{V}^{(\mathrm{ref})} \frac{\mu}{\mu^{(\mathrm{ref})}} \tag{4.6}$$

In practice, the square of the visibility is used rather than its modulus because it is related to the spectral power density of the interferogram and more importantly because it is less biased (Coudé du Foresto et al. 1997; Perrin 2003). It is important to note that the method described here is only valid if the piston (atmospheric OPD) is small. Any departure from this hypothesis will be referred here after as piston noise.

4.1.3 Influence of noise

Because the measurement of the visibility is affected by residual noise, a set of n consecutive measurements will lead to n slightly different values of $\mathcal{V}^{(\star)}$. The final estimate of a visibility measurement is given by the average of the n different visibility measurements. If $\sigma_{\mathcal{V}}$ is the standard deviation of the estimated visibility, the standard error on $\mathcal{V}^{(\star)}$ is

$$\epsilon_{\mathcal{V}} = \frac{\sigma_{\mathcal{V}}}{\sqrt{n}} \tag{4.7}$$

The variations of the estimated visibility can be attributed to different noise sources: (i) the detector noise, (ii) residual noise coming from the filtering of the photometric signals (also called deconvolution noise), (iii) the presence of piston noise, (iv) chromatism coming either from the instrument or from atmospheric refraction and (v) differential rotation of the polarzation between the beams.

Any observation is affected by photometric noise and the signal M_{P_j} recorded by the detector P_j is actually the sum of the beam intensities $P_j(t)$ with an additive noise, hereafter denoted b_{P_j} which is uncorrelated with the data. The photometric measurement taken by each detector is therefore given by:

$$M_{P_j}(t) = P_j(t) + b_{P_j}(t) \tag{4.8}$$

This additional noise has to be taken into account and properly corrected for as it influences the photometric signals but also the square of the coherence factor. This can be done by using a proper estimator of P_j (denoted $\hat{P}_j$) which is obtained by filtering the photometric channels with a Wiener filter (Press et al. 2007). The quality of this estimator (or deconvolved signal) however strongly depends on the signal to noise ratio of the photometric signals and it is necessary to adopt a selection criterion to reject the data having a low SNR. Indeed, if the photometric signals are too low, the denominator in Equation 4.3 is small as well, and the errors are amplified. Therefore, if the minimum value of $\hat{P}_j$ is below a certain rejection threshold, expressed in multiples of the filtered-noise standard deviation σ_{b_j}, the interferogram is discarded and the fringe visibility is not measured. This threshold must be carefully chosen in order to optimize the noise correction while not discarding most of the interferograms.

When the piston noise is negligible, the fringe signal in the Fourier space is simply given by the convolution of the fringe pattern in the OPD space with the source spectral intensity distribution. The interferometric information is therefore not given by a single frequency in the Fourrier space but is spread over a finite bandwidth (see Figure 4.2). If the spectrum of the target is known, both the spectral and spatial information can be entirely retrieved. In the presence of piston noise, the Fourier transform of the fringe is corrupted and is spread well beyond the nominal frequency range and cannot be attributed to the source spectral intensity distribution. In such a case, the spectral information is lost and only the square modulus of the coherence factor over the observation bandpass can be retrieved by integrating the power contained in the high frequency peak corresponding to the interferometric signal.

The relative importance of these three different noises (i.e. detector, deconvolution and piston noise) on the measurement of the square coherence factor can be assessed by studying the correlation between the noise measured in the two interferometric outputs (when available). Indeed, as illustrated in Figure 4.1, most fibered interferometers possess two outputs that are in phase opposition[6]. On the one hand, the detector noise is uncorrelated between the two outputs as it is entirely detector-dependent. Conversely, the piston noise is fully correlated as the fluctuating OPD error is common to both channels. Last, the deconvolution noise, while not being exactly equal at the two outputs as the deconvolution process is applied to different measurements, is strongly correlated. The estimator of the square coherence factor for each channel i is therefore given by (Coudé du Foresto et al. 1997):

$$M^{(i)}_{\mu^2} = \mu^2 + b_c + b^{(i)}_{uc} \tag{4.9}$$

where b_c and $b^{(i)}_{uc}$ are the correlated and uncorrelated parts of the noise, respectively. By computing the difference of these estimators measured in the two channels, it is possible to isolate the contribution of the correlated part of the noise from the uncorrelated one and compare their respective weights. These noises directly depend on the speed of the OPD scan v. Indeed, on the one hand, the piston noise decreases for faster scanning speed as the atmospheric-induced perturbations do not have the time to significantly change the OPD during a scan. On the other hand, the detector noise increases with increasing v because for a given observation waveband, the interferometric signal is spread over a wider range of frequencies. By changing the speed v of the OPD scan, it is therefore possible to find the best compromise minimizing the total noise.

---

[6] Except for the interferometers using a unique single-mode fiber as beam combiner (e.g. the Palomar Fiber Nuller and CELINE, Haguenauer & Serabyn 2006; Mennesson et al. 2006; Serabyn & Mennesson 2006; Martin et al. 2008; Hanot et al. 2010b) that only possess a unique output.

4.2 Statistical method

The classical method that we just described has been extensively used for more than a decade now and is pretty efficient. However, it is intrinsically limited by the residual intensity and piston noise as well as by the calibration process demanding the observation of a reference star. Indeed, the latter obviously requires the transfer function of the interferometer to be stable enough over timescales of 10-30 minutes and a good knowledge of the reference object. Instead of the data reduction procedure that we just described, we propose in this section to use a statistical analysis based on the probability distributions of the photometric and interferometric signals. The basic principle is the following: instead of scanning the OPD to record the interferogram, the phase is set to a fixed value that is as close as possible from the zero OPD and is maintained using fringe trackers. The interferometric signal, together with the photometric signals and the background level are recorded. The distribution of the fast fluctuations of those signals induced mainly by the atmosphere are then used to retrieve the astrophysical information (either the visibility or the null depth). The use of this technique allows the phase, intensity, and background errors to be (mostly) removed as well as the accuracy on visibilities to be improved by at least an order of magnitude. Moreover, the stability of the transfer function is also increased leading to better calibrations.

4.2.1 Paper: Improving null depth measurements using statistical distributions: theory and first results with the Palomar Fiber Nuller, *C. Hanot, B. Mennesson, S. Martin, K. Liewer, F. Loya, P. Riaud, O. Absil and E. Serabyn*

In this paper, published in the Astrophysical Journal, we describe in details the use of a data reduction method using statistical distributions of the null depth and intensity errors to improve the accuracy of null depth measurements. This method could basically be seen as a posteriori fringe tracking (also called “coherent integration”, Jorgensen et al. 2007), except that the interferometric measurements are not stacked to improve the SNR but instead, their distribution are used to retrieve the astrophysical information with a much better accuracy. After explaining in details the theory that is related to this method, we apply it to data obtained with the Palomar Fiber Nuller (PFN) on the star α Boo. We then compare the performances of our method with the classical data reduction approach but also with previous results obtained with long baseline interferometry (the PFN having only a short 3.4 m baseline). Finally, we discuss the effect of the different error sources that can potentially limit the accuracy of our method. Even though it is illustrated with data obtained with the PFN, there is nothing instrument-specific about the technique presented hereafter. We therefore anticipate that this method can be applied to any two beam interferometer. Note that unlike in Section 3.3.1, we here after take $I_{\rm min}/I_{\rm max}$ instead of $I_{\rm min}/(I_{\rm min}+I_{\rm max})$ as a definition for the null depth. This definition is indeed a good approximation of the latter for small values of the null depth.

The Astrophysical Journal, 729:110 (13pp), 2011 March 10 doi:10.1088/0004-637X/729/2/110

IMPROVING INTERFEROMETRIC NULL DEPTH MEASUREMENTS USING STATISTICAL DISTRIBUTIONS: THEORY AND FIRST RESULTS WITH THE PALOMAR FIBER NULLER

C. Hanot[1], B. Mennesson[2], S. Martin[2], K. Liewer[2], F. Loya[2], D. Mawet[2], P. Riaud[1], O. Absil[1], and E. Serabyn[2]
[1] Institut d'Astrophysique et de Géophysique, University of Liège, Allée du 6 Août, 17 Bât B5c, 4000 Liège, Belgium; hanot@astro.ulg.ac.be
[2] Jet Propulsion Laboratory, California Institute of Technology, 4800 Oak Grove Drive, Pasadena, CA 91109, USA

Received 2010 July 6; accepted 2011 January 9; published 2011 February 15

ABSTRACT

A new "self-calibrated" statistical analysis method has been developed for the reduction of nulling interferometry data. The idea is to use the statistical distributions of the fluctuating null depth and beam intensities to retrieve the astrophysical null depth (or equivalently the object's visibility) in the presence of fast atmospheric fluctuations. The approach yields an accuracy much better (about an order of magnitude) than is presently possible with standard data reduction methods, because the astrophysical null depth accuracy is no longer limited by the magnitude of the instrumental phase and intensity errors but by uncertainties on their probability distributions. This approach was tested on the sky with the two-aperture fiber nulling instrument mounted on the Palomar Hale telescope. Using our new data analysis approach alone—and no observations of calibrators—we find that error bars on the astrophysical null depth as low as a few 10^{-4} can be obtained in the near-infrared, which means that null depths lower than 10^{-3} can be reliably measured. This statistical analysis is not specific to our instrument and may be applicable to other interferometers.

Key words: instrumentation: high angular resolution – instrumentation: interferometers – methods: data analysis – methods: statistical

1. INTRODUCTION

Since the first discovery of an exoplanet around a solar-type star (Mayor & Queloz 1995), the quest to find Earth-like exoplanets and even more importantly to detect the presence of life on them has become a major topic in astrophysics. However, the direct imaging of such systems is very challenging because of the high spatial resolution and dynamic range required. One possible way to overcome these difficulties is to use nulling interferometry (Bracewell 1978). In this approach, one destructively combines the light coming from two or more apertures in order to dim the bright on-axis starlight and reveal faint objects or structures in the immediate vicinity.

The analysis of interferometric data in general, and nulling interferometric data in particular (Colavita et al. 2009), is a complex task because accurate calibration of the instrument is needed to extract the scientific information. In the case of interferometric nulling, the quantity of interest is the astrophysical null depth (N_a), which is the inverse of the rejection ratio and directly relates to the target's spatial brightness distribution. In practice, however, the measured interferometric null depth is not strictly equal to the astrophysical null depth, because of the effects of instrumental noise and error sources such as phase differences, intensity mismatch, and global intensity fluctuations. It had been thought that a proper determination of the astrophysical null depth requires the mean values of these instrumental error sources to be accurately known (e.g., Serabyn 2000; Lay 2004). The classical method used for deriving astrophysical null depths—and visibilities—has therefore been to average different sequences recorded on the science star and estimate the instrumental bias by observing a calibrator star (Colavita et al. 2009). This technique has been extensively used for years for both classical and nulling interferometry, but suffers from well-known limitations: (1) the final accuracy depends on the scientific knowledge of the calibrator star, (2) the accuracy is limited by the stability of the observing conditions, and (3) calibrator observations are time consuming.

To circumvent these limitations, we describe here a new method of calibrating astrophysical null depths, based on measuring the properties of the observed null depth *distribution*. The basic idea is to record a time sequence of the rapid null depth fluctuations, and then retrieve the underlying astrophysical information by modeling the observed statistics of the null depth distribution. Using such a statistical analysis, we show in the following that it is possible to retrieve astrophysical null depths with much better accuracy than classical approaches allow. Moreover, our initial stellar observations indicate that this statistical approach does not require any observation of calibrator stars, at least down to null depth measurement accuracies as low as a few 10^{-4} (the exact number depends on the instrument setup being used). In this paper, we first explain the principle and theory of this new statistical data analysis strategy, and then apply it to initial astronomical null data obtained with the Palomar Fiber Nuller (PFN; Serabyn & Mennesson 2006; Mennesson et al. 2006; Martin et al. 2008), a nulling-based interferometric "coronagraph" developed at the Jet Propulsion Laboratory. However, we emphasize that the new reduction method can potentially be applied to any null and/or visibility measurements in general.

2. THE STATISTICS OF THE NULL DEPTH

2.1. The Expression for the Null

We begin from the expression for the observed null depth of a two-beam interferometer for a point source in the presence of error sources, as given by Serabyn (2000). In the case of two planar monochromatic wave fronts, the combined stellar intensity measured at constructive interference (+) and destructive interference (−) at time t is given by

$$I_{\pm}^{*}(t) = \frac{1}{2}\left[I_1^{*}(t) + I_2^{*}(t) \pm 2\cos\left(\Delta\phi(t)\right)\cos\left(\alpha_{\mathrm{rot}}\right)\sqrt{I_1^{*}(t)I_2^{*}(t)}\right] \tag{1}$$

$$= \langle I^*(t)\rangle\left[1 \pm \cos(\Delta\phi(t))\cos(\alpha_{\rm rot})\sqrt{1-(\delta I(t))^2}\right], \quad (2)$$

where $I_1^*(t)$ and $I_2^*(t)$ are the individual stellar intensities of beams 1 and 2 at the beam combiner, respectively, $\langle I^*(t)\rangle = (I_1^*(t) + I_2^*(t))/2$ is the average input beam intensity, $\delta I(t) = (I_1^*(t) - I_2^*(t))/(I_1^*(t) + I_2^*(t))$ is the fractional deviation from the mean intensity, $\Delta\phi(t) = \phi_1(t) - \phi_2(t)$ is the relative phase delay, and $\alpha_{\rm rot}$ is the relative polarization rotation angle.

The null depth, defined as the inverse of the rejection ratio, is given by

$$N(t) = \frac{I_-^*(t)}{I_+^*(t)} = \frac{I_-(t) - I_b(t)}{I_+(t) - I_b(t)}, \quad (3)$$

where $I_\pm(t)$ are the constructive and destructive interference intensities including the background level and $I_b(t)$ is the background intensity collected by the interferometer. If $\Delta\phi(t)$, $\delta I(t)$, and $\alpha_{\rm rot}$ are all $\ll 1$, the null depth for a point source in the absence of background can be approximated by

$$N(t) \simeq \frac{1}{4}[(\delta I(t))^2 + (\Delta\phi(t))^2 + \alpha_{\rm rot}(t)^2]. \quad (4)$$

For a source of finite extent, the observed null depth also depends on the astrophysical null depth N_a, determined by the leakage of the source spatial brightness distribution through the null fringe pattern.[3] For small values of N_a, the observed null depth can be expressed as (Serabyn 2000)[4]

$$N(t) \simeq N_a + \frac{1}{4}[(\delta I(t))^2 + (\Delta\phi(t))^2 + \alpha_{\rm rot}(t)^2]. \quad (5)$$

Sometimes, interferometers do not measure the background intensity $I_b(t)$ nor the constructive interference term $I_+(t)$ at the same time as the destructive signal $I_-(t)$, but the observing procedure provides some estimates of their values which we denote as $\hat{I}_b(t)$ and $\hat{I}_+(t)$, while $\hat{I}_+^*(t) = \hat{I}_+(t) - \hat{I}_b(t)$. This means that one does not access the actual null, but an estimate of it given by

$$\hat{N}(t) = \frac{I_-(t) - \hat{I}_b(t)}{\hat{I}_+(t) - \hat{I}_b(t)} = N(t)\frac{I_+^*(t)}{\hat{I}_+^*(t)} + \frac{I_b(t) - \hat{I}_b(t)}{\hat{I}_+^*(t)} \quad (6)$$

or

$$\hat{N}(t) = I_r(t)N(t) + N_b(t), \quad (7)$$

where $N_b(t) = (I_b(t) - \hat{I}_b(t))/\hat{I}_+^*(t)$ is the background-induced instantaneous error in the estimated null and $I_r(t) = I_+^*(t)/\hat{I}_+^*(t)$ is the relative intensity deviation at time t.

For small values of N_a, $\delta I(t)$, $\Delta\phi(t)$, and $\alpha_{\rm rot}(t)$, one can use Equation (5) for $N(t)$, and the estimated null $\hat{N}(t)$ can be approximated by

$$\hat{N}(t) \simeq I_r(t)\left[N_a + \frac{1}{4}[(\delta I(t))^2 + (\Delta\phi(t))^2 + (\alpha_{\rm rot}(t))^2]\right] + N_b(t). \quad (8)$$

Although it does not correspond exactly to the actual instantaneous null level (which we cannot measure unless all peak and background measurements are made simultaneously), $\hat{N}(t)$ is the basic measured quantity derived from the observations which is used in this paper. All that matters for the accuracy of our data analysis is that we have (1) the correct description of $\hat{N}(t)$ as a function of the astrophysical null and instrumental noise terms, i.e., Equation (8), and (2) some way to evaluate these various noise terms (or more exactly their distributions), which is the object of the following section.

2.2. Analytical Model for the Statistical Distribution of Null Values

Because it would be extremely difficult to zero out or perfectly calibrate all instantaneous error terms, we take here the opposite tack and ask what can be learned from the observed distribution of the null depth fluctuations. We thus begin by deriving the mathematical expression for the probability distribution corresponding to the null depth estimate given by Equations (6)–(8) when the relative phase, the intensity mismatch, the background, and the relative intensity all fluctuate randomly with small amplitudes.

We first assume that the polarization term, $\alpha_{\rm rot}(t)$, is constant, so that we can neglect its time variability in the statistical analysis. For symmetrically placed beams within a common aperture, polarization mismatches should be small compared to phase and intensity errors, and this approximation is valid down to null levels of 10^{-4} or lower (Haguenauer & Serabyn 2006; Martin et al. 2008).[5] Neglecting this term, the measured null (Equation (8)) then consists of the sum of three terms multiplied by a fourth, and then the product is added to a fifth term. Of these, only the astrophysical null term is fixed (for a given baseline vector). We next assume that the remaining error terms in Equation (8)—the relative intensity uncertainty $I_r(t)$, the beam intensity mismatch $\delta I(t)$, the beam differential phase $\Delta\phi(t)$, and the background uncertainty terms—are uncorrelated random variables (this assumption is justified in Section 4.3). We further assume here that each of these have normal distributions (see Sections 4.1, 4.2, and 4.4 for a complete description of the probability distributions of these terms), with means μ_i and standard deviations σ_i. Each individual probability density function (PDF) is then given by

$$f_i(z_i) = \frac{1}{\sqrt{2\pi}\sigma_i} e^{\frac{-(z_i-\mu_i)^2}{2\sigma_i^2}}, \quad (9)$$

where the index i refers equally to the $I_r(t)$, $\delta I(t)$, $\Delta\phi(t)$, and $N_b(t)$ distributions and z_i is the corresponding random variable.

However, the $\delta I(t)$ and $\Delta\phi(t)$ distributions do not appear linearly but quadratically in the null distribution. In the case where $\delta I(t)$ and $\Delta\phi(t)$ both follow normal distributions, the PDFs of $(\delta I(t))^2/4$ and $(\Delta\phi(t))^2/4$ are given by

$$f_i\left(\frac{z_i^2}{4}\right) = \frac{1}{\sqrt{2\pi}\sigma_i}\frac{e^{-(4z_i+\mu_i^2)/2\sigma_i^2}}{\sqrt{4z_i}}\cosh\left(\frac{\mu_i\sqrt{4z_i}}{\sigma_i^2}\right). \quad (10)$$

The two distributions, $(\delta I)^2/4$ and $(\delta\phi)^2/4$, are illustrated in Figure 1 for realistic values of their means and standard deviations. The next step in building the nulling PDF is to sum

---

[3] For a given baseline orientation, the astrophysical null N_a can be expressed in terms of the source complex visibility $\mathcal{V}$ as $N_a = (1 - |\mathcal{V}|)/(1 + |\mathcal{V}|)$.

[4] The theory we present here can be extended for larger values of N_a and error sources by keeping the full expression of $I_\pm^*$ in the definition of the null depth.

[5] For long baseline interferometers, the polarization effect can be measured on calibrator stars and accurately corrected as it generally varies slowly over time.

the phase and the intensity mismatch distributions. If $(\Delta\phi(t))^2$ and $(\delta I(t))^2$ are two independent random variables, the density function $f_{\delta I^2/4+\Delta\phi^2/4}(y)$ is given by the convolution of their respective density functions (Rohatgi 1976, p. 141). If we denote y as being $(z^2_{\Delta\phi^2} + z^2_{\delta I^2})/4$, this convolution can be expressed as follows:

$$f_{\frac{\delta I^2}{4}+\frac{\Delta\phi^2}{4}}(y) = (f_{\frac{\Delta\phi^2}{4}} \otimes f_{\frac{\delta I^2}{4}})(y) \tag{11}$$

$$= \int_{-\infty}^{+\infty} f_{\frac{\Delta\phi^2}{4}}(y_1) f_{\frac{\delta I^2}{4}}(y - y_1)\, dy_1. \tag{12}$$

Adding the astrophysical null term, N_a, in Equation (12) then corresponds to a further convolution of Equation (12) with a Dirac function $\delta(N_a)$. The result is simply a translation of the density function by N_a (see Figure 1):

$$f_{\frac{\delta I^2}{4}+\frac{\Delta\phi^2}{4}+N_a}(y) = f_{\frac{\delta I^2}{4}+\frac{\Delta\phi^2}{4}}(y - N_a). \tag{13}$$

Now folding the effect of the relative intensity uncertainty $I_r(t)$ into the expression for the measured null (Equation (6)), one computes the distribution of the product of $I_r(t)$ with $((\delta I(t))^2/4 + (\Delta\phi(t))^2/4 + N_a)$. Assuming that these are uncorrelated random variables (Rohatgi 1976, p. 141), the resulting null depth distribution is

$$f_{\hat{N}}(z_{I_r}) = \int_{-\infty}^{+\infty} \frac{1}{|y|} f_{\frac{\delta I^2}{4}+\frac{\Delta\phi^2}{4}+N_a}(y) f_{I_r}\left(\frac{z_{I_r}}{y}\right) dy. \tag{14}$$

The analytical solution for this integral exists for phase and intensity fluctuations following Gaussian distributions. However, the distribution $f_{\hat{N}}(z_{I_r})$ displays a singularity for $y = 0$.

The final expression of the measured null distribution (see Equation (8)) is obtained by convolving Equation (14) with the equivalent background null depth distribution f_{N_b}:

$$f_{\hat{N}}(N) = f_{\hat{N}}(z_{I_r}) \otimes f_{N_b}(z_{N_b}). \tag{15}$$

Summarizing all the steps described in this section, the final analytical expression for the measured null depth can be retrieved from the individual distributions as follows:

$$f_{\hat{N}}(N) = f_{N_b} \otimes \left[\int_{-\infty}^{+\infty} \frac{1}{|y - N_a|} f_{I_r}(f_{\frac{\delta I^2}{4}} \otimes f_{\frac{\Delta\phi^2}{4}} \otimes N_a)\right]. \tag{16}$$

The measured null distribution expressed by Equation (16) depends on nine independent parameters: the means and standard deviations of the four error distributions and the astrophysical null. In the simpler case of a system where only a phase error impacts the measured null distribution, the null PDF depends only on three parameters: the mean and standard deviation of the phase error and the astrophysical null. Figure 1 illustrates that $\mu_{\Delta\phi}$ and $\sigma_{\Delta\phi}$ define together the full width at half-maximum (FWHM) and the skewness of the PDF, while N_a only changes its horizontal position.

2.3. Fitting Strategies

Two methods can be used to generate null depth distributions to be fitted to the data. In the first one, referred to hereafter as the "analytical method," the distribution is generated analytically using the measured means and standard deviations of the background and intensity distributions. The second method, called the numerical method, generates simulated distributions using the measured intensity and background distributions, together with simulated phase error sequences having normal distributions, according to Equation (8). For illustration, we apply our techniques to data obtained with the PFN, a deployable near-infrared (≃2.16 μm) interferometric coronagraph developed at the Jet Propulsion Laboratory and recently installed at the Palomar Hale telescope (Serabyn & Mennesson 2006; Mennesson et al. 2006; Martin et al. 2008). As described in the following sections, this method strongly reduces both statistical and systematic errors and can avoid the observation of calibrator stars (depending on the instrument). Therefore, we call them, respectively, the analytical and numerical self-calibrated methods.

2.3.1. Analytical Self-calibrated Method (ASC)

The first strategy makes use of theoretical expression (16) to calculate null depth distributions, assuming that all instrumental terms follow Gaussian statistics. No temporal data sequences are simulated, only the null probability distribution, which depends on nine parameters: the astrophysical null and the mean and standard deviations of the four Gaussian error terms (relative phase, intensity mismatch, relative intensity, and background variations). The number of unknown parameters depends on the exact interferometric configuration and must be kept as small as possible in order to give a unique solution to the problem. In most interferometers, the individual beam intensities and the background intensity are monitored as part of the observing sequence, which leaves only three free parameters to be fitted: the mean and standard deviation of the phase error and the astrophysical null depth. In the case of the PFN, two symmetrically placed sub-apertures on the primary mirror are interfered, and using a rapidly spinning wheel, interleaved (<200 ms) sequences of the interferometrically combined (nulled) signal, the individual beam intensities, and the background are recorded. Using this data, we fit the recorded relative intensity mismatch $\delta I(t)$, relative intensity $I_r(t)$, and background $N_b(t)$ with Gaussian profiles (see Section 4 for validation of this hypothesis). The resultant mean and standard deviation values are then injected into Equation (16). The remaining three free parameters of Equation (16), i.e., the differential phase parameters $\mu_{\Delta\phi}, \sigma_{\Delta\phi}$, and the astrophysical null N_a, are then adjusted so as to fit the calculated curve to the observed null (Equation (6)) distribution. As detailed in Section 2.5, except for the marginal case where the phase fluctuations are close to 0 (typically $\sigma_{\Delta\phi} < 0.005$ rad), only one combination of these three parameters provides a suitable fit to the observed null data distribution. The pair ($\mu_{\Delta\phi_a}$, $\sigma_{\Delta\phi_a}$) defines both the FWHM and the skewness of the modeled null distribution, while N_a adjusts the horizontal position of the distribution peak (see Figure 1), and only one combination of $\mu_{\Delta\phi}$, $\sigma_{\Delta\phi}$, and N_a, fits the distribution.

Figure 1 illustrates the construction of the analytical null depth distribution from the individual distributions while Figure 2 (left) illustrates the analytical fitting strategy on a nulling sequence measured on the sky with the PFN. After being fitted by Gaussian distributions, $\mu_{\delta I}, \sigma_{\delta I}, \mu_{I_N}, \sigma_{I_N}, \mu_{N_B}$, and σ_{N_B} are injected into Equations (9) and (10) to compute their impact on the measured null distribution. The influence of the intensity mismatch is represented by the long gray dashed curve in Figure 1. Assuming a Gaussian distribution of the phase error as well, different values of $\mu_{\Delta\phi}$, $\sigma_{\Delta\phi}$, and N_a are used to generate distribution curves. The impact of their distributions is also

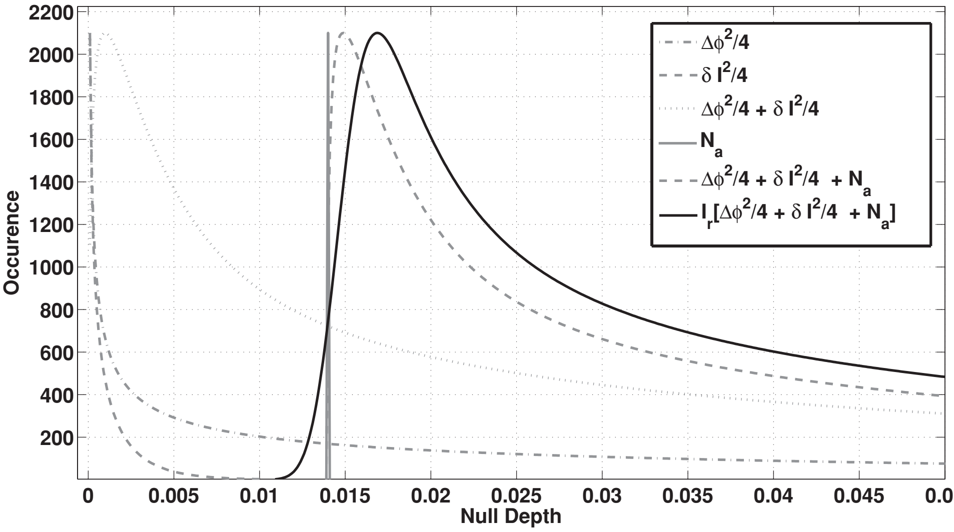

Figure 1. Illustration of the construction of the null distribution from the individual contributions. The phase and intensity terms (resp. $(\Delta\phi)^2/4$ and $(\delta I)^2/4$) are first summed, which corresponds to the convolution of their respective probability distribution. The astrophysical null is then added. This step corresponds to the convolution by a Dirac function. As a result, the probability distribution is translated horizontally by N_a. The last step consists in multiplying $(\Delta\phi)^2/4 + (\delta I)^2/4 + N_a$ by the relative intensity uncertainty I_r. The final distribution of the reconstructed null depth is represented by the black curve. The different curves represent realistic individual distributions of the phase and intensity errors, the astrophysical null, and their sum. For each instrumental error terms $\Delta\phi(t)$, δI(t), and $I_r(t)$, a Gaussian distribution is assumed.

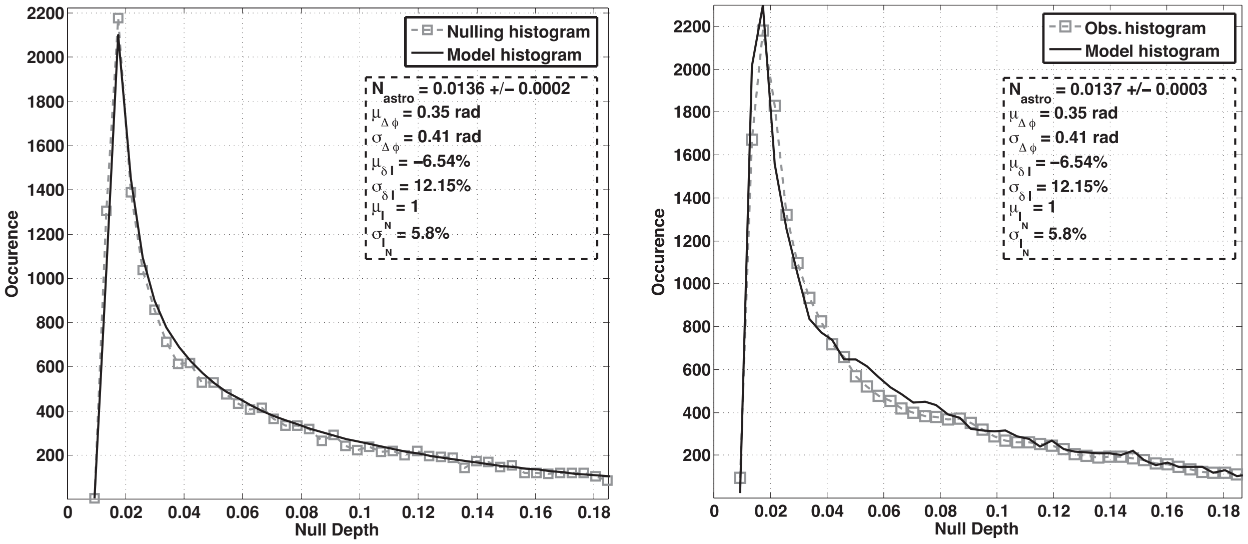

Figure 2. Left: fit using the analytical self-calibration method on a data set obtained on α Boo with the PFN in 2009 July. The astrophysical null corresponding to the best fit is 0.0136 ± 0.0002. Right: same fit but using the numerical self-calibration approach. Note that the simulated distribution now presents more structure, as it integrates the actual distributions of background and intensity terms. The astrophysical null corresponding to the best fit is 0.0137 ± 0.0003.

illustrated in Figure 1 by the gray dashed and dotted curve for the phase error and by the gray plain curve for the astrophysical null. All these distributions are finally combined together according to Equation (16). The resulting black curve can then be compared to the measured distribution (Figure 2).

2.3.2. Numerical Self-calibration Method (NSC)

Unlike the ASC, the numerical self-calibration approach (NSC) does not make any assumption about the distributions of the intensity mismatch, background, and total intensity terms, which are assumed to be measured within the null sequence or close in time. Instead of fitting the distribution of these three measured signals by Gaussian distributions, we use the data—and hence actual distributions—recorded for each of these quantities and inject them directly into Equation (8).

In the case of the PFN for instance, interleaved (<100 ms) measurements of the individual beams, interferometric (close to null), and background intensities are recorded over sequences of a few minutes. Although the background and individual beam signals are not recorded exactly at the same time as the null, their distributions can be measured with very high fidelity. In order to fit a sequence of observed null values, we combine these observed distributions with a generated random phase error (with a normal distribution) of the same size (same number of data points) according to Equation (8). We only make two assumptions when using this method: (1) the differential phase follows a Gaussian distribution and (2) the individual beam intensities are uncorrelated. The latter condition, which seems valid for the PFN measurements (see Section 4), implies that the distribution of the differential intensity term $\delta I(t)$ derived from $I_1^*(t)$ and $I_2^*(t')$ measured at different times is the same as if the individual intensities were measured simultaneously. The main advantage of the numerical technique is that the data monitored by the instrument (i.e., the individual beam intensities and the background) are directly injected into the model. Therefore, no matter what the real distributions are for those terms, no bias is introduced into the modeled probability distribution. However, as the random generation of the differential phase vector produces slightly different distributions and best-fit parameters for different seeds, the numerical method adds some intrinsic uncertainty. This "fitting noise" is computed by generating many random phase errors and measuring the standard deviation of the resulting best-fit astrophysical null depths. This uncertainty adds quadratically to the statistical error defined in the next section. Consequently, the final error bar quoted on the astrophysical null derived by the numerical method is slightly larger than in the analytical case, but the potential sources of bias are reduced. Figure 2, right panel, shows an example of the probability distribution fitting (same α Boo sequence as above) using the numerical method.

2.4. Error Bars and Residual Comparison

In this section, we compare the results obtained with the two fitting approaches. To perform this comparison, we make use of the retrieved parameter corresponding to the best fits, the goodness of the fit, and the relative residuals between the models and the data. To compute the goodness of the fit and derive the optimum fit parameters, we minimize a reduced Pearson χ^2 quantity, defined as

$$\chi^2 = \frac{1}{N_{\mathrm{bins}} - 4} \sum_{i=1}^{n} \frac{\left(f_{\hat{N}}^{\mathrm{Obs}}(i) - f_{\hat{N}}^{\mathrm{Theo}}(i)\right)^2}{f_{\hat{N}}^{\mathrm{Theo}}(i)}, \qquad (17)$$

where $f_{\hat{N}}^{\mathrm{Obs}}$ and $f_{\hat{N}}^{\mathrm{Theo}}$ are, respectively, the observed and theoretical null probability distributions and $N_{\mathrm{bins}} - 4$ is the number of independent degrees of freedom. Following usual recommendations for robust fitting of probability distributions (Cochran 1954), we use a number of histogram bins equal to $\simeq\sqrt{N_{\mathrm{pts}}}$, where N_{pts} is the number of measurement points over the full range of observed null values. Also, only the largest null depth interval for which the occurrence within each bin is $\geqslant 5$ is used for the fitting. Unlike the NSC, the probability distribution obtained with the ASC method must be re-scaled prior to computing the χ^2 to ensure that the total number of occurrences in the theoretical distribution corresponds to the total number of measurements within the data set. Mathematically, it comes down to introducing a scaling factor C to match the integral of the observed and theoretical distributions over the domain of definition, i.e.,

$$C \cdot \int_{N_{\mathrm{min}}}^{1} f_{\hat{N}}^{\mathrm{Theo}}(n)\, dn = \int_{N_{\mathrm{min}}}^{1} f_{\hat{N}}^{\mathrm{Obs}}(n)\, dn, \qquad (18)$$

where N_{min} is the minimum observed null value of the distribution.[6]

Overall, the analysis of different data sets with both fitting methods provided similar results, with reduced χ^2 ranging between 1 and 1.5, meaning reasonably good statistical agreement between the model and the observations. The computation of realistic error bars must combine two different components which add quadratically: (1) statistical (random) errors and (2) systematic errors. Systematic errors, such as those arising from slow drifts in the experimental setup (quasi-statics; e.g., Colavita et al. 2009), are not captured by the statistical analysis of a single sequence and will be discussed in Section 3. A thorough description of the different sources of quasi-static errors will also be presented in Section 4. We only compute and quote statistical errors in this section.

For an individual sequence, the statistical uncertainty σ_{stat} on the derived astrophysical null is assessed using the χ^2 statistical properties (see Press et al. 2007, Section 15.6.4). N_a is varied around its optimal value while the χ^2 is minimized by adjusting the other two parameters. The error bar on N_a corresponds to the N_a variation required to increase the reduced χ^2 by a tabulated increment based on the desired confidence level and the number of degrees of freedom in the fit. A 68.3% confidence level was adopted on the quoted error bar, and the analysis of the covariance of the fit with the other two parameters (i.e., $\mu_{\Delta\phi}$ and $\sigma_{\Delta\phi}$) is presented in the Appendix. This estimation of the retrieved parameter error bars is only valid if the observed null values are affected by zero mean Gaussian noise. As a sanity check, we then also conducted a bootstrapping analysis—independent of the actual noise properties—resampling and replacing the observed null values to generate many (500) "fake" sequences. Analyzing the corresponding histograms yields astrophysical null (68.3% confidence interval) statistical uncertainties similar to those derived using the χ^2 approach.

As an illustration, the left panel of Figure 2 shows the best analytical self-calibrated fit (black curve) to the null distribution observed (gray dashed line and squares) on the bright star α Boo with the PFN (one particular two-minute long sequence). The reduced χ^2 is 1.17 and the derived astrophysical null calculated with a 1σ confidence interval is 0.0136 ± 0.0002 (see the Appendix for more details). The error bar quoted here is the statistical error only. The main advantage of this analytical fitting method is its mathematical consistency and precision. However, it assumes normal and uncorrelated noise distributions for all noise sources, instead of injecting their observed distributions into the model. These assumptions will be justified and explained in Section 4. Another characteristic of this approach is that because of the $1/|y|$ term in Equation (14), the distribution is not defined for a null depth $N = 0$. However, this issue can be solved by simply removing the bin containing $N = 0$ during the fitting process.

The right panel of Figure 2 represents the best fit obtained with the numerical approach on the same α Boo data set. The reduced Pearson's χ^2 is 1.23. The derived astrophysical null depth is $N_a = 0.0137 \pm 0.0003$, in excellent agreement with the value obtained using the analytical approach and Gaussian statistics for all instrumental terms. The quoted error bar accounts for both the statistical uncertainty and the numerical "fitting noise" discussed in Section 2.3.2.

To complete this comparison, Figure 3 shows the relative difference between the measured null distribution and the distribution obtained with both the analytical method (gray curve, circular markers) and the numerical fitting method (black curve, square markers). As can be seen in this figure, the two different statistical data reduction methods are very

---

[6] The null depth in interferometry is generally considered to be defined between 0 and 1. However, the instantaneous measured null can be <0 because of the background fluctuations. This is why the limit of integration must be defined between the minimum measured null depth and 1.

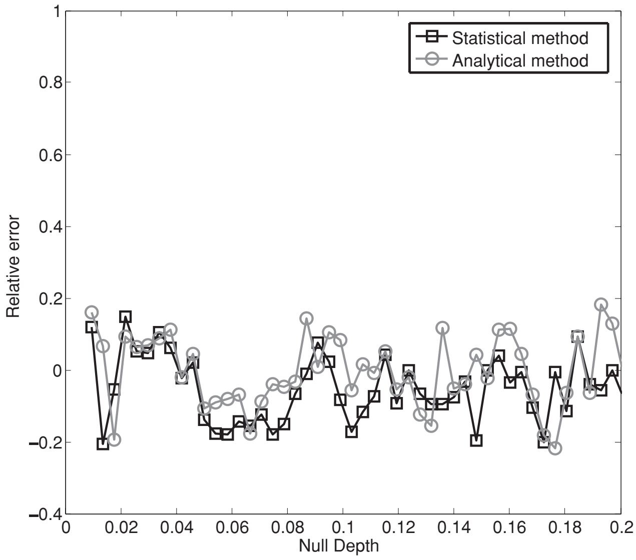

Figure 3. Relative error $((f_{\hat{N}}^{\rm Obs} - f_{\hat{N}}^{\rm Theo})/f_{\hat{N}}^{\rm Obs})$ between the fitted null distributions and the measured one as a function of the null depth. The gray curve with circular markers represents the relative error relative to the analytical self-calibrated method while the black curve with square markers represents the relative error obtained with the statistical method. Both relative residuals are similar with rms values ≃0.05.

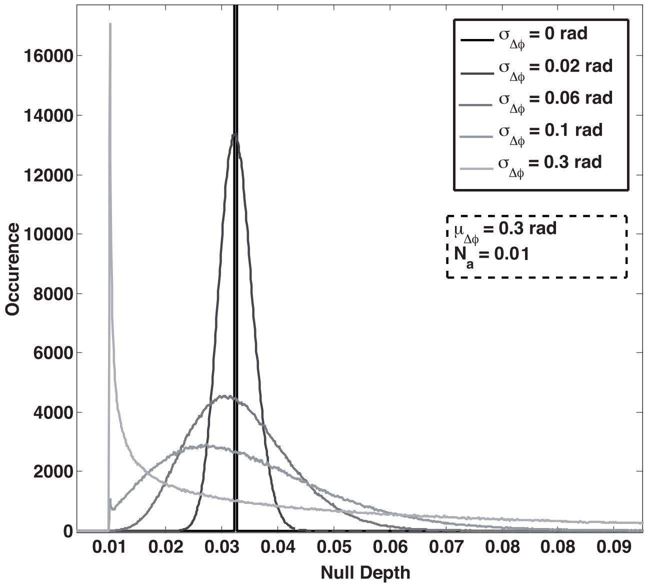

Figure 4. Simulated null depth distributions for an astrophysical null of 0.01, a constant mean phase error of 0.3 rad, and different values of the phase error rms. All the other error sources have been set to 0.

equivalent in terms of accuracy: the relative residuals between their distributions and the measured one are similar. This is particularly true for small null depth values ($N < 0.05$) where most of the astrophysical information is located. Overall, this comparison shows that very similar results are obtained on α Boo with the analytical and numerical methods.

2.5. Amplitude of the Fluctuations

In this section, we demonstrate the conditions that must be fulfilled by the error fluctuations in order to produce a distribution that can be fitted by a unique combination of the parameters. For that, we consider the simpler case where only phase errors are present.

First, let us consider the extreme case of a perfectly stable system ($\sigma_{\Delta\phi} = 0$) but with an error on the phase shift ($\mu_{\Delta\phi} \neq 0$). The measured null distribution is then a Dirac function that peaks at $\hat{N} = N_a + (\mu_{\Delta\phi})^2/4$ (see Figure 4). Therefore, only the sum, $N_a + (\mu_{\Delta\phi})^2/4$, can be determined but not the astrophysical null.

Of course, using a statistical approach for analyzing perfectly constant data does not make much sense and is not realistic. However, it shows that the phase fluctuations must have a minimal amplitude to make a statistical approach applicable. Now, let us consider the more realistic case of a system having both a phase fixed bias and phase fluctuations. Equation (10) expresses the impact of phase fluctuations on the null depth distribution. From this equation, it can be seen that the larger the fluctuations, the broader the corresponding distribution (see Figure 4). If the FWHM of this distribution is smaller than the bin size used for computing the null distribution, it appears as a Dirac function (which corresponds to a fixed phase error) and the fitted parameters cannot be found. Now, if the phase distribution can be properly sampled in several bins, the three parameters that must be fitted ($\mu_{\Delta\phi}$, $\sigma_{\Delta\phi}$, and N_a) can be retrieved. More importantly, the solution found is unique. For small phase fluctuations, Equation (10) can be approximated by a Gaussian function whose FWHM is $2\sqrt{2\ln 2} \times \sigma_{\Delta\phi}\sqrt{\mu_{\Delta\phi}}$. The criterion for a unique solution to our fit is therefore that this FWHM is larger than a few (k) times the histogram bin size (i.e., k bin size $<2\sqrt{2\ln 2} \times \sigma_{\Delta\phi}\sqrt{\mu_{\Delta\phi}}$). From this equation, it can be seen that for larger mean phase offsets, the minimum phase fluctuation required to meet this criterion decreases. This is due to the fact that the null depth depends quadratically on the phase error. In practice, simulations have shown that the phase distribution must be sampled over at least six bins ($k \geqslant 6$). Figure 5 shows, on simulated data sets, the minimum amplitude of the phase fluctuations required as a function of the mean phase error for a bin size of 0.001. This bin size directly depends on the number of data points available within a data set (see Section 2.3.1). It means that increasing the observing time (and therefore the number of data points within a data set) allows the use of smaller bin sizes and hence even easier parameter retrieval. In this figure, a fit is considered successful when all three parameters are found within some a priori tolerable error. For N_a, it means that the error is smaller than the histogram bin size. For the two other parameters, it means that their effect on the null depth ($\Delta\phi^2/4$) is also smaller than the histogram bin size. It is interesting to note that even small fluctuations compared to the mean phase errors are sufficient to retrieve the astrophysical null depth with a very good accuracy. This also means that it is possible to measure N_a even if the fluctuating phase error never reaches zero, and so even when the true astrophysical null value is never reached. Finally, it is important to note that the results obtained with the PFN illustrating this paper correspond to parameter combinations located well within the *"parameter-retrieved"* zone of Figure 5.

3. ON SKY PERFORMANCE: CLASSICAL VERSUS STATISTICAL REDUCTION METHODS

In order to investigate the validity and accuracy of our statistical data reduction approach, we applied it to astronomical data obtained with the PFN during a 2009 July observing run. In order to evaluate the astrophysical null accuracy achieved with our statistical analysis, we present here the results obtained on a series of consecutive independent measurements of α Boo with the PFN. We explore both the repeatability of the results

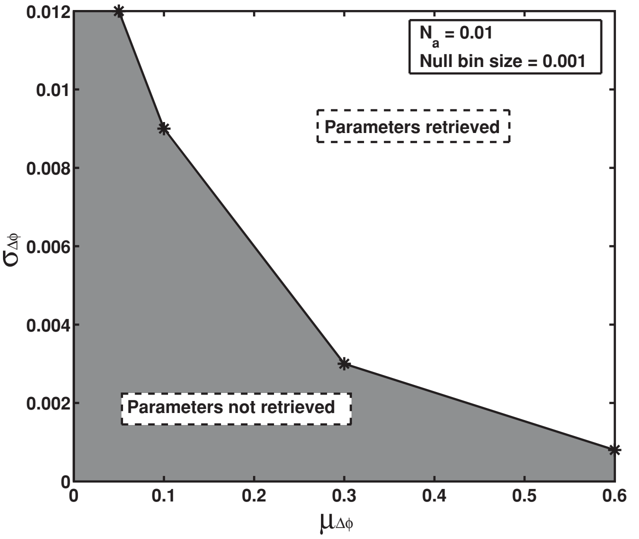

Figure 5. For $N_a = 0.01$ and a bin size of 0.001, this plot represents, as a function of the mean phase error, the minimum value of the phase rms required to fit unambiguously the distribution and retrieve the astrophysical null N_a. Note that on real data obtained with the PFN, we are located well within the parameter retrieved zone (see Section 2.3.1 and after).

(precision assessment) and their consistency with values previously reported by long baseline interferometry (LBI, accuracy and bias assessment).

We use here a set of five independent null sequences recorded on α Boo with the PFN in 2009 July and compare the astrophysical nulls, N_a, and precisions derived from (1) the "classical" null (or visibility) data reduction method and (2) from the probability distribution analysis. We then compare our results with the stellar diameter measurement obtained on this same star with LBI, discussing the aspects of accuracy and systematic errors.

3.1. Classical Reduction Method

Very few nulling data from ground-based telescopes have been analyzed so far, as only two nulling interferometers are operating: the Keck Interferometer Nuller (Colavita et al. 2009) and the BLINC Nuller (Hinz et al. 2000). Until now, the method used to analyze nulling data was analogous to that used for calibrating visibility measurements. The principle is to first evaluate the null depth observed on the science target by averaging the fluctuating instantaneous null depth over a significant number of points. This measurement is biased due to the fast fluctuations of phase and intensity errors. The same measurement is then conducted on a calibrator star of well-known diameter, located close to the science target and with a similar magnitude at the wavelength of observation (Mérand et al. 2005). For both stars, the measured null depth $\langle N(t)\rangle$ is the sum of the astrophysical null N_a and the mean instrumental null $\langle N_{\mathrm{i}}(t)\rangle$ averaged over the sequence:

$$\langle N(t)\rangle = N_a + \langle N_{\mathrm{i}}(t)\rangle \tag{19}$$

$$\langle N_{\mathrm{cal}}(t+\Delta t)\rangle = N_{a,\,\mathrm{cal}} + \langle N_{\mathrm{i,\,cal}}(t+\Delta t)\rangle, \tag{20}$$

where the astrophysical null depth on the calibrator star ($N_{a,\,\mathrm{cal}}$) is assumed to be known thanks to an accurate photosphere model or from independent interferometric observations. Therefore, assuming that the instrumental null is constant, one estimates the scientific target's astrophysical null as

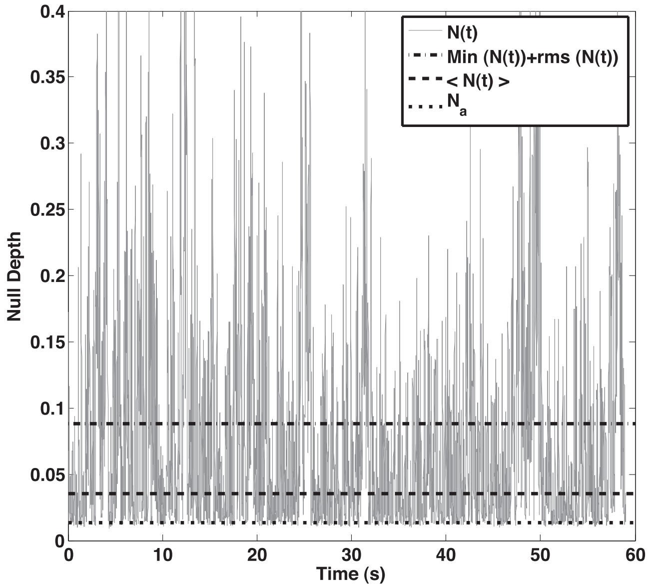

Figure 6. Null depth fluctuations measured on the α Boo data set. The dash-dotted line represents the highest null depth value which is taken into account in the classical data reduction approach. The dashed line corresponds to the mean null depth of the sequence prior to calibration ($\simeq$0.035) and the dotted line to the astrophysical null that is measured by the numerical statistical method (0.0137 ± 0.0003).

$$N_a = N_{a,\,\mathrm{cal}} + \langle N(t)\rangle - \langle N_{\mathrm{cal}}(t+\Delta t)\rangle. \tag{21}$$

Obviously, the accuracy on N_a depends both on the calibrator's astrophysical null uncertainty and on the stability of the instrumental null (or the ability to extrapolate its value accurately based on bracketing calibrator observations).

The method used to emulate a "classical analysis" of our null data is the following. First the "bad" (large instantaneous nulls) data points within each data set are rejected, both for the target and the calibrator. Only the data having null values between the minimum measured null N_{min} and $N_{\mathrm{min}} + \sigma_N$ are kept, where σ_N is the rms of the null data (see Figure 6, dash-dotted line). This is also called the sigma clipping method. The null depth of an individual object sequence is then computed as the mean of the remaining data points (see Figure 6, dashed line). The same approach is applied to both the scientific target and the calibrator data, and the calibrated astrophysical null depth is then computed using Equation (21). The black stars in Figure 7, left panel, represent the calibrated null depths obtained with this classical data analysis on five consecutive α Boo data sets. These data have been calibrated using five data sets obtained on α Her. The error bar on the individual measurements is given by the quadratic sum of the target statistical error, the systematic error, and the calibrator total error (statistical error and diameter uncertainty). The individual statistical error bars are computed from the variance of the null depth fluctuations within each data set (after applying data clipping) and is equal to 0.018 on α Boo. The systematic error is more difficult to calculate and can be assessed both by comparing the measured null depth with the one expected from previous measurements of α Boo's stellar diameter and by comparing the individual statistical errors with the variance of the null over the five data sets. This comparison leads us to the conclusion that the systematics should be low compared to the statistical errors. Therefore, assuming no/low systematics and averaging over the

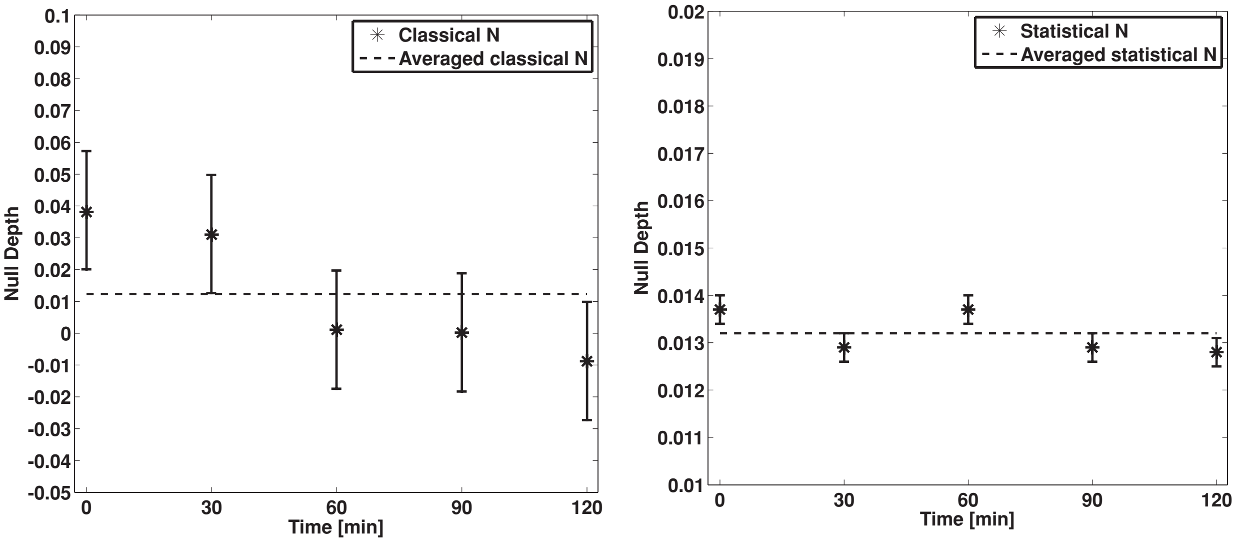

Figure 7. Comparison between astrophysical null values obtained with both classical and statistical (numerical) data analysis approaches on α Boo with the PFN. Left panel: results obtained using the classical reduction. The results drift significantly over time and the individual null depth error bars obtained on each data set are 0.02. The mean measured astrophysical N is 0.0123 ± 0.008. Right panel: results obtained using the statistical method. The measured nulls are very stable, with individual error bars around 0.0003. The mean astrophysical null measured is 0.0132 ± 0.00013, where the error bar assumes no systematic uncertainties (see the text for details). Note that the y scale is different in the two figures.

Table 1
Comparison Between Limb Darkened (LD) Diameters Found by the PFN using both the Classical and the Numerical Statistical Data Reduction Method and by Long Baseline Interferometry

Method	Name	N_a	θ (mas)
Classic. nulls	α Boo	0.0123 ± 0.008	$20.25^{+6.4}_{-9.8}$
Stat. nulls	α Boo	0.0132 ± 0.00013	20.96 ± 0.09
LBI vis.	α Boo	0.0131 ± 0.00010	20.91 ± 0.08

Note. Note that the null depth value given for LBI is an equivalent null on a 3.4 m baseline derived from the measurement of the angular diameter.

five data points, the astrophysical leakage measured on α Boo is 0.0123 ± 0.008 (see Table 1). The significant slow drift of the measured nulls in Figure 7, left panel, clearly illustrates that the classical method is very sensitive to the instrumental/seeing conditions and to the fact that the calibrator was only observed *after* the five α Boo sequences and not in between them. The large error bars derived—even in the quite optimistic case of no systematics—demonstrate that in fact, with the short PFN interferometric baseline and when using the classical data reduction method, α Boo's near-infrared diameter cannot be measured reliably.

3.2. Statistical Reduction Method

On the other hand, our statistical data analysis approach uses the whole range of null values recorded and neither uses nor requires any calibration star. Using the same five α Boo data sets, the individual astrophysical nulls measured using statistics have much smaller individual error bars (0.0003) and are very stable over the whole 2 hr of observation (Figure 7, right panel). Using the five data sets obtained on α Boo, a set of $(N_{a,i}, \sigma_{\mathrm{stat},i})$ best-fitting values is derived. From that ensemble, we compute the weighted mean value of N_a with weights $w_i = 1/\sigma^2_{\mathrm{stat},i}$. The weighted mean astrophysical null value derived over the full sequence is 0.0132. Assuming *no systematic errors* and simply propagating the individual error bars ($\sigma_{\mathrm{stat},i}$), the final statistical error bar is given by $\sigma_{\mathrm{stat}}^{-2} = \sum_i \sigma_{\mathrm{stat},i}^{-2}$ and amounts to 0.00013. This yields an astrophysical null estimate of $N_a = 0.0132 \pm 0.00013$ for α Boo (see Table 1).

Of course, systematic errors can be presented in the data, for instance arising from slow drifts in the experimental setup (quasi-statics) which are not captured by the statistical analysis of a single sequence. However, conversely to the classical method case, no obvious long-term drift is visible versus time. The weighted standard deviation computed over the sequence is 0.0004, in fairly good agreement with the quoted individual error of 0.0003, pointing to small systematics if any. This weighted standard deviation can also serve as an estimate of the systematic error per individual measurement (e.g., Colavita et al. 2009). The systematic error on the mean is likely smaller than that per individual measurement, but we do not have enough data to check for such reduction of the systematics with respect to the number of measurements. Consequently, we estimate the final error bar on α Boo's measured astrophysical null to be at the few 10^{-4} or lower.

Another way to estimate systematics and constant biases is to compare the astrophysical null derived by the statistical method with previous measurements obtained by LBI. This is the object of the following section. A detailed description of the potential sources of quasi-static errors as well as their impact on the null depth is also presented in Section 4. Finally, observations of calibrators can obviously be used in conjunction with the statistical data analysis to further reduce the effect of residual biases.

3.3. Comparison to LBI Data

For a naked star represented by a limb-darkened disk of diameter θ_{LD} with a limb-darkening coefficient A_λ, the observed astrophysical null is given by (Absil et al. 2006, 2011)

$$N_{a,\mathrm{LD}} = \left(\frac{\pi B \theta_{\mathrm{LD}}}{4\lambda}\right)^2 \left(1 - \frac{7A_\lambda}{15}\right)\left(1 - \frac{A_\lambda}{3}\right)^{-1}, \quad (22)$$

where λ is the central wavelength of observation and B is the baseline length. For the PFN, these values are 2.16 μm and 3.20 m, respectively. This expression can be simplified in the case of uniform disk models by setting $A_\lambda = 0$.

LBI measurements of α Boo in the K band (where limb-darkening effects and corresponding uncertainties are reduced) provide very accurate results. We use the value of 20.91 ± 0.08 mas derived by FLUOR/IOTA (Perrin et al. 1998; Lacour et al. 2008). This value is also very consistent with the previous measurement of 20.95 ± 0.20 mas obtained at I2T (di Benedetto & Rabbia 1987).

Using the 0.350 linear limb-darkening coefficient predicted in the K band for a 4300K giant star with $\log g = 2.0$ (Claret et al. 1995), we get an astrophysical null depth of 0.01314 ± 0.00010 at the PFN baseline. This is excellent agreement with our measured value of 0.001320 ± 0.00013 (or ± 0.0004 when being conservative with respect to systematics) reported above, which corresponds to a limb-darkened diameter of 20.96 ± 0.09 mas (see Table 1). The discrepancy between the PFN and LBI α Boo measurements is then at the 10^{-4} level and within the error bars of each measurement. This demonstrates that in the illustrative case of α Boo, our measurement is not only precise but also very accurate. It suggests that if any bias is present in our calibrator-free measurements of α Boo, they are at the few 10^{-4} level or below. A similar analysis of PFN data using the statistical reduction method confirms this result on a larger sample of eight bright giants/supergiants (B. Mennesson et al. 2011, in preparation). In comparison, the very best 1σ null accuracy reported by LBI is $\simeq 0.002$ in the mid-infrared (Colavita et al. 2009) and $\simeq 0.0025$ in the near-infrared (Kervella et al. 2004; equivalent to a visibility accuracy of 0.005 for an unresolved source). This indicates that using the self-calibrated data reduction approach, a gain of an order of magnitude in null (or visibility) accuracy can be achieved.

In fact there is little that is specific to the PFN instrument in our approach, and the statistical data reduction method could in principle be applied to any two-beam interferometer working around null with a fringe tracker. Since null and visibility measurements are equivalent, the statistical analysis may thus also prove useful to regular long baseline visibility interferometry (B. Mennesson et al. 2011, in preparation).

4. POSSIBLE LIMITATIONS

We explore in this section some possible limitations of the statistical data reduction technique, which may appear when trying to measure very deep astrophysical null depths. Limitations arise from well-identified sources: temporal effects, chromatic effects, and deviations from the assumptions used in the modeling. There are only two assumptions made in the self-calibration technique: no temporal correlation between the individual beam intensities and Gaussian distribution of the error sources.[7] In the following, we investigate these different effects, assess their contributions to the final null depth estimates, and suggest some mitigation techniques.

4.1. Intensity Distributions

Conversely to the numerical method, where the measured relative intensity uncertainty $I_r(t, \Delta t)$ and intensity mismatch $\delta I(t)$ are directly injected into the model, the analytical approach assumes these distributions to be Gaussian and computes their mean and standard deviation to feed the analytical expression of the measured null distribution (see Section 2.2). Therefore, a possible limitation of the analytical approach could occur if these distributions are not Gaussian.

Figure 8 shows the typical relative intensity uncertainty and intensity mismatch distributions measured with the PFN. While the left-hand panel compares the $I_r(t)$ measured distribution (gray crosses) with a Gaussian distribution (black curve), the right-hand one does the same for the $\delta I(t)$ distribution. As can be seen, both distributions can be reliably fitted by a Gaussian distribution. The goodness of the fit reduced χ^2 values are $\simeq 0.99$ for both $I_r(t)$ and $\delta I(t)$. The bottom panel of these two figures illustrates the relative residuals between the observed distribution and the best Gaussian fit. For both fits, the residuals are close to zero for the entire central part where most of the information is located. Such a good agreement between the measured distributions and Gaussian distributions makes us confident these assumptions are justified and can be used but we note that a very slight skewness may be present.

4.2. Background Distribution

The analytical self-calibration method (unlike the NSC which uses the recorded background level) makes the assumption that the distribution of the background level is normal and fits a Gaussian profile on the recorded data to feed the analytical expression of the estimated null depth (Equation (16)). However, background drifts can occur during observations either because of instrumental (e.g., electronic drifts) or observational reasons (the background depending on the sky position and time of observation) and can cause biases in the determination of the null depth. Figure 9 represents the distribution of the equivalent background null measured on α Boo over 2 minutes. The gray squares represent the actual measured distribution while the black curve is the best Gaussian fit corresponding to this distribution. Once again, the goodness of the fit is excellent with a $\chi^2 \simeq 0.98$. However, it must be stressed that this assumption is only verified for the particular PFN observations illustrated in this paper and must be checked when using other instruments.

4.3. Correlation Issues

In our statistical (both numerical and analytical) self-calibrated method (Section 2.2), we made the assumptions that the different noise terms (background, differential intensity, overall intensity, and differential phase) were temporally uncorrelated, so we could compute the theoretical null distribution from the individual noise distributions.

The cross-correlation of the intensity and phase terms is difficult to estimate. However, the optical/near-infrared coherence length of the atmosphere is generally much smaller than the distance between an interferometer's sub-apertures. Consequently, as the interferometric baseline increases, an even smaller correlation is expected between differential phase and intensity. Even with the compact PFN system, the typical value for Fried's radius is 70 cm (Roddier 1983) at 2.2 μm, to be compared with an interferometric baseline of 3.4 m. In the case of single-mode fiber injection, the intensities of the individual beams are primarily driven by the local tip-tilt and overall phase corrugations of the individual apertures and have no relation to the differential phase between the apertures. This suggests that the absence of correlation between the different noise terms is to first order justified both for the PFN and LBI in general.

---

[7] Note that in the case of the numerical method, only the phase error distribution must be assumed to be Gaussian.

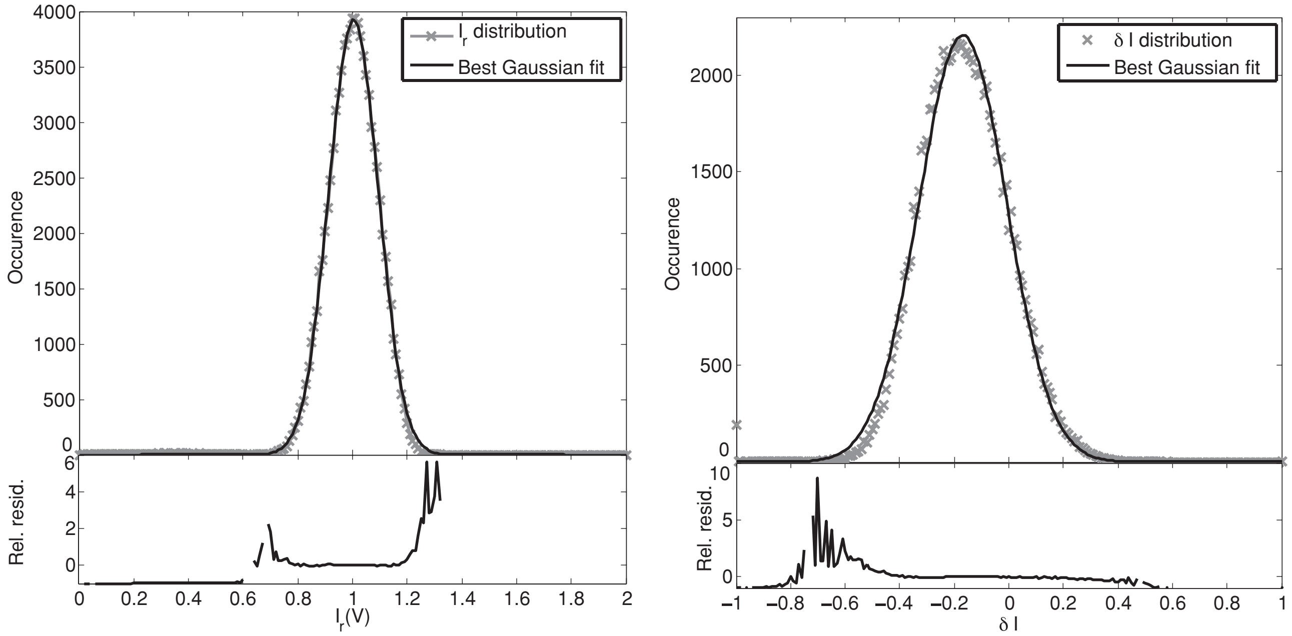

Figure 8. Left: top panel shows a comparison between the measured relative intensity uncertainty distribution (gray crosses) with the best fit of this distribution obtained with a Gaussian distribution (black curve). The Gaussian fit almost perfectly matches the measured distribution (except in the wings). The goodness of the fit is excellent with $\chi^2 = 0.9993$. Bottom panel: relative residual between the fit and the data ($(I^{\mathrm{Obs}} - I^{\mathrm{Gauss}})/I^{\mathrm{Obs}}$). Right: the same comparison but for the relative intensity mismatch. The gray crosses represent the measured $\delta I(t)$ distribution while the black curve represents the Gaussian distribution that best fits the measured distribution. Once again, the fit is excellent with a χ^2 of 0.9952. Bottom panel: relative residual between the observed intensity mismatch and the best Gaussian fit.

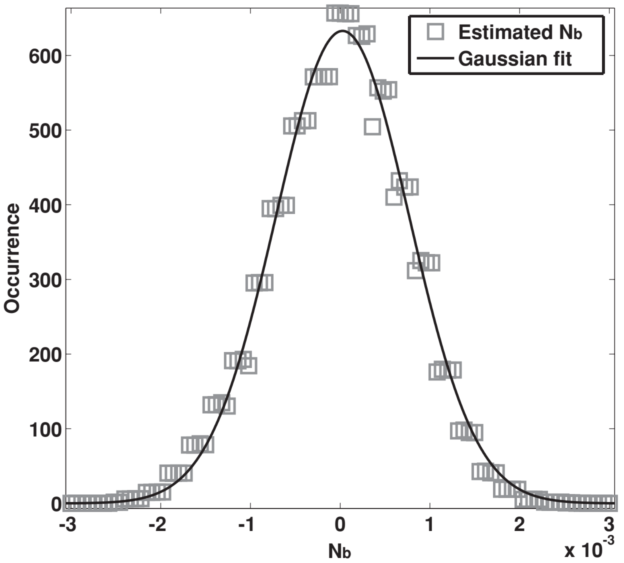

Figure 9. Comparison between the distribution of the background-induced instantaneous error and a Gaussian profile. The quality of the fit between the Gaussian model and the N_b distribution is good with a $\chi^2 = 0.98$.

The actual amount of correlation between the two beam intensities can be assessed by comparing the correlation of $I_1(t)$ with $I_1(t + \Delta t)$, $I_2(t)$ with $I_2(t + \Delta t)$, and $I_1(t)$ with $I_2(t + \Delta t)$. Figure 10 illustrates such a comparison for a typical data set obtained with the PFN. For time delays close to zero both beam intensities are of course perfectly correlated with themselves (dark and light gray dashed curves). The correlation then decreases following a Gaussian-like curve until typical time delays of ~0.2 s are reached. The correlation is then very close to zero (<to a couple of percent). This information directly gives us an indication of the atmospherical conditions. Indeed, as long as the turbulent cells stay above the individual apertures, some correlation will remain between the beam intensity measurements at times t and $t + \Delta t$. Considering that our apertures are 1.5 m wide, we expect to lose completely the correlation between $I_1(t)$ (resp. $I_2(t)$) and $I_1(t + \Delta t)$ (resp. $I_2(t + \Delta t)$) when Δt is such that the turbulent cell has moved by more than 1.5 m. Given the correlation time obtained from Figure 10, we can infer a wind speed during the observations of ~7.5 m s^{-1}, which is consistent with typical conditions at Palomar Observatory. On the other hand, the profile of the correlation between $I_1(t)$ and $I_2(t + \Delta t)$ is completely different. Indeed, the measured values are always under 5%, even at short time delays. We can therefore quantitatively confirm that even for interferometric observations with small baselines and operated under good atmospheric conditions, no significant correlation exists between the two beam intensities.

There is no physical reason why the background should correlate with any of the other terms. However, it is possible that the background intensity and the beam intensities are correlated to some extent if they are measured sequentially on the same detector (remanence). Such an effect depends on the hardware used for each instrument. We have computed its effect on the PFN measurements by computing the correlation between the mean beam intensities and background measurements over each chop cycle. We find that the correlation, if any, is smaller than 5%.

4.4. *Differential Phase Distribution*

For both statistical reduction techniques presented, the differential phase—computed at the central observing wavelength, see Section 4.6—is assumed to exhibit a Gaussian distribution over the recorded nulling sequence. The validity of this assumption is difficult to assess from our data. As long as the instrument

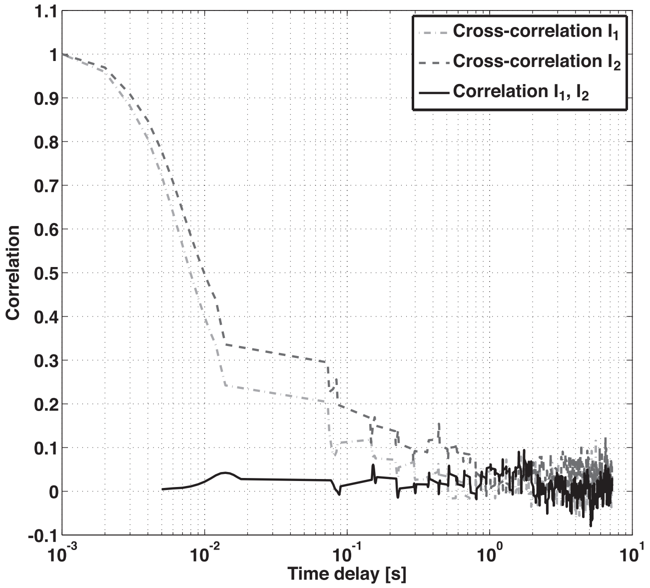

Figure 10. Typical intensity correlation measured during an observation with the PFN. The dashed dark gray line corresponds to the correlation between the beam 1 intensity at time t ($I_1(t)$) and the same beam intensity at time $t + \Delta t$ ($I_1(t + \Delta t)$). The dashed light gray line represents the same correlation but computed for beam 2, and the black line is the correlation between the two different beam intensities for different time delays.

tracks around a constant optical path difference (OPD) position, it seems a reasonable assumption. In the case of the PFN, the two beams come from the same AO-corrected wave front. Tracking a single OPD comes down to the fact that the AO system, which essentially acts as a fringe tracker, tries to maintain the same reference flat wave front over the sequence. Some studies have shown that indeed, the phase residuals after an AO system are Gaussian, which supports our assumption (Cagigal & Canales 2000). If for some reason the fringe tracker or AO system loses lock, or if the OPD is obviously oscillating between several distinct positions, the resulting distribution will no longer be Gaussian, and the corresponding data should be discarded. The reduced Pearson χ^2 defining the quality of the probability distribution fit (Equation (17)) is a good quantitative tool to assess the validity of the Gaussian OPD distribution. If the measured χ^2 are much larger than one, the error bars on the final astrophysical ND should be increased accordingly. Determining the potential bias caused by any departure from a Gaussian OPD distribution is beyond the scope of this paper, but can likely play a role for measuring reliable nulls at very low levels.

4.5. Temporal Effects

The nulling expression established above (Equation (8)) is valid for instantaneous nulls. However, a photometer or camera will work with a limited frequency response or a finite individual integration time δt. In practice, this means that even when all of the instrumental terms of Equation (4) go through zero instantaneously, the measured null will in general be higher. Assuming that the polarization mismatch term is negligible, the best measurable null at any time t will be limited to

$$N_{\min} = \frac{\sigma^2_{\delta I(t,dt)} + \sigma^2_{\Delta\phi(t,dt)}}{4}, \tag{23}$$

where $\sigma^2_{\delta I(t,dt)}$ and $\sigma^2_{\Delta\phi(t,dt)}$ are, respectively, the variance of the intensity mismatch and of the differential phase, both measured over a time interval δt. The effect of finite temporal integration is then to cause a (positive) bias to the observed null depth. If the individual integrations are short enough compared to the typical fluctuation timescale, this bias can be kept to a very low level. Moreover, it could be at least partially calibrated via observations of reference stars. In the case of the PFN for instance, we use 2–10 ms individual integrations, to be compared with $\simeq$100 ms for the typical coherence time of atmospheric turbulence at K band. Using a Kolmogorov spectrum for the turbulence and using the PFN short baseline, we find for instance that the atmospheric phase rms is less than 1 nm over 10 ms, limiting the minimum null depth $\simeq 2 \times 10^{-6}$. Similarly, the intensity mismatch term follows atmospheric timescales, and its variance over 10 ms is not expected to cause any significant bias either. Laboratory nulling experiments with fiber nuller setups have already produced 10 ms nulls at the $\simeq 10^{-6}$ level with visible laser light (Haguenauer & Serabyn 2006) and 10^{-4} nulls with dual polarization broadband light over the full K band. In the latter case, dispersive and/or polarization effects are likely dominating the error budget, and the effect of finite integration is not found to play a role up to 50 ms. Finally, astrophysical nulls at the 0.001 (or even slightly lower) level have been measured on Vega with the PFN (B. Mennesson et al. 2011, in preparation), showing experimentally that temporal effects are at most at this level (and probably much smaller) on the PFN. The optimum individual integration time is thus a trade-off between sensitivity and dynamic range.

4.6. Chromatic Effects

Usually, interferometric/nulling observations are conducted over a finite spectral bandwidth. We concentrate here on the effects of the chromatic phase term, expected to dominate over the chromatic aspects of intensity or polarization mismatch. For a polychromatic observation, the phase error ($\Delta\phi(t)$) is the sum of the piston error calculated at the band center ($\Delta\phi_c(t)$) and the chromatic phase error ($\Delta\phi_\lambda(\lambda, t)$). Serabyn (2000) has demonstrated that the influence of these phase errors on a polychromatic null depth measurement is given by

$$N_\phi(t) = \frac{\Delta\phi_c^2(t)}{4} + N_{\text{chrom}}, \tag{24}$$

where $N_{\text{chrom}} = \int_{\lambda_{\min}}^{\lambda_{\max}} \frac{\Delta\phi_\lambda^2(\lambda,t)}{4}\, d\lambda$ is the chromatic null bias. So even in the case where the differential phase at the center of the band is zero, a positive bias is present (either constant or slowly varying, see below) and one measures $N_\phi(t) = N_{\text{chrom}}$. This additive bias directly impacts the astrophysical null depth measurement.

In the case of the PFN, this chromatic term is minimized by inserting glass plates of different thickness in each of the two beams. The chromatic bias is experimentally found to be lower than 10^{-4} in the laboratory. On the sky, the dispersive phase is no longer a strictly static term coming from the instrument. It is also impacted by differential atmospheric refraction across the band and varies over the night according to the target's position with respect to zenith. Detailed calculations are beyond the scope of this paper, but this effect is small ($<10^{-4}$) across the K band with the PFN short baseline when observing within 20° of zenith. Additionally, solutions exist to strongly reduce or completely eliminate this effect: disperse over several spectral bins, always orient the interferometric baseline perpendicular to the refraction direction (trivial on a single-dish interferometer with multiple sub-apertures), or use atmospheric dispersion compensators at the telescope. Moreover, this refraction effect is fortunately very repeatable and can be precisely calibrated by observing reference stars at the same zenith angle.

4.7. *Summary of Limitations*

The assumptions proper to the analytical method (Gaussian distribution of background and intensity terms, correlation issues) all seem individually valid in the case of the PFN. The analytical method also provides very similar results to those obtained by the numerical method, which makes fewer assumptions. The assumption that the differential phase follows a Gaussian distribution cannot be directly checked with the PFN data, but seems reasonable with respect to theoretical expectations.

Temporal and chromatic effects (as well as polarization effects, which we completely ignored for the PFN) may come into play at the 10^{-4} level, even more when considering the application to LBI which uses very long non-common beam paths. However, these systematic effects—slowly varying for the most part—can either be minimized by instrumental design or strongly reduced via observations of calibrator stars.

A more serious limitation to the reduction method presented is that its ultimate sensitivity may be limited by the small integration times needed to freeze the phase and intensity fluctuations. Infrared cameras with very low read noise will definitely help. Taking long sequences will also help, up to the point where systematics will dominate. More work is clearly needed to understand the trade-off between individual integration time, sensitivity, and final accuracy.

5. CONCLUSIONS

The theory of a new data reduction method for interferometric nulling (or visibility) observations has been presented in this paper. Based on the analysis of null distributions, this technique allows the retrieval of high dynamic range astrophysical null depth measurements, at contrast levels far exceeding the usual limits set by mean instrumental performance and fluctuations. The ultimate performance of this statistical data reduction depends on the specific design of the interferometric instrument and on the observing strategy. This technique is potentially applicable to any interferometric setup using a fringe tracking capability and any type of beam recombination (co-axial or multi-axial) into a single-mode waveguide. Applying our data reduction method to stellar observations obtained at the K band ($\simeq$2.2 μm) with the first-generation fiber nulling instrument installed at the Palomar 5 m (Hale) telescope, we demonstrated for the first time that: (1) deep and accurate nulling is not restricted to mid-infrared wavelengths but may be extended to the near-infrared domain, providing substantial gains in resolution and sensitivity and (2) nulling accuracies significantly lower than 10^{-3} (systematics and statistical errors included) can be achieved without any observation of calibrator stars. Although this remains to be further validated with an optimized instrument, simulations suggest that this new analysis will enable direct detection of faint structures at the $\simeq 10^{-4}$ level within the near diffraction limit of large AO-equipped ground-based telescopes, i.e., at angular separations ranging from $\simeq$20 to 150 mas. Implications for high accuracy LBI, both from the ground and from space, remain to be quantitatively explored. But since the statistical approach allows the detection of astrophysical signals well below the mean contrast level *and its rms fluctuations*, we anticipate that the instrumental stability requirements could be strongly relaxed. This implies that the constraints on intensity and phase fluctuations may be strongly reduced. This is a most attractive prospect for deep nulling interferometry from space. A similar statistical analysis may also be conducted successfully for regular coronagraphic instruments (Riaud & Hanot 2010).

This work was carried out at the Jet propulsion Laboratory, California Institute of Technology, under contract with the National Aeronautics and Space Administration. The data presented in this paper are based on observations obtained at the Hale Telescope, Palomar Observatory, as part of a continuing collaboration between Caltech, NASA/JPL, and Cornell University. We wish to thank the Palomar Observatory staff for their assistance in mounting the PFN and conducting the observations at the Hale telescope. The research was supported by the Fond National de la Recherche scientifique de Belgique (FNRS), by the Fonds pour la formation à la Recherche dans l'Industrie et dans l'Agriculture de Belgique (FRIA), and by the Communauté Francaise de Belgique-Action de recherche concertée-Académie Wallonie-Europe and by the Center for Exoplanet Science. The authors thank the referee for a careful review and for giving us relevant comments that helped to significantly improve the paper.

APPENDIX

CONFIDENCE INTERVALS AND COVARIANCE

In Section 2.3, we described our fitting strategies and developed the minimization process used to fit the distribution corresponding to an individual null sequence. The statistical error bar σ_{stat} on the derived astrophysical null depth is then determined by applying small fluctuations to N_a around its best-fit value. For every new value of N_a, the two other parameters ($\mu_{\Delta\phi}$ and $\sigma_{\Delta\phi}$) are adjusted to minimize the χ^2. As the number of degrees of freedom of our system is known and is $N_{\mathrm{bins}} - 4$, it is possible to calculate the $\Delta\chi^2$ relative to a certain confidence level. The error bars are generally evaluated for 1σ confidence levels, and so we use this criteria. σ_{stat} corresponds to the increment in N_a required to increase the reduced χ^2 from its minimum value χ^2_{min} to $\chi^2_{\mathrm{min}} + \Delta\chi^2$. For the data set obtained on α Boo with the PFN, the 1σ error bar corresponds to a very small χ^2 increment, $\Delta\chi^2 = 0.07$, and we find $\sigma_{\mathrm{stat}} = 3 \times 10^{-4}$ for the NSC (see Figure 11, left). Another way of calculating the error bars consists of using bootstrapping methods. We double-checked our confidence interval using this technique and found similar error bars ($\simeq 3 \times 10^{-4}$). This error bar takes into account the fitting noise that is not present for the ASC.

The central and right panels of Figure 11 represent the normalized χ^2 of our fits projected in two different parameters planes (i.e., N_a versus $\mu_{\Delta\phi}$ for the central panel and N_a versus $\sigma_{\Delta\phi}$ for the right one). The contours on these maps are displayed for increments of the χ^2 of $\Delta\chi^2 = 0.5$. These maps illustrate the covariance of the fits with the two free parameters: the mean and standard deviation of the phase error fluctuations. They show that relatively large variations on the fitted values of these phase parameters, between 0.05 and 0.1 rad, only produce a marginal effect on the measured astrophysical null, smaller than 10^{-3}, but produce very large effects on the fit quality. This result is important as it clearly illustrates the resilience of our approach to possible error on the assessment of the phase fluctuations.

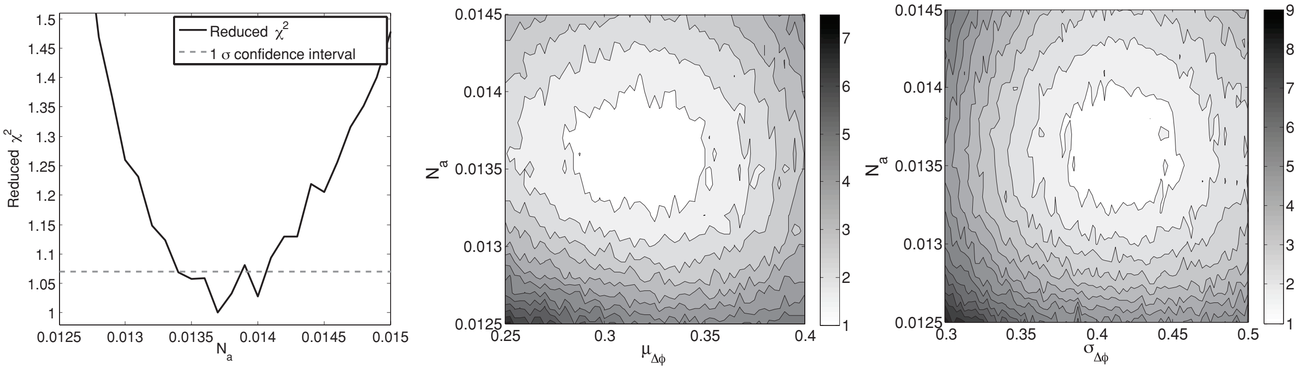

Figure 11. Left: variation of the reduced χ^2—measuring the goodness of the fit to the observed data—as a function of the astrophysical null depth N_a. The mean and standard deviation of the phase error are left as free parameters and adjusted to minimize the χ^2 for each new value of N_a. Center: projected χ^2 map of our model in the N_a vs. $\mu_{\Delta\phi}$ plane. For each point, $\sigma_{\Delta\phi}$ is chosen to minimize the χ^2. Right: same map but projected in the N_a vs. $\sigma_{\Delta\phi}$ plane. For these two maps, the contours are overplotted for each χ^2 interval of 0.5.

REFERENCES

Absil, O., den Hartog, R., Gondoin, P., Fabry, P., Wilhelm, R., Gitton, P., & Puech, F. 2006, A&A, 448, 787

Absil, O., den Hartog, R., Gondoin, P., Fabry, P., Wilhelm, R., Gitton, P., & Puech, F. 2011, A&A, in press (erratum)

Bracewell, R. N. 1978, Nature, 274, 780

Cagigal, M. P., & Canales, V. F. 2000, J. Opt. Soc. Am. A, 17, 1312

Claret, A., Diaz-Cordoves, J., & Gimenez, A. 1995, A&AS, 114, 247

Cochran, W. G. 1954, Biometrics, 10, 417

Colavita, M. M., et al. 2009, PASP, 121, 1120

di Benedetto, G. P., & Rabbia, Y. 1987, A&A, 188, 114

Haguenauer, P., & Serabyn, E. 2006, Appl. Opt., 45, 2749

Hinz, P. M., Angel, J. R. P., Woolf, N. J., Hoffmann, W. F., & McCarthy, D. W. 2000, Proc. SPIE, 4006, 349

Kervella, P., Coudé du Foresto, V., Segransan, D., & di Folco, E. 2004, Proc. SPIE, 5491, 741

Lacour, S., et al. 2008, A&A, 485, 561

Lay, O. 2004, Appl. Opt., 43, 6100

Martin, S., Serabyn, E., Liewer, K., Loya, F., Mennesson, B., Hanot, C., & Mawet, D. 2008, Proc. SPIE, 7013, 70131Y

Mayor, M., & Queloz, D. 1995, Nature, 378, 355

Mennesson, B., Haguenauer, P., Serabyn, E., & Liewer, K. 2006, Proc. SPIE, 6268, 626830

Mérand, A., Bordé, P., & Coudé Du Foresto, V. 2005, A&A, 433, 1155

Perrin, G., Coude Du Foresto, V., Ridgway, S. T., Mariotti, J., Traub, W. A., Carleton, N. P., & Lacasse, M. G. 1998, in ASP Conf. Ser. 154, Cool Stars, Stellar Systems, and the Sun, ed. R. A. Donahue & J. A. Bookbinder (San Francisco, CA: ASP), 2021

Press, W., Teukolsky, S., Vetterling, W., & Flannery, B. 2007, Numerical Recipes 3rd Edition: The Art of Scientific Computing (Cambridge: Cambridge Univ. Press)

Riaud, P., & Hanot, C. 2010, ApJ, 719, 749

Roddier, F. 1983, in European Southern Observatory Astrophysics Symposia, Vol. 17, ed. J.-P. Swings & K. Kjaer (Garching: ESO), 255

Rohatgi, V. 1976, An Introduction to Probability Theory Mathematical Statistics (New York: Wiley)

Serabyn, E. 2000, Proc. SPIE, 4006, 328

Serabyn, E., & Mennesson, B. 2006, in IAU Colloq. 200, Direct Imaging of Exoplanets: Science and Techniques, ed. C. Aime & F. Vakili (Cambridge: Cambridge Univ. Press), 379

5

A survey for companions in young stellar moving groups with AMBER

Contents

5.1 The AMBER instrument at VLTI 86
  5.1.1 The VLTI 86
  5.1.2 The AMBER instrument 87
  5.1.3 FINITO: a fringe tracker for the VLTI 89
5.2 Presentation of the scientific program 89
  5.2.1 Why using long baseline interferometry? 89
  5.2.2 Observing strategy 91
5.3 Survey status 93
  5.3.1 Methodology 95
  5.3.2 Results on a sample of early-type stars 96
  5.3.3 β Pictoris: a new hope 99

In the previous chapters, we have demonstrated – if necessary – how challenging the direct imaging of exoplanets can be. In this chapter, we show how ground-based long baseline interferometry can be complementary to other observation techniques to take images of faint off-axis companions at very small angular separations. We indeed propose to search for low-mass companions around nearby stars in well known young moving groups and associations. Thanks to the high angular resolution of the VLTI, we are able to probe regions very close to these stars where no other instrument can directly detect companions. The high accuracy of phase closure measurements with the AMBER instrument delivers a dynamic range up to five magnitudes. We first introduce the VLTI facility and the AMBER instrument that we have used to carry out our observations. We then explain our target selection process and derive the expected sensitivity of our survey, mostly in the brown dwarf regime and in a few cases down to the planetary regime. We finally give the current status of our survey and discuss the technical limitations that we have faced during this observing campaign.

5.1 The AMBER instrument at VLTI

Today, many scientific programs require the use of high angular resolution techniques such as the observation of active galactic nuclei (AGN), the direct imaging of circumstellar disks in the inner stellar regions around the stars, the detection of extra-solar planets or even the simple measurement of stellar angular diameters. In this respect, long baseline interferometry plays a central role in astrophysics as it provides a unique way to resolve very small astrophysical structures down to the milli-arcsecond level. In this section, we present a unique European interferometric facility, the VLTI, which is located in South-America and one of its instruments: AMBER. After a brief overview of their principle and performance, we will introduce FINITO, the three beams VLTI fringe tracker, which aims at reducing the fluctuating atmospheric-induced OPD.

5.1.1 The VLTI

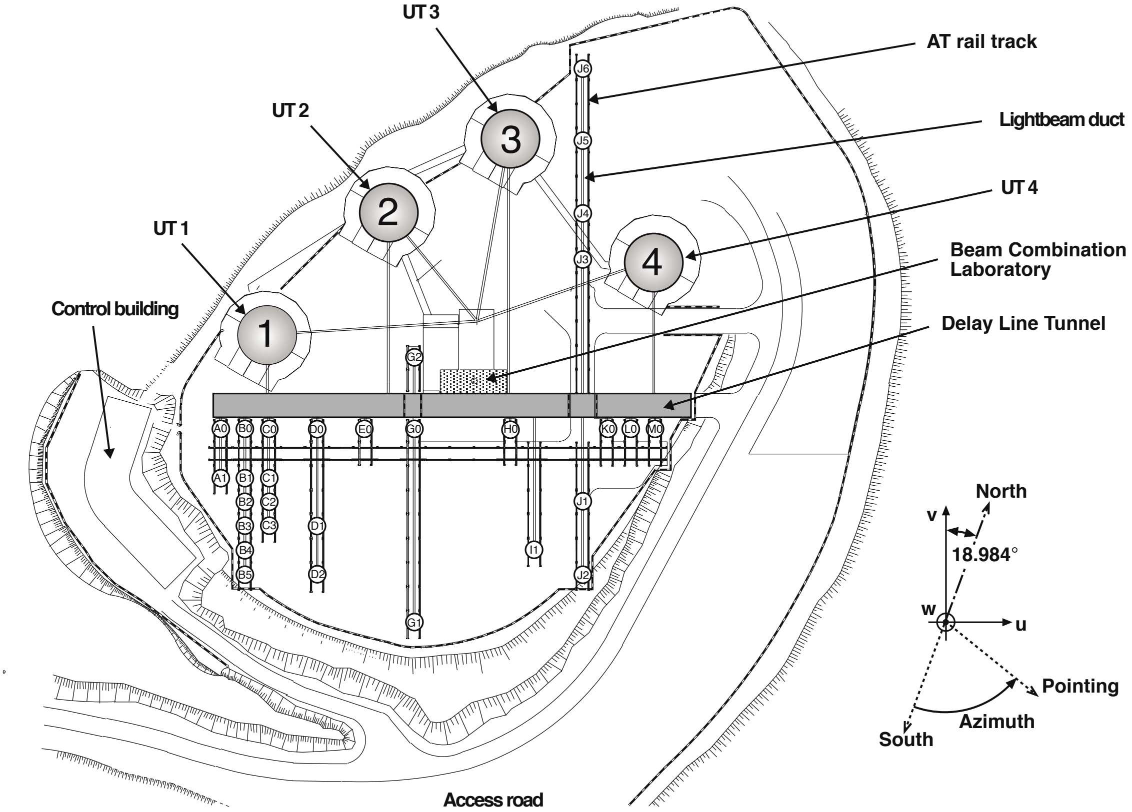

Figure 5.1: Map of the VLTI facility. The Unit Telescopes (UT) and the location of the Auxiliary Telescopes (AT) are represented by circles whose sizes are proportional to the diameter of the apertures. The AT rail tracks are represented by two bold parallel lines and the beam path by a single plain line. The subterranean tunnel is the grey rectangle at the center of the map just under the beam combination laboratory (rectangle filled with points). Image from ESO.

The Very Large Telescope Interferometer (VLTI) at the Cerro Paranal Observatory (Chile) is one of the world's largest and most advanced infrared interferometers. Built and operated by the European

Southern Observatory (ESO), it can currently combine together the light from either the four 8.2 m Unit Telescopes (UTs) or the four 1.8 m Auxiliary Telescopes (ATs). All the six baselines ranging from 47 m to 130 m are available with the UTs while the ATs can be combined among three configurations of four telescopes, ranging from compact (~ 20 m) to large (~ 130 m). Once fully deployed, the VLTI will provide a maximum angular resolution of ~ 2 mas in the K band using baselines up to 202 m in length.

The VLT Unit telescopes are based on alt-azimuth mounts. Their optical layout is of the Ritchey-Chrétien type and can therefore operate in either Cassegrain, Nasmyth or Coudé focus. The coudé focus is obtained by transferring one of the Nasmyth foci in the telescope basement by means of relay optics. It is from this particular focus that the light beams can be sent to the interferometric focus. Because the size of the the UTs is significantly larger than the atmospheric turbulent cells above Cerro Paranal, all of them are equipped with an adaptive optics system (MACAO, Arsenault et al. 2004)) that improves the overall performance of the facility. The auxiliary telescopes on the other hand have been designed specifically for interferometry and manufactured by *AMOS* (Belgium). Also based on alt-azimuth design, these telescopes are placed in ultra-compact enclosures, together with all necessary electronics and a complete temperature control system. Thanks to this design, the ATs can be relocated at 8 different observing positions (up to 30 when fully operational) allowing the interferometric baselines to be changed as a function of the various observing programs requirements. Unlike the UTs, the Auxiliary Telescopes are not equipped with AO but with a more simple tip/tilt correction device called STRAP (System for Tip-tilt Removal with Avalanche Photodiodes). However, a low order AO system (NAOMI) is under study in order to improve the performances of the ATs at shorter wavelengths (J band).

The light beams collected by the various telescopes are brought together by means of underground relay optics and coherently combined in the interferometric lab. Six of the eight delay line tracks are currently up and running, theoretically allowing for six beams to be combined at the same time. Two scientific instruments, AMBER and MIDI, are currently offered to the observers of the VLTI. A third one, PIONIER (Precision Integrated-Optics Near-Infrared Imaging ExpeRiment) is now available. This visitor instrument has recently produced its first on-sky fringes in October 2010 and combines for the first time at VLTI, the light from four telescopes simultaneously (Berger et al. 2010). It therefore significantly improves the *uv* coverage during the observations and will allow better images to be reconstructed from interferometric observations. Finally, PRIMA for Phase-Referenced Imaging and Micro-arcsecond Astrometry (Quirrenbach et al. 1998; Leveque et al. 2003) is currently in its commissioning phase and is designed to perform two simultaneous interferometric observations of two objects that are separated by up to 1 arcmin.

5.1.2 The AMBER instrument

AMBER is one of the first generation interferometric instruments at the VLTI. Designed to fulfill three key science programs that are young stellar objects (YSOs), active galactic nuclei (AGN) and hot giant extra-solar planets, this interferometer can recombine up to three beams with either low, moderate or high spectral resolution. After 6 years of development between 1998 and 2004, the instrument was installed at Paranal and obtained its first fringes in March 2004.

The principle of AMBER is to perform a multiaxial recombination of multiple beams that have been individually filtered by single mode fibers (see Figure 5.2). First, each individual light beam coming from up to three telescopes is injected into single-mode fibers. When injected into the fibers, the electromagnetic field is forced to follow the fundamental mode of the fiber; thereby rejecting all the turbulent modes of the atmosphere present in the input wavefront. The wavefront corrugations are translated into intensity and optical path difference fluctuations (see Section 3.3.4). The individual intensities at the output of each fiber are monitored in real time by extracting a fraction of their flux with a beam splitter before

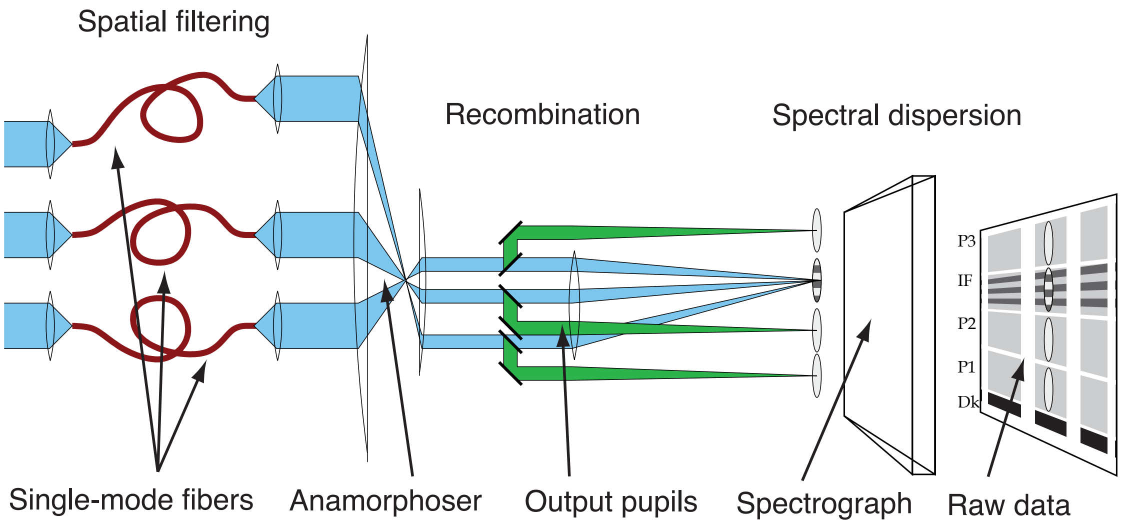

Figure 5.2: Schematic principle of the AMBER warm optics (from Petrov et al. 2007)). First, each beam is spatially filtered by single-mode optical fibers. At the fibers output, the beams are collimated and spatially re-organized in a non redundant scheme. The multiaxial recombination simply consists in focusing the three beams with a common converging optics. Thanks to a cylindrical optics anamorphoser, this fringed Airy disk is fed into the input slit of a spectrograph. In the focal plane of the spectrograph, each column of the detector contains a monochromatic image of the slit with 3 photometric (P1, P2, P3) zones and one interferogram (IF).

the beam combination (see Section 4.1.1). The beams then pass through anamorphic optics that make them highly elongated (this step is essential to optimize the flux passing through the spectrograph's slit). The third step consists in reorganizing the different beams to create non redundant baselines (i.e., the Fourrier transform of the individual baselines peaks at different frequencies). A common optics focuses the three beams onto a spectrograph slit that disperses the fringe pattern along one of the axes. The same spectral dispersion process is applied to the three photometric beams. The dispersed interferogram as well as the dispersed photometric channels are finally imaged onto an infrared camera which is divided into four different zones. Therefore, each column of the detector contains a monochromatic image of the slit with three photometric zones (P1, P2, P3) and the interferogram (IF), see Figure 5.2 .

AMBER has been designed to work from the J band to the K band (from 1.1 to 2.4 microns). However, since single-mode fibers cannot be fully efficient over such a broad wavelength range, the system has been replicated and optimized for these three wavebands (J, H and K). Three spectral modes are offered to the observers: (a) the High Resolution mode offers a spectral resolution $R = 12000$ and is only available in K band (HR-K), (b) the Medium Resolution mode ($R = 1500$) is available in both H and K bands (MR-H and MR-K), (c) finally, the Low Resolution mode allows the three wavebands J, H and K to be observed simultaneously with a spectral resolution $R = 35$.

The sensitivity of AMBER depends on various parameters such as the type of telescope being used (UTs or ATs), the spectral resolution and the use or not of a fringe tracking system during the observations. The magnitude limit under good conditions (seeing$< 0\farcs6$, clear sky) therefore varies between $K = 7.5$ with the low resolution mode on the UTs with group tracking and $K = 5$ for the highest spectroscopic resolution mode on the ATs with fringe tracking. Under such atmospheric conditions and after a rigorous calibration process, systematics on the visibility measurements in both H and K bands can be expected to be at the 2% level (Demory et al. 2009). Phase closures, which are less sensitive to the atmospheric conditions can also be measured with a very high accuracy. Indeed, Absil et al. (2010) have proven that RMS calibration errors down to 0.2° can be obtained with AMBER in medium resolution mode. A careful calibration plays a central role in the accuracy that can be achieved on these observables. Each scientific observation must be preceded and followed by the observation of a calibrator star in order to calibrate the so-called *transfer function* of the instrument (see Section. 4.1). This function gives an estimation of the relation at a time t between a raw (measured) observable and its real astrophysical value. The closer the time between the observation of the calibrator and the science star, the better the calibration.

5.1.3 FINITO: a fringe tracker for the VLTI

The two main issues that engineers and scientists have to face when designing and using interferometers are the sensitivity of the instrument and the rapidly fluctuating phase error between the various interferometer's arms. Because of their optical complexity, interferometers have usually a throughput of 1% at the most. As a consequence, they are limited to bright targets. The usual solution to increase the sensitivity of instruments consists in increasing the integration time in order to improve the SNR on the detector. Unfortunately, this cannot be used on interferometers without the use of a fringe tracker that temporally and spatially "freezes" the interference pattern. Without this device, the atmospheric turbulence introduces a rapidly fluctuating differential phase between the different beams. This differential phase makes the fringes of the interferogram jitter on the detector and therefore blurs their contrast as soon as an integration time longer than the atmosphere's coherent time is used. Fringe trackers are therefore extremely valuable instruments, especially for the higher spectral resolution modes, whose sensitivity are even more limited due to the fact that the fringes are dispersed over a larger number of pixels.

FINITO, which stands for Fringe-tracking Instrument of NIce and TOrino, is the VLTI three beam fringe tracker that operates in the H band (Gai et al. 2004; Le Bouquin et al. 2009a). Its basic principle is to modulate the optical path length of two of the three beams and process the resulting fringe scans in real time to measure the fringe phases at a frequency between 500 Hz and 2 kHz. An error signal is sent to the OPD controller which in return sends a correction signal to the delay lines. However FINITO can only operate in reasonably good observing conditions, i.e., when the seeing is below $1\farcs2$, the coherence time of the atmosphere τ_0 is above 2.5 ms and the airmass is under 1.5. And its limiting correlated magnitude is still low : from $H = 3$ to $H = 5$ with the ATs, depending on the conditions.

5.2 Presentation of the scientific program

Based on the characteristics of the AMBER instrument described in the previous section, we worked on finding a niche for the detection of faint off-axis companions (mainly brown dwarfs) with the VLTI. In this section, we first explain the interest of interferometry in performing a survey of faint companions and its complementarity with other observing techniques. Then, after explaining the observation strategy, we present the current status of the survey and its perspectives.

5.2.1 Why using long baseline interferometry?

Since the discovery of the first exoplanet by Mayor and Queloz in 1995, the science related to very low-mass companions around main sequence stars has become one of the most popular subjects in astrophysics. Tremendous efforts have already been made to detect and characterize exoplanets. Today, more than 500 exoplanets have been detected, mostly by radial velocity (RV) measurements. Many low-mass (sub)-stellar companions have also been found in the meanwhile. These surveys have however pointed out the under-abundance of bound brown dwarfs compared to giant planets at short separations. This phenomenon, called the “Brown Dwarf Desert”, is generally considered as the most obvious evidence

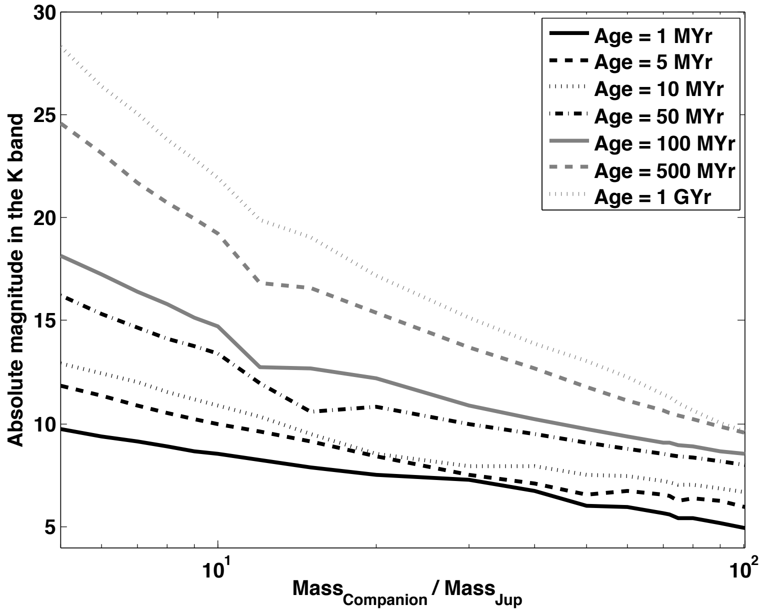

Figure 5.3: Mass-magnitude relationship for young (sub-)stellar objects at different ages. This diagram has been obtained using the evolutionary models for solar metallicity low-mass stars from Baraffe et al. (1998).

of different formation mechanisms for stellar binaries and planetary systems. This desert was however rather unexpected because free-floating brown dwarfs are very common (Kirkpatrick et al. 2000; Luhman et al. 2003; Chiu et al. 2006; Slesnick et al. 2006) and because standard models describing stellar-mass binary companions – either using the initial mass function (Kroupa 1995) or other processes (Duquennoy & Mayor 1991) – did not predict it.

Until now, two main techniques have proven to be sensitive to bound brown dwarfs: RV and adaptive optics (AO) aided by PSF subtraction techniques (such as coronagraphy). On the one hand, RV surveys are sensitive to brown dwarfs at "short" periods around mature main sequence stars ($\leq$ 3–5 AU, e.g., Marcy & Butler (2000); Grether & Lineweaver (2006)). On the other hand, AO surveys are sensitive to brown dwarfs at large angular separations ($>$ 30 AU, e.g., McCarthy & Zuckerman (2004); Carson et al. (2005); Metchev et al. (2008)). However, a large fraction of the giant planets and low-mass companions are suspected to be formed in between these two separation ranges. The circumstellar zone between 3 and 30 AU around nearby stars (20-50 pc) is difficult to reach because imaging these high contrast binaries requires a high angular resolution, a small inner working angle and a high dynamic range. For instance, a 50 M_{Jup} brown dwarf at 15 AU from a nearby solar-type main sequence star would have a contrast ranging between 10 and 15 magnitudes at a separation smaller than $1''$. Two solutions to these challenges have recently emerged: infrared interferometry for the high angular resolution, and nearby young moving groups for the high contrast. Indeed, according to the stellar atmosphere models based on a "hot start" scenario (see Introduction, Baraffe et al. 1998, 2002), the absolute K magnitude of a 20 M_{Jup} object is $M_K = 8.3$ at 10 Myr whereas $M_K = 17$ at 1 Gyr (see Figure 5.3). Moreover, young moving groups are located closer to the Sun and are slightly older than the main star forming regions, which reduces the chances to face bright circumstellar disks and gives enough time for planets to form.

A first step in this direction has been taken by Kraus et al. (2008), who have recently used non redundant aperture masking to achieve the full diffraction limit of a single 10-m Keck telescope. In doing so, they have detected 12 new stellar and sub-stellar companions around young stars in the nearby OB association Upper Scorpius. The range of separations that can be reached with this instrument is between $0\farcs03$ and $0\farcs5$ (i.e., between 4 and 70 AU for UpSco). What we propose here is to complement such a

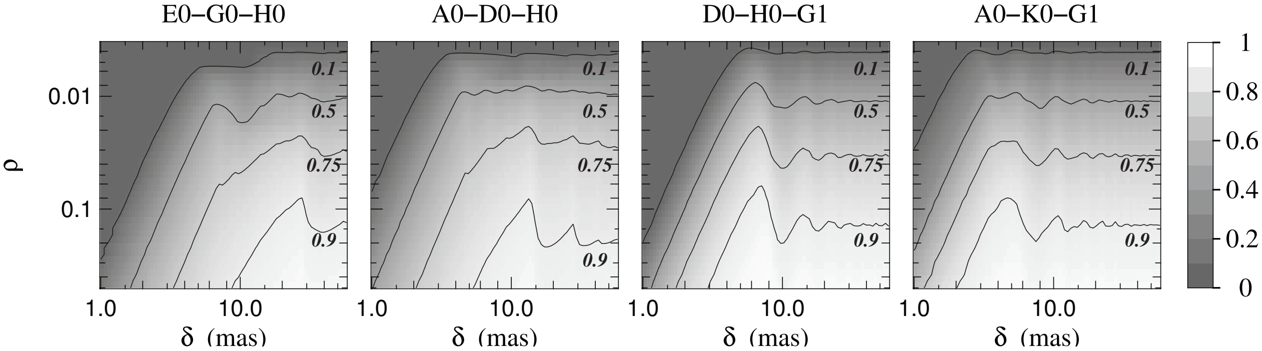

Figure 5.4: Detection efficiency (grey scale + contours) for off-axis companions as a function of the companion contrast ρ (y-axis) and the search area size δ (x-axis), assuming a closure phase accuracy $\sigma_\phi = 0.5°$ (recently demonstrated by Absil et al. (2010) with AMBER on the ATs). Contours have been plotted for detection efficiencies of 0.9, 0.75, 0.5 and 0.1, using four baseline triangles on the VISA array. The detection probability at a contrast of 5 magnitudes (1:100) is about 50% for all configurations at angular distances above 5 mas. The longest triangle (A0-K0-G1) has the best performances at shorter angular separations (maximum detection efficiency down to 3 mas). Courtesy of J.B. Lebouquin.

survey by looking for stellar and sub-stellar companions around young stars in the Southern hemisphere, where most young moving groups reside. Using the VLTI instead of non redundant aperture masking will improve the angular resolution by a factor 10, while achieving the same dynamic range (∼ 1:100). It is therefore designed to be sensitive to brown dwarfs from 3 milli-arcsec to $0\farcs2$ (see Figure 5.4), which means typically from 0.1 AU to 10 AU (at 50 pc) in terms of orbital radii. This survey is complementary to both non redundant aperture masking and AO surveys, which cover larger angular separations up to hundreds of AU. As already stressed in Section 1.3 such a survey is not redundant with RV techniques either, which are generally not well suited to study the young (and therefore active) stellar objects considered here due to the poor spectro-photometric stability of such stars.

5.2.2 Observing strategy

The goal of the observing program we are conducting is to look for high contrast (sub-)stellar companions close to young nearby stars using AMBER on the ATs. We use for that closure phase measurements as they are particularly sensitive to asymmetric brightness distribution while being immune to atmospheric turbulence. We use the MR-K mode as it currently provides the best stability on closure phase measurements (0.2° recently demonstrated by J.-B. Lebouquin on the ATs, see Figure 5.5 and by Absil et al. (2010)). Furthermore, since we observe with the longest available baselines (A1-G1-K0, 129 m), it is suspected that some companions will be strongly resolved so that the phase closure information will be rapidly modulated over the K band. The use of AMBER in its medium resolution mode (MR-K) should prevent the signal from being undersampled (which is not guaranteed in LR mode). Finally, we will use phase- or group-delay tracking with FINITO, which increases both the closure phase stability and the SNR as the fringes are present on every single frame. For our (rather faint) targets, we expect an overall closure phase accuracy of 0.5°, which translates into a typical reachable contrast of 1:100 (see Figures 5.4 and 5.6). Our program is ambitious and some of our targets reach the sensitivity limits of AMBER on the ATs. This is however a price to pay to optimize the detection threshold of our survey.

Our targets are chosen among young moving groups, using as a main constraint the limiting magnitude of AMBER on the ATs ($K \leq 5$). This restricts our programme to the closest moving groups accessible from Paranal:

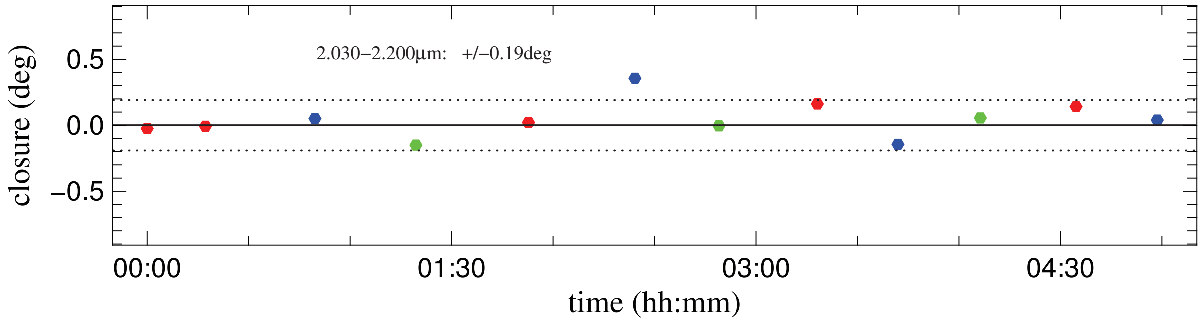

Figure 5.5: Stability of closure phases with AMBER for 3 stars with $K \simeq 3$ observed by J-B Lebouquin using the ATs. It is clear on this figure that a closure phase accuracy of $\sigma_\phi = 0.2°$ is realistic for stars around $K = 3$. The stars in our list are fainter with $K \simeq 5$, which means a factor of 6 in terms of flux. If we are limited by photon noise, this also means that the accuracy on the phase will be reduced by a factor of $\sqrt{6} \simeq 2.5$. Therefore, we can consider that a $\sigma_\phi = 0.5°$ is achievable.

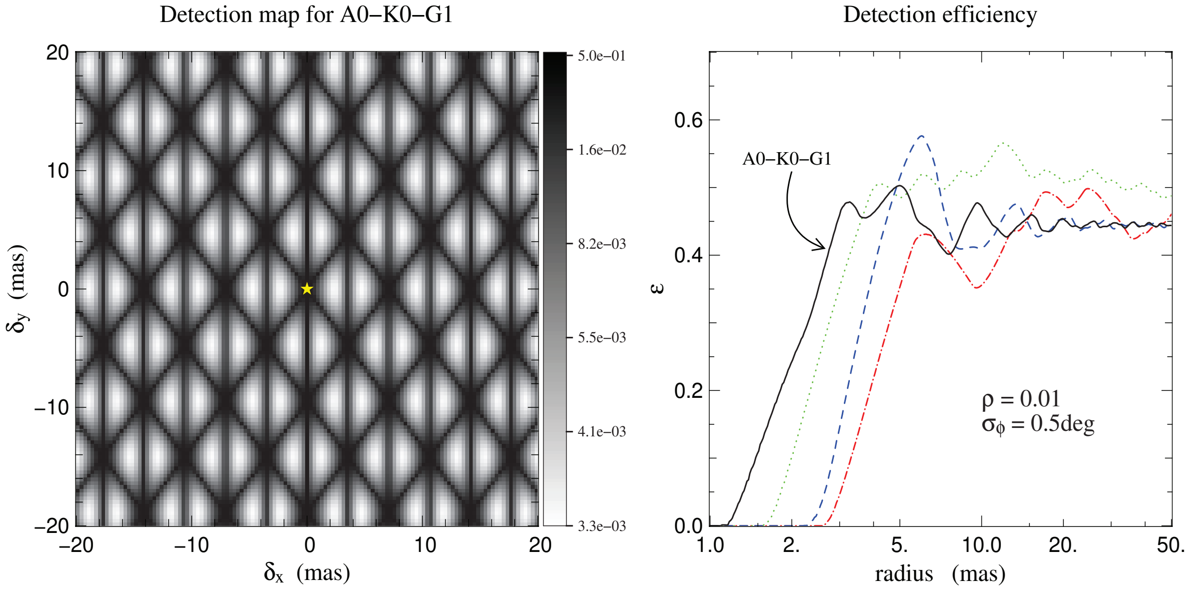

Figure 5.6: *Left*: Cartesian representation of the detectable companion contrast as a function of its position for a similar array as the one we used for our observations. The regions where the faintest companions can be detected (∼ 1:300) are displayed in white for a closure phase accuracy of $\sigma_\phi = 0.5°$. *Right*: Detection efficiency versus companion separation, assuming a flux ratio ρ of 1:100 and a closure phase accuracy of $\sigma_\phi = 0.5°$.

- *β Pictoris moving group*: composed of 47 candidate stars (Torres et al. 2008) with $K = [3.5 - 6]$, includes a ∼ 35 M_{Jup} brown dwarf. Estimated age: 12 Myr.
- *Tucana-Horlogium association*: composed of 42 high probability members with $K = [2.5 - 5.5]$, estimated age of ∼ 30 Myr.
- *AB Doradus moving group*: relatively old association (∼ 70 Myr), composed of 37 proposed members with $K = [4.5 - 6.7]$.
- *ϵ Chameleontis association*: composed of 12 members with $K = [4.6 - 5]$, with an estimated age around 5 Myr.
- *Hercules-Lyra moving group*: Oldest moving group in our sample, with an estimated age of 200 Myr, is composed of stars with $K = [3.8 - 6.4]$.

A total of 23 targets with K = [3.5-5.5] have been selected according to our criteria with only 3 of them

Name	Sp. type	Dist. [pc]	Mov. group	Age [Myr]	K_{mag}	Sensitivity [M_{Jup}]
HD 166	K0 V	13.7	Her - Lyr	200	4.3	>200
HD 203	F2 IV	39.1	β Pic	12	5.2	70
HD 3003	A0 V	47	Tuc - Hor	30	5.0	90
HD 12894	F2 V	47.2	Tuc - Hor	30	5.5	112.5
HD 17332	G0 + G5	32.6	AB Dor	50 - 70	5.5	100 - 130
HD 25457	F5 V	19.2	AB Dor	50 - 70	4.2	110 - 140
HD 35850	F7/8 V	26.8	β Pic	12	4.9	45
HD 36705	KI	14.9	AB Dor	50 - 70	4.7	70 - 90
HD 39060	A5 V	19.3	β Pic	12	3.5	73
HD 45270	G1 V	23.5	AB Dor	80 - 150	5.0	90 - 120
HD 48189	G1.5 V	21.7	AB Dor	80 - 150	4.5	105 - 125
HD 104174	B9 Vn	95	ϵ Cha	5	5	150 - 180
HD 104237	A pe	95	ϵ Cha	5	4.6	190 - 220
Gj 560b	K5 V	16.4	Her - Lyr	200	5.5	>200
HD 139664	F5 V	17.5	Her - Lyr	200	3.8	>200
HD 146624	A0 (V)	43.1	β Pic	12	4.7	100
HD 155555	K1 VP	31.4	β Pic	12	4.7	70
HD 195627	F0 V	27.6	Tuc - Hor	30	4.8	85
HD 196982a	M4 Ve	9.5	β Pic	12	4.9	13.5
HD 196982b	M4 Ve	9.5	β Pic	12	4.9	13.5
HD 197481	M1 Ve	9.9	β Pic	12	4.5	15
HD 206860	G0 V	18.4	Her - Lyr	200	4.6	>200
HD 213845	F7 V	29.7	Her - Lyr	200	4.3	>200

Table 5.1: List of the 23 targets with $K < 5.5$ for a survey of young stars in moving groups. For each target, its spectroscopic type, distance, age, the moving group it belongs to and the K magnitude are summarized. An estimation of the sensitivity we can reach to off-axis companion is also computed for each target based on the COND evolutionary models (Baraffe et al. 1998, 2002).

having K > 5. Based on our expected closure phase accuracy, we have computed the lowest detectable companion mass (see Table 5.1) using the evolutionary tracks of Baraffe et al. (1998, 2002). In the most favorable cases, we should reach 13 $M_{\rm Jup}$, which corresponds to the limit between the brown dwarf and planetary regimes.

The final objective of this survey consists in two main points. First, we will study the *multiplicity of low- and intermediate-mass stars at young ages*. In particular, we will study the effect of age on the distribution of periods for sub-stellar objects. Interferometry could bring a decisive input in that context as it provides maximum sensitivity in the separation range where most bound brown dwarfs are supposed to be formed (if they follow standard binary star formation models). Secondly, we will *put into test theoretical evolution models for low-mass objects*. Thanks to the medium spectral resolution of AMBER, we will on the one hand obtain first estimations of the fundamental parameters of the detected companions (effective temperature, surface gravity) that can be used to constrain models. On the other hand, since the potential companions will have rather short periods (typically < 10 yr), we will be able to directly deduce the dynamical masses of the central star and its companion by following up the orbital motion at different phases. This will bring a much-needed absolute calibration for evolutionary models.

5.3 Survey status

Within our sample of 23 targets, 12 are observable during Spring and the rest in Fall. Based on extrapolations from previous AO and micro-lensing surveys, we expect to detect between 0 and 4 low-mass companions. Three observing runs have already been awarded to this program in the past two years,

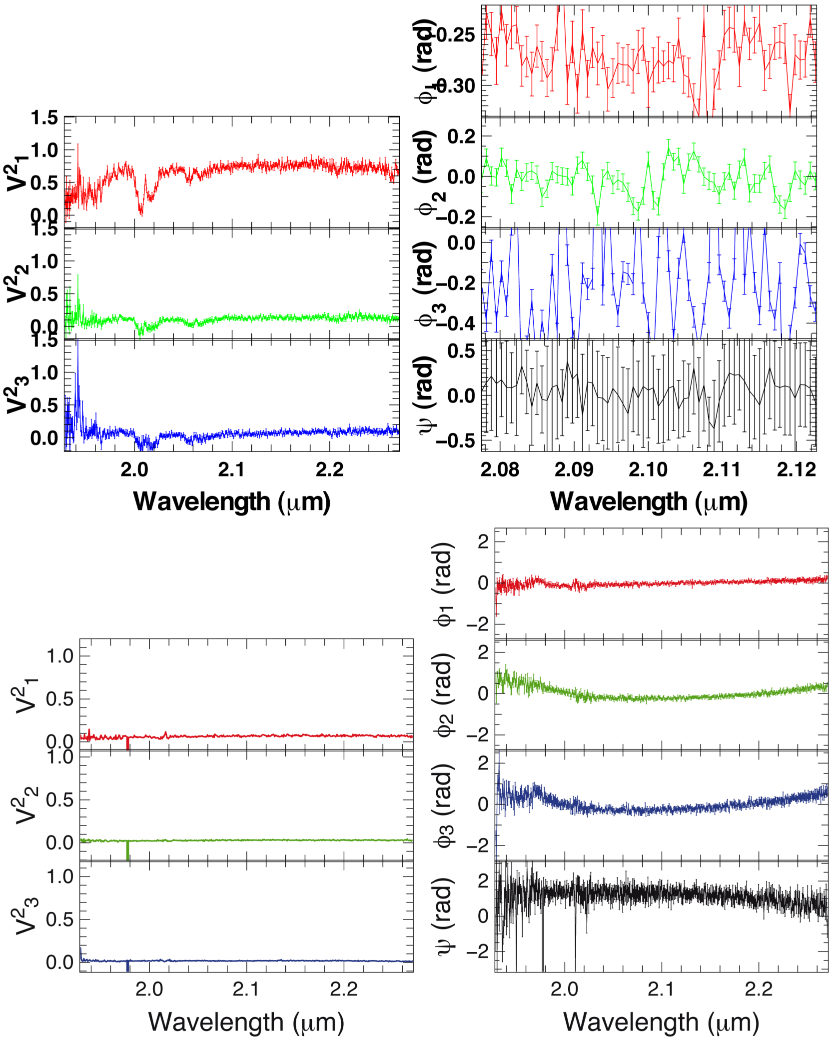

Figure 5.7: *Top*: Data of HD36705 (K = 4.7) illustrating the technical problem encountered with AMBER during the whole P84 run. One of the three delay lines (#3) was not properly working. As a result, the visibilities of the baseline using this delay line are below 10% (V_2^2 & V_3^2). Therefore, the corresponding error on the measured phase is close to 30° in the worst case which makes the closure phase technique useless. The phase stability on the working baseline ($\phi 1$) is $2-3°$ rms and the error bar is even lower ($\sim 1°$), which would be sufficient to meet our goals. *Bottom*: Data of HD138716 (K = 2.2) illustrating the quality of the data obtained during the whole P85 run on a very bright backup target. The V^2 around zero is the consequence of technical problems encountered with FINITO. Indeed if the fringes are not tracked properly during the observations, they are blurred and their visibilities rapidly drop.

in P84 (November 2009), P85 (June 2010) and P86 (November 2010). Unfortunately, the first 9 nights have not been successful at all, due mainly to weather losses and technical issues.

Figure 5.7 illustrates the effect of the technical problems during P84 (top panel) and P85 (bottom panel) on the quality of our data. Indeed, a low level data reduction shows that, during the P84 run, the visibilities for two of the three baselines are systematically under 10% while the third one is well above 50%. This is due to a tracking problem of delay line #3 which could not stabilize the OPD on two baselines. The contrast of the fringes being poor on these two channels, the corresponding errors on phase measurements are huge (30° for the worst channel, see Figure 5.7, top) while it is of only $2-3°$ rms for the only working baseline. As the closure phase accuracy is directly proportional to the individual phase errors, this observable on which our observing strategy is based, cannot be exploited. In P85, half of the observing time has been lost due to weather conditions (telescopes closed). During the other half, a large number of technical problems have also been encountered among which glitches on DL #5 and 6 and numerous AT4 reboots that finally led us to a baseline change (A0-K0-I1). The technical problems encountered with FINITO have also led to a blurring of the fringes. These technical issues have led to very bad SNR in our datasets with visibilities close to zero on the three baselines while the observed targets are unresolved. Once again, the consequence of poor signal quality is directly translatedinto the accuracy on the phase measurements (see Figure 5.7, bottom). Finally, our last run of November 2010 has also been catastrophic because of weather conditions. For one of the 3.5 nights, the telescopes were closed because of high humidity and wind. The rest of the time, the conditions were of poor quality with the seeing ranging between $1\farcs5$ and $4\farcs5$ and fluctuating rapidly.

Besides our observing program, G. Chauvin (who is also co-investigator of our program), has led an observing campaign that ended in P81 and that was focusing on young main sequence stars with spectral types earlier than F. The brightness of the targets that he has selected was similar to ours with $K = [2.5 - 5]$. Using the data analysis tools that we have developed for our survey, we have undertaken the analysis of this data set. The results that we obtained with this observing campaign are presented in Section 5.3.2.

Starting in Fall 2011 (P88), our program will be pursued with the PIONIER visitor instrument at VLTI. The latter is designed to reach very high accuracies on both visibility and closure-phase measurements and will improve our sensitivity to sub-stellar bounded companions. Even though it has only been recently commissioned, this instrument has already proven its stability since accuracies of $0.1° - 0.2°$ on the phase closure have recently been demonstrated by J.-B. LeBouquin on the ATs. Moreover, the sensitivity of PIONIER is significantly improved compared to AMBER as stars with magnitudes of $K < 6.5$ can be observed in the high precision mode of the instrument. The interferometric observations of our 23 sources, augmented with the 11 that have already been observed by G. Chauvin et al., will provide a first statistical estimation on the presence of brown dwarfs orbiting close to their parent stars. Most of these objects have been or will soon be observed by AO, which will complete our survey for larger orbital radii and thereby provide a complete and unique database on the brown dwarf desert for orbital separations from 0.1 AU up to a few hundreds AU.

5.3.1 Methodology

The interferometric program we proposed with AMBER is challenging because we use the instrument on relatively faint objects and because we need to reach high precisions on the closure-phase measurement. For such a demanding program, the method used to reduce and analyze the data is crucial. A detailed description of the data reduction strategy is out of the scope of the present work and we focus in this section on the data analysis part. The method used to constrain the presence of an off-axis point source from phase closure measurements is the following. First, the field-of view of the instrument is calculated. For AMBER on the VLTI, it is mainly limited by the use of single-mode fibers and depends on the atmospheric turbulence. Based on the mean observing conditions during the run ($\sim 0\farcs8$), the analysis is limited to angular separations smaller than a certain value defined by the separation at which the off-axis transmission is divided by 4 with respect to the on-axis transmission. Unfortunately, another element limits even more the field-of-view: time smearing, which is due to phase variations induced by the Earth's rotation. This effect is increasingly restrictive as the observing time required to get one data point increases. Second, the spectral resolution is tuned (re-binned) in order to average the fluctuation of the phase measurements and decrease the error bars. During this step, it is however important to keep the spectral resolution high enough to make sure that the spectral variations of the phase due to the presence of a potential companion within the FOV are properly sampled. For a 50 mas field-of-view and an observing wavelength range comprised between 2.00 and 2.26 μm, the appropriate bin size

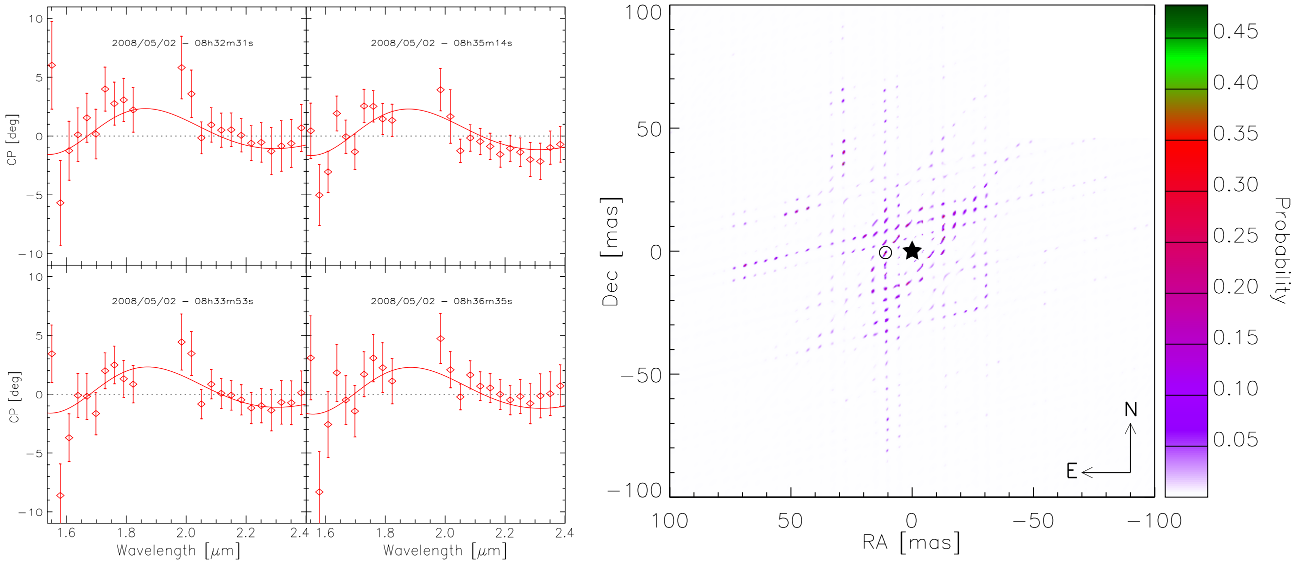

Figure 5.8: *Left*: Representation of the whole data set (with error bars) obtained on α Pav and of the best-fit model (red curves) found on a 100 mas radius FOV. This model corresponds to a companion with a contrast of 1.5×10^{-3} located at Cartesian coordinates ΔRA = 11 mas and ΔDec = −0.6 mas relative to the central star. *Right*: Probability of a binary model to reproduce our data set, for various positions of the secondary companion across a 100 mas radius FOV.

is 50 nm which leads to the definition of 5 spectral channels inside the waveband. Third, a complete screening of the FOV is achieved in order to identify the possible closure phase signature of an off-axis companion. For that, a fake companion is added to the photospheric model of the observed star (di Folco et al. 2004) at various locations within the FOV and with different contrasts with respect to the primary. The χ^2 distance between the model and the observations is then measured for each of these locations (Figure 5.8, left). The χ^2 map is then built by selecting the best companion contrast minimizing the residual error at each location. This map is then converted into a probability map using probability distribution functions (Figure 5.8, right). From this map, the most probable solution/position can be found and compared to a model with the central star alone in order to infer the significance of the detection. Finally, in case of non detections, sensitivity limits can be derived from the χ^2 map (or equivalently, probability map), by searching at each point of the FOV for the companion contrast that would produce a χ^2 larger than a pre-defined threshold, set to 3σ significance level in our case. Once the upper limit to the detectable companion contrast is computed at each point of the FOV, global sensitivity limits can be built by inspecting the histogram of the 3σ detection levels across the considered FOV. Figure 5.10 illustrates, with data obtained on β Pictoris, a comparison between the derived sensitivity of AMBER as a function of the angular separation and those provided by radial velocity and adaptive optics techniques.

5.3.2 Results on a sample of early-type stars

Our program focusing on the detection of companions around young late-type stars has not given results yet because of the poor observing conditions and numerous technical problems during our observing nights. However, a similar program focusing on earlier-type stars (A- to F-type stars) and led by French colleagues from IPAG (Grenoble) has been more successful. They selected a sample of 12 young stars (12 − 30 Myrs old) among the Tucana-Horlogium and β Pictoris moving groups with K magnitudes ranging between 2.5 and 5. Several observing nights have been obtained during 2008 (P81 and P82),

Name	Sp. type	Dist. [pc]	Mov. group	Age [Myr]	Companion	Upper limit
51 Eri	F0 V	29.8	β Pic	12	?	4.4%
α Pav	B2 IV	56.3	Tuc - Hor	30	?	1.6%
β 01 Tuc	B9 V	42.9	Tuc - Hor	30	?	3.6%
β 02 Tuc	A2 V	53.0	Tuc - Hor	30	Y	N/A
ϵ Hyi	B9 V	47.1	Tuc - Hor	30	N	2.3%
η Tel	A0 V	47.8	β Pic	12	/	/
η Tuc	A1 V	48.8	Tuc - Hor	30	N	5.0%
HD 172155	A7 V	29.3	β Pic	12	/	/
HD 207964	B2 IV	46.5	Tuc - Hor	30	Y	N/A

Table 5.2: List of the 9 targets observed by Chauvin et al. in 2008. For each star, we specify whether a companion is detected, using "Y" for a detection, "N" for a non-detection and "?" when the result is doubtful. For all the non-detections and doubtful cases, the upper limit of the companion contrast is also given. This upper limit corresponds to the lowest contrast (relative to the central star) that an off-axis companion can have before being incompatible with the data (with a 3σ confidence level).

and 9 of the 12 targets have been observed with AMBER in the low resolution spectroscopic mode. In this section, we present the results of our analysis of the data obtained for these stars and the constraints we derive on the presence of companions in their innermost stellar environment ($\sim$ 0.2 – 8 AU). The presence of several known binaries is being confronted to our observations and sensitivity maps to off-axis companions are derived for all sources. The list of observed stars is summarized in Table 5.2. For each target, we provide the basic physical properties (distance, age, type) and we specify whether a companion is detected from our data or not. When no detection is reported, we also give an upper limit to the contrast of a companion in the field of view. These upper limits are calculated based on a 3σ confidence level. Based on our results, we demonstrate the ability of AMBER to detect companions having contrast ratios, with respect to their primary star, down to the 10^{-2} level. In the next paragraphs, we briefly discuss the results obtained on each source.

51 Eri

51 Eri is a F0 V star having a magnitude $K = 4.5$ and located in the β Pictoris moving group (Zuckerman et al. 2001; Zuckerman & Song 2004; Lépine & Simon 2009). No giant planet with a mass $> 4M_{\mathrm{Jup}}$ is present beyond $1''.4$ (Heinze et al. 2010) and no disk has yet been detected (Rebull et al. 2008). The closure phase data display spectral variations which could be explained by the presence of a companion. However, our single data point is not sufficient to differentiate this signature from observational systematic errors and we suspect that the error bars may be overestimated because the χ^2 are well below 1. We derive an upper limit to the contrast of a companion within 100 mas of 51 Eri of 4.4%. To compute this limit, the error bars have been modified to artificially set the χ^2 to unity for the solution with no companion in the FOV. The solution minimizing the χ^2 corresponds to a companion with a contrast of 3.2% located 25 mas away from the central star. This solution is possible but the contrast is below the detection limit for this target and the position cannot be constrained.

α Pav

α Pav (Peacock) is a bright ($K = 2.4$) spectroscopic binary located in the the Tucana-Horlogium MG (Zuckerman et al. 2001; Zuckerman & Song 2004). Halbwachs (1981) estimated the maximum separation between the two stars to be 2.6 mas with a mass ratio < 0.1. Our measurements display accurate closure phase measurements with error bars down to 1° on average. Very small variations of the closure phases are observed. The data are compatible with both non-detection and a companion with a contrast

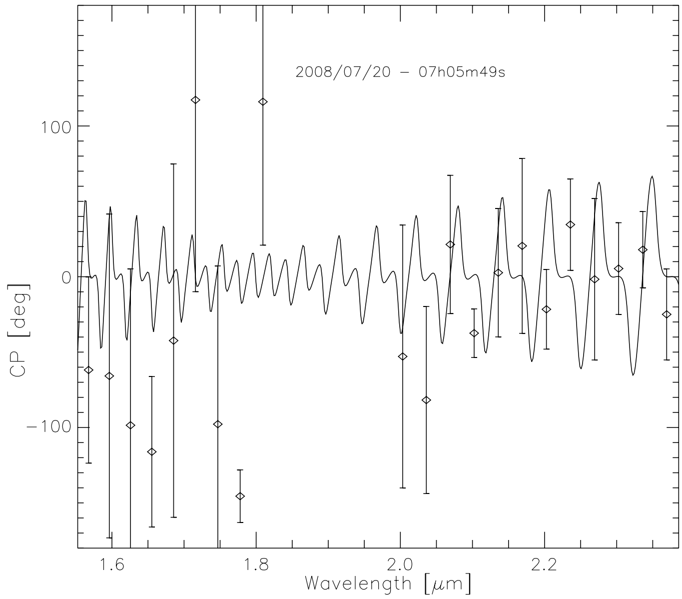

Figure 5.9: Representation of a relevent observation block (with error bars) obtained on β 02 Tuc and of the best-fit model (black curves) found on a 200 mas radius FOV. The closure phase signal fluctuates rapidly with an amplitude > 100°. This clearly indicates the presence of a companion of similar magnitude as the primary and located at a large angular separation. Based on this figure, we cannot guarantee that the closure phase spectral variations are properly sampled.

ratio of $\sim 2\%$. However, the χ^2 map displays numerous possible solutions within 50 mas of the primary but no estimation of the position can be given. The upper limit for this star is at the 1.6% contrast level.

β 01 Tuc

β 01 Tuc ($K = 4.5$) belongs to the Tucana-Horlogium MG (Zuckerman et al. 2001; Zuckerman & Song 2004). This system is composed of 6 stars. No companion with a mass $> 44 M_{\rm Jup}$ has been found by RV measurements around the primary up to orbital periods of 100 days (Lagrange et al. 2009a). Our K band measurements are stable and display a small offset of the closure phase with respect to zero. The H band data on the other hand are significantly noisier. An upper limit of 3.6% is found within our field of view (separations < 100 mas). The best solution is found by placing a companion with a contrast of 3.4% at a angular distance of $\sim$ 9.5 mas, but the significance is too low to confirm the detection.

β 02 Tuc

β 02 Tuc is a visual binary composed of an A2 V primary ($K = 4.1$) and an A7 V to F0-1 V secondary. They are separated by 0.″38 to 0.″58 (Neuhäuser et al. 2003; Tokovinin & Cantarutti 2008) and have similar magnitudes ($\Delta V = 1.2$). The binary is clearly resolved by our AMBER observations (see Figure 5.9). However, because the secondary is at the outer edge of the FOV and because we use the low spectral resolution mode, we are not sampling sufficiently the closure phase spectral fluctuations. Moreover, because of the large separation between them, the fringe packets corresponding to the two sources might be spatially separated which would make our standard reduction method unreliable. Additional work is required to properly analyze these data.

ϵ Hyi

ϵ Hyi is a B9 V star with $K = 4.2$ and belonging to the Tucana-Horlogium MG (Zuckerman et al. 2001; Zuckerman & Song 2004). Our data are compatible with the absence of companion, and set an upper limit of 2.3% on the companion contrast.

η Tel

The data we have obtained on η Tel are not of very good quality and are difficult to interpret. No result can be given yet and an additional effort must be put on the data reduction.

η Tuc

η Tuc is a relatively faint star for AMBER ($K = 4.8$), and is located in the the Tucana-Horlogium MG. The presence of companions in the innermost region around this star is somewhat controversial. Indeed, astrometric measurements obtained with the Hipparcos satellite (Eggleton & Tokovinin 2008), and a potential IR excess detected by IRAS faint source catalogue (Mannings & Barlow 1998) seem to suggest the presence of a bound companion. Lagrange et al. (2009b) have used RV techniques to give a $19 M_{\rm Jup}$ upper limit on the presence of potential companions with period shorter than 100 days and Neuhäuser et al. (2003) and Ehrenreich et al. (2010) did not detect any off-axis source in AO-assisted images at larger separations either. Our data do not show any evidence for the presence of a companion in the direct vicinity of η Tuc (< 100 mas). However, our upper limits are relatively weak with contrast limits at the 5% level.

HD 172155

The data obtained on this star are difficult to analyze and some additional work must be done on the data reduction aspect.

HD 207964

HD 207964 is a visual binary system similar to β 02 Tuc. The separation between the two stars is about $0\farcs31$ (WDS catalogue) and the contrast between them is low ($\Delta V = 0.2$). Like for β 02 Tuc, the signature of the binary is clearly detected but is at the outer edge of the FOV and might be undersampled or corrupted by the non-optimal data reduction process for such a kind of systems. More work is required.

5.3.3 β Pictoris: a new hope

The aforementioned results obtained on early-type stars with AMBER during 2008 are encouraging but limited due to the low number of available data points per target and to the relatively poor observing conditions. By adding more data points, it is possible to both improve the precision on the closure phase measurements (and therefore the contrast) and increase the *uv* coverage, which helps in constraining the position of the object. In this section, we present the precisions that can be achieved under optimal circumstances (good weather, large number of data points).

Absil et al. (2010) have recently observed with AMBER the well known young main sequence star β Pictoris. This young (12 Myr, Zuckerman et al. (2001)), nearby (19.3 pc) and bright ($K = 3.5$) star

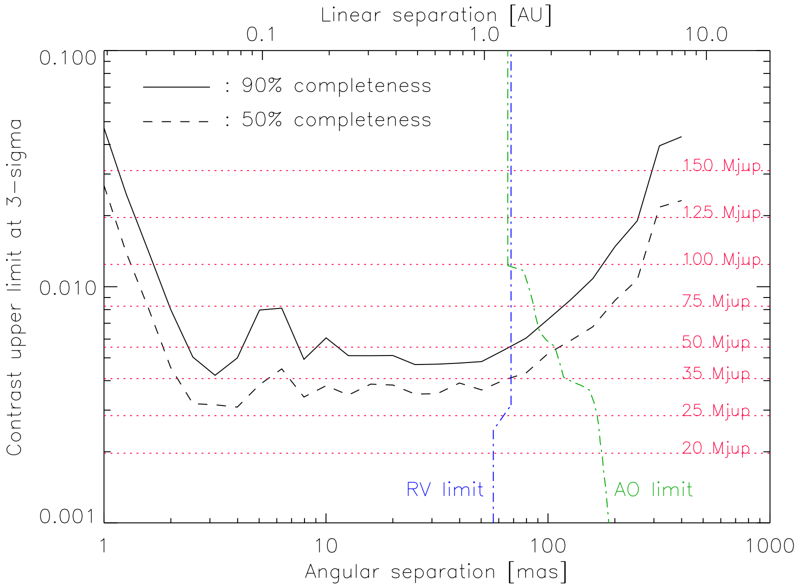

Figure 5.10: Sensitivity curves showing the 3σ upper limit to the contrast of off-axis companions as a function of the angular separation for 50% and 90% completenesses. The translation of these contrasts into masses has been done using the COND evolutionary models (Baraffe et al. 1998, 2003). The discovery spaces of RV and AO observations have been calculated based on the works of Galland et al. (2006) and Boccaletti et al. (2009), respectively. Figure from Absil et al. (2010).

is a perfect target for interferometry and is famous because it is surrounded by an extrasolar planetary system composed of a recently imaged exoplanet (Lagrange et al. 2009b, 2010) and an optically thin debris disk (Smith & Terrile 1984; Heap et al. 2000). Absil et al. (2010) have used these observations, initially aimed at analyzing the planetary system spin-orbit orientation, to look for companions in the innermost region of the system (< 6 AU).

The data obtained on β Pic have been acquired during four different nights from 2010 January 24 to 28 with AMBER in medium spectral resolution mode. A total of 12 observing blocks (OBs) were completed. However, to decrease time smearing effects and optimize the instrument FOV, these blocks have been divided into 26 OBs to reduce their lengths to 15 min. Even then the FOV had to be restricted to 50 mas (~ 1 AU). The closure phase measurements displayed an excellent stability with rms calibration errors ranging between 0.20° and 0.37°. Thanks to these data, Absil et al. (2010) demonstrated the capability of AMBER to detect the presence of companions over 90% of the search zone with contrasts down to 5×10^{-3} at the 3σ significance level. Such a level of contrasts corresponds, around β Pic, to a brown dwarf object with a mass of $\simeq 47\,M_{\mathrm{Jup}}$.

Figure 5.10 illustrates the derived sensitivity of AMBER during this observation as a function of the angular separation and compares it with radial velocity and adaptive optics techniques. It shows that VLTI/AMBER reaches its optimum sensitivity in the $2 - 60$ mas region, where a median contrast of 3.5×10^{-3} (5.0×10^{-3}) can be reached at a 50% (90%) completeness level using the ATs. The completeness indicates the fraction of locations within the FOV for which the sensitivity is lower or equal to the mentioned contrast upper limit.

Despite the weak scientific return that we have obtained from our program so far, this result proves the capability of AMBER, and very likely also of PIONIER, to meet our requirements, and thereby to find low mass companions orbiting close to our targets, if they exist.

6

CELINE: The ULg nulling testbed

Contents

6.1 Why develop a nulling testbench? 101
6.2 Beam combiners for nulling interferometry 102
6.3 CELINE instrumental layout 104
  6.3.1 Sources and injection 105
  6.3.2 Phase control and signal chopping 106
  6.3.3 Beam combination and detector 108
6.4 Results 108
  6.4.1 Data analysis 108
  6.4.2 Nulling results with monochromatic light 109
6.5 Perspectives 111

In the previous chapter, we demonstrated the ability of current stellar interferometers to detect companions $\sim 10^3$ *times fainter than their host star and located at angular separations as small as a couple of milli-arcseconds. Unfortunately, such a dynamic range is not sufficient for the detection of Earth-like exoplanets orbiting around solar type stars. A possible solution, that we introduced in Chapters 3 and 4, is called nulling interferometry and consists in combining destructively the light from two or more collectors to dim the starlight and to reveal faint companions in its vicinity. Among the sub-sytems of nulling interferometers, the phase shifters and the modal filters are very important. In this chapter we present an experiment called CELINE (CELestial Infrared Nulling Experiment), whose main purpose is to test achromatic phase shifters that have been developed for TPF-I/Darwin, as well as photonic single-mode fibers. It also serves as a demonstrator for future ground-based nulling facilities in the near infrared (from 1.4 to 4* μ*m). After presenting the principles and design of the experiment, we will show preliminary results and explain the future upgrades and perspectives of the instrument.*

6.1 Why develop a nulling testbench?

Interferometry is a powerful tool that allows to reach extremely high resolving powers and disentangle the signal of two close-by sources. Unfortunately, as illustrated in Section 3.3, the interferometric signature of an off-axis source becomes increasingly difficult to measure when the contrast between the companion and the central source increases.To circumvent this problem, a solution, called nulling interferometry, has been explained in details in Section 3.3 and consists in recombining destructively the light coming from separate apertures in order to cancel the on-axis starlight and reveal the presence of faint companions in its vicinity. A lot of research and development has already been done on the topic and deep broadband starlight rejection (also called null depth) down to 10^{-5} have been obtained in the lab at thermal infrared wavelengths ([8-12 μm]) (Peters et al. 2010). These results prove the feasibility of Earth-like exoplanet detections with spaceborne infrared nulling interferometers. Unfortunately, ground-based interferometers are strongly perturbed by atmosphere turbulences and many develoments are still required to perform ground-based interferometric observations at very high contrast. Today, the developments of ground-based nulling are led by very few instruments: the Keck Interferometer Nuller (Serabyn et al. 2004; Colavita et al. 2009), BLINC at MMT (Hinz et al. 2000), the LBTI (Hinz et al. 2004) and the Palomar Fiber Nuller (Haguenauer & Serabyn 2006; Martin et al. 2008) with starlight suppressions at the 10^{-3} level (Hanot et al. 2011; Mennesson et al. 2011b).

Since a decade, many researches and developments have been done in Liège in the field of nulling interferometry among which the realization of end-to-end simulators for nulling interferometric projects (Absil et al. 2006a, 2007; Defrère et al. 2008, 2010) and achromatic phase shifters for the Darwin/TPF-I mission (see Appendix A and Mawet et al. (2006)). The CELestial Infrared Nulling Experiment (CELINE) tends to pursue the R&D heritage at the University of Liège. Its goal is do develop key technologies for current or future ground-based nulling facilities in the near- and mid-infrared (H, K and L bands) such as the Palomar Fiber Nuller or ALADDIN (Absil et al. 2007) and test the APS Fresnel rhombs that have been elaborated at ULg (Mawet et al. 2006; Hanot et al. 2007).

6.2 Beam combiners for nulling interferometry

One of the main issues that one must face while designing an interferometer is to keep the optical layout as simple and symmetric as possible. Indeed, as we try to make two beams interfere, only perfectly identical beams (same intensity, polarization, etc...) will produce a perfect destructive interference. For that, one must try to make the optical paths identical for all beams. However, doing so is difficult and can lead to complex optical combination schemes, especially when the number of beams to interfere increases. In this section, we describe three widely used beam-combiners for pupil-plane nulling interferometry[7].

Co-axial beam combiners

The principle of co-axial beam combination is illustrated in Figure 6.1 (top left). It consists in superimposing pair-wise the beams using 50/50 beam splitters. The output of such a beam combiner is composed of two interferometric signals that are in phase opposition. These outputs can then be focused onto a single-mode fiber to get rid of the wavefront aberrations. This scheme suffers from two main drawbacks. First, the non common path between the two beams is significant. In particular, both beams are affected by the same beam splitter but while beam 1 is transmitted, beam 2 is reflected (and vice-versa for the second output). Even though beam splitters are theoretically symmetrical in transmission and reflection, differences of coating or chromatic dispersion phenomena can lead to intensity, phase and polarization mismatches. To compensate for such problems, symmetric layouts have been developed such that the two beams are affected both in transmission and in reflection. The price to pay is an overall increase of optical complexity. Second, co-axial beam combiners can only recombine the individual beams pairwise. When the number of beams increases, the optical complexity increases rapidly.

---

[7] What we refer to as pupil plane interferometers are interferometers whose outputs are imaged in a pupil plane.

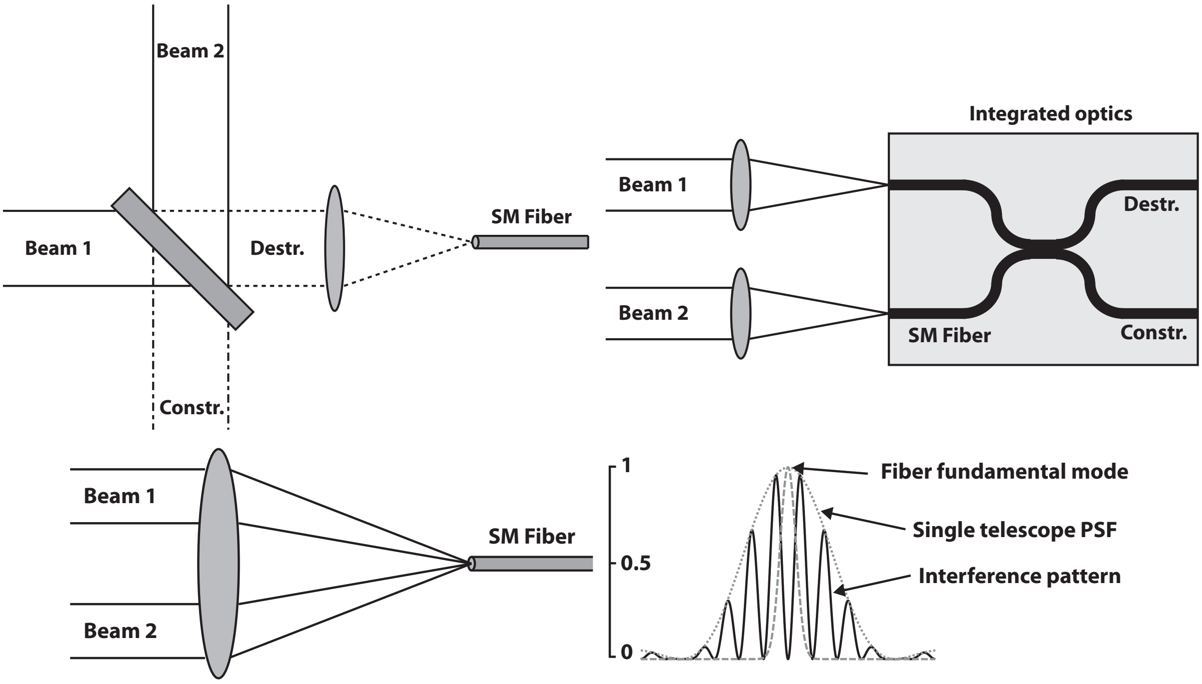

Figure 6.1: *Top-left*: Co-axial beam recombination scheme. The two pupils are overlapped on a beam splitter. In doing so, we get two outputs corresponding respectively to the constructive and the destructive interferences. *Top-right*: Beam recombination using integrated optics. The beams are injected into individual SM waveguides that are recombined using an optical circuit engraved on a silicon chip. *Bottom*: Principle of SM fiber beam combiners. Two incoming beams are focused onto a single mode fiber. At the focus, Fizeau fringes are formed with an intensity variation in space as shown on the right. In the fiber, the pupils are overlapped and the interferometric signal is filtered. At the output of the fiber, the fringes can no longer be imaged and only a photometric signal can be measured.

Integrated optics beam combiners

Beam combiners based on integrated optics (IO) provide a very elegant and compact solution. Integrated circuits have been used for a long time in electronics to transport and recombine electric fields. IO beam combiners are based on the same principle to interferometrically combine light beams using optical waveguides lying on a solid substrate of a few centimeters (see Figure 6.1, top right). This very compact device replaces both the modal filters and the semi-transparent beam splitters used to recombine the beams. Beam combination is performed within the chip by advanced optical circuits/functions. The main drawback of such a combiner is the chromaticity. Indeed, in every single-mode fiber, a chromatic dispersion phenomenon is present. This dispersion is very difficult to control and can significantly differ for the various fibers composing the chip. If it is the case, this error introduces a fixed bias to the measured null depth and can jeopardize the detection of faint companions. Similarly to co-axial beam combiners, the complexity of IO combiners rapidly augments when the number of beams increases. This complexity decreases the overall throughput of such devices. However, such a device is very versatile and can give access to all the photometric channels simultaneously, therefore allowing accurate calibrations.

Off-axis single-mode fiber beam combiners

Single-mode fiber beam combiners are the simplest of all three systems here described. They consist in a focusing optical element and a single-mode waveguide. The individual beams are all focused onto the SM fiber which both acts as a modal filter and a beam combiner. The main advantage of this technique is its simplicity of implementation and the fact that all beams share the same focusing optics, therefore reducing the non common path errors in the beam combiner. Moreover, the complexity of the recombination process stays the same when increasing the number of interferometric beams. The price to pay however is that no matter the number of beams, only one output and therefore one photometric information is available at a time. The main issue though is that the injection efficiency is low for two beam interferometers (∼ 35%) and increases when a larger number of pupils are recombined. Unlike the two other designs, SM fiber beam combiners have only one output which is the interferometric signal, the second one, in phase opposition, being filtered out. Such a design therefore requires beam chopping in order to have access to the individual beam intensities.

6.3 CELINE instrumental layout

The main drivers of the nulling interferometer design we present in this chapter are simplicity and versatility. Indeed, the simpler the design, the less degree of freedom one has to constrain during the alignment of the system and the less sources of errors are present in the instrument.

For this reason, the CELINE instrumental layout is based on the off-axis single mode fiber beam combination (Haguenauer & Serabyn 2006). Such a beam combination technique has been used in two nulling interferometers which are the Palomar Fiber Nuller (Haguenauer & Serabyn 2006; Martin et al. 2008) and the MAII testbed (Buisset et al. 2007), and has proven its capabilities. Indeed, broadband (20% bandwidth) null depth of $\sim (1.5)\,10^{-5}$ have been obtained in the H band (Mennesson 2007) and contrasts down to 10^{-6} have even been obtained with a monochromatic laser in the visible (Haguenauer & Serabyn 2006).

Our instrumental layout is entirely designed to optimize the off-axis combination technique and is illustrated in Figure 6.2. The light source feeds the interferometer through a single mode fiber. An on-axis parabola first collimates the beam which is then separated into two circular apertures with a mask. These two apertures have a diameter of 10 mm and are separated by 60 mm. The pupil mask is not adjustable (size of apertures, baseline, etc..) and is attached to the input fiber launcher in order to reduce the number of degrees of freedom. Once these two beams are defined, OPD compensators that consist in tilted parallel Infrasil 301 plates take care of co-phasing the two arms. Two shutters then sequentially block the beams in order to have access to the individual beam intensities, the background level and the interferometric signal. Achromatic phase shifters designed for specific wavebands are then inserted to induce a relative π phase shift between the two channels. Finally, after a new pupil mask that gets rid of some diffracted light (Fresnel propagation), the two beams are focused by a parabola into the output single mode fiber. After being filtered by the fiber, the output signal is focused onto a single-pixel detector.

This testbench, although very simple, presents many advantages:

- The number of optical elements is minimized with only two mirrors. The optical wavefront quality is therefore increased and the throughput losses are limited.
- The optical layout has a high degree of symmetry.
- The beams share the same optics and are focused into the same single mode fiber. Therefore, the non common path errors are minimized (no polarization rotation, no chromatism effects from coating differences, etc...).

Now that the overall description of the testbench has been made, let us explain in more details the three main blocks that compose the instrument (see Figure 6.2).

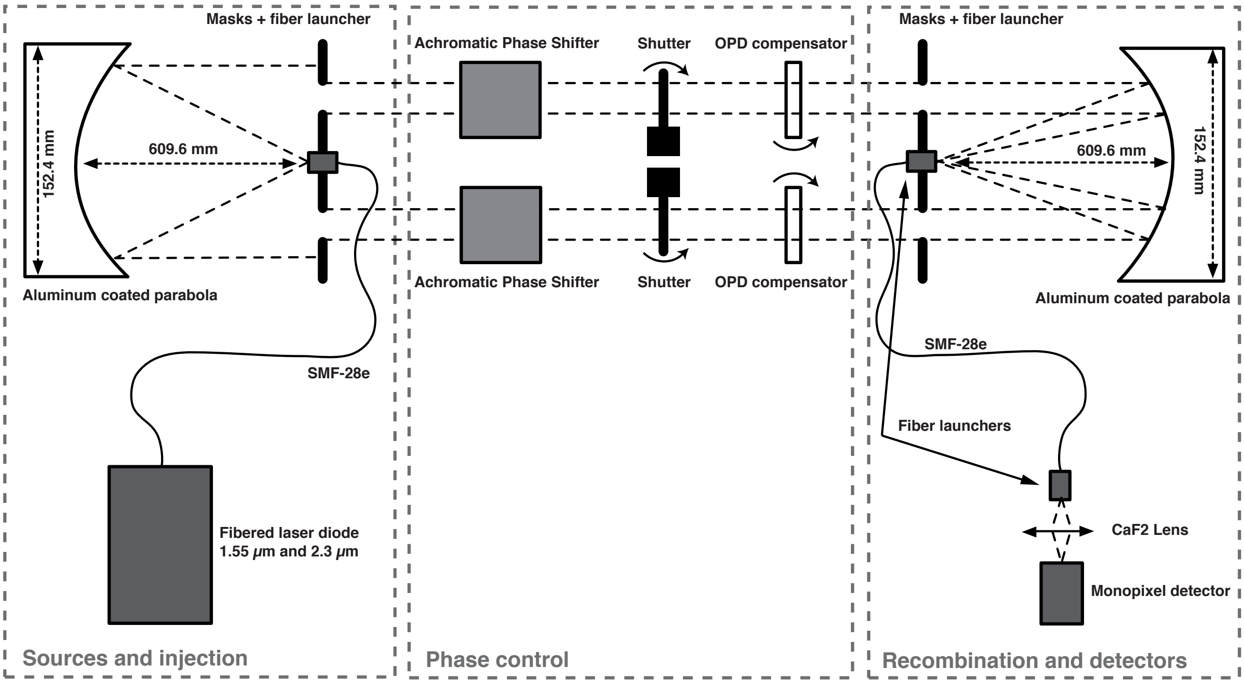

Figure 6.2: Layout of the CELINE nulling testbench. The laser source is injected into a single mode fiber and directly feeds the nuller. After being collimated by a parabola which is 6 inches wide, the main beam is divided into two circular apertures of 10 mm separated by 60 mm. The two interferometric arms are then phase shifted by a half-wave. This step is done by combining tilted Infrasil 301 parallel plates together with achromatic phase shifters (Waveplates or Fresnel rhombs). The beams are then sequentially blocked by two shutters in order to measure the 4 different interferometric signals (individual beam intensities, interferometric signal and background intensity). After passing through another pupil mask, identical to the first one, the beams are focused into a single mode fiber which acts both as a beam combiner and as a modal filter. The output of this fiber is finally focused onto a single-pixel InGaAs infrared detector.

6.3.1 Sources and injection

Four different laser sources are available with wavelengths ranging from 450 nm to 2500 nm: (i) a 650 nm diode that is used for alignment (ii) a 1550 nm diode (iii) a 2300 nm diode and (iv) a 2W supercontinuum white light source with operational wavelengths between ~ 450 nm and ~ 2500 nm[8]. While the 650 nm laser diode is only used for alignment purposes, the two other monochromatic diodes (1550 nm and 2300 nm) are used for testing monochromatic nulling in H and K bands. Finally the supercontinuum white light source will be coupled with H and K filters to perform broadband (~ 20% bandwidth) nulling. All these sources are fiber-coupled into an SMF 28e single mode fiber. This fiber has a cutoff wavelength < 1260 nm and works up to the K band. Unlike the classical SMF-28 and most single-mode fibers designed for telecom applications, the SMF-28e fiber is designed to minimize OH absorption lines. For longer wavelengths however, the filtering capabilities decrease and the fiber starts to absorb. However, for our current applications in both H and K bands, the SMF-28e is sufficiently transparent and allows us to quickly switch between the different light sources without doing any additional adjustment. Later on, to optimize the performances and the throughput in K band, we plan on upgrading the testbench with fluoro-zyrconate singlemode fibers whose parameters will be optimized as a function of the testbench operational wavelength range and numerical aperture.

The fiber end is mounted on a three axis flexure mount that provides a sub-micrometer injection accuracy. The light injected into the bench is then directly collimated by a 6 inches-wide parabola

---

[8] This source is currently not available on the bench but is planned for future upgrades.

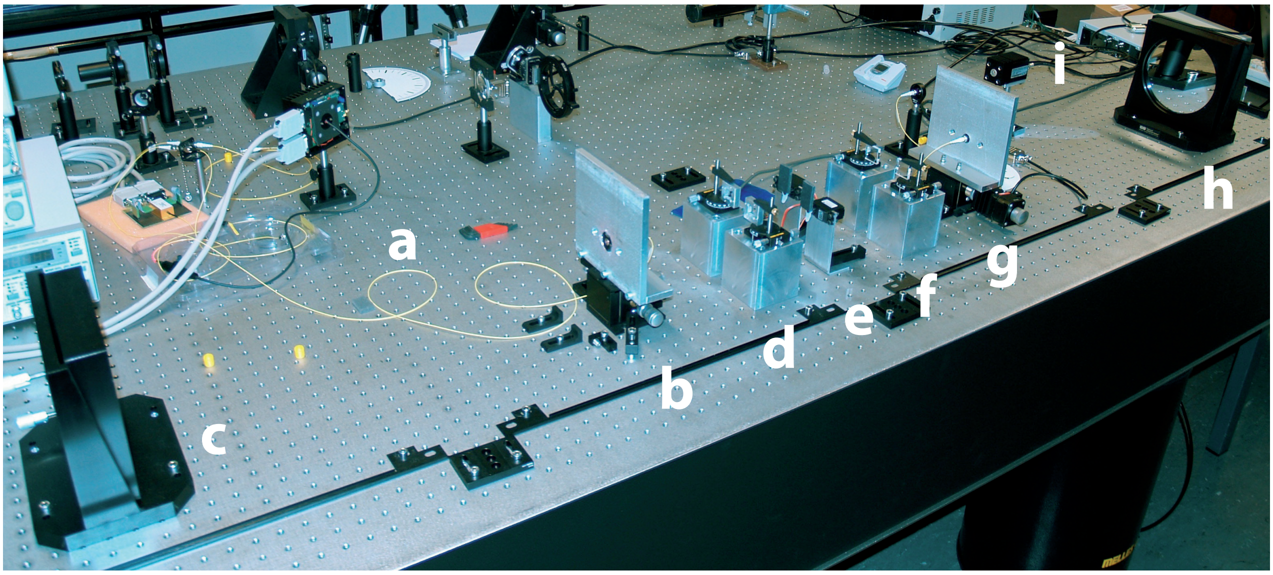

Figure 6.3: Picture of the CELINE testbench. Following the light path, you can see: (a) the input single mode fiber, (b) the pupil mask and fiber launcher, (c) the 6 inches-wide parabola, (d) the achromatic waveplates, (e) the two shutters, (f) the tilted Infrasil 301 parallel plates, (g) the second pupil mask and the output fiber fiber mount, (h) the second 6 inch-wide parabola, and (i) the single-pixel detector.

having a f/4 focal ratio. This focal ratio corresponds to the numerical aperture of the SMF-28e fiber. The reason for choosing such a large parabola is for versatility purposes. Indeed, one of the main goals of the testbench is to test Fresnel rhombs achromatic phase shifters (Mawet et al. 2007; Hanot et al. 2007) (see Section 6.3.2 and Appendix A), which require a minimum spacing of 60 mm between the beams. After the collimation, the light passes through a pupil mask that produces two circular apertures of 10 mm. The pupil mask and the fiber launcher are on a common mount to reduce the number of optical elements to be aligned.

6.3.2 Phase control and signal chopping

The central part of the interferometer is the heart of the instrument as it contains the optical components that control the differential phase between the interferometer arms and the device used to extract the various interferometer signals. Indeed, the drawback of interferometers using off-axis single mode beam combination is that there is no direct access to the individual beam intensities and to the background level. An additional piece of hardware must therefore be used to have access to this information. This device consists in two masks mounted on servo-motors blocking sequentially each interferometric beam. The frequency at which these motors operate can be tuned from a fraction of Hertz to about 10Hz. Figure 6.4 shows an exemple of chopped signals recorded by the nuller. The four different signals (i.e., the individual intensities, the background and the interferometric signal) are clearly visible over two chop cycles of ~4.25 second each.

One of the most critical part of a nulling interferometer is certainly the phase shifters, as the null depth depends on the accuracy at which the relative phase shift between the two beams is introduced. The best achievable polychromatic null depth N depends quadratically on the phase error (Serabyn 2000):

$$N = \frac{\int_{\lambda_{min}}^{\lambda_{max}} \Delta\phi(\lambda)^2\, \eta(\lambda)\, \mathrm{d}\lambda}{4 \int_{\lambda_{min}}^{\lambda_{max}} \eta(\lambda)\, \mathrm{d}\lambda} \tag{6.1}$$

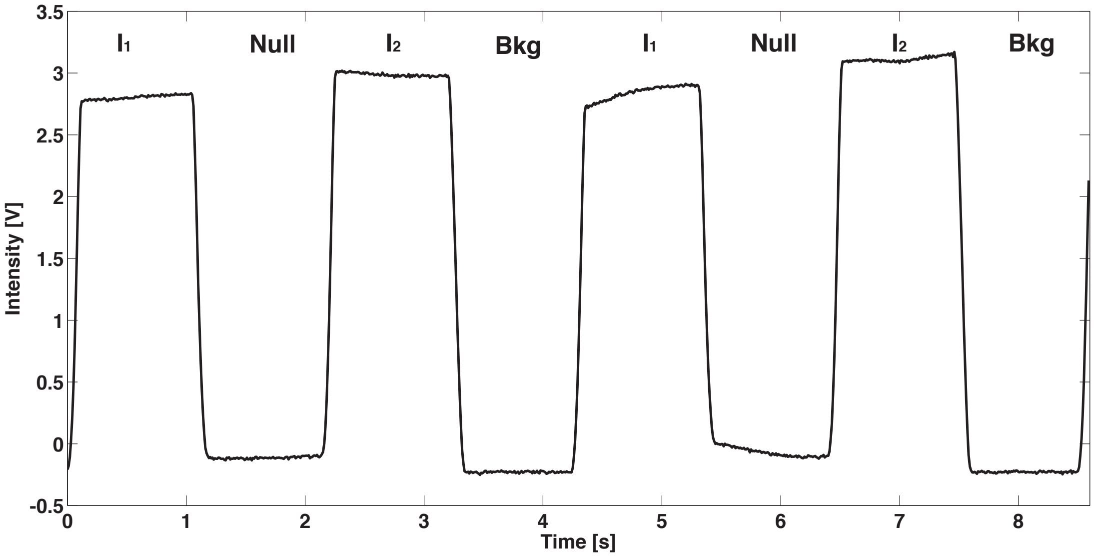

Figure 6.4: Chopped signal measured by the detector during two chop cycles of 4.25 s. The four chopping states are clearly visible with successive measurements of beam 1 intensity, of the interferometric (or nulling) signal, of beam 2 intensity and of the background intensity.

where λ is the wavelength, $\lambda_{\min}$ and $\lambda_{\max}$ are respectively the minimum and maximum wavelengths of the instrument's waveband, $\Delta\phi(\lambda)$ is the phase shift error and $\eta(\lambda)$ is the spectral instrumental response.

On our tesbench, the first step for phase control is to match the two beam optical paths by inserting in each beam path an Infrasil 301 parallel plate. These two plates have been polished together to minimize their thickness difference (< 150 nm) and are polished with a flatness better than $\lambda/10$ peak to valley at $\lambda = 630$ nm. By tilting one of the two plates, the optical path through Infrasil changes. It is therefore possible to accurately equalize the optical paths. Because the CELINE design is very symmetric, it is not necessary to use more complex delay lines since a proper alignment of the nulling bench leaves very small OPD residuals already. Indeed, first measurements in the lab show that the differential optical path between the two beams is $< 10\,\mu$m. The second step consists in introducing the relative π phase shift between the two beams. This phase shift, together with the OPD compensation must be as close to π as possible over the whole waveband (see Equation 6.1). For that, two achromatic phase shifter (APS) designs are planned to be used : (i) achromatic waveplates and (ii) Fresnel rhombs.

Waveplates are optical elements which introduce a relative phase shift between the polarization components s and p of the incident light. For example, parallel plates made of birefringent materials have such properties. The achromatic halfwave plates that we use for CELINE are made of two waveplates and have been optimized to provide an achromatic π phase shift over the H band. By combining quartz and MgF_2 waveplates with respective thicknesses of 1.5268 mm and 1.199 mm it is possible to reach null depths down to $\sim 4 \times 10^{-5}$ over the full H band.

Fresnel rhombs are optical grisms that make use of total internal reflection to introduce a phase shift between the vectorial s and p polarization components. Classical Fresnel rhombs are limited by the intrinsic index dispersion of the rhomb bulk material (Anderson 1988). Engraving a subwavelength grating (often called zero order grating, or ZOG) on the Total Internal Reflection (TIR) interface or simply depositing a single thin layer of a well chosen material leads to a significant improvement (Mawet et al. 2005a, 2006) . The Fresnel rhombs we use for our experiment are made of ZnSe and have been optimized for the thermal infrared, and especially for the wavelength range $[6 - 11]\,\mu$m. Even then, its phase shifting capability in both H and K bands is sufficient to reach null depths down to $\sim 10^{-4}$ at these wavelengths. More details about the design, manufacturing expected performance of Fresnel rhombs can be found in Appendix A.

6.3.3 Beam combination and detector

After having been phase shifted with respect to each other, the two interferometric beams pass through a new mask which is strictly identical to the mask defining the pupils. The purpose of this mask is to block the light diffracted outside of the pupil. Then, the two beams are focused into the single mode fiber by a 6 inches-wide parabola. The couple parabola/fiber is the same one for the front end of the bench than for the back end. The horizontal motion of the 3 axis flexure mount on which the fiber mount is placed is controled by a stepper motor. The stepper motor controls the alignment of the fiber used for the beam combination with an accuracy of 39 nm. This stepper motor is currently operated manually but should soon work in close loop to optimize the instrumental null depth in real time. Finally, the output of the single mode fiber is focused onto a Hamamatsu InGaAs single-pixel detector that is sensitive up to 2.56 μm.

6.4 Results

Since the very first fringes obtained in February 2010, the CELINE testbed already reached interesting contrast levels. In this section, we summarize the first results obtained with the instrument and detail the current limitations that we have to face.

6.4.1 Data analysis

The data analysis method we use for reducing the data acquired with CELINE has been proposed by Hanot et al. (2011) and Riaud & Hanot (2010) and is introduced in a general context in Chapter 4. The principle is to use the null depth histogram to retrieve the astrophysical information despite the instrumental fluctuating noise. In the lab with a point-like source, a nuller should theoretically give an astrophysical null $N_a = 0$. Any departure from 0 shows the limitations of the instrument that are not corrected for by the statistical data reduction method.

The shutters (see Figure 6.4) allow us to measure successively the individual beam intensities $I_1(t)$ and $I_2(t)$, $I_b(t)$ the background intensity and $I_-(t)$ the combined intensity of the two beams *"at null"* with frequencies ranging from a fraction of Hertz up to 10 Hertz. The null depth is normally defined as follows

$$N(t) = \frac{I_-(t) - I_b(t)}{I_+(t) + I_-(t) - 2I_b(t)} \tag{6.2}$$

where $I_+(t)$ is the interferometric signal that would be measured for constructive interference, i.e., without the achromatic π phase shift. However, in the case of single-mode fiber beam combiner based interferometers, the simultaneous access to the different intensities of Equation 6.2 is not possible and the observed null depth for each chop cycle is estimated from the non contemporaneous photometries as follows:

$$\hat{N}(t) = \frac{\hat{I}_-(t)}{\hat{I}_+(t)} \tag{6.3}$$

where

$$\begin{aligned}
\hat{I}_-(t) &= I_-(t) - \hat{I}_b(t) && (6.4)\\
\hat{I}_b(t) &= \frac{1}{\Delta t}\int_{t_0+\Delta t}^{t_0+2\Delta t} I_b(t)\,\mathrm{dt} && (6.5)\\
\hat{I}_+(t) &= 2\left[\hat{I}_1(t) + \hat{I}_2(t)\right] - 4\hat{I}_b(t) && (6.6)\\
&= \frac{2}{\Delta t}\left[\int_{t0-2\Delta t}^{t0-\Delta t} I_1(t)\,\mathrm{dt} + \int_{t0-\Delta t}^{t0} I_2(t)\,\mathrm{dt}\right] - 4\hat{I}_b(t) && (6.7)
\end{aligned}$$

t_0 being defined as the starting time of a chop cycle (which begins with the measurement of $I_-(t)$) and Δt the length of a chopping state corresponding to a quarter of the chopping period.

Unfortunately, as we explained in Chapter 3 and Chapter 4, in presence of fluctuating noise sources such as phase errors ($\Delta\phi(t)$) and intensity mismatch ($\delta I(t)$), the observed null depth varies quickly as a function of time. The dependence of the null depth on these error sources is (Equation 3.30)

$$N(t) = \frac{\Delta\phi(t)^2}{4} + \frac{\delta I(t)^2}{16} + N_a \tag{6.8}$$

where N_a is the astrophysical null depth. Moreover, when the simultaneous access to the nulling signal and to the various photometric channels is not possible, the null depth distribution does not only depend on the intensity mismatch and fast phase fluctuations but also on the fluctuations of the background level and of the collected stellar intensity. One must therefore add to Equation 6.8 two more noise contributors (Hanot et al. 2011) which are: (i) the normalized intensity uncertainty, defined as $I_r(t) = (I_1(t) + I_2(t) - 2I_b(t))/(\hat{I}_1(t) + \hat{I}_2(t) - 2\hat{I}_b(t))$, and (ii) the equivalent background null depth uncertainty which is given by $N_b(t) = (I_b(t) - \hat{I}_b(t))/(\hat{I}_+(t) + \hat{I}_-(t) - 2\hat{I}_b(t))$. The expression of the null depth then becomes:

$$N(t) = I_r(t)\left[\frac{\Delta\phi_d(t)^2}{4} + \frac{\delta I(t)^2}{16} + N_a\right] + N_b(t) \tag{6.9}$$

These fluctuating noise sources can jeopardize the accurate determination of the astrophysical null depth. The approach proposed by Hanot et al. (2011) consists in fitting the histogram corresponding to Equation 6.9 by a model using the intensities and phase distributions to recover the astrophysical information.

Indeed, with CELINE, the distributions of $\delta I(t)$, $I_r(t)$ and $N_b(t)$ are monitored. Therefore, as discussed in Chapter 4, the nulling histogram of Equation 6.9 only depends on the phase error distribution $\Delta\phi(t)$ and on the astrophysical null depth N_a. If we consider that $\Delta\phi(t)$ follows a normal distribution, it is then possible to fit a nulling histogram model having only 3 free parameters : μ_ϕ the mean phase error, σ_ϕ its standard deviation and N_a. This technique allows a much better accuracy and dynamic range to be reached on the measurement of the astrophysical null depth as we are not limited by the mean errors like in most data reduction methods, but by the uncertainties on their distribution. Moreover, for on sky observations, it has the advantage of not requiring calibration sequences, provided that instrumental systematics are low. In the lab, since we use a point like source generated by a laser injected into a single-mode fiber, the measured astrophysical null depth is supposed to be 0. Therefore, any departure of the measured N_a from zero translates into an instrumental bias that is not compensated for by the reduction method

6.4.2 Nulling results with monochromatic light

The CELINE testbench is in its building and debugging phase. The results that we present here have been obtained with the very first light of the instrument and do not represent the final limitations of our

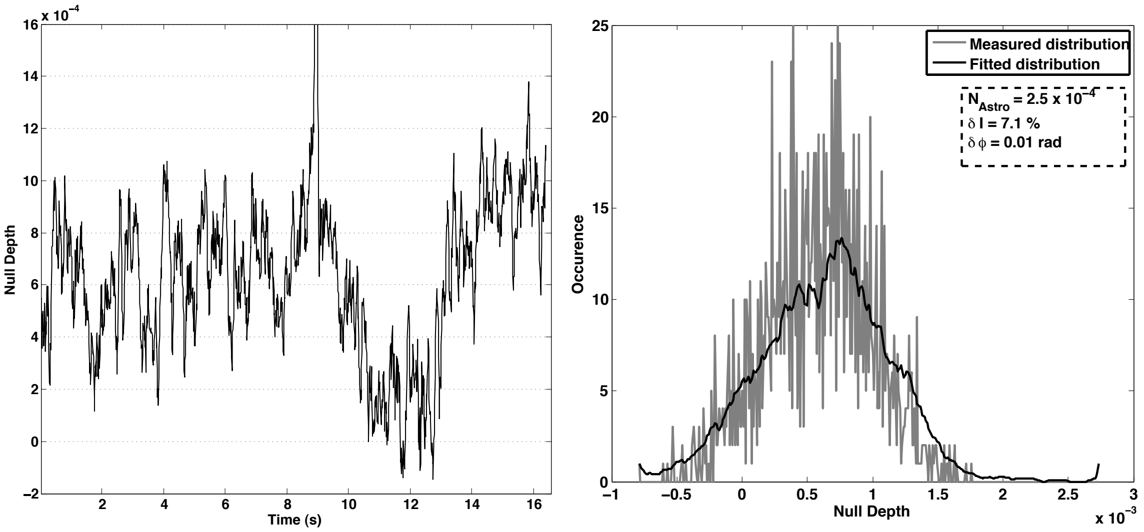

Figure 6.5: Left: Nulling sequence of 16 s obtained with the 1550 nm monochromatic laser source. During the measurements, the null depth averaged over periods of 1 s is constantly below 10^{-3}. Between the 10th and 13th seconds, the null depth even dropped down to 2×10^{-4}. Right: Null depth distribution corresponding to the left panel sequence. The grey curve represents the measurement distribution while the black curve is the smoothed best fit of the nulling distribution (we performe a smooth of the curve in order to better see the quality of the fit which would otherwise overlap). It corresponds to an "astrophysical" null depth N_a of 2.5×10^{-4}.

experiment. They have been obtained with the 1550 nm laser diode during the alignment phase of the testbench. Figure 6.5 (left) shows a nulling sequence of 16 s. During these 16 s, the measured mean null depth averaged on 1 s sequences is constantly below 10^{-3}. The null depth even dropped down to a mean level of 1.8×10^{-4} during 3 s. Over longer timescales, current measurements show a slow drift of the null depth (see Figure 6.6, right). This drift comes from a relaxation of the three axis flexure mount holding the recombination fiber along the horizontal axis. It is however possible to control this drift by implementing a control loop acting on the x-axis stepper motor of the flexure mount (and therefore on beam combination into the single-mode fiber). As it can be seen on the left panel of Figure 6.6, most of the null depth fluctuations are due to low frequency perturbations (< 1 Hz). As a consequence, the loop controlling the stepper motor does not need to work at high frequencies.

Figure 6.5 (right) represents the null depth distribution during this nulling sequence. The grey curve corresponds to the measured distribution while the black one is the best fitted distribution using the Monte-Carlo statistical self-calibration method (Hanot et al. 2011). The fitted null depth corresponding to this distribution is 2.5×10^{-4}. The mean intensity mismatch and phase errors during this sequence are respectively $\delta I = 7.1\%$ and $\mu_{\phi} = 0.01\mathrm{rad}$. The biased induced on the raw null depth is at a couple of 10^{-4} but is mostly corrected by the statistical data reduction method. The remaining bias is due to the uncertainties on the measurement of these two errors (i.e. due to $\sigma_{\delta I}$ and $\sigma_{\delta\phi}$). Indeed, the effect of intensity mismatch on the null depth is also given by $\sigma_{\delta I}^2/16 \simeq 3 \times 10^{-4}$. If this uncertainty is low over short timescales, it increases drastically over longer timescales (a couple of minutes) because of a drift of the beam injections (see Figure 6.6, right). One way to increase the performances and the stability of CELINE will be to control the injection of the beams into the single-mode fiber in real time using the stepper motor (as proposed in Section 6.3.3). This stepper motor has already been implemented in the bench but the control loop is still to be done.

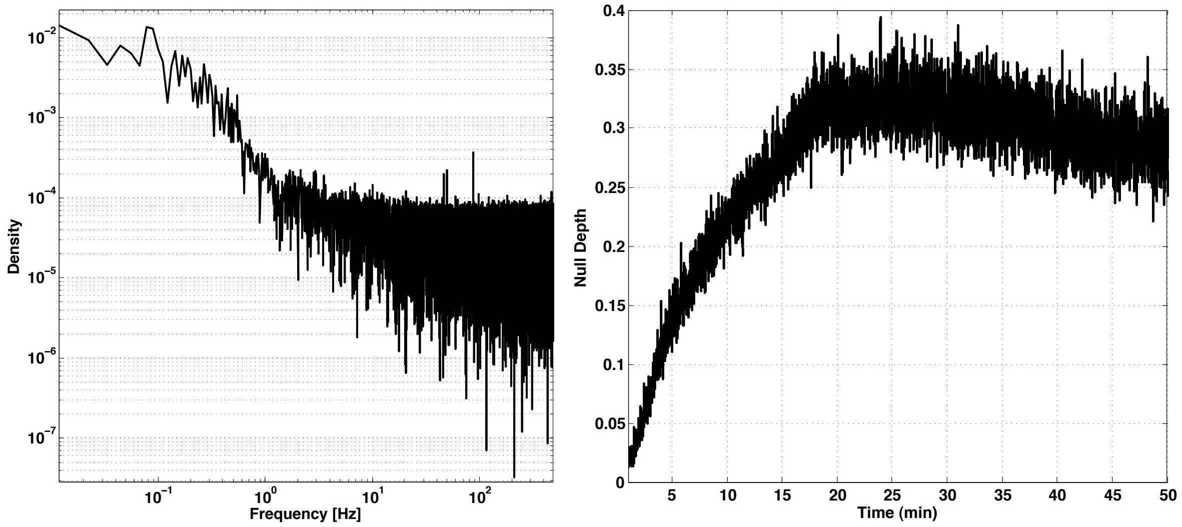

Figure 6.6: *Left*: Power spectral density of a null depth sequence measured by the CELINE testbed. This PSD clearly illustrates that most of the null fluctuations are due to low frequency perturbations (i.e., < 1 Hz). *Right*: Illustration of the measured null depth long-timescale drift during an acquisition of 50 min.

6.5 Perspectives

Even though we are still at the early stages of the development of the instrument, the results obtained are already promising with a monochromatic null depth down to 2×10^{-4} at 1550 nm with the very first light of the instrument. The objectives that we are pursuing with the testbench are numerous and will start with an upgrade of the bench with a supercontinuum white light source. This very bright and broadband laser source will allow us to perform broadband measurements in both H and K bands at very high contrasts. Our goal is to reach broadband null depths between $\sim 10^{-4}$ and 10^{-5} in both of these bands. For that, we will use achromatic waveplates for the H band and Fresnel rhombs for H and K bands. For K band measurements, in order to optimize the throughput and the wavefront filtering capabilities, we will upgrade the bench with fluoro-zyrconate single-mode fibers, specially optimized (numerical aperture, core diameter) for the use of CELINE in K band. We are also planning to test the capabilities of photonic fibers for off-axis beam combination. Indeed, such fibers have never been tested as modal filters and beam combiners for nulling interferometry. Unlike standard fibers that are characterized by a Gaussian transmission mode, their fundamental mode is given by a Bessel J1 function. Their interest, however, comes from their broadband qualities as well as their typical spectral bandwidth of 50% ($R \simeq 2$).

Finally, the ultimate goal of our testbench is to use CELINE as a technology demonstrator for future ground based nulling facilities working in the L band, such as ALADDIN. This will require of course a major upgrade of the bench with a new source, new APS, a new detector and new single-mode fibers optimized for this waveband.

7

The Palomar Fiber Nuller: detecting faint companions inside the diffraction limit of a single telescope

Contents

7.1 Principle of the PFN 114
  7.1.1 Instrumental layout 114
  7.1.2 Alignment 117
7.2 Laboratory results 118
  7.2.1 Broadband nulling 118
  7.2.2 Baseline rotation 120
7.3 Observing at high contrasts within the diffraction limit 121
  7.3.1 Paper: **High Contrast Stellar Observations within the Diffraction Limit at the Palomar Hale Telescope**, *B. Mennesson, C. Hanot, E. Serabyn, S. Martin, K. Liewer, F. Loya and D. Mawet* 121
  7.3.2 Paper: **New Constraints on Hot Dust within a few AU of Vega**, *B. Mennesson, E. Serabyn, C. Hanot, S. Martin, K. Liewer, D. Mawet* 133
7.4 Future upgrades: going deeper and fainter 143
  7.4.1 Looking for young exoplanets with the PFN 143

The Palomar Fiber Nuller (PFN) is a transportable nulling interferometer developed at the Jet Propulsion Laboratory which aims at looking for faint companions close to bright stars using the 200" Hale telescope of the Palomar observatory. It also contributes to the development of key technologies for future space-based nulling interferometers such as TPF-I/Darwin and FKSI. In this chapter, we first show deep broadband nulling results obtained in the laboratory as well as a study of the null depth stability during a full baseline rotation. we then present the first scientific results that we obtained during our engineering runs. They consist in the accurate measurement of red giants stellar angular diameters and the determination of upper limits on the presence of circumstellar emission around Vega (either a companion or a circumstellar disk). Finally, we will explain the future upgrades that are planned for the PFN and briefly discuss its expected performances for the detection of (sub-)stellar companions.

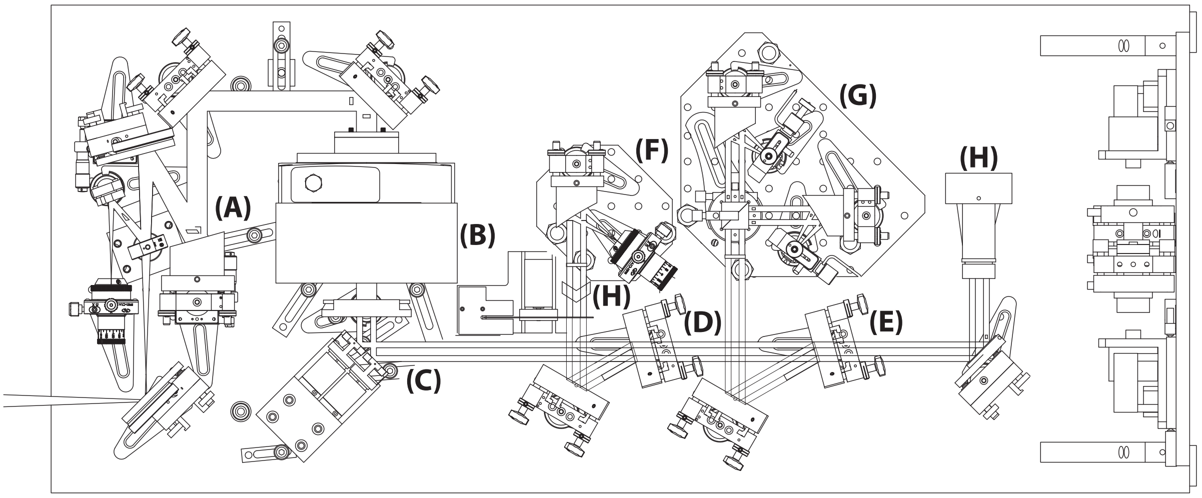

Figure 7.1: PFN layout: The wavefront-corrected beam coming from the telescope feeding our instrument is first collimated using an off-axis parabola (A). The pupil rotator (K mirror, B) then rotates the sky image with respect to the baseline orientation. A pupil mask and two piezo mirrors (C) define the two 1.5 x 3m subapertures and control the piston and tip-tilt errors in real time. A pair of dichroics (D and E) splits the light into three spectral bands: (i) the K band feeds the nulling output (F), (ii) the H band is used for fringe tracking (G), and (iii) the J band is focused onto an angle tracking camera (H).

7.1 Principle of the PFN

The Palomar Fiber Nuller is a so-called nulling coronagraph. Unlike long baseline interferometers such as the VLTI or CHARA, the PFN recombines destructively two 1.5×3 m sub-apertures of the $200''$ Hale telescope at the Palomar observatory. After being phase shifted with respect to each other, the two beams are focused onto a common single mode fiber which is used both as a beam combiner and as a modal filter. The instrument being downstream of the telescope AO, the wavefront arriving to the PFN is already corrected for most atmospheric-induced aberrations, leaving the differential OPD between the two beams smaller than 200 nm rms. Moreover, because the two beams are coming from a single telescope, pupil rotators can be used to rotate the baseline in order to modulate the signal coming from an asymmetric off-axis source. In the following sections, we explain in more details the principle and technical characteristics of the instrument.

7.1.1 Instrumental layout

Figure 7.1 shows the implemented nulling breadboard. A converging beam from the AO bench enters the instrument at the lower left, is collimated (A) and passes through the pupil rotator (B). Next, a mask composed of two elliptical holes define the two apertures. Then, the beams are reflected from the dual tip/tilt/piston mirrors (C) which control the pointing and relative phase of the beams. Encountering the first dichroic beamsplitter (D), the K band light is reflected and directed towards an off-axis parabola where, after passing through a chopper wheel and a beam compressor, it is focused onto a fluoride glass single mode fiber (F). The shorter wavelength radiation passes through the dichroic and reaches a second one (E), where the H band light is reflected. This light is directed to the fringe tracker (G). The transmitted beam, containing wavelengths shorter than 1.5 μm, goes toward the alignment and pointing camera (H). Just before this camera, a converging lens on a flipper mount can be inserted or removed from the beam path in order either to monitor the pointing positions of the beams or to image the pupils.

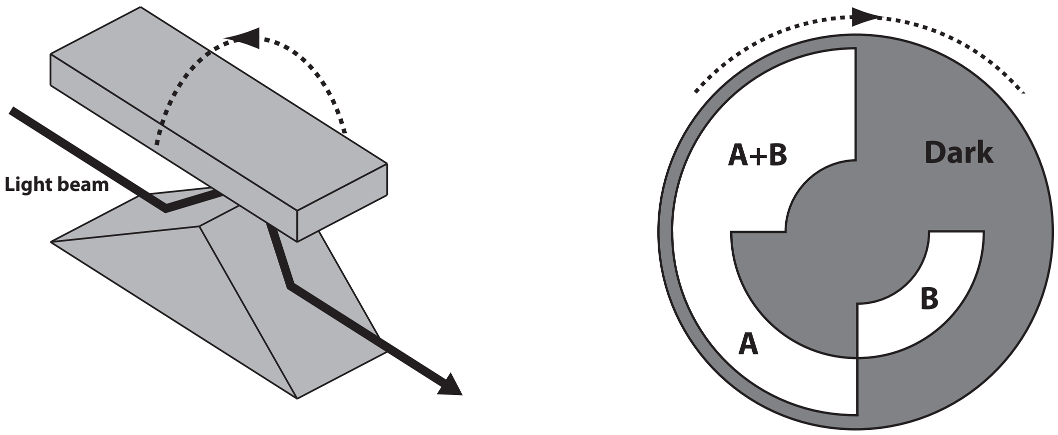

Figure 7.2: *Left*: Schematic representation of a K-mirror. *Right*: the PFN chopper wheel.

Beam chopping

As explained in Chapter 6, one of the drawbacks of the single mode fiber beam combiners is that the interferometric signal, the individual beam intensities and the background level cannot be monitored simultaneously. The nulled beam is therefore chopped using a mechanical chopper, which allows the successive measurement of the intensity of each beam (I_A, I_B) individually, of the interferometric signal (I_{A+B}), and of the dark (or background) level. Using these sequential signals, an estimation of the null depth is computed for the epochs of the chop cycles for which the interferometric signal is measured. The statistical self-calibrated reduction method developed by Hanot et al. (2011) and introduced in Chapter 4 is used to accurately measure the astrophysical null depths and correct for the non-synchronicity of the measurement of the different signals.

Pupil rotator

Rotating the baseline of a nulling interferometer is mandatory to extract the signal of an off-axis (sub-) stellar companion (Bracewell 1978; Martin et al. 2008). In space, the baseline rotation can be done by physically rotating the array but this solution is usually not realistic for ground based interferometers. For the PFN, which combines two sub-apertures instead of distant telescopes, the baseline rotation can however be done. To rotate the fringe system with respect to the plane of the sky, three solutions can be considered:

- the mask defining the apertures can be rotated, but this requires that the nulling optics can accept the apertures at all angles; this is not the case in the design described in this section, in which only a limited rotation is possible because of the fixed phase control mirrors
- for a ground-based telescope, the focal plane optical system sometimes may be rotated; this is the case at Palomar
- the pupil itself can be rotated by using a K-mirror (see Figure 7.2, left) or a Dove prism; using this solution allows the apertures and downstream optics to remain fixed but adds some complication to the alignment control.

Accurate alignment of this device is crucial. Indeed, any difference between the position and tilt of the K-mirror's rotation axis with the instrument beam axis will cause the various beams to move in the pupil plane during the pupil rotation process. As a consequence, the injection efficiency and piston errors change during the pupil rotation and the null depth can be strongly corrupted. Also the K-mirror's components must be accurately assembled to avoid similar internally produced effects. In order to keep

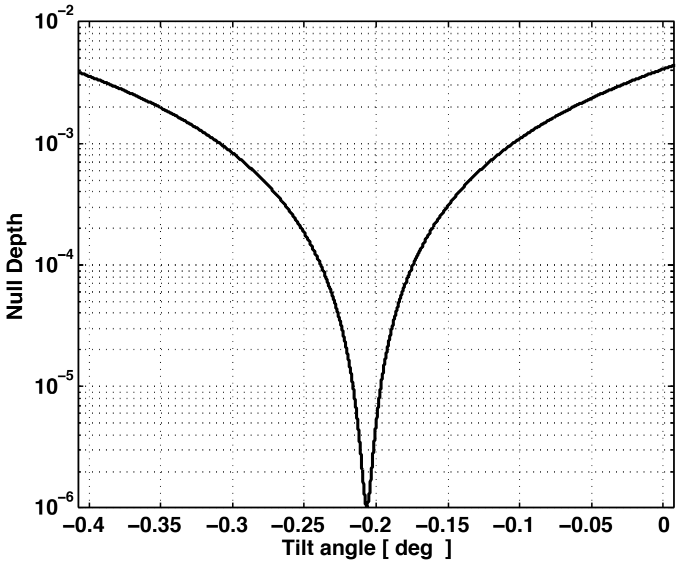

Figure 7.3: Null depth limitation due to the phase shifter as a function of the chevron's tilt angle. The plain curve corresponds to a polychromatic null in the wavelength range [2.05 – 2.35] μm.

this null depth variation as small as possible and make possible the real time tracking of the beam position with the piezo mirrors, the tilt angle must remain smaller than 1×10^{-3} rad. This fine alignment has ben performed in the JPL's nulling laboratory.

Phase shifter

The relative π phase shift that needs to be introduced between the two interferometer's arms to supress the on-axis light is provided by a combination of piezo mirrors and an infrasil chevron (see. Figure 7.1, H). By tilting the chevron prism, the optical path of the two beams through the infrasil changes. This optical path difference can be tuned together with the piston introduced by the piezo mirrors to achromatize the phase shift. This optimization process is done by minimizing the following expression:

$$\int_{\lambda_{min}}^{\lambda_{max}} \left[\Delta l_{\mathrm{air}} + n_{\mathrm{Infr.}}(\lambda) \Delta l_{\mathrm{Infr.}}(\lambda) - \frac{\lambda}{2} \right] \mathrm{d}\lambda \tag{7.1}$$

where λ is the wavelength, Δl_{air} and $\Delta l_{\mathrm{Infr.}}$ are respectively the optical path difference between the two beams in the air and in the infrasil prism, and $n_{\mathrm{Infr.}}(\lambda)$ is the infrasil refractive index. Figure 7.3 shows the result of this minimization process as a function of the chevron's tilt angle. The best possible polychromatic null depth between 2.05 and 2.35 μm is 1.0×10^{-6}.

Fringe trackers

A pair of fringe tracking detectors use the H band light to maintain the null to a level better than that provided by the AO system. The fringe tracking light is split 50/50 and sent to two single mode fibers which feed the light to thermoelectrically cooled detectors, in the same arrangement as the null detector. By laterally displacing the receiving fiber from the exact center of the interference fringe, any desired phase can be chosen. For fringe tracking, one fiber is displaced to the left by a sufficient distance to bring the interference phase to $-\pi/2$, the other is displaced to the right by $\pi/2$. Thus the two detectors see signals with identical intensities (F1 and F2) but opposite sensitivity to phase changes. The phase ϕ of the nulled beams is calculated using the fringe tracker outputs as

$$\sin(\phi) \simeq \frac{F_1 - F_2}{F_1 + F_2}.$$

Initially, the fringe tracker phase is measured at the null of the K band light and then the fringe tracking software maintains this phase by controlling the piston mirrors.

Detectors

Three kinds of detectors are used on the PFN. The null and fringe tracker detectors are 250 μm diameter InGaAs detectors with extended wavelength response. They have four-stage thermoelectric coolers that allow them to operate at a temperature of $-85°$ C. The null detector has a spectral response going up to 2.6 microns while the fringe tracker detector cutoff is 1.9 microns (with slightly lower noise). At the Palomar 200″ telescope, the apertures used are 1.5×3 m ellipses and give about 400 pW at H band (fringe trackers) and 150 pW at K band (nulling, mean signal) at the detectors for an M type star with a K magnitude of zero. The detector amplifiers have a large gain ($\simeq$ 100) with a 100 Hz bandwidth. The expected SNR in the fringe tracking channels is about 3000 (on the fringe peak) and is dominated by photon noise. For the nulling signal, the bandwidth is $\sim$ 10 Hz and the SNR is 2500 on the stellar signal. For the nuller the primary noise contribution is from the detector readout noise. With such a sensitivity, the PFN is restricted to the observation of bright stars ($K \geq 0$) and contrasts are limited to 10^{-3} while our instrument is potentially capable of better performances (contrasts of 10^{-4} have been achieved in the lab, see Section 7.2.1 for more details). A major upgrade for the PFN will therefore be the replacement of the mono-pixel detector by a much more sensitive *HAWAII* infrared array. The use of the camera will allow the PFN to increase its sensitivity to stars having K magnitudes up to 5 with an SNR of a couple of thousands (see Section 7.4 for more details). The third detector is a CCD camera collecting all the wavelengths below 1.5 μm. This camera is used both for tracking the pointing very accurately and imaging the two pupils.

7.1.2 Alignment

Several picomotors and piezo-electrically controlled stages are used to maintain the alignment. At the left of Figure 7.1 the first fold mirror allows the input beam shear to be controlled and the second fold mirror adjusts the pointing. A combination of adjustments to these mirrors is made to position the incoming light centrally with respect to the dual aperture mask. An initial measurement of the beam shear can be made using the integrated beam intensities measured by the pointing camera; when these are balanced, the beams are centered. The tip/tilt stages can then be used to point the incoming beams individually onto the nulling fiber. The chopper wheel is rotated to allow adjustment of each beam in turn. At this point, a pair of flat optics composed of the first beam splitter and a mirror are used to adjust both the pointing and the shear for the injection of the beams into the single-mode fiber. Having established the alignment, the position of the beams is measured on the pointing camera and a control loop then maintains the pointing using the tip/tilt mirror. The fringe trackers can be adjusted by making small position changes to their respective fibers so as to bring them to the correct phase.

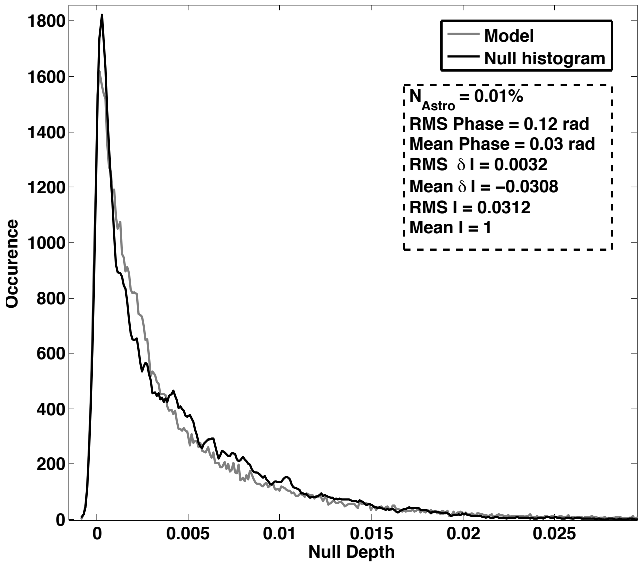

Figure 7.4: Comparison of the nulling histogram with the best fitted statistical model. The corresponding null depth is 10^{-4} with a mean intensity missmatch of $\mu_{\delta I} = 3.08\%$ and a mean phase error $\mu_{\Delta\phi} = 0.03$ rad.

7.2 Laboratory results

The laboratory results that we present in this section have been obtained at JPL's nulling lab in July 2009. They mostly consist in determining the best null depth (or contrast ratio) that can be achieved and the stability of the null depth when the baseline is rotated. These results give a direct information on the best possible performances that can be expected from the PFN on the sky.

When used in the laboratory, the light feeding the instrument, normally coming from the telescope when used on-sky, is replaced by a reflective injection bench that mimics the Hale telescope. Two infrared light sources with much different power have been used for this experiment to ensure that the SNR cannot be the limiting factor: a classic Halogen lamp (rather weak) and a powerful Fianium 2W supercontinuum white light source. The operational bandwidth of the instrument is set by the combination of the detector response with the K filter bandpass. The estimated bandpass of the instrument is $[2.05; 2.35]\,\mu$m which corresponds to a 14% bandwidth. The recorded data has then been analyzed using the statistical self-calibration method (Hanot et al. 2011) described in Section 4.2.

7.2.1 Broadband nulling

The result of the experiment is shown in Figure 7.4. The best-fit histogram model corresponds to a null depth of 1.0×10^{-4} and is stable over the whole nulling sequence (120 sec). The intensity mismatch during the measurement is about 3% and the mean phase error corresponding to this best fit is 0.03 rad. Even though null depths of 10^{-4} are sufficient for operation on ground-based facilities, which are limited by other external error sources (atmosphere refraction, residual wavefront errors, etc...), a floor null at this level was rather unexpected. Indeed, this type of nulling interferometer had already proven its ability to reach 10^{-6} null depths (Haguenauer & Serabyn 2006). There are several error sources to explain our result. For example, it can either be related to ghost beams due to spurious reflections in the instrument, or to intensity, phase or polarization errors. In the following sub-sections, we make a thorough description of these different sources that can limit our experiment and give an estimate of the level at which they contribute to the null depth limitation.

Intensity errors

As described in details in Section 4.2, polarization rotation as well as intensity and phase mismatch can limit the measured null depth. Unlike the first two effects, the intensity error distribution is monitored during the nulling sequence. It has a mean $\mu_{\delta I} = 3.08\%$ and a standard deviation of $\sigma_{\delta I} = 0.32\%$ which means that the intensity mismatch statistically almost never reaches 0 and thereby introduces a bias in the recorded mean null depth. However, as the statistical distribution is monitored, this effect is taken into account in the statistical data reduction method that automatically corrects for this bias. Therefore, only an error on the measurement of the mean intensity mismatch can potentially lead to a bias on the null depth determination. If we conservatively consider that such an error is of the order of $\sigma_{\delta I}$, the corresponding bias is $< 10^{-6}$. Therefore, intensity mismatch is not the main contributor to our 10^{-4} null depth limitation.

Phase errors

Polychromatic phase errors are composed of two components: piston error ($\Delta\phi_{\lambda_0}$), and chromatic dispersion ($\Delta\phi_c(\lambda)$). The corresponding effect on the null depth is

$$N_\phi = \frac{\int_{\lambda_{\min}}^{\lambda_{\max}} \left(\Delta\phi_{\lambda_0} + \Delta\phi_c(\lambda)\right)^2 \, \eta(\lambda)\, \mathrm{d}\lambda}{4 \int_{\lambda_{\min}}^{\lambda_{\max}} \eta(\lambda)\, \mathrm{d}\lambda} \tag{7.2}$$

where $\eta(\lambda)$ is the spectral instrumental response. If the distribution of the piston error fluctuations ($\Delta\phi_{\lambda_0}^2/4$) is taken into account into the histogram model, this is not the case of the chromatic effect, which introduces a bias. This bias is given by the residual of the phase shift achromatization process of Equation 7.1. With our instrumental setup, this residual is 1.0×10^{-6} (see Section 7.1.1). According to this analysis, the purely chromatic phase dispersion ($\Delta\phi_c(\lambda)^2/4$) does not seems to be the main contributor to the 1.0×10^{-4} null depth limitation. However, the introduced phase shift strongly depends on the chevron tilt angle. For example, Figure 7.3 shows that an error on the tilt angle as low as 1 arcmin can lead to a chromatic null limitation of $\sim 1.0 \times 10^{-4}$. Given the specifications on the chevron's rotation stage, the impact of a tilt error on our null depth should be limited to $\sim 2.0 \times 10^{-5}$. Furthermore, we performed monochromatic null depth measurements to assess the actual impact of chromatic effects on the null depth. For that we inserted a narrowband Br γ filter in front of the detector and optimized the phase shift for this wavelength. The measured null depth did not show any significant improvement, demonstrating that indeed, chromaticity is not our main limitation.

Ghosts

Another critical point is the presence of ghost beams due to spurious reflections inside the chevron prism. The prism is AR coated so that the reflection coefficient inside is $\sim 1\%$. At the output of the prism, the brightest ghost beam is parallel to the main beam and has a relative intensity of 1.0×10^{-4}. Therefore, this ghost could very well explain our current limitations. However, the optical design of the chevron has been made such that the ghost beam created by spurious reflections that is parallel to the main beam is laterally sheared by more than the beam size. We used diaphragms to block any light outside the main beams but we did not see any improvement in the measured null depth. We can therefore exclude ghosts as being the source of the limitation of our contrasts

Polarization

Rotation of the polarization can decrease the null depth produced by the interferometer (Serabyn 2000; Hanot et al. 2011). With a single-mode fiber beam combiner, this effect is supposed to be negligible compared to other noise sources (Haguenauer & Serabyn 2006). However, as it has never been characterized with the PFN, we cannot rule out the possibility that the polarization significantly reduces the performances. Polarizers have therefore been inserted just before the off-axis parabola focusing the beams into the fiber. We then recorded nulling sequences for different orientations of the polarizer. The limitation induced on the floor null depth that can be reached was difficult to measure but is of the order of 10^{-5}. Note that the focusing off-axis parabola (OAP) can introduce some differential polarization as it comes after the polarizer. We modeled this effect with the *ZEMAX* software and found that the rotation of the polarization induced by this OAP is smaller than the 10^{-5} level.

Summary of the error budget

Table 7.1 summarizes the impact of the different error sources on the measured null depth. Unfortunately, none of them can explain our current limitation at the 10^{-4} level, even when combined all together. One possible limitation that we did not get a chance to test is the real filtering capabilities of the single mode fiber being used. Indeed, if not perfectly filtered, the imperfections of the combined wavefront could limit the measured null depth. This imperfect filtering can be due, for example, to the fact that a fraction of the beam light is injected into the fiber cladding and then transmitted through it instead of the fiber core. This hypothesis will be the subject of future laboratory tests at JPL.

Table 7.1: Summary of the potential limitations of the PFN null depth with their respective contributions.

Error source	Impact on the null depth
Intensity	$< 10^{-6}$
Chromaticity	$< 10^{-5}$
Ghosts	$< 10^{-5}$
Polarization	$\sim 10^{-5}$
Total	$\leq 3 \times 10^{-5}$

7.2.2 Baseline rotation

Reaching deep rejection ratios is important in nulling interferometry, but stabilizing this contrast while rotating the baseline is also mandatory to distinguish instrumental modulations from potential planetary signatures. For this experiment, we performed two sequences of baseline rotation separated by two hours. The baseline is rotated each time over 180° by steps of 10°. A full rotation of 360° is not useful in the case of two-aperture interferometers as their transmission functions are symmetric. After taking these two sequences, we computed the null depth difference between the two baseline rotations for each baseline orientation. A more reliable value of the null depth stability during baseline rotation could have been assessed by repeating this process several time. Unfortunately, this experiment is time consuming and we did not have the time to do it completely. The result is plotted in Figure 7.5. The mean null depth difference over a 180° rotation is -1.9×10^{-5} and the RMS of the fluctuations is 9.3×10^{-5}. From these values, we can derive the 3σ detection limit of the instrument, which is $\sim 3 \times 10^{-4}$. This corresponds to a sensitivity within the diffraction limit of the telescope of $\Delta K \simeq 8.5$ (angular separations between 30 mas and 200 mas).

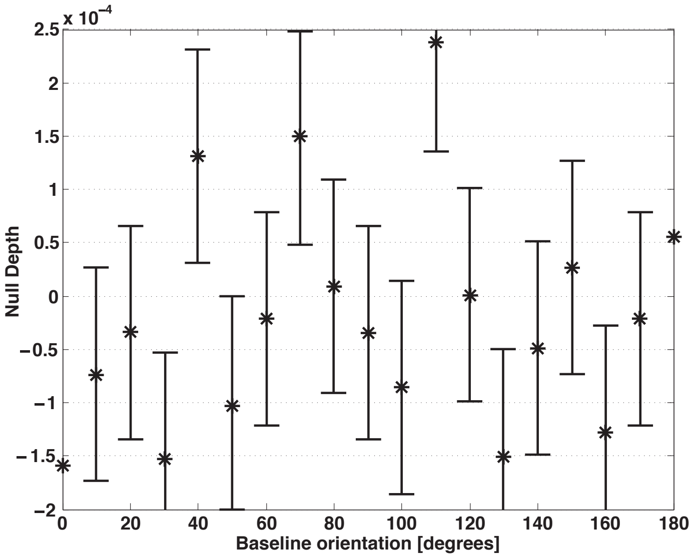

Figure 7.5: Modulation of the null depth between different nulling measurements taken during 2 hours as a function of the baseline orientation.

7.3 Observing at high contrasts within the diffraction limit

As described in the first part of this thesis, coronagraphs are very efficient devices for imaging faint structures around stars. However, one of their main limitation is their inner working angle. Indeed, if they suppress the starlight, they also usually suppress the off-axis light up to distances of $1 - 3\lambda/D$ depending on the coronagraph being used. Detection of faint structures closer than a couple of λ/D is therefore difficult. Unlike standard coronagraphs, the half-transmission point characterizing the IWA of the PFN is only $\lambda/3D$ (with $D = 5.08$ m for the Hale telescope). This particular ability to detect faint off-axis structures within the diffraction limit of the telescope makes it complementary to both coronagraphy and long baseline interferometry. In this section, we present the first on-sky result that we obtained with the PFN during three observing campaigns in 2008 and 2009.

7.3.1 Paper: High Contrast Stellar Observations within the Diffraction Limit at the Palomar Hale Telescope, *B. Mennesson, C. Hanot, E. Serabyn, S. Martin, K. Liewer, F. Loya and D. Mawet*

Early 2008, the PFN was still an experimental instrument requiring commissioning (or engineering) time to test its capabilities and reliability when used at the telescope. We received a total of 3×2 engineering nights on the Hale telescope (Palomar observatory) for which the PFN is designed. In order to calibrate the instrument, we decided to use the PFN for measuring the stellar diameter of 8 red-giant stars of various angular diameters ranging from 14 to 44 mas. By comparing our results with the diameter measurements previously done by long baseline interferometry (LBI), we could characterize the accuracy of the PFN for astrophysical null depth ranging from slightly under 1% up to almost 10%. In the following paper (submitted to ApJ), we demonstrate that, by combining the use of the PFN together with the null self-calibrated method (Hanot et al. 2011), it is possible to reach similar accuracies on the measurement of stellar angular diameters with our nulling interferometer and a 3.4 m baseline than with "classical" long baseline interferometers. Apart from taking care of the installation and alignment of the instrument on the telescope for the various observing runs, my scientific contribution to this work has been to develop the data reduction pipeline for the PFN based on the statistical data reduction method (Hanot et al. 2011). I then used this pipeline to reduce the interferometric data and compute realistic error bars on our measurements, leading to the results presented in this paper.

Draft version February 11, 2011
Preprint typeset using LaTeX style emulateapj v. 11/10/09

HIGH CONTRAST STELLAR OBSERVATIONS WITHIN THE DIFFRACTION LIMIT AT THE PALOMAR HALE TELESCOPE

B. Mennesson[2], E. Serabyn[2], C. Hanot[1],S. Martin[2], K. Liewer[2], F. Loya[2], D. Mawet[2]
[1]AEOS, University of Liège,
Allée du 6 Août, 17 Bât B5c, 4000 Liège, Belgium and
[2]Jet Propulsion Laboratory, California Institute of Technology,
4800 Oak Grove Drive, Pasadena, California 91109, USA

Draft version February 11, 2011

ABSTRACT

We report on high accuracy high resolution (< 20mas) stellar observations obtained with the Palomar Fiber Nuller (PFN), a near infrared ($\simeq$ 2.2 microns) interferometric coronagraph installed at the Palomar Hale telescope, which uses destructive interference between two elliptical (3 m x 1.5 m) sub-apertures of the primary to reach high dynamic range inside the diffraction limit of the full telescope. In order to validate the PFN's instrumental approach and its data reduction strategy - based on the newly developed "Null Self-Calibration" (NSC) method -, we observed a sample of eight well characterized bright giants and supergiants. The quantity measured is the source astrophysical null depth, or equivalently the object's visibility at the PFN interferometric baseline. For the targets α Boo, α Her, β And and α Aur, PFN measurements are in excellent agreement with previous stellar photosphere measurements from long baseline interferometry. For the mass losing stars β Peg, α Ori, ρ Per and χ Cyg, circumstellar emission and/ or asymmetries are detected. Overall, these early observations demonstrate the PFN's ability to measure astrophysical null depths below 10^{-2} (limited by stellar diameters), with $1\,\sigma$ uncertainties as low as a few 10^{-4}. Such visibility accuracy is unmatched at this spatial resolution in the near infrared, and translates into a contrast better than 10^{-3} within the diffraction limit. With further improvements anticipated in 2011 - a state of the art infrared science camera and a new extreme adaptive optics (AO) system -, the PFN should provide a unique tool for the detection of hot debris disks and young self-luminous sub-stellar companions in the immediate vicinity of nearby stars.

Subject headings: infrared: stars — instrumentation: coronagraphs — stars: circumstellar matter — stars: individual (α Boo, α Her, β Peg, β And, α Ori, ρ Per, α Aur, χ Cyg)

1. INTRODUCTION

High contrast at high angular resolution is required in various fields of astrophysics, notably for the direct imaging and spectroscopic characterization of exo-planetary systems, where faint planets or debris disks are located in the close vicinity ($\simeq$ 0.1 to $\simeq$ 5AU) of their much brighter parent stars. While a few recent detections have been made in the favorable case of young self-luminous exoplanets in relatively wide orbits (Kalas et al. 2008; Marois et al. 2008a; Lagrange et al. 2010), the inner planet forming region remains unexplored at high contrast.

Near infrared coronagraphs working with current-generation AO systems mounted on large (diameter D > 5 m) ground based telescopes have inner working angles limited to 300 mas or more. In the case of traditional Lyot coronagraphs (Liu et al. 2009; Hinkley et al. 2007), this limit is directly fixed by the size of the occulting focal plane mask. In the case of phase coronagraphs, the current practical resolution limit for high contrast (say 10^{-4} or better) imaging at near infrared wavelengths on large telescopes is also $\simeq$ 5 to 10 λ/D because of residual wavefront errors (Boccaletti et al. 2004). Operation closer to the axis ($\simeq \lambda/D$) is only possible with extreme AO, such as is demonstrated by observations with a 1.5 m diameter well corrected subaperture (Serabyn et al. 2010). Future coronagraphs such as SPHERE (Boccaletti et al. 2008) and GPI (Marois et al. 2008b), using extreme AO on large 8 m telescopes, will soon allow improved performance close to the optical axis. However, even with these next generation instruments, high contrast in the near infrared will only be available at $\simeq$ 2 to 3 λ/D.

Near infrared interferometry operates in a very different angular regime. The resolution ranges from 20 to 30 mas when using sub-apertures of 5 to 8 m telescopes, to a mas or better using separate telescopes. However, due to calibration difficulties, the contrast of ground based interferometers, whether relying on visibility or phase closure measurements has so far been limited to a few 10^{-3} at best (Absil 2006; Colavita et al. 2009; Duvert et al. 2010; Zhao et al. 2008). Clearly, some new advances are needed in order to bridge the traditional gap between coronagraphs, limited in angular resolution, and long baseline interferometers, limited in dynamic range. This is the object of the fiber nulling technique, which allows deep cancellation of the on-axis light gathered by two (or more) apertures, and the detection of faint nearby sources. In principle, the approach can be equally applied to long baseline interferometers or to sub-apertures of a large telescope. The technique was validated in the laboratory, using monochromatic visible light (Haguenauer & Serabyn 2006) initially, and then broadband near infrared light in H (Mennesson et al. 2006) and K (Martin et al. 2008) bands. In the sim-

bertrand.mennesson@jpl.nasa.gov

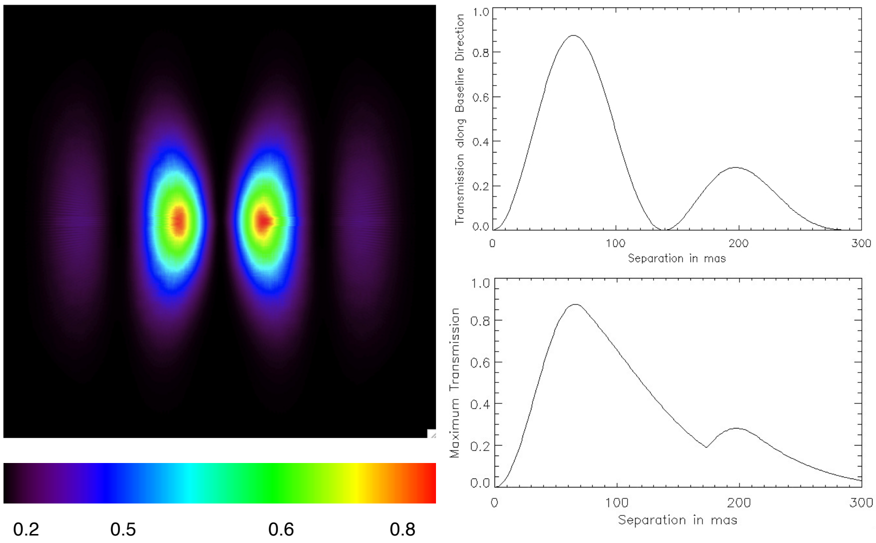

FIG. 1.— Left: PFN sky transmission over 0.6" x 0.6" field of view, assuming a "horizontal" 3.20 m baseline separating two elliptical sub-apertures (3 m x 1.5 m). Top right: PFN transmission vs separation, along baseline direction. Bottom right: Maximum transmission versus baseline rotation angle, as a function of separation.

ple case of two beams, the principle is to combine them into a single-mode fiber while maintaining a π differential phase shift. Multi-axial and co-axial recombination schemes equally work, as long as the various beams are finally injected into a common single-mode fiber. Since the individual apertures wavefronts are spatially filtered by the fiber, the accessible cancellation level is primarily fixed by the residual optical path difference (OPD) between the two apertures, and *not* by the individual wavefront errors (Mennesson et al. 2002a). This fundamental property allows the occurrence of frequent deep quasi-instantaneous (a few ms) cancellation levels, even when the individual stellar wavefronts are characterized by the Strehl ratio of current AO systems ($\simeq$ 50% at K band). Nulling two apertures of diameter d separated by a distance b, on-axis sources are cancelled out, while the half power transmission point corresponds to an off-axis separation $\lambda/4$b, providing sensitivity to sources well within the diffraction limit of single telescopes. The field of view is limited by the single-mode fiber to $\simeq$ λ/d at FWHM.

As an initial validation of the technique on the sky, we have installed a fiber nulling system on a single telescope, at the Palomar 200 inch. This so-called "Palomar Fiber Nuller" (or PFN) was built as a technological demonstrator and restricted to the observations of *very bright stars*. After a presentation of the optical set-up, we detail the observing methodology and the data reduction strategy specifically developed for the PFN. Finally, as a verification of the technique against existing measurements, we discuss the results obtained in 2008 and 2009 on eight well known giants and supergiants.

2. OPTICAL SET-UP AND METHODOLOGY

A full description of the PFN hardware is given in a recent technical design and performance paper (Martin et al. 2008). The PFN system observes in K band ($\simeq$ 2.2 microns) and uses two elliptical 3m x 1.5m sub-apertures located a distance b=3.20 m apart. Its sky transmission pattern is represented in Figure 1, showing a 50% transmission point at 35 mas, to be compared with the 200 mas FWHM sub-aperture field of view, and the full telescope 90 mas PSF. In essence, a fiber nuller system mounted on a large telescope offers a natural complement to a traditional coronagraph: from a resolution standpoint, it starts working where a regular coronagraph stops and vice versa. In fact, when used on a single telescope, a fiber nuller system could in principle be fed by an optical stop reflecting the very central part of the field (e.g. inner 2-3 λ/D) and hence work in conjunction with a regular coronagraph.

The PFN optical set-up is illustrated in Figure 2. It is mounted on a stand alone 4' x 2' bread-board inserted downstream of the Palomar AO system, in place of the standard near infrared PHARO camera. Under average seeing conditions and for the bright stars considered here, the AO system (Troy et al. 2000) delivers to the PFN an input wavefront with a typical 200 to 250 nm rms figure in the K band. The AO system can be thought at as a first order fringe tracker, maintaining the relative phase difference between the two beams to be nulled. After the AO bench, a fold mirror delivers the f/16 converging beam to the PFN. After collimation, the stellar beam first goes through a "K-mirror" used to rotate the pupil with respect to the PFN. The beam subsequently goes through a fixed mask with two elliptical holes defining the fiber nuller sub-apertures (3 m x 1.5 m equivalent sizes on the primary) and interferometric baseline (3.20 m equivalent length on the primary). A split mirror allows independent control of the beams optical paths and directions. A dichroic inserted in each of the 2 sub-beams (denoted "A" and "B") provides angle tracking in the J band. The K band science beams go through a spatial chopper providing alternate measurements of dark ("D", including detector and background contributions), interferometric ("A+B") and individual (A, B) beam intensities (Figure 4) over cycles of $\simeq$ 200 ms.

A chevron shaped piece of infrasil glass brings the two science beams closer to each other (for better injection

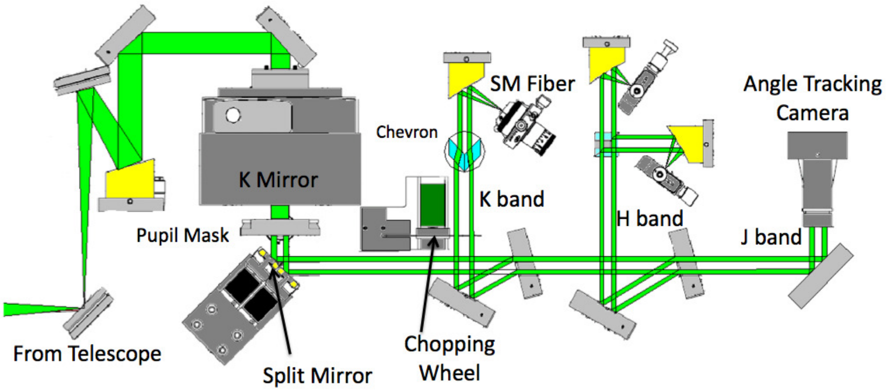

FIG. 2.— Palomar Fiber Nuller optical layout. The pupil rotator (”K mirror”) rotates the image of the fixed pupil mask on the telescope primary. H band light fringe tracker operational in the laboratory, but not tested on the sky. The K band single-mode fiber’s output is detected on a single pixel photometer (unshown). See text for details.

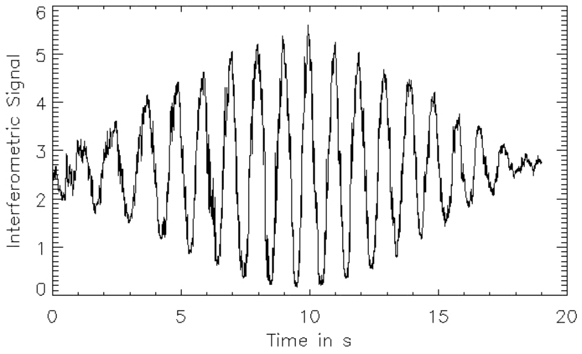

FIG. 3.— Fringe scan recorded on α Her by varying the OPD in one arm of the PFN (raw data sampled every 10 ms). AO correction and J band angle tracking typically stabilize the individual beams photometry at the 3-10% rms level over five minutes. Such interferograms are used to locate the central fringe (best null) position

efficiency into the fiber, typically 40%) and introduces a constant differential glass thickness between the beams. This differential thickness is set to the value minimizing the wideband null over the K band, using same principle as previously demonstrated in N band (Mennesson et al. 2003). Finally, a common off-axis parabola is used for recombination, injecting the two beams into a single-mode fiber. The fiber output is then re-imaged onto a fast single-pixel infrared (InGaAs) photometer. For a given target, the observations start by optimizing the flux injected into the fiber for each of the sub-beams using the two tip-tilt mirrors of the PFN. While the stellar position is maintained on the angle tracking camera (J band), the optical path difference (OPD) between the beams is scanned via a PZT driven mirror (split mirror), and a broadband interferogram is recorded on the K band detector (Figure 3). This fringe scan allows the determination of the central fringe (deepest broadband null) position and the instrument phase is set at this ”null” OPD position. Typically 1 to 5 minute long chopped sequences are then recorded per target, alternating rapidly between individual beams, dark and null signal measurements. In the cases of α Her and β Peg, the K-mirror was rotated to provide different baseline orientations on the sky and to begin to test the baseline rotation and signal modulation aspects.

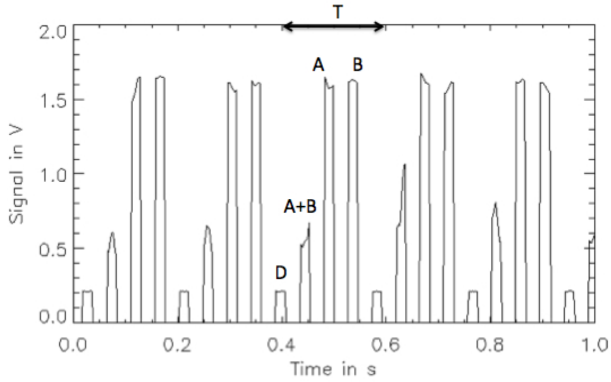

FIG. 4.— Chopped signal recorded on α Her. Cycle period: T=186 ms, sampling interval = 2 ms. Five successive cycles are shown, each with alternate measurements of dark (”D”, including detector and background contributions), interferometric (”A+B”) and individual (”A”, ”B”) beam intensities. Data recorded around beam transitions are discarded.

3. PFN’S OBSERVABLE AND DATA REDUCTION

Given a series of $\simeq$ 200 ms long cycles (Figure 4), each consisting of successive dark (D), interferometric (A+B) and individual (A,B) measurements, one computes two quantities: the observed instantaneous null depth $N_{obs}(t)$, and the model null depth $N_{model}(t)$. Appendix 1 shows in details how these two quantities are generated from the data, and presents our data reduction technique, using the statistical distributions of each of these two quantities rather than their instantaneous or mean values. The basic idea is that although none of the instrumental error terms are monitored at the exact time of a null measurement, their probability distributions can be accurately determined by using values recorded at slightly different times (inside the same chop cycle). A full description of this statistical data analysis method, including its first sky performance assessment and anticipated limitations, is presented in a recent paper (Hanot et al. 2011). An essential result is that when modeling the whole distribution of observed null values, one can very efficiently separate the instrumental effects from the underlying astrophysical null depth N^a. Another major advantage of the method, which we refer to as null (or visibility) self-calibration (NSC), is that to first order, no observations of calibrator stars are needed

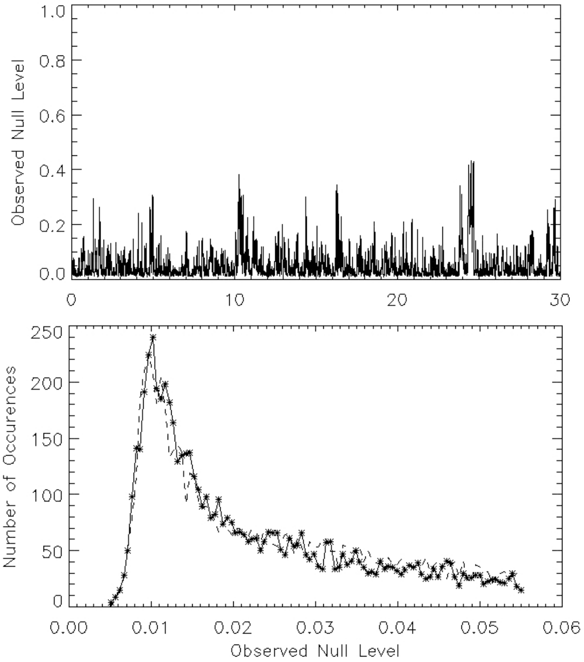

Fig. 5.— Top: null sequence obtained on β Peg (typical results, July 2009). Bottom, plain curve: observed null histogram. Bottom: dashed curve: best fit model null histogram. The best fit parameters are: $N^a = 0.0089 \pm 0.0004$, mean differential phase = 0.29 radian, differential phase rms = 0.48 radian. Best fit χ^2 = 1.12.

to estimate the instrumental effects. As an example, Figure 5 shows a typical null sequence and the result of a null distribution fit in the case of PFN observations of β Peg. Three parameters - and their associated error bars- are retrieved from the modeling: the astrophysical null depth, located close to the distribution peak position, as well as two instrumental parameters: the differential phase mean value and standard deviation over the sequence.

The agreement between the observed and best fit modeled distributions is generally excellent, with reduced χ^2 consistently around unity for all observations reported hereafter, making us confident that the modeling approach is sound. We described the NSC method and presented a first analysis of its applicability to the PFN data in Hanot et al. 2011. This previous work concentrated on observations of α Boo, showing that the derived null depths were extremely reproducible, and suggesting that any bias, if present at all in these particular measurements, is at the few 10^{-4} level or lower. In the following section, we seek to confirm this result on a larger sample of stars observed with the PFN, and better establish the current accuracy of the method.

4. RESULTS AND INTERPRETATION

We carried astronomical test observations of resolved giants and supergiants already well characterized by long baseline interferometry (LBI) at 2.2 microns, some of them with previously detected excess emission above the photosphere. Our objective here is to explore both the repeatability of the measurements (precision assessment), and their consistency with values reported by LBI (accuracy and bias assessment). Table 1 summarizes the astrophysical nulls measured by the PFN on eight stars over five nights: July 21 2008, November 11 & 12 2008, and July 10 & 11 2009. The 2009 data were obtained with an upgraded angle tracking camera and an achromatic beam recombination system, providing better null accuracy (typically 0.1% rms or better). To analyze the measurements, we use the relationships established in Appendix 2, which link the observed astrophysical null depth to the source physical characteristics in a few simple cases: uniform disks, limb darkened disks and binary systems.

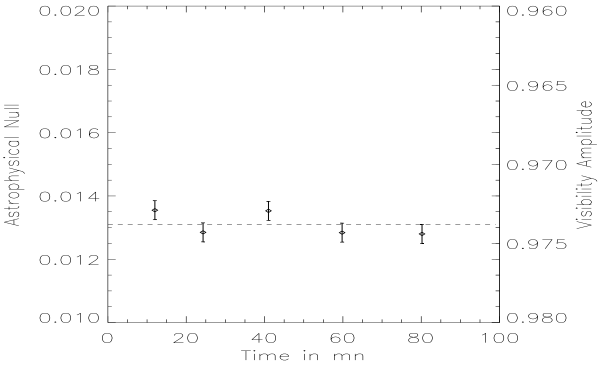

Fig. 6.— Astrophysical null depth (left vertical axis) and corresponding object's visibility (right vertical axis) measured as a function of time for α Boo. No calibrator star is used, visibilities are derived using the null self-calibration technique. All individual null error bars are about 0.0003. The overall astrophysical null estimate is 0.0132 ± 0.00013, or equivalently V= 0.9739 ± 0.00026. The dashed line indicates the expected null depth (or visibility) at the PFN baseline, using α Boo's limb darkened diameter measured independently by near infrared long baseline interferometry (Perrin et al. 1998).

As discussed in section 3, some instrumental parameters can also be derived from the observed null distributions, in particular the residual phase jitter after AO correction.The derived K band phase jitter ranges from 0.3 radian ($\simeq$ 100 nm) rms under good seeing conditions (July 2009) to 0.6 radian ($\simeq$ 200nm) rms under bad seeing conditions (November 2008). Taking into account the spatial averaging of the phase over each sub-aperture, these figures are well aligned with the AO performance, which predicts a typical residual wavefront rms error of 200 to 250 nm over the full telescope aperture.

4.1. *Individual stars results*

4.1.1. *α Boo*

Figure 6 shows a series of five consecutive null, or equivalently, visibility measurements obtained on α Boo over a period of an hour. The peak to peak variation of measured null values is 0.0007, illustrating the precision of the NSC data processing and the stability of the measurements. The astrophysical null depth derived for α Boo, using no calibrator observations, is 0.0132 ± 0.00013. The error bar quoted here comes purely from propagating the statistical errors determined on each individual measurement, assuming that each of them is affected by a zero mean gaussian noise, i.e. that there is no systematic errors (Hanot et al. 2011).

In comparison, the most accurate long baseline inter-

TABLE 1
Summary of PFN observations of giants and supergiants

Star	Type	Az	N_m^a	σ_m	N_p^a	σ_p	Excess	Date	Chop
α Boo	K1.5III	117	0.0132	0.00013	0.0131	0.0001	No	07/10/09	y/n
α Her	M5Iab	117	0.0306	0.0010	0.0316	0.0014	No	07/10/09	y/n
		72	0.0335	0.0010	0.0316	0.0014	No	07/10/09	n
		162	0.0333	0.0010	0.0316	0.0014	No	07/10/09	n
		all	0.0325	0.0016	0.0316	0.0014	No	07/10/09	y/n
β Peg	M2.5II-III	87	0.0089	0.0004	0.0082	0.0002	No	07/10/09	y
		117	0.0113	0.0007	0.0082	0.0002	Yes	07/11/09	y
β And	M0III	57	0.0070	0.0009	0.0061	0.0002	No	07/11/09	y
α Ori	M2Iab	117	0.081	0.004	0.066	0.0003	Yes	11/11/08	y/n
ρ Per	M4II	117	0.074	0.007	0.0083	0.0002	Yes	11/12/08	y
α Aur	G8III + G1III	72	0.052	0.004	0.051	< 0.001	No	11/12/08	n
χ Cyg	S Mira	117	0.029	0.0025	0.019	< 0.001	Yes	07/21/08	n

Note. — Az is the baseline azimuth measured in degrees East of North. Circumstellar excess is reported when the astrophysical null N_m^a measured by the PFN is at least $3\,\sigma$ above the "photospheric" null N_p^a predicted for naked stars by LBI. $\sigma = \sqrt{\sigma_m^2 + \sigma_p^2}$, where σ_m and σ_p indicate the uncertainties on the measured PFN nulls and on the predicted photospheric nulls, respectively. Date format is dd/mm/yy. The "chop" column indicates whether fast chopping between the beams was enabled during the observations. 2009 data exhibit better accuracy thanks to hardware improvements. Targets labeled in italic (*β Peg, α Ori, ρ Per* and *χ Cyg*) are variable mass losing stars. All four show significant excess emission in the PFN measurements, while none of the other stars does.

ferometric observations of α Boo, carried at IOTA with the FLUOR instrument, determine a limb darkened (LD) diameter of 20.91 mas ± 0.08 mas (Perrin et al. 1998), and an effective temperature of 4300 K. Further observations (Lacour et al. 2008) also conclude that no strong photometric asymmetry or bright stellar companion is present in the immediate stellar environment (within $\simeq$ 1 AU). Using the 0.350 linear limb darkening coefficient predicted in the K band for a 4300K giant star with log g =2.0 (Claret et al. 1995) and equation 14 of Appendix 2, α Boo's expected astrophysical null depth is then 0.0131 ± 0.0001 at the PFN baseline, in excellent agreement with the observed value. Taking into account the transmission pattern of the PFN (figure 1), our 1σ null uncertainty of 1.3 x 10^{-4} translates into an upper (3-sigma) limit of 8 x 10^{-4} on the K band relative brightness of a companion located 35 to 100 mas away (along the baseline direction), i.e. between 0.4 AU and 1.1 AU at α Boo's distance. This limit is comparable to the 8 x 10^{-4} companion brightness upper limit derived at 1 AU from H band visibility and phase closure measurements using the IOTA 3 telescope interferometer (Lacour et al. 2008). However, the IOTA measurements synthesized a total aperture size of 35 x 15 m., i.e. much larger than the Palomar 5m telescope. This illustrates the point that accurate null measurements do not only provide better contrast. They also provide better spatial resolution for a given baseline since smaller sources can be reliably resolved.

4.1.2. *α Her*

The astrophysical null depth observed on α Her shows some slight variation versus azimuth angle. This could reflect some photospheric asymmetries or the presence of a companion in the 300 mas PFN field of view, as previously inferred by visible speckle interferometry (McAlister et al. 1993). However, the null vs azimuth variation measured by the PFN is at the 1.5 sigma level and can not be considered statistically significant. Consequently, we adopt for α Her an astrophysical null of 3.25% ± 0.16%, now covering all observed azimuth angles. Using the linear limb darkening coefficient of 0.436 predicted for α Her physical characteristics (Claret 2000), the LD diameter derived from the PFN null measurement is 33.60 mas ± 0.82 mas. This value is in excellent agreement with the LD diameter of 33.14 mas ± 0.76 mas measured by long baseline interferometry with FLUOR/IOTA (Perrin et al. 2004), yielding a theoretical null of 3.16% ± 0.14% at the PFN baseline.

4.1.3. *β Peg*

β Peg is an M2.5II-III pulsating variable giant, with an effective temperature of 3600 K and log g =1.2, and a predicted limb darkening coefficient of 0.389 (Claret et al. 1995). Some significant null depth variation is detected between the two PFN azimuth positions. At 87 degrees azimuth angle, the observed null depth is 0.0089 ± 0.0004, corresponding to an apparent LD diameter of 17.40 mas ± 0.39 mas. At 117 degrees the astrophysical null depth increases to 0.0113 ± 0.0007, and the apparent LD diameter to 19.60 mas ± 0.61 mas. For comparison, the LD diameter derived for this object from previous long baseline interferometry measurements is 16.75 mas ± 0.24 mas (di Benedetto & Rabbia 1987), corresponding to an astrophysical null of 0.0082 ± 0.0002. The PFN measurements show excess emission at one azimuth (4.5σ detection) and asymmetries at the $\simeq$ 10% level. This could be either due to extended atmospheric layers or to the presence of a companion contributing at least 0.3% of the K band flux. Interestingly, β Peg is already known to host a warm ($\simeq$1500K) H_2O upper outside layer, with column density of the order of 2 10^{18} molecules.cm^{-2} (Tsuji 2001). Rather than actual photospheric asymmetries, the observed null depth fluctuation may then reflect variations of the upper molecular layer's opacity with respect to azimuth.

4.1.4. *β And*

β And is an M0 giant with a temperature of 3800 K and log g =1.5, and a predicted limb darkening K band coefficient of 0.383 (Claret et al. 1995). The PFN null value is 0.70% ± 0.09%, yielding (Eq. 14) a LD diameter of 15.40 mas ± 0.99 mas. In comparison, the LD diameter measured by long baseline interferometry (di Benedetto & Rabbia 1987) is 14.35 mas ± 0.19 mas (di Benedetto & Rabbia 1987), yielding an expected null depth of 0.61 % ± 0.02%. The PFN and LBI measurements consequently agree at the 1 σ level.

4.1.5. *α Ori*

α Ori is a famous and well studied semi-regular pulsating bright supergiant, for which we measure an astrophysical null of 8.1% ± 0.4%. In comparison, the most accurate K band limb darkening measurements of α Ori's photosphere (θ_{LD}=43.65 ±0.10 mas, and A=0.090), obtained through long baseline interferometric observations on IOTA (Perrin et al. 2004), yield a null depth of 6.6% ± 0.03% at the PFN's baseline. This is significantly lower than our observed value, pointing to some extra source of emission above the photosphere. Following the "MOLsphere" model also suggested by Perrin et al. for this star, which incorporates an upper geometrically thin 2050 K molecular layer located 0.33 stellar radius above the photosphere with a 0.06 K band opacity, the null depth increases to 7.0%. The properties of such a layer may obviously have changed since the IOTA observations, and our single null measurement does not allow the various parameters to be individually constrained. As an illustration, an upper layer with the same characteristics but located at a higher altitude (0.66 R^{*}) could reproduce the observed 8.1% null depth.

4.1.6. *ρ Per*

ρ Per is an M4II semi-regular variable star with an effective temperature of $\simeq$ 3500 K and log g =0.8, yielding an estimated limb darkening K band coefficient of 0.394 (Claret et al. 1995). The PFN measures an astrophysical null value of 7.4% ± 0.7%, which is considerably larger than the value of 0.83% ± 0.02% expected using its measured LD diameter (16.75 mas ± 0.24 mas (di Benedetto & Rabbia 1987)). This is the largest excess above photospheric emission observed among the stars in our sample, pointing to a possible recent mass loss event since the measurements reported by Di Benedetto & Rabbia. More observations are required to constrain the source of extra emission, but extended outer molecular layers are expected around this kind of semi-regular M giants and could be responsible for the observed excess.

4.1.7. *Capella*

α Aurigae (Capella) is a bright nearby (12.9 pc) binary system (G8III / G1III), with the two components close to equally bright in the visible. The most recent parameters derived from radial velocity measurements (Torres et al. 2009) provide a primary diameter of 8.50 mas and a secondary diameter of 6.27mas, with respective effective temperatures of 4920K and 5680K. Assuming blackbody emission, this yields a K band secondary to primary flux ratio r= 0.70. At the time of the PFN observations (besselian epoch=2008.8666), the derived (Hartkopf & Mason 2006) separation is 41.5 mas, for an azimuth of 135.5 degrees East of North. This is 63.5 degrees with respect to the PFN baseline. Using these orbital parameters together with the stellar data from Torres et al., equations (8) and (15) yield an expected null depth of 5.1% for this binary system. This prediction is in very good agreement with our observed value of 5.2% ± 0.4%. It is worth noting that if Capella A had been the only star in the fiber's field of view, the observed astrophysical null would have been only 0.26%. This clearly illustrates the PFN's ability to detect companions well within the diffraction limit.

4.1.8. *χ Cyg*

χ Cyg is a well studied S-type Mira star, with extended upper atmospheric molecular layers (mostly CO in our bandpass) evidenced by many high spatial resolution observations (Young et al. 2000; Mennesson et al. 2002b; Lacour et al. 2009). In particular, Lacour et al. have used the IOTA interferometer in H band to measure precise time-dependent values of the stellar diameter, and evidenced the presence and displacement of a warm molecular layer. According to these measurements, the stellar radius, corrected for limb darkening, has a mean value of 12.1 mas and shows a 5.1 mas amplitude pulsation. Using the sinusoidal fit of diameter versus phase derived from these IOTA observations, we get for χ Cyg a LD diameter of 23.24 mas at the time of the PFN measurements (variability phase =0.72). Adopting at K band, the same limb darkening power law as was measured in H band by Lacour et al. ($\alpha \simeq 2.5$), and using equations 8 and 11, the null depth would be 1.88% at the PFN baseline. Assuming instead that there is no limb darkening in the K band, the null increases to only 1.96%, which provides an upper limit to the null expected from the photosphere alone.

The PFN null value of 2.9% ± 0.25% is significantly larger, most likely reflecting extra emission from circumstellar regions and layers. Considering a single spherical molecular layer with a 33 mas diameter and a stellar temperature of 2500 K, (typical values derived by Lacour et al. around a luminosity phase of 0.72), we find that a layer contributing 11% of the total K band flux reproduces the null observed by the PFN. Interestingly, the same layer would contribute 8.9% of the total H band flux, a value very well aligned with the findings of IOTA.

4.2. *Discussion*

Figure 7 compares the stellar nulls measured by the PFN to the values expected from near IR long baseline interferometric measurements of the stellar photospheres. The agreement is excellent for standard giants and supergiants (α Boo, α Her, β And), and for the well studied binary system α Aur. In all four cases, the discrepancy between the observed and expected null values is smaller than 0.1%, and well within the error bars derived from the PFN and LBI measurements. The weighted mean difference between the two types of measurements (PFN - LBI) is + 2.1 10^{-4}, with a weighted

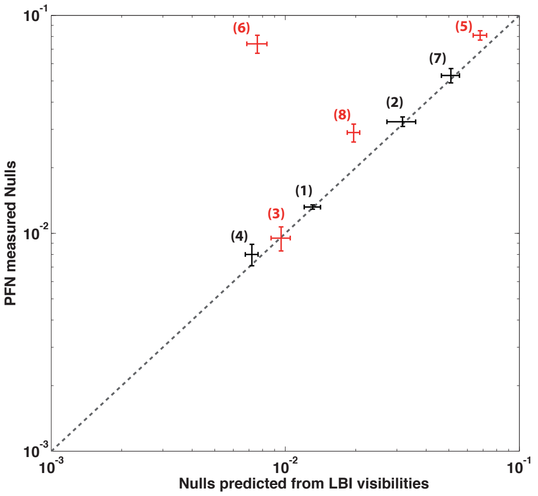

FIG. 7.— Stellar nulls measured by the Palomar Fiber Nuller compared to values expected from near IR long baseline interferometry (LBI) and stellar modeling (photosphere only). (1): α Boo (Perrin et al. 1998; Lacour et al. 2008), (2): α Her (Perrin et al. 2004), (3): β Peg (di Benedetto & Rabbia 1987), (4): β And (Richichi et al. 2005), (5): α Ori (Perrin et al. 2004), (6): ρ Per (Richichi et al. 2005), (7): α Aur (Torres et al. 2009; Hartkopf & Mason 2006), (8): χ Cyg (Lacour et al. 2009). Departure from naked photosphere models is found for three of the Miras and semi-regular variable stars (red), all of which known to exhibit extended outer molecular and dust shells (α Ori, ρ Per and χ Cyg) above the photosphere. The large discrepancy measured on ρ Per suggests a recent mass loss event.

standard deviation of 3.1 10^{-4}. These overall results indicate that the fiber nulling approach not only produces repeatable null or visibility measurements, but accurate ones, with no noticeable bias down to the few 10^{-4} level. This confirms our previous accuracy estimation based on α Boo data only (Hanot et al. 2011): the fiber nuller data acquisition and reduction strategies allow very accurate null (and visibility) measurements. Without any observation of calibrator stars, the typical accuracy is already an order of magnitude better than that obtained by the long baseline interferometers, whose best reported null accuracy is 0.2% in the mid-infrared, and about 0.25% in the near infrared (i.e. 0.5% rms visibility accuracy (Kervella et al. 2004)).

Significant departure from centrally symmetric naked photosphere models is only detected for the four variable mass losing stars in the sample, which also makes us confident in the validity of the technique. Some significant excess and variation versus azimuth is detected on β Peg. Clear excesses are detected around α Ori and χ Cyg, which are known to exhibit extended outer molecular layers above the regular photosphere. The large excess measured on ρ Per suggests a recent significant mass loss event, and is reported here for the first time.

The overall consistency of the PFN short baseline results with those obtained by much larger arrays illustrates the point that accurate null measurements do not only provide better contrast. They also provide better spatial resolution for a given baseline since smaller sources can be reliably resolved and characterized.

5. CONCLUSIONS AND PERSPECTIVES

Very precise stellar visibility (or null) measurements have been demonstrated in the near infrared using the fiber nulling approach and a dedicated statistical data analysis (NSC) at Palomar. In an effort to assess the absolute accuracy of the method, we have compared our results to those provided by long baseline interferometry (LBI) on eight bright giants and supergiants, and found excellent agreement in all cases. For "well behaved stars", for which no circumstellar excess emission was previously detected, our results are consistent with the high resolution photospheric measurements from LBI, at the few 10^{-4} level. For all of the mass losing stars observed, we either detect slight asymmetries (at the 0.2-0.3% level around β Peg), or excess emission above the photosphere (at the $\simeq 1$ % level around α Ori and χ Cyg, and at much higher level around ρ Per). These results, obtained with a 3.2 m baseline, illustrate the points that (i) accurate null measurements are accessible in the near infrared in spite of much larger phase fluctuations than in the mid-infrared, (ii) accessing better contrast also provides better spatial resolution for a given baseline.

With the Palomar extreme AO system coming on-line in 2011, and with a new state of the art science camera becoming available, simulations indicate that contrasts of the order of 10^{-4} to 10^{-3} should be readily accessible with the PFN on $m_K = 6$ stars, as close as 30 mas from the axis. We will test these predictions and further assess the accuracy limits of the system by observing well known high contrast binary systems, as well as calibrator stars. We will engage in parallel in a survey of bright debris disks around nearby A stars, looking for hot dust populations similar to those recently inferred by long baseline interferometry, but with a higher dynamic range than previously available, typically 10^{-3} or better.

Finally, the fiber nuller observing and post processing approach can in principle be extended to separate telescopes using single-mode fibers for recombination, as long as a fringe tracker with standard performance ($\simeq$ 200 nm rms jitter) and some dispersion capability are available (Mennesson et al. in preparation). We are then studying the application of our approach to long baseline near infrared interferometry, where the issues of dispersion, polarization, phase and intensity fluctuations are more acute than behind a single telescope, but where contrast performance similar to that of the PFN would provide very high resolution observations at unprecedented dynamic range.

Acknowledgments

This work was performed at the Jet Propulsion Laboratory, California Institute of Technology, under contract with NASA. The data presented are based on observations obtained at the Hale Telescope, Palomar Observatory, as part of a continuing collaboration between Caltech,NASA/JPL, and Cornell University. We wish to thank the Palomar Observatory staff for their assistance in mounting the PFN and conducting the observations at the Hale telescope.

Appendix 1: Observed Null Depth and Statistical Modeling

Given a series of $\simeq$ 200 ms long chop cycles (Figure 4), each consisting of successive dark ("D"), interferometric

("A+B") and individual ("A", "B") measurements, one computes the quantities:

$$\hat{I}_N(t) = (A+B)(t) - \hat{D}(t) \tag{1}$$

$$\hat{I}_1(t) = \hat{A}(t) - \hat{D}(t) \tag{2}$$

$$\hat{I}_2(t) = \hat{B}(t) - \hat{D}(t) \tag{3}$$

$$\hat{I}_P(t) = \hat{I}_1(t) + \hat{I}_2(t) + 2\sqrt{\hat{I}_1(t).\hat{I}_2(t)} \tag{4}$$

$$N_{\rm obs}(t) = \frac{\hat{I}_N(t)}{\hat{I}_P(t)} \tag{5}$$

Within a given cycle, the quantity (A+B)(t) is the instantaneous interferometric signal (close to null) recorded every 2 ms, while Â(t), B̂(t) and D̂(t) are the measured averages of A, B and D over the same cycle. $\hat{I}_N(t)$, $\hat{I}_P(t)$, $\hat{I}_1(t)$ and $\hat{I}_2(t)$ serve as estimates of the instantaneous null, peak and individual stellar signals $I_N(t)$, $I_P(t)$, $I_1(t)$ and $I_2(t)$ at the time of an (A+B) interferometric measurement. $N_{\rm obs}(t)$ is the observed normalized instantaneous null depth, as derived from the measured chopped signals.

In the case of the PFN, the two beams are injected into a *common* single-mode fiber. Neglecting any differential polarization effects in the beam train, the recorded interferometric signal (A+B)(t) can be approximated by:

$$\begin{aligned}(A+B)(t) = {} & I_1(t) + I_2(t) \\ & + 2|V|.\sqrt{I_1(t)I_2(t)}.\cos(\phi(t)+\phi_V) + D(t)\end{aligned} \tag{6}$$

Where $|V|$ is the complex modulus of the source visibility at the PFN's baseline, ϕ_V its phase (zero for a symmetric and mostly unresolved source), and $\phi(t)$ the instantaneous differential phase between the beams. Writing $\phi(t)+\phi_V=\pi+\Delta\phi(t)$, where $\Delta\phi(t)$ is the phase offset from null, and using equations 1 to 6, $N_{\rm obs}(t)$ can then be modeled as:

$$\begin{aligned}N_{\rm model}(t) = {} & \frac{I_1(t) + I_2(t) - 2|V|.\sqrt{I_1(t)I_2(t)}.\cos(\Delta\phi(t))}{\hat{I}_P(t)} \\ & + \frac{(D(t) - \hat{D}(t))}{\hat{I}_P(t)}\end{aligned} \tag{7}$$

As the astrophysical null depth N^a relates to the object's complex visibility V according to:

$$N^a = \frac{1-|V|}{1+|V|}, \tag{8}$$

visibilities and astrophysical null depths can be used equivalently. Since the astrophysical null depth accuracy directly represents the accessible dynamic range of the instrument, we report all observations here in terms of the astrophysical null, as is usually done in nulling interferometry. This is also more convenient when working at source visibility values close to 1, which is the case of the PFN observations.

All PFN data are analyzed using the general expression above (equation 7) and proceeding as follows. A temporal sequence of model nulls $N_{\rm model}(t)$ is generated, with the same length as the observed sequence $N_{\rm obs}(t)$. In this model sequence, the instantaneous dark D(t) and individual stellar intensity signals $I_{1,2}(t)$ are unknown at the time of a given null measurement (A+B)(t). We use instead their instantaneous values recorded at slightly different times inside the same chop cycle: D(t'), $I_1(t'') = A(t'') - \hat{D}(t)$ and $I_2(t''') = B(t''') - \hat{D}(t)$. For the instantaneous differential phase term $\Delta\phi(t)$, gaussian statistics are assumed over the sequence - in good agreement with studies of residual phase after AO correction (Cagigal & Canales 2000) - , and a corresponding random phase vector is generated. The distribution of model null values is then computed and fitted to the distribution of observed null values. In practice, if $P_{\rm obs}(N_i)$ is the observed null probability density around null value N_i and $P_{\rm model}(N_i)$ is the modeled one, one performs a goodness of fit test by forming the Pearson χ^2 quantity:

$$Q = \sum_i \frac{(P_{\rm obs}(N_i) - P_{\rm model}(N_i))^2}{P_{\rm model}(N_i)} \tag{9}$$

The remaining free parameters of the model distribution, which are not directly derived from the chopped data, are the object's astrophysical null (or equivalently its visibility modulus), the differential phase mean and standard deviation values. For each value of these parameters, one generates a null sequence $N_{\rm model}(t)$ and computes the corresponding distributions. The three unknown parameters are then determined by minimizing the reduced χ^2, which is found consistently between 1.0 and 1.3. The associated statistical 1 σ error bars are computed using the χ^2 statistical properties. However, this error bar estimation method is only valid if the observed null distribution ($P_{\rm obs}(N_i)$) is affected by a zero mean gaussian noise. We then also conduct a bootstrapping analysis -independent of the actual noise properties -, resampling and replacing the observed null values, hence generating many (500) "fake" sequences. Analyzing the corresponding histograms yields astrophysical null 1σ (68.3% confidence interval) uncertainties similar to those derived using the traditional χ^2 approach. This statistical data analysis is conducted for all null sequences obtained with the PFN. A complete description of this method, referred to as numerical null self-calibration, is given in a recent paper (Hanot et al. 2011).

Finally, we note that in the case of deep nulls ($N_{\rm obs}(t) << 1$), the effects of the various instrumental and astrophysical terms can be separated, and the model null expression reduces to:

$$\begin{aligned}N_{\rm model}(t) = {} & (N^a + \frac{(\delta I)^2(t)}{4} + \frac{(\Delta\phi)^2(t)}{4}).(\frac{I_P(t)}{\hat{I}_P(t)}) \\ & + \frac{(D(t) - \hat{D}(t))}{\hat{I}_P(t)}\end{aligned} \tag{10}$$

where several instrumental null terms come into play. The main contributors (always positive) are the beam intensity mismatch term in $(dI)^2$(t), - with dI defined as $dI(t) = [I_1(t) - I_2(t)]/[I_1(t) + I_2(t)]$ -, and the phase mismatch term in $(\Delta\phi)^2(t)$, where $\Delta\phi$ is the instantaneous phase difference between the beams (referred to π). The $(\frac{I_P(t)}{\hat{I}_P(t)})$ term shows the effect of an imperfect estimation of the peak signal on the observed null, while the $\frac{(D(t)-\hat{D}(t))}{\hat{I}_P(t)}$ term shows the impact of the dark signal uncertainty.

Appendix 2: Astrophysical Null Depth Expressions

Denoting by $I(\vec{\theta})$ the observed sky brightness distribution, including both the source spatial brightness distribution and the lobe antenna of the fiber, the object complex visibility V is defined as:

$$V(\lambda) = \frac{\int I(\vec{\theta}) e^{j.2\pi\vec{B}.\vec{\theta}/\lambda} d\vec{\theta}}{\int I(\vec{\theta}) d\vec{\theta}} \tag{11}$$

where B is the interferometric baseline and λ the observing wavelength. In the case of the PFN, B corresponds to the center to center distance between the two elliptical 1.5m x 3m sub-apertures of the primary 5m diameter mirror. Based on the optical model of the telescope and on engineering data, the PFN interferometric baseline is 3.20 m As for the observing wavelength, PFN measurements are made in a waveband covering 2.05 to 2.35 microns. Based on the detector chromatic efficiency and the K band filter transmission curve, the effective (center) wavelength of the PFN is determined to be $\lambda = 2.16$ microns. This effective wavelength exhibits very small variations (<3nm) versus stellar temperature, and is therefore assumed constant for all stars considered here.

When the object is centrally symmetric, one obtains:

$$N^a(\lambda) = \frac{\int I(\vec{\theta}) \sin^2(\pi\vec{B}.\vec{\theta}/\lambda) d\vec{\theta}}{\int I(\vec{\theta}) d\vec{\theta}} \tag{12}$$

In particular, for a naked star represented by a uniform disk (UD) of diameter $\theta^* << \lambda/B$, the observed astrophysical null depth is given by:

$$N^a(\lambda) = (\frac{\pi B \theta^*}{4\lambda})^2 \tag{13}$$

For a more realistic model, in which a naked star is represented by a limb darkened disk of diameter θ^{LD}, with a linear limb darkening coefficient A(λ), the observed astrophysical null depth is (Absil et al. 2011):

$$N^a(\lambda) = (\frac{\pi B \theta^{LD}}{4\lambda})^2 . (1 - \frac{7A}{15}) . (1 - \frac{A}{3})^{-1} \tag{14}$$

Finally, for a binary source, one still has $N^a = (1 - |V|)/(1 + |V|)$, and the complex visibility V is given by:

$$V = \frac{V_1 + r.V_2 e^{j.2\pi\vec{B}.\vec{\theta}_{1-2}}}{1 + r} \tag{15}$$

where V_1 and V_2 are the visibilities derived for each of the two stars, r is their flux ratio at the observing wavelength, and $\vec{\theta}_{1-2}$ is their angular separation.

REFERENCES

????
08. 1
Absil, O. 2006, PhD thesis, University of Liège
Absil, O., den Hartog, R., Gondoin, P., Fabry, P., Wilhelm, R., Gitton, P., & Puech, F. 2011, A&A, In press
Boccaletti, A., Abe, L., Baudrand, J., Daban, J., Douet, R., Guerri, G., Robbe-Dubois, S., Bendjoya, P., Dohlen, K., & Mawet, D. 2008, in Society of Photo-Optical Instrumentation Engineers (SPIE) Conference Series, Vol. 7015, Society of Photo-Optical Instrumentation Engineers (SPIE) Conference Series
Boccaletti, A., Riaud, P., Baudoz, P., Baudrand, J., Rouan, D., Gratadour, D., Lacombe, F., & Lagrange, A.-M. 2004, PASP, 116, 1061
Cagigal, M. P., & Canales, V. F. 2000, J. Opt. Soc. Am. A, 17, 1312
Claret, A. 2000, A&A, 363, 1081
Claret, A., Diaz-Cordoves, J., & Gimenez, A. 1995, A&AS, 114, 247
Colavita, M. M., Serabyn, E., Millan-Gabet, R., Koresko, C. D., Akeson, R. L., Booth, A. J., Mennesson, B. P., Ragland, S. D., Appleby, E. C., Berkey, B. C., Cooper, A., Crawford, S. L., Creech-Eakman, M. J., Dahl, W., Felizardo, C., Garcia-Gathright, J. I., Gathright, J. T., Herstein, J. S., Hovland, E. E., Hrynevych, M. A., Ligon, E. R., Medeiros, D. W., Moore, J. D., Morrison, D., Paine, C. G., Palmer, D. L., Panteleeva, T., Smith, B., Swain, M. R., Smythe, R. F., Summers, K. R., Tsubota, K., Tyau, C., Vasisht, G., Wetherell, E., Wizinowich, P. L., & Woillez, J. M. 2009, PASP, 121, 1120
di Benedetto, G. P., & Rabbia, Y. 1987, A&A, 188, 114
Duvert, G., Chelli, A., Malbet, F., & Kern, P. 2010, A&A, 509, A66+
Haguenauer, P., & Serabyn, E. 2006, Appl. Opt., 45, 2749
Hanot, C., Mennesson, B., Martin, S. R., Liewer, K., Loya, F., Mawet, D., Riaud, P., Riaud, P., Absil, O., & Serabyn, E. 2011, accepted in ApJ
Hartkopf, W. I., & Mason, B. D. 2006, Sixth Catalog of Orbits of Visual Binary Stars
Hinkley, S., Oppenheimer, B. R., Soummer, R., Sivaramakrishnan, A., Roberts, Jr., L. C., Kuhn, J., Makidon, R. B., Perrin, M. D., Lloyd, J. P., Kratter, K., & Brenner, D. 2007, ApJ, 654, 633
Kalas, P., Graham, J. R., Chiang, E., Fitzgerald, M. P., Clampin, M., Kite, E. S., Stapelfeldt, K., Marois, C., & Krist, J. 2008, Science, 322, 1345
Kervella, P., Coudé du Foresto, V., Segransan, D., & di Folco, E. 2004, in Society of Photo-Optical Instrumentation Engineers (SPIE) Conference Series, Vol. 5491, Society of Photo-Optical Instrumentation Engineers (SPIE) Conference Series, ed. W. A. Traub, 741–+
Lacour, S., Meimon, S., Thiébaut, E., Perrin, G., Verhoelst, T., Pedretti, E., Schuller, P. A., Mugnier, L., Monnier, J., Berger, J. P., Haubois, X., Poncelet, A., Le Besnerais, G., Eriksson, K., Millan-Gabet, R., Ragland, S., Lacasse, M., & Traub, W. 2008, A&A, 485, 561
Lacour, S., Thiébaut, E., Perrin, G., Meimon, S., Haubois, X., Pedretti, E., Ridgway, S. T., Monnier, J. D., Berger, J. P., Schuller, P. A., Woodruff, H., Poncelet, A., Le Coroller, H., Millan-Gabet, R., Lacasse, M., & Traub, W. 2009, ApJ, 707, 632
Lagrange, A., Bonnefoy, M., Chauvin, G., Apai, D., Ehrenreich, D., Boccaletti, A., Gratadour, D., Rouan, D., Mouillet, D., Lacour, S., & Kasper, M. 2010, Science, 329, 57
Liu, W. M., Hinz, P. M., Hoffmann, W. F., Brusa, G., Miller, D., & Kenworthy, M. A. 2009, ApJ, 693, 1500
Marois, C., Macintosh, B., Barman, T., Zuckerman, B., Song, I., Patience, J., Lafrenière, D., & Doyon, R. 2008a, Science, 322, 1348
Marois, C., Macintosh, B., Soummer, R., Poyneer, L., & Bauman, B. 2008b, in Society of Photo-Optical Instrumentation Engineers (SPIE) Conference Series, Vol. 7015, Society of Photo-Optical Instrumentation Engineers (SPIE) Conference Series

Martin, S., Serabyn, E., Liewer, K., Loya, F., Mennesson, B., Hanot, C., & Mawet, D. 2008, in Society of Photo-Optical Instrumentation Engineers (SPIE) Conference Series, Vol. 7013, Society of Photo-Optical Instrumentation Engineers (SPIE) Conference Series

McAlister, H. A., Mason, B. D., Hartkopf, W. I., & Shara, M. M. 1993, AJ, 106, 1639

Mennesson, B., Crawford, S. L., Serabyn, E., Martin, S., Creech-Eakman, M., & Hardy, G. 2003, in ESA Special Publication, Vol. 539, Earths: DARWIN/TPF and the Search for Extrasolar Terrestrial Planets, ed. M. Fridlund, T. Henning, & H. Lacoste, 525–528

Mennesson, B., Haguenauer, P., Serabyn, E., & Liewer, K. 2006, in Society of Photo-Optical Instrumentation Engineers (SPIE) Conference Series, Vol. 6268, Society of Photo-Optical Instrumentation Engineers (SPIE) Conference Series

Mennesson, B., M., O., & C., R. 2002a, J. Opt. Soc. Am. A, 19, 596

Mennesson, B., Perrin, G., Chagnon, G., du Coudé Foresto, V., Ridgway, S., Merand, A., Salome, P., Borde, P., Cotton, W., Morel, S., Kervella, P., Traub, W., & Lacasse, M. 2002b, ApJ, 579, 446

Perrin, G., Coude Du Foresto, V., Ridgway, S. T., Mariotti, J., Traub, W. A., Carleton, N. P., & Lacasse, M. G. 1998, in Astronomical Society of the Pacific Conference Series, Vol. 154, Cool Stars, Stellar Systems, and the Sun, ed. R. A. Donahue & J. A. Bookbinder, 2021–+

Perrin, G., Ridgway, S. T., Coudé du Foresto, V., Mennesson, B., Traub, W. A., & Lacasse, M. G. 2004, A&A, 418, 675

Richichi, A., Percheron, I., & Khristoforova, M. 2005, A&A, 431, 773

Serabyn, E., Mawet, D., & Burruss, R. 2010, Nature, 464, 1018

Torres, G., Claret, A., & Young, P. A. 2009, ApJ, 700, 1349

Troy, M., Dekany, R. G., Brack, G., Oppenheimer, B. R., Bloemhof, E. E., Trinh, T., Dekens, F. G., Shi, F., Hayward, T. L., & Brandl, B. 2000, in Society of Photo-Optical Instrumentation Engineers (SPIE) Conference Series, Vol. 4007, Society of Photo-Optical Instrumentation Engineers (SPIE) Conference Series, ed. P. L. Wizinowich, 31–40

Tsuji, T. 2001, A&A, 376, L1

Young, J. S., Baldwin, J. E., Boysen, R. C., Haniff, C. A., Lawson, P. R., Mackay, C. D., Pearson, D., Rogers, J., St.-Jacques, D., Warner, P. J., Wilson, D. M. A., & Wilson, R. W. 2000, MNRAS, 315, 635

Zhao, M., Monnier, J. D., ten Brummelaar, T., Pedretti, E., & Thureau, N. D. 2008, in Society of Photo-Optical Instrumentation Engineers (SPIE) Conference Series, Vol. 7013, Society of Photo-Optical Instrumentation Engineers (SPIE) Conference Series

7.3.2 Paper: New Constraints on Hot Dust within a few AU of Vega, *B. Mennesson, E. Serabyn, C. Hanot, S. Martin, K. Liewer, D. Mawet*

Bright and compact stars are rare targets in the sky. Indeed, most of the stars that are very luminous in the near infrared ($K \geq 0$) are nearby (super) giant stars (cfr. targets selected for the PFN engineering runs, Section 7.3.1). The problem with stars having such angular diameters is that the amount of light leaking through the nuller is large, with null depth limitations around 1% in the best cases. Detection of faint off-axis structures is therefore more limited than around smaller or more distant stars. Vega however, is a perfect target for interferometry. Indeed, it is a very bright ($K = 0.13$) and compact source, with an angular diameter $\theta_{\rm UD} = 3.26 \pm 0.01$ mas. The expected stellar leakage due to its finite size is therefore very small with the PFN ($\sim 4 \times 10^{-4}$), which enables the characterization of its direct vicinity (typically from 0.25 to 1 AU) with unprecedented precision. Vega is a star that has been extensively studied in the past by various instruments and is known since the eighties (Aumann et al. 1984) for being surrounded by a large debris disk extending up to 330 AU at 24 μm (Su et al. 2005; Rieke et al. 2005a). More recently, near-IR interferometric observations have unveiled the presence of a hot debris disk in the innermost regions around Vega. An excess emissions of $1.26 \pm 0.28\%$ has been measured in the K band (Absil et al. 2006b, 2008), while mid-IR limits of $\simeq 2\%$ have been derived with both the MMT/BLINC (Liu et al. 2009) and KIN (unpublished results). In the following paper (submitted to ApJ), we present the results of our observations of Vega with the PFN. From these results obtained with three different baseline orientations, we derive upper limits on the presence of a point-like off-axis source and a circumstellar disk. We then use the results of previous interferometric observations of the star to constrain even more the source of the observed IR excess. My contribution to this work has been to perform the thorough data analysis of these interferometric data which required to reach such high accuracy on the null depth measurements without having to use the observation on a calibrator star. This level of accuracy and contrast ratio would not have been possible without the use of the statistical-self calibrated method that I developped (Hanot et al. 2011).

Draft version February 11, 2011
Preprint typeset using LaTeX style emulateapj v. 11/10/09

NEW CONSTRAINTS ON COMPANIONS AND DUST WITHIN A FEW AU OF VEGA

B. Mennesson[2], E. Serabyn[2], C. Hanot[1],S. Martin[2], K. Liewer[2], F. Loya[2], D. Mawet[2]
[1]AEOS, University of Liège,
Allée du 6 Août, 17 Bât B5c, 4000 Liège, Belgium and
[2]Jet Propulsion Laboratory, California Institute of Technology,
4800 Oak Grove Drive, Pasadena, California 91109, USA

Draft version February 11, 2011

ABSTRACT

We report on high contrast near infrared ($\sim 2.2\,\mu$m) observations of Vega obtained with the Palomar Fiber Nuller, a dual sub-aperture rotating coronagraph installed at the Palomar Hale telescope. Our data show consistent astrophysical null depth measurements at the $\simeq 10^{-3}$ level or below for three different baseline orientations spanning 60 degrees in azimuth, with individual 1 σ uncertainties $\leq 7 \times 10^{-4}$. These high cancellation and accuracy levels translate into a dynamic range greater than 1000:1 inside the diffraction limit of the 5 m telescope beam. Such high contrast performance is unprecedented in the near infrared, and provides improved constraints on Vega's immediate ($\simeq$ 20 to 250 mas, or $\simeq$ 0.15 to 2 AU) environment. In particular, our measurements rule out any potential companion in the [0.25 - 1AU] region contributing more than 1% of the overall near infrared stellar flux, with limits as low as 0.2% near 0.6 AU. These are the best upper limits established so far by direct imaging for a companion to Vega in this inner region. We also conclude that any dust population contributing a significant ($\geq$ 1%) near infrared *thermal* excess can arise only within 0.2 AU of the star, and that it must consist of much smaller grains than in the solar zodiacal cloud. Dust emission from further than $\simeq$ 2 AU is also not ruled out by our observations, but would have to originate in strong scattering, pointing again to very small grains.

Subject headings: infrared: stars — instrumentation: coronagraphs — stars: circumstellar matter — stars: individual (Vega)

1. INTRODUCTION

Planets are believed to form out of the material in circumstellar disks known to exist around young stars. The pre-planetary disks are generally quite bright, and have been very well studied at high angular resolution by interferometry in recent years (Monnier et al. 2005; Millan-Gabet et al. 2006; Tannirkulam et al. 2008). As planets are formed, the opacity of the primordial disk rapidly decreases, and a transition is observed to the regime of debris disks, with inner warmer regions commonly referred to as "exo-zodiacal clouds". Because zodiacal dust grain lifetimes are much shorter than stellar lifetimes, it is believed that zodiacal dust must be regenerated (Backman & Paresce 1993) to be present around main sequence stars. The inner (0.1 to 10 AU) distribution of exozodiacal dust in debris disks thus reflects dynamical interactions at the heart of planet formation, and so are of great scientific interest. More generally, the determination of the exo-zodiacal emission level and its central (< 10AU) spatial distribution around nearby main sequence stars has been long identified (Beichman & Velusamy 1997; Mennesson & Mariotti 1997) as crucial information, both for planetary formation and planet- disk interaction models, and for the design of direct exoplanet imaging space missions.

However, exo-zodiacal disks are generally much fainter and difficult to observe than proto-planetary disks. Debris disks observed to date around nearby stars (Holland et al. 1998; Siegler et al. 2007) are located predominantly far from their host stars (tens to hundreds of AU), and so are more analogous to our solar system's dusty Kuiper belt, located beyond our planetary belt, than to the $\sim$ AU-scale zodiacal disk inside our solar system's asteroid belt. This observational bias results from several factors: (i) small potential exozodiacal disk sizes, (ii) faintness relative to the host stars, and (iii) the use of long (far-infrared) observing wavelengths more sensitive to very cool dust. Detection of faint exozodiacal emission very near bright stars thus requires high angular resolution, and either a means of suppressing starlight or a high dynamic range. Near and mid-infrared high-resolution high-contrast interferometric instruments such as Fiber Linked Unit for Optical Recombination (FLUOR) on the CHARA array (Absil et al. 2006), the Bracewell Infrared Nulling Camera (BLINC) at the MMT (Liu et al. 2004) and the Keck Interferometer Nuller (KIN) (Colavita et al. 2009) have all tackled this issue of zodiacal light characterization. In both wavelength ranges, similar contrast levels were obtained in the inner 10 AU region of nearby main sequence stars: typically 0.2% at 1 σ. Quite surprisingly, this common instrumental performance has so far yielded many more excess detections in the near infrared than in the mid-infrared. Indeed, most mid-infrared results so far are upper limits: out of 23 nearby main sequence stars with no previously known far-infrared excess surveyed by one of the two main KIN key science programs, only one of them shows clear mid-infrared excess at the current detection levels (Millan-Gabet et al. 2011, in preparation). Conversely, in spite of the higher contrast expected, a larger fraction ($\simeq$ 20%, O. Absil and D. Defrère, private communication) of main sequence stars have shown sig-

bertrand.mennesson@jpl.nasa.gov

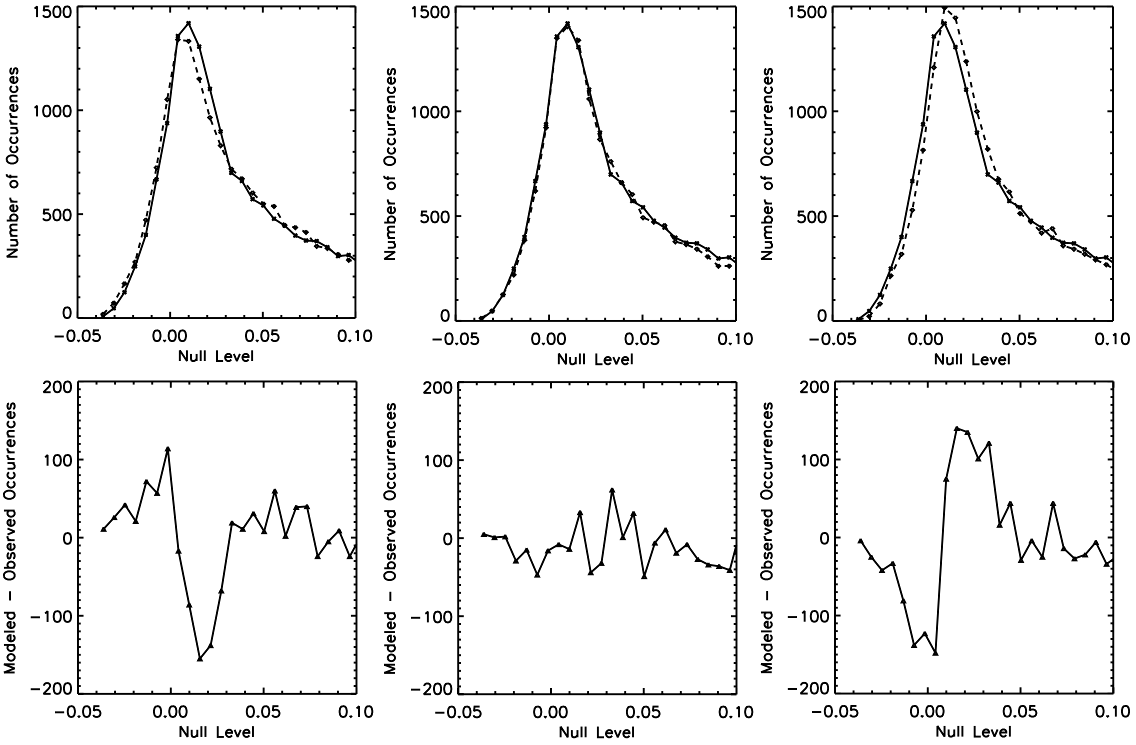

Fig. 1.— Different models of the null depth distribution observed on Vega for a baseline azimuth of 117°. Data points represented by asterisks show the observed number of occurrences in a given null interval, while diamonds indicate the values derived for a given model distribution. The underlying astrophysical null depth - close to the distribution peak- is found to be $N_a = 0.0012 \pm 0.0005$ (1σ) for the best fit model (reduced χ^2 of 1.15) represented in the center top panel. The top left and top right panels show the fits obtained when fixing the astrophysical null depth respectively -3σ and +3 σ away from the best fit value. The respective reduced χ^2 of these models are 1.64 and 1.96. The lower panels show the residuals between the modeled and observed distributions for each of the three assumed astrophysical null values, illustrating the sensitivity of the method to null offsets as low as 0.0015.

nificant (1%) near infrared excesses in their inner 10 AUs (Absil et al. 2006, 2008, 2009; Akeson et al. 2009; di Folco et al. 2007). More detections of this kind are currently being unearthed by an on-going FLUOR survey. Interestingly, these same stars were surveyed in the mid-infrared with BLINC and KIN, and no excess was detected so far at current thresholds, except in the case of β Leo (Stock et al. 2010). These results have been interpreted as implying the presence of hot ($\geq$ 500K) dust populations around a significant fraction of A to G main sequence stars - although the survey of a larger sample is required to derive robust statistics. Importantly, these putative bright exozodiacal disks appear much hotter than the zodiacal cloud, making the near infrared an optimal region for characterization of such hot dust. This also suggests that debris disk characteristics may strongly differ from our own zodiacal cloud, and that high contrast, near infrared interferometric observations might be a very powerful tool for conducting a statistical survey of exo-zodiacal disks.

In this context, a near infrared high dynamic range (10^{-4} to 10^{-3}) interferometric capability could provide an ideal solution for conducting deep surveys of exozodi clouds around nearby stars. It was one of the major drivers for the development of the fiber nulling approach (Haguenauer & Serabyn 2006; Serabyn & Mennesson 2006; Mennesson et al. 2006) and the deployment of the Palomar Fiber Nuller (PFN) at the 5 m Hale telescope (Martin et al. 2008; Mennesson et al. 2010; Serabyn et al. 2010). High contrast observations with this technique promise to further our understanding of the hot dust phenomenon, whose actual origin remains unclear. Indeed, this excess could theoretically arise from thermal emission from hot dust - extended or restricted to annular inner regions-, more point-like structures such as clumps (perhaps resonant clumps), low mass companions, or even hot planetary embryos similar to those inferred around PMS stars such as AB Aur (Millan-Gabet et al. 2006), SR 21 (Eisner et al. 2009), and FU Ori (Malbet et al. 2005).

Full descriptions of the PFN coronagraph hardware, observing procedure, and data reduction strategies are given in recent papers (Martin et al. 2008; Mennesson et al. 2010; Serabyn et al. 2010; Hanot et al. 2011). Vega was observed with the PFN in July 2009 with a constant 3.40 m baseline and three different azimuthal orientations spanning a range of 60 degrees. At each orientation, a four minute long sequence of null depth measurements was recorded. A statistical analysis of the measured fluctuating null depth distribution (Figure 1) is used to recover the underlying astrophysical null depth N_a, which is directly related to the source visibility [1]. More precisely, the astrophysical null depth is derived by minimizing a goodness of fit χ^2 test comparing the observed null distribution to a model distribution. Complete details about this "Null Self Calibration" method are given in Hanot et al. 2011. The error bar (1σ confidence in-

---

[1] The astrophysical null depth is given by $N_a = \frac{(1-|V|)}{(1+|V|)}$, where V is the object's complex visibility

TABLE 1
Summary of Vega PFN observations

Az (°)	N_a	σ	Residual Null	Excess 3σ Upper Limit
87	-1×10^{-4}	7×10^{-4}	-5×10^{-4}	1.6×10^{-3}
117	12×10^{-4}	5×10^{-4}	8×10^{-4}	2.3×10^{-3}
147	10×10^{-4}	6×10^{-4}	6×10^{-4}	2.4×10^{-3}

Note. — Az is the baseline azimuth measured in degrees East of North. N_a is the measured astrophysical null. The residual null (or "excess leakage") is computed by subtracting the null depth expected from Vega's photosphere, which is 4.0 10^{-4} at the PFN 3.40m baseline and 2.16 μm effective wavelength.

Since larger-scale debris disks detected in the FIR show a statistical dimming with stellar age (e.g. Siegler et al. 2007), the search for smaller-scale exozodiacal emission is likely best begun around fairly young, nearby stars with other evidence of dust. A prime candidate is therefore Vega, a nearby (7.8 pc) bright (0 mag) A0V star, with one of the first detections of excess FIR emission from a large debris disk (Aumann 1985). Many of Vega's properties are well characterized, including its nearly pole-on orientation, its pole-to-equator temperature variation and limb darkening (Aufdenberg et al. 2006), and its nearly face-on large-scale debris disk (Wilner et al. 2002; Su et al. 2005). Moreover, some data regarding potential exozodiacal dust around Vega also exist: MIR limits on excess emission of ≃ 2% derived by MMT/BLINC (Liu et al. 2004, 2009) and by KI nulling (unpublished results), and a small near-infrared (NIR) short-baseline visibility deficit (Absil et al. 2006) suggesting the presence of some very hot dust. Vega is thus perhaps an ideal first candidate for observations with the Palomar Fiber Nuller (PFN).

2. PFN VEGA OBSERVATIONS AND RESULTS

terval) on N_a is first obtained by variation around its optimal value, using regular χ^2 statistics. However, this error bar estimation is only valid if the noise is dominated by a zero mean gaussian process. We then also conducted a bootstrapping analysis -independent of the actual noise properties -, resampling and replacing the observed null values, and generating many (500) fake null sequences derived from the observed data. Analyzing the corresponding sequences yields astrophysical null 1σ (68.3% confidence interval) uncertainties very similar to those derived using the χ^2 approach. The final error bar quoted on N_a is the largest of the uncertainties derived by the χ^2 and by the bootstrapping methods.

Table 1 summarizes Vega's astrophysical null depths derived as a function of baseline azimuth angle. All measured nulls have 1σ error bars smaller than 0.001. The orientation averaged null depth estimate, taking measurements scattering and individual uncertainties into account, is N_a= 0.0008 ± 0.0004 (weighted mean and weighted standard deviation). In comparison, adopting Vega's latest gravity darkened photospheric model (Aufdenberg et al. 2006), the expected null depth is 0.0004 at 2.2μm at the PFN 3.40 m baseline. (In fact Vega's photosphere is hardly resolved at this spatial resolution, and a more crude uniform disk model provides the same value at the 10^{-5} level). The residual null obtained after subtracting the 0.0004 diameter limited null depth characterizes a potential "excess leakage" above the photosphere. Its orientation average is then 0.0004 ± 0.0004, showing that the PFN observations do not detect any emission above that predicted for the photosphere that is statistically significant.

For each baseline orientation, Table 1 indicates the residual null measured on Vega (i.e the excess leakage obtained after subtraction of the photospheric null) and its 3σ upper limit. In order to convert the measured excess leakage to a true astrophysical excess, one must correct for the nuller sky transmission pattern, which is limited to about 300 mas FWHM (Mennesson et al. 2010). The maximum (3σ) relative flux compatible with the data is then derived at each of the 3 baseline orientations. At any given location in Vega's immediate environment (within ≃ 2.3 AU in radius), only the lowest of these 3 limits is retained. This yields the final "upper flux limit map" (Figure 2 left), i.e. the maximum (relative) K band flux of a companion as a function of its location. At the very center of the field, within 0.05 AU of Vega, the contribution of any off-axis source would be nulled out, and so no useful flux constraint can be derived. Similarly, our data do not reflect emission from sources located much further than ≃ 3AU, i.e. beyond the single-mode fiber field of view. Our data are most sensitive to the central [0.25 - 1 AU] region where we can rule out the presence of any companion contributing more than 1% of the overall K band flux. This corresponds to the best point source upper limits derived so far by direct detection in this range of separations around Vega. At a given distance from Vega, the derived companion flux limit is a function of azimuth, reflecting the observed slight azimuthal variations as well as our incomplete (60° span) baseline rotation. Figure 2 (upper right) shows as an example the upper limits derived at 0.6 AU as a function of azimuth angle, with values ranging from 0.2% to 0.6%. The residual "spikes" visible at azimuths of ≃ 30 and ≃ 210 degrees are expected, as these angles are 90 degrees away from the mean baseline orientation (117 degrees).

Potential stellar mass companions have already largely been ruled out within 10 AU of Vega by astrometric and radial velocity limits (Absil et al. 2006). But unlike gravitational techniques, our direct detection measurements can also impose strong constraints on the existence of extended sources of dust in the inner 1AU, e.g. on the relative contribution and physical characteristics of any putative hot debris disk around Vega. As there is strong evidence (Peterson et al. 2006; Aufdenberg et al. 2006) that Vega is viewed very nearly pole-on (inclination of ∼ 5°), here we only consider circularly symmetric disk structures. As a convenient case to study, we further concentrate hereafter on geometrically thin (0.01AU) circular rings located at various radii.

As can be seen in Figure 2 (bottom right), the relative flux of a circular dust ring is best constrained by our data between 0.2 AU (≃ 25 mas) and 1.1 AU (≃140mas). In particular, we find that the existence of a geometrically thin ring contributing more than 0.6% of Vega's

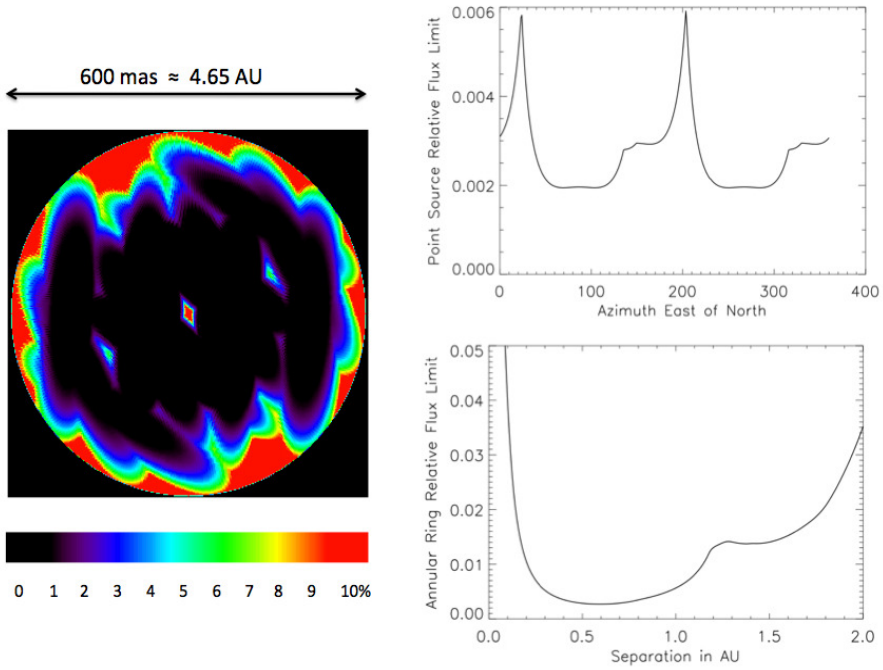

Fig. 2.— Vega circumstellar emission upper limits derived from PFN data recorded at three baseline orientations. Left: map of the maximum (3 σ) point source levels (relative to Vega) consistent with the PFN data. North is up, East is to the left. Field of view radius is 300 mas around Vega ($\simeq$ 2.3 AU). As expected, constraints on a putative companion get looser at the edge of the fiber field of view, and at the center of the field, where destructive interference occurs for all baseline orientations. Right, top: Upper limit at 0.6 AU (= 47mas) as a function of source position angle. Right, bottom: azimuthal average of left map. This corresponds to the 3 σ upper flux limit for a geometrically thin ring around Vega. It is consistently below 0.6% between 0.2AU ($\simeq$ 25mas) and 1.0 AU ($\simeq$ 130mas), and as low as 0.3% around 0.6 AU.

K band flux is ruled out (at the 3σ level) anywhere between 0.25 and 1AU. Similarly, over the same region, our results imply that a uniform source of emission can not contribute more than 0.4% of excess in the near infrared. Clearly, if a hot debris disk is responsible for a substantial amount ($\geq$ 1%) of near infrared extra-emission, our observations indicate that it must either arise from within $\simeq$ 0.2 AU, i.e in the close vicinity of the dust sublimation region, and/or from colder ($\leq$ 800 K) regions located further away than $\simeq$ 1 to 2 AU. Further observational data are required to assess the viability of these two dust population scenarios and derive more physical information on the nature of a potential near infrared excess around Vega. This is the objective of the next section.

3. COMPARISON TO EXISTING HIGH CONTRAST HIGH RESOLUTION DATA

3.1. *NIR and MIR data*

Here we review the existing data about the potential magnitude of an infrared excess within a few AU of Vega. Very few instruments have the required combination of spatial resolution and contrast to provide such information.

Very accurate near infrared observations of Vega have been obtained in K band with the FLUOR instrument of the CHARA long baseline interferometric array (Absil et al. 2006; Aufdenberg et al. 2006). In particular, these measurements show a "visibility deficit" at short baselines, which Absil et al. attribute to the probable presence of a hot debris disk, contributing about 1.3% of Vega's flux within the FLUOR field of view ($\simeq$ 7.8 AU). In the mid infrared (at 10.6 μm), single telescope nulling observations have been conducted on the MMT using the BLINC instrument (Liu et al. 2004, 2009), concluding that there is no resolved emission from the circumstellar environment (at separations greater than 0.8 AU) above 2.1% (3 σ limit) of the level of the stellar photospheric emission. Additionally, the authors find that the null does not vary significantly with observations at different rotations of the interferometer baseline (over a range of about 90 degrees), indicating that there is no evidence of an inclined disk-like structure. Broadband (8 to 13 μm) mid infrared measurements at higher spatial resolution were recently obtained by long baseline - separated aperture- nulling at the Keck Interferometer. In particular, measurements obtained as part of the instrument shared risk commissioning (June 2007, unpublished data), detected no significant excess either, with the excess leakage estimated to be 0.33% ± 0.25% at an effective wavelength of 9 μm.

Figure 3 summarizes the excess leakages measured with the PFN and CHARA instruments in the near infrared, and with the MMT and the Keck Interferometer Nuller (KIN) in the mid-infrared. The KIN results cover a small range in azimuth due to the fixed KI baseline, while the CHARA, PFN and MMT results cover larger azimuth ranges: respectively 40, 60 and 95 degrees. To get a consistent view of the results provided by the different instruments, we converted the CHARA visibility deficit observed with their 34 m baseline into an equivalent excess leakage of 0.55% ± 0.1%. From the CHARA, MMT and KIN measured excess leakages, and using the simple ring model suggested above for the PFN data, we derive constraints on the relative flux of a putative geometrically and optically thin dust ring around Vega (Figure 4). As in the case of the PFN observations (section

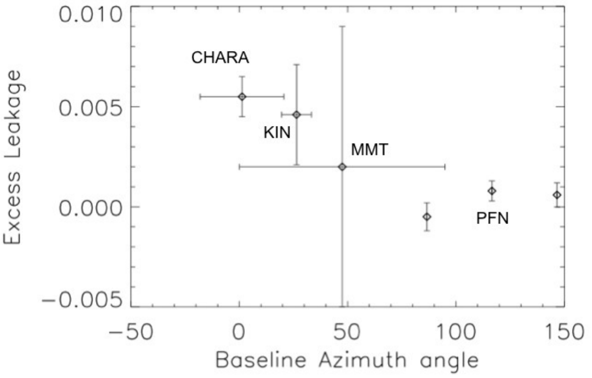

Fig. 3.— Excess leakage measured on Vega by various instruments at different baseline orientations (azimuth East of North in degrees). In all cases, the photospheric null has been subtracted and an excess leakage traces possible resolved sources of extra emission. CHARA data use a 34 m baseline at K band, and show a $> 5\sigma$ excess. In comparison, no significant excess is detected by the Palomar Fiber Nuller (PFN, baseline=3.4 m, also at K band), nor by the Keck Interferometer Nuller (KIN, baseline = 85 m, $\lambda \simeq 9$ μm) or the MMT (baseline =4 m, $\lambda \simeq 10.6$ μm).

3), this is done by folding in the sky transmission pattern for each of these 3 facilities. In the case of KIN, we use the transmission pattern computed at the time of the observations, including the effects of the short and long baseline fringes, together with the field of view limitations introduced by the camera optics (focal plane pinhole and finite spectral dispersion). Full details can be found in Colavita et al. 2009, as well as in Millan-Gabet et al. 2011 and Serabyn et al. 2011, both in preparation. For the MMT, we computed the expected sky transmission pattern from a 10.6 micron nuller formed of two 2.5 m sub-apertures separated by 4m. As in the case of the PFN, no excess was detected in the mid-infared by the KIN and MMT instruments, and the corresponding curves in Figure 4 represent the ring flux 3σ upper limits as a function of distance to the star. Also clearly apparent is the nice complementarity of the KIN and MMT mid-infrared data in terms of spatial scales covered.

For the CHARA (full K band) data, we take into account the transmission pattern of a single-mode fiber optimized for coupling the light of a 1 m telescope (FWHM$\simeq$ 500 mas), the interferometric fringe pattern (34 m baseline), and the coherence loss effects at the edge of the field. The dashed dotted curve of Figure 4 shows the resulting excess flux detected - and its $\pm$ 1 σ boundaries - as a function of ring separation. The CHARA data alone hardly constrain the location of the excess within FLUOR's field of view. However, the constraints from the PFN (Figure 4) clearly show that any significant NIR excess (e.g. compatible with the CHARA data) must originate from within $\simeq$ 0.2AU, and/or from further away than $\simeq$ 2 AU. We now examine hereafter these two possibilities in more detail, assuming that Vega's brightness distribution did not change significantly between the May 2005 CHARA observations and the July 2009 PFN ones. Otherwise, no meaningful comparison can be made.

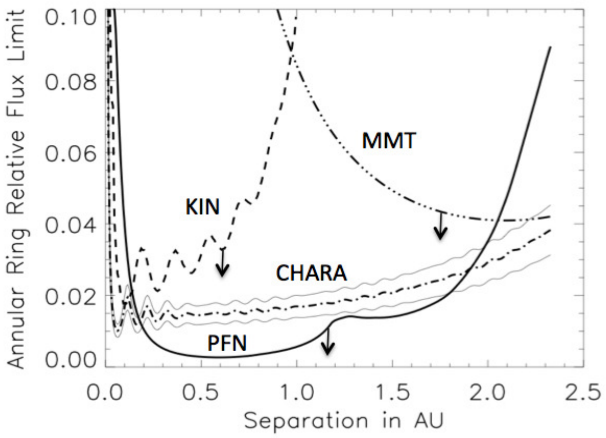

Fig. 4.— Flux constraints (relative to Vega) of a geometrically thin annular dust ring located at various stellocentric distances. The CHARA dash dotted curve (with its bracketing $\pm$ 1σ boundaries) is derived from the excess reported at K band (Absil et al. 2006). All other curves are upper limits (3σ) derived from the KIN (9 microns), MMT (10.6 microns) and PFN (K band) null measurements. Assuming no significant changes in the dust distribution between 2005 and 2009, the PFN data constrain the CHARA NIR excess to reside either within $\simeq$ 0.2 AU and/or outside of $\simeq$ 2AU of Vega.

3.2. *Interpretation*

From the CHARA excess detection, and from Vega's tabulated flux, we can compute the corresponding absolute 2.2 μm flux of a narrow circumstellar ring, as a function of its distance to the star. Similarly, from the KIN and MMT upper limits, we calculate the (3 σ) upper limits to the absolute flux contributed by a dust ring around Vega (at 9 microns for KIN and at 10.6 microns for the MMT). From these NIR flux levels and from the MIR upper limits, we derive the "minimum" near to mid infrared ring flux ratio compatible with the data (plain curve, Figure 5 left). In comparison, the dashed curve shows the NIR/MIR flux ratio expected from dust emitting like a black-body at thermal equilibrium with the star, i.e. with a temperature radial profile going as $L^{0.25}/r^{0.5}$. For the stellar luminosity L, we use Vega's equatorial plane flux computed in Aufdenberg et al. 2006 (table 3), and find an equivalent luminosity of 28.9 $L\odot$. This value is smaller than Vega's observed - nearly pole-on - 37 $L\odot$ luminosity because of the large temperature gradient between the pole and the equator. For any realistic dust ring radius (i.e $T < 2000K$, and $r \geq 0.1$ AU), the minimum NIR/MIR flux ratio observed is found to be significantly larger than that derived from a simplistic black-body assumption, by a factor of 3 or more. Considering a dust temperature profile decreasing more slowly than in the black-body case, as observed for instance in the solar system zodiacal cloud by COBE/DIRBE ($T(r) \propto L^{\delta/2}/r^{\delta}$ with δ=0.467, (Kelsall et al. 1998)), the predicted flux ratio is even lower (Figure 5 left, dotted curve). Thus, relative to a single-temperature black body or grey body, either the MIR emission must be suppressed (by e.g., a low MIR emissivity), or the NIR emission must be strongly enhanced (e.g. by scattering) to be detected by CHARA.

3.2.1. *Thermal emission*

Detailed Mie calculations show that the emissivity of a spherical dust particle is roughly unity at wavelengths shorter that $2\pi a$, where a is the radius of the particle, falling off as λ^{-n}, with n $\simeq$ 1-2, at longer wave-

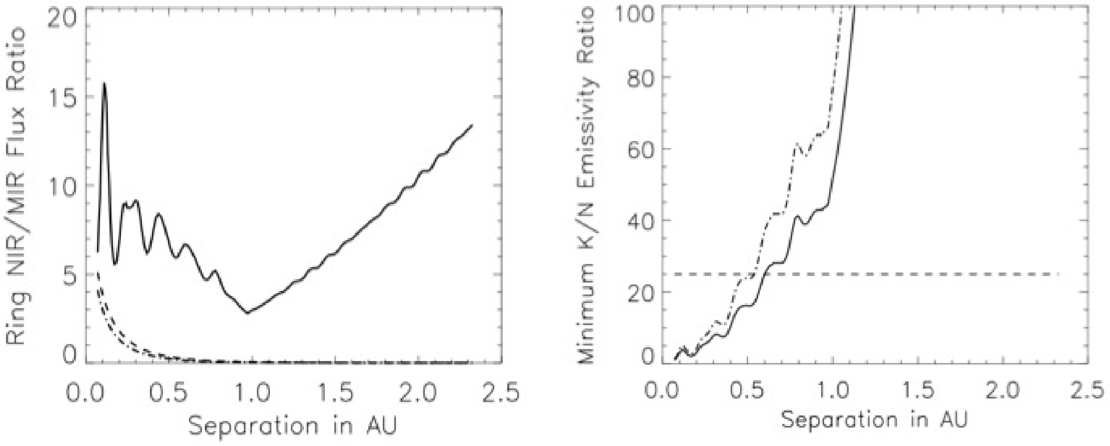

FIG. 5.— Left: near to mid infrared flux ratio of a geometrically thin dust ring located at various distances from Vega. Plain curve: minimum value consistent with the CHARA, KIN and MMT data. Dashed curve: value predicted for dust emitting as a black-body in thermal equilibrium with the star. Dash-dotted curve: value predicted for dust emitting as a grey body with a dust temperature profile analogous to the solar system case. The latter two curves assume for Vega an equatorial luminosity of 28.9 $L_{\odot}$. Right: Minimum near to mid infrared emissivity ratio compatible with the data, assuming pure thermal emission from a geometrically thin ring (plain curve: black-body model, dash-dotted curve: grey body model). For ring separations larger than $\simeq$ 0.6 AU, the emissivity ratio takes values larger than predicted by a λ^{-2} power law (horizontal dashed line), pointing to a non thermal emission process.

lengths. If the ring infrared brightness were dominated by thermal emission rather than scattering effects, Figure 5 (right) shows that beyond about 0.6 AU, the minimum NIR/MIR emissivity ratio required exceeds the value expected from a λ^{-2} emissivity law (the steepest emissivity decline predicted by Mie theory). The possibility of thermal emission from dust located further than 2AU is then ruled out. The CHARA observed excess would have to arise from a very narrow region, located between the sublimation radius (0.1 to 0.15 AU, given the uncertainties on grain properties and Vega's equatorial flux), and the 0.2AU upper limit set by the NIR PFN data. In addition, we find (Figure 5 left) that the NIR/MIR emissivity ratio must be greater than 3.5 everywhere between 0.1 and 0.2 AU to fit the data, and probably a few times higher since this is a $3\,\sigma$ lower limit . This implies dust grains significantly smaller than the MIR wavelength, i.e. micron sized or smaller.

This implication is quite different from the case of our own zodiacal disk, for which a flat opacity spectrum until 150 microns implies a significant population of larger ($\simeq$ 10 to 100 microns) grains (Fixsen & Dwek 2002). Any ring-like distribution of small grains around Vega would thus differ significantly from our own zodiacal disk in spatial distribution and grain size. collisions in a denser disk would be much more frequent. The small size of the grains is surprising, as radiation pressure is expected to expel small grains rapidly to tens or hundreds of AUs. One possibility is that the small grains are not expelled effectively by radiation pressure, a case that arises if the grains are predominantly very non-spherical or extremely small. This would for instance happen for grains similar in size to the nano (1-10 nm) dust particules trapped near the Sun and recently detected by the STEREO spacecraft (Mann et al. 2010). In this case the bright emission ring would be located near the sublimation radius, as we find. Another possibility is that small grains are continuously fed to the inner region because of dynamical perturbations and collisions in the outer colder disk of Vega, induced for instance by migrating planets. The resulting dust would then be transported inward by Poynting-Robertson drag and strong stellar winds, as recently suggested around ϵ Eri (Reidemeister et al. 2011). In a more speculative vein, abundant close-in small grains may on the other hand correspond to a bright turnaround region: as larger grains fall inward due to Poynting-Robertson drag, they encounter increasing collision rates, leading to decreasing grain sizes and increasing emission, until the grains become small enough for radiation pressure to dominate and expel them. Finally, the ring-like distribution may instead signify clearing or shepherding by nearby planets.

3.2.2. *Starlight scattering*

Conversely, if scattering strongly dominates over thermal emission at NIR wavelengths, and is much less efficient at MIR wavelengths, both the inner ($<$ 0.2AU) and outer ($>$ 2AU) dust populations are a priori compatible with the data. A complete simulation of dust properties is necessary to explore these two possibilities, and will be the object of a forthcoming paper (Defrere et al. 2011, in preparation). However, from a first analysis based on astronomical silicates (Draine & Lee 1984), small grains - typically micron sized or smaller - seem again necessary to produce strong scattering efficiency enhancement in the NIR. Finally, we note that if starlight scattering was responsible for a significant ($>$ 1%) NIR excess emission, it would essentially have the same color as Vega, and may have well remained undetected before the spatially resolved high accuracy CHARA observations.

4. CONCLUSIONS

Using the Palomar Fiber Nuller and the null self calibration technique, we have demonstrated high contrast imaging capabilities within the diffraction limit at the Palomar Hale telescope. We presented the deepest stellar nulls measured to date in the NIR (0.0008 ± 0.0004), providing new constraints on exo-zodiacal emission in the inner few AU around Vega. In particular, our data show that, if present at all, any significant ($\geq$ 1%) source of extended NIR excess must either be confined very close to the dust sublimation radius (and arise in either scattering or thermal emission), and/or come from a colder grain population located beyond 2 AU (compatible with scattering only). The absence of a corresponding MIR excess implies that such a NIR excess would most likely come from very small grains, micron sized or smaller.

Accurate ground-based nulling measurements have so far been limited to the mid-infrared, where one takes advantage of the reduced turbulence and improved wavefront quality. Our Palomar results demonstrate that although shorter wavelengths have intrinsically higher phase fluctuations, high contrast interferometry is also possible in the near infrared, providing higher spatial resolution and much better sensitivity from the ground. With the new PALM-3000 extreme AO system (Bouchez et al. 2008) coming on-line at Palomar in 2011, simulations indicate that contrasts of the order of 10^{-4} to 10^{-3} should be readily accessible with our system on $m_K = 3$ to $m_K = 6$ stars, as close as 30 mas from the central star (Mennesson et al. 2010; Serabyn et al. 2010).

As illustrated by our initial PFN measurements of Vega, single telescope observations at this contrast and spatial resolution allow new constraints on the amount and spatial structure of exo-zodiacal light around nearby main sequence A stars. Additionally, the fiber nuller and null self-calibration techniques can be extended to long baseline interferometers, - as long as fringe tracking and dispersion capabilities are available (Mennesson 2011, in preparation) -, so that 10^{-3} contrast or better should also be accessible at much higher spatial resolution. This opens up the possibility of extending the high contrast NIR exo-zodi survey to nearby FGK main sequence stars, where hot dust is expected at smaller separations. This is a very attractive prospect, as exo-zodiacal light structure is a powerful tracer of planetary system's formation history and current dynamical activity, and also an important design parameter for future direct imaging missions targeting exoplanets in the habitable zone. Indeed, clumpy and/or large exo-zodi levels will be a hindrance to all types of missions, whether relying on visible coronagraphy or MIR interferometry.

Acknowledgments

This work was performed at the Jet Propulsion Laboratory, California Institute of Technology, under contract with NASA. The data presented are based on observations obtained at the Hale Telescope, Palomar Observatory, as part of a continuing collaboration between Caltech, NASA/JPL, and Cornell University. We wish to thank the Palomar Observatory staff for their assistance in mounting the PFN and conducting the observations at the Hale telescope.

REFERENCES

Absil, O., di Folco, E., Mérand, A., Augereau, J., Coudé du Foresto, V., Defrère, D., Kervella, P., Aufdenberg, J. P., Desort, M., Ehrenreich, D., Lagrange, A., Montagnier, G., Olofsson, J., ten Brummelaar, T. A., McAlister, H. A., Sturmann, J., Sturmann, L., & Turner, N. H. 2008, A&A, 487, 1041

Absil, O., di Folco, E., Mérand, A., Coudé du Foresto, V., Augereau, J.-C., Aufdenberg, J. A., Kervella, P., Ridgway, S. T., Berger, D. H., ten Brummelaar, T. A., Sturmann, J., Strumann, L., Turner, N. H., & McAlister, H. A. 2006, A&A, in press

Absil, O., Mennesson, B., Le Bouquin, J., Di Folco, E., Kervella, P., & Augereau, J. 2009, ApJ, 704, 150

Akeson, R. L., Ciardi, D. R., Millan-Gabet, R., Merand, A., Folco, E. D., Monnier, J. D., Beichman, C. A., Absil, O., Aufdenberg, J., McAlister, H., Brummelaar, T. t., Sturmann, J., Sturmann, L., & Turner, N. 2009, ApJ, 691, 1896

Aufdenberg, J. P., Mérand, A., Coudé du Foresto, V., Absil, O., Di Folco, E., Kervella, P., Ridgway, S. T., Berger, D. H., ten Brummelaar, T. A., McAlister, H. A., Sturmann, J., Sturmann, L., & Turner, N. H. 2006, ApJ, 645, 664

Aumann, H. H. 1985, PASP, 97, 885

Backman, D. E., & Paresce, F. 1993, in Protostars and Planets III, 1253–1304

Beichman, C., & Velusamy, T. 1997, in Bulletin of the American Astronomical Society, Vol. 29, Bulletin of the American Astronomical Society, 1310–+

Bouchez, A. H., Dekany, R. G., Angione, J. R., Baranec, C., Britton, M. C., Bui, K., Burruss, R. S., Cromer, J. L., Guiwits, S. R., Henning, J. R., Hickey, J., McKenna, D. L., Moore, A. M., Roberts, J. E., Trinh, T. Q., Troy, M., Truong, T. N., & Velur, V. 2008, in Society of Photo-Optical Instrumentation Engineers (SPIE) Conference Series, Vol. 7015, Society of Photo-Optical Instrumentation Engineers (SPIE) Conference Series

Colavita, M. M., Serabyn, E., Millan-Gabet, R., Koresko, C. D., Akeson, R. L., Booth, A. J., Mennesson, B. P., Ragland, S. D., Appleby, E. C., Berkey, B. C., Cooper, A., Crawford, S. L., Creech-Eakman, M. J., Dahl, W., Felizardo, C., Garcia-Gathright, J. I., Gathright, J. T., Herstein, J. S., Hovland, E. E., Hrynevych, M. A., Ligon, E. R., Medeiros, D. W., Moore, J. D., Morrison, D., Paine, C. G., Palmer, D. L., Panteleeva, T., Smith, B., Swain, M. R., Smythe, R. F., Summers, K. R., Tsubota, K., Tyau, C., Vasisht, G., Wetherell, E., Wizinowich, P. L., & Woillez, J. M. 2009, PASP, 121, 1120

di Folco, E., Absil, O., Augereau, J., Mérand, A., Coudé du Foresto, V., Thévenin, F., Defrère, D., Kervella, P., ten Brummelaar, T. A., McAlister, H. A., Ridgway, S. T., Sturmann, J., Sturmann, L., & Turner, N. H. 2007, A&A, 475, 243

Draine, B. T., & Lee, H. M. 1984, ApJ, 285, 89

Eisner, J. A., Monnier, J. D., Tuthill, P., & Lacour, S. 2009, ApJ, 698, L169

Fixsen, D. J., & Dwek, E. 2002, ApJ, 578, 1009

Haguenauer, P., & Serabyn, E. 2006, Appl. Opt., 45, 2749

Hanot, C., Mennesson, B., Martin, S. R., Liewer, K., Loya, F., Mawet, D., Riaud, P., Riaud, P., Absil, O., & Serabyn, E. 2011, accepted in ApJ

Holland, W. S., Greaves, J. S., Zuckerman, B., Webb, R. A., McCarthy, C., Coulson, I. M., Walther, D. M., Dent, W. R. F., Gear, W. K., & Robson, I. 1998, Nature, 392, 788

Kelsall, T., Weiland, J. L., Franz, B. A., Reach, W. T., Arendt, R. G., Dwek, E., Freudenreich, H. T., Hauser, M. G., Moseley, S. H., Odegard, N. P., Silverberg, R. F., & Wright, E. L. 1998, ApJ, 508, 44

Liu, W. M., Hinz, P. M., Hoffmann, W. F., Brusa, G., Miller, D., & Kenworthy, M. A. 2009, ApJ, 693, 1500

Liu, W. M., Hinz, P. M., Hoffmann, W. F., Brusa, G., Wildi, F., Miller, D., Lloyd-Hart, M., Kenworthy, M. A., McGuire, P. C., & Angel, J. R. P. 2004, ApJ, 610, L125

Malbet, F., Lachaume, R., Berger, J.-P., Colavita, M. M., di Folco, E., Eisner, J. A., Lane, B. F., Millan-Gabet, R., Ségransan, D., & Traub, W. A. 2005, A&A, 437, 627

Mann, I., Czechowski, A., & Meyer-Vernet, N. 2010, Twelfth International Solar Wind Conference, 1216, 491

Martin, S., Serabyn, E., Liewer, K., Loya, F., Mennesson, B., Hanot, C., & Mawet, D. 2008, in Society of Photo-Optical Instrumentation Engineers (SPIE) Conference Series, Vol. 7013, Society of Photo-Optical Instrumentation Engineers (SPIE) Conference Series

Mennesson, B., Haguenauer, P., Serabyn, E., & Liewer, K. 2006, in Society of Photo-Optical Instrumentation Engineers (SPIE) Conference Series, Vol. 6268, Society of Photo-Optical Instrumentation Engineers (SPIE) Conference Series

Mennesson, B., Hanot, C., Serabyn, E., Martin, S. R., Liewer, K., Loya, F., & Mawet, D. 2010, in Society of Photo-Optical Instrumentation Engineers (SPIE) Conference Series, Vol. 7735, Society of Photo-Optical Instrumentation Engineers (SPIE) Conference Series

Mennesson, B., & Mariotti, J. M. 1997, Icarus, 128, 202

Millan-Gabet, R., Monnier, J. D., Akeson, R. L., Hartmann, L., Berger, J.-P., Tannikurlam, A., Melnikov, S., & Billmeier, R. 2006, ApJ, in press

Monnier, J. D., Millan-Gabet, R., Billmeier, R., Akeson, R. L., Wallace, D., Berger, J.-P., Calvet, N., D'Alessio, P., Danchi, W. C., Hartmann, L., Hillenbrand, L. A., Kuchner, M., Rajagopal, J., Traub, W. A., Tuthill, P. G., Boden, A., Booth, A., Colavita, M., Gathright, J., Hrynevych, M., Le Mignant, D., Ligon, R., Neyman, C., Swain, M., Thompson, R., Vasisht, G., Wizinowich, P., Beichman, C., Beletic, J., Creech-Eakman, M., Koresko, C., Sargent, A., Shao, M., & van Belle, G. 2005, ApJ, 624, 832

Peterson, D. M., Hummel, C. A., Pauls, T. A., Armstrong, J. T., Benson, J. A., Gilbreath, G. C., Hindsley, R. B., Hutter, D. J., Johnston, K. J., Mozurkewich, D., & Schmitt, H. R. 2006, Nature, 440, 896

Reidemeister, M., Krivov, A. V., Stark, C. C., Augereau, J., Löhne, T., & Müller, S. 2011, A&A, 527, A57+

Serabyn, E., & Mennesson, B. 2006, in IAU Colloq. 200: Direct Imaging of Exoplanets: Science and Techniques, ed. C. Aime & F. Vakili, 379–384

Serabyn, E., Mennesson, B., Martin, S., Liewer, K., Mawet, D., Hanot, C., Loya, F., Colavita, M. M., & Ragland, S. 2010, in Society of Photo-Optical Instrumentation Engineers (SPIE) Conference Series, Vol. 7734, Society of Photo-Optical Instrumentation Engineers (SPIE) Conference Series

Siegler, N., Muzerolle, J., Young, E. T., Rieke, G. H., Mamajek, E. E., Trilling, D. E., Gorlova, N., & Su, K. Y. L. 2007, ApJ, 654, 580

Stock, N. D., Su, K. Y. L., Liu, W., Hinz, P. M., Rieke, G. H., Marengo, M., Stapelfeldt, K. R., Hines, D. C., & Trilling, D. E. 2010, ApJ, 724, 1238

Su, K. Y. L., Rieke, G. H., Misselt, K. A., Stansberry, J. A., Moro-Martin, A., Stapelfeldt, K. R., Werner, M. W., Trilling, D. E., Bendo, G. J., Gordon, K. D., Hines, D. C., Wyatt, M. C., Holland, W. S., Marengo, M., Megeath, S. T., & Fazio, G. G. 2005, ApJ, 628, 487

Tannirkulam, A., Monnier, J. D., Millan-Gabet, R., Harries, T. J., Pedretti, E., ten Brummelaar, T. A., McAlister, H., Turner, N., Sturmann, J., & Sturmann, L. 2008, ApJ, 677, L51

Wilner, D. J., Holman, M. J., Kuchner, M. J., & Ho, P. T. P. 2002, ApJ, 569, L115

7.4 Future upgrades: going deeper and fainter

With an estimated SNR of only 2500 on a $K = 0$ star, the sensitivity is obviously the current weak point of the PFN. The first three runs have confirmed this statement, As we have not been able yet to observe stars fainter than $K = 1$. The main reason for that is the rather noisy mono-pixel detector being used. Fortunately, the project has inherited of the much more sensitive *HAWAII* camera from the Palomar Testbed Interferometer (PTI) and a 4 year grant has been awarded to upgrade the PFN accordingly. This camera should allow us to reach 10^{-4} contrast levels around $K = 5$ stars (and also 10^{-3} around $K = 7.5$ stars). Recent on-sky results have proven that null depth accuracies at a couple of 10^{-4} can already been obtained on bright stars with the current setup and AO system (Hanot et al. 2011; Mennesson et al. 2011a,b), and laboratory experiments have demonstrated the capabilities of the PFN to reach 10^{-4} contrast levels. Last but not least, the new XAO system (Palm-3000) coming online at Palomar in 2011 should also help us to reach higher contrast ratios. With near-IR Strehl ratios $> 90\%$, it will leave wavefront residuals twice as small as currently observed ($\sim$ 100 nm rms compared to $\sim$ 190 nm rms, Bouchez et al. 2008).

7.4.1 Looking for young exoplanets with the PFN

The Fiber Nuller has been designed to search for faint off-axis companions close to bright stars. This section aims at giving the sensitivity that the PFN could achieve in terms of companion masses, based on the COND evolutionary models for low-mass objects (Baraffe et al. 1998, 2002). As explained in

Table 7.2: List of the 20 best targets with $K < 5$ visible from Palomar Observatory for a survey of (sub-)stellar companions around stars inside young moving groups. For each target, its spectroscopic type, distance, age and the moving group it belongs to are summarized. An estimation of the reachable sensitivity to off-axis companion is also computed for each target based on the COND evolutionary models (Baraffe et al. 1998, 2002).

Name	Spec. Type	Moving group	Age [Myr]	Dist. [pc]	m_k	Mass [M_{Jup}]
HD 166	K0V	Her Lyra	200	13.7	4.31	20
HD 14062	F5V	β Pic	12	39	5.131	7
HD 17332	G0	AB Dor	50-70	32.6	5.517	11
HD 25457	F5V	AB Dor	50-70	19.2	4.181	11
HD 60178J	A2V	Castor	300	15.8	1.23	45
HD 87696	A7V	UMa	300	25	4.00	35
HD 91480	F1V	UMa	300	25	4.33	35
HD 89744	F7V	AB Dor	50-70	39	4.45	13
HD 91480	A7V	UMa	300	25	4.33	35
HD 106591	A3V	UMa	300	25	3.10	45
HD 111456	F5V	UMa	300	25	4.55	30
HD 113139	F2V	UMa	300	25	3.95	35
HD 115043	G1Va	UMa	300	25	5.33	25
HD 116657	A1	UMa	300	25	2.82	45
HD 116842	A5V	UMa	300	25	3.15	45
HD 129798	F2V	UMa	300	25	5.25	25
HD 172167	A0V	Castor	386	7.8	0.13	45
HD 203280	A7IV	Castor	200	15	2.07	40
HD 206860	G0V	Her Lyra	200	18.4	4.56	23
HD 210027	F5V	Castor	200	11.7	2.56	28

Sections 1.3 and 5.2, young main sequence stars in general, and those belonging to moving groups in particular, are very interesting targets as their companions are intrinsically more luminous than in the case older ones, but the thick protoplanetary disks that surround pre-main sequence stars have already disappeared. Similarly to our program with AMBER on the VLTI, we selected the targets among the closest moving groups and associations and only kept those with $K < 5$ for which we expect to reach null depths of 10^{-4}. We then restricted the selection to the 20 targets providing the best sensitivities in terms of companion masses. Table 7.2 summarizes the list of these targets, together with the PFN sensitivity for each of them, expressed in Jupiter masses.

The perspective for such a survey with the PFN is very promising, with sensitivities down to 7 $M_{\rm Jup}$ for the best targets. Moreover, substellar companions with masses $< 50\,M_{\rm Jup}$ can be detected around all the stars within our sample. Making a survey among the brightest young stars inside moving groups in the northern hemisphere with the PFN would be very complementary to current AO and interferometric surveys, as it will provide more angular resolution than classical AO observations and will provide more contrast than current interferometric facilities. On the scientific point of view, combining the observations of these 20 stars with the interferometric observations obtained with the VLTI on 34 targets located in the southern hemisphere will give us a unique statistical information on the presence of substellar companions orbiting close to their host stars.

8

Filling the gap: combining interferometry with coronagraphy

Contents

8.1 Principles 145

8.1.1 Beam combination with a coronagraph 145

8.1.2 Pupil densification 147

8.2 Application to stellar angular diameter measurements 148

8.2.1 Paper: **Combining coronagraphy with interferometry as a tool for measuring stellar diameters**, *P. Riaud and C. Hanot* 149

In this thesis, we presented in details two techniques used in high resolution and high contrast imaging which are coronagraphy and (nulling) interferometry. Even though these techniques seem to be different at first sight, intermediate solutions exist to combine the advantages of both methods. A first attempt to merge the two techniques has been presented in the last chapter dedicated to the PFN. Indeed, the Palomar Fiber Nuller is a so called nulling coronagraph as it combines destructively the light coming from sub-apertures of a single telescope. In this chapter, we present another intermediate solution between nulling interferometry and coronagraphy, which is multi-aperture coronagraphy. After describing briefly the particularity and advantages of this technique, we will introduce a paper describing the interest of such a technique for the accurate measurement of stellar angular diameters.

8.1 Principles

Both coronagraphy and (nulling-) interferometry have been extensively presented in this thesis. In this section, we combine the two approaches and present the principle of multi-aperture coronagraphy. After explaining the connections between the latter, coronagraphy and interferometry, we will present the concept of pupil densification which is a mandatory step for using coronagraphy on a diluted aperture.

8.1.1 Beam combination with a coronagraph

The principle of a multi-aperture coronagraph is shown in the bottom panel of Figure 8.1 for a two beam design, and compared to both standard coronagraphic and Fizeau interferometer layouts. The concept

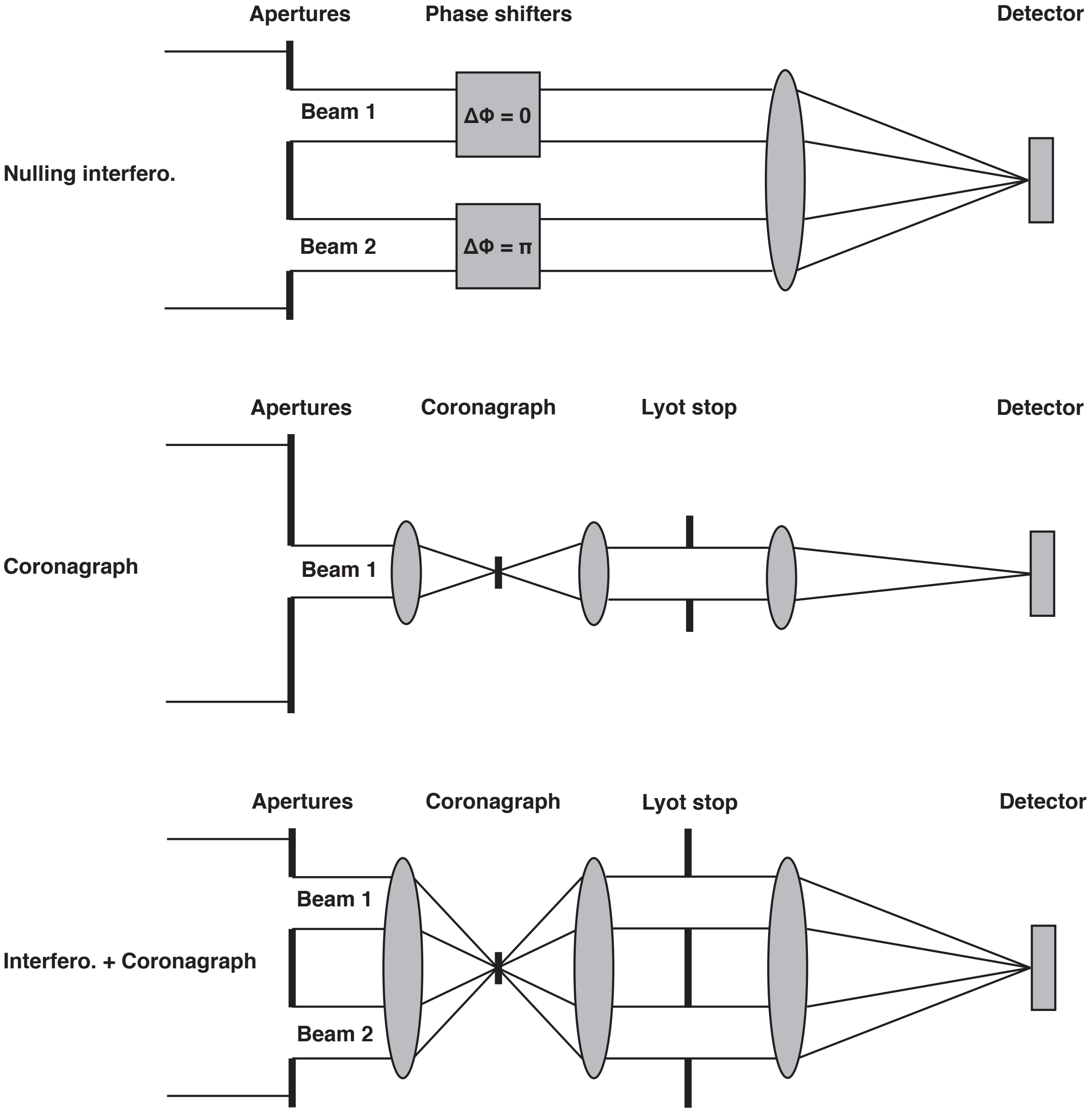

Figure 8.1: Comparison between the layouts of a nulling interferometer, a single-pupil coronagraph and a multi-aperture coronagraph. On top, a two beam nulling interferometer is represented. It collects the light from its two apertures and introduces a relative π phase shift between them. The two beams are then focused onto a detector (or a single mode fiber) and the nulling signal is recorded. The middle scheme represents a typical focal-plane coronagraphic system. The light collected by the telescope is focused onto a coronagraph. After being collimated, the beam then passes through a Lyot stop which rejects the diffracted light. The resulting coronagraphic image is formed on the detector. The bottom panel represents the layout of a multi-aperture coronagraph. Instead of using phase shifters, the multiple beams are focused onto a common coronagraph. After collimation, the beams are redefined by Lyot stops and then focused onto a detector in order to form the multi-aperture coronagraphic image.

is the following: the light collected by the different apertures are focused by converging optics. At the focus, a coronagraph is inserted in order to cancel the on-axis light just like for single aperture designs. The beams are then collimated and re-defined by Lyot stops (one for each beam), which cancel the diffracted light. Finally, the two beams are focused on a detector to create the coronagraphic image. As can be seen on Figure 8.1, this design is similar to a nulling interferometer for which the phase shifters have been replaced by a coronagraphic system (i.e., a pair of focusing optics plus a coronagraph and Lyot stops). The advantage of such a design compared to nulling interferometers is that it can be extended to any number of apertures without adding complexity to the layout. Unlike nulling interferometers, which are limited to 4 up to 6 telescopes at the most, multi-aperture coronagraphs can provide sharp imaging capabilities. The problem however with diluted arrays of telescopes is that their combined PSF is broad and composed of many fringes, unlike the narrow Airy peak of single aperture systems. This particularity strongly limits the efficiency of coronagraphic devices. Indeed, depending on its inner working angle, the coronagraph will only cancel the light of the first 2-3 fringes corresponding to the on-axis light while the other ones will leak through the system, potentially outshining the presence of a faint off-axis source. A solution to that, called pupil densification (Labeyrie 1996), is presented in the next section.

8.1.2 Pupil densification

The distribution of intensities in the focal plane of a Fizeau interferometer of a point source is given by

$$I_{\text{pt. src.}}(\vec{\theta}, \vec{\theta}_{\text{pt. src.}}) = I(\vec{\theta} + \vec{\theta}_{\text{pt. src.}})A(\vec{\theta} + \vec{\theta}_{\text{pt. src.}}) \tag{8.1}$$

where $\vec{\theta}$ is the vector of coordinates in the plane of sky, $\vec{\theta}_{\text{pt. src}}$ the coordinate vector of the point source being observed, $I(\vec{\theta})$ the interference function (see Section 3.2) and $A(\vec{\theta})$ the Airy function representing the PSF of the individual apertures of the interferometer. In the case of a diluted interferometer (i.e., small apertures compared to the baseline), the Airy function is wide compared to the fringe spacing and the intensity of the source is dispersed over many fringes (see Figure 8.2). When the sizes of the apertures become significant compared to the baseline, the PSF of the individual telescopes shrinks and the energy is concentrated in a smaller number of fringes. Unfortunately, apart for a few exceptions like the LBTI (see Section 3.4), most interferometers have small apertures compared to their baselines and the image of a point like source in Fizeau mode is dispersed over many fringes. More than the loss of SNR, such a PSF strongly reduces the imaging capabilities of the interferometer. To overcome this issue and use diluted apertures to image very small details in space such as the surface of exoplanets, Labeyrie (1996) proposed to densify the pupils and form so called hyper-telescopes (of several kilometers in diameter). The principle of pupil densification is illustrated in Figure 8.2 and consists in artificially increasing the relative sizes of the aperture compared to the baseline. Once imaged, the remapped pupils form interference patterns similar to those of interferometers having dense pupils, but only inside a small field of view. This technique has two advantages. First, if we denote as $\gamma_d = (d_0/D_0)/(d_i/D_i)$ the pupil concentration coefficient, with D_i and d_i the entrance pupil diameters of the array and the apertures respectively, and D_o and d_o the corresponding diameters after densification, the FWHM of the densified interferometric PSF is divided by γ_d compared to the PSF at the Fizeau focus. Similarly to single aperture telescopes, a narrower PSF means better imaging capabilities and the distribution of intensities given by Equation 8.1 for non densified interferometers now becomes:

$$I_{\text{pt. src.}}(\vec{\theta}, \vec{\theta}_{\text{pt. src.}}) = I(\vec{\theta} + \gamma_d\vec{\theta}_{\text{pt. src.}})A(\vec{\theta} + \gamma_d\vec{\theta}_{\text{pt. src.}}) \tag{8.2}$$

Second, the fraction of energy q_e concentrated in the central fringe (or peak) increases quadratically with γ_d:

$$q_e = N\left(\frac{\gamma_d\, d_i}{D_i}\right)^2, \tag{8.3}$$

where N is the number of apertures in the array.

Thanks to these two properties, interferometers with densified pupils, also called hyper-telescopes, behave similarly to telescopes having the size of the whole array. Moreover, because the fraction of

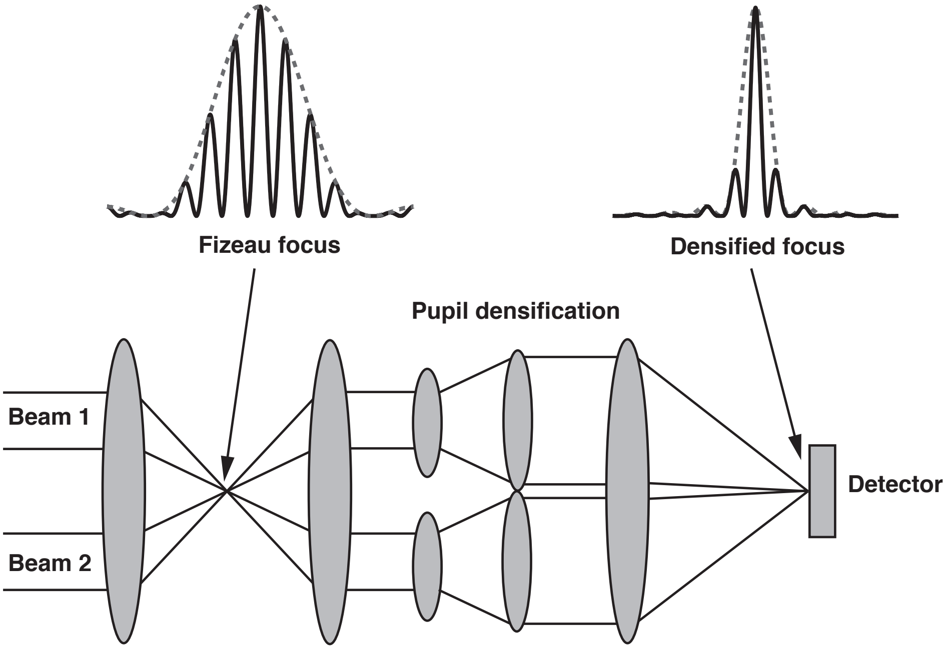

Figure 8.2: Principle of pupil densification for a two beam interferometer.

energy concentrated on the central peak is high, coronagraphic devices can be efficiently used to dim the starlight and reveal faint off-axis structures in its vicinity. A few years ago, Boccaletti et al. (2000) and then Riaud et al. (2002) have proposed a concept of space-based hyper-telescope equipped with a phase-mask coronagraph as a possible solution to image and characterize Earth-like exoplanets in the thermal-infrared. By comparing the performances of such a system with classical Bracewell nulling interferometers, they showed that combining interferometry with coronagraphy could outperform the latter and reduce the integration time needed for exoplanet detection.

8.2 Application to stellar angular diameter measurements

Since the first measurement of a stellar angular diameter by Michelson and Pease with an interferometer on Mt. Wilson in 1920, the determination of angular diameters has remained one of the main applications of stellar interferometry. Indeed, with baselines longer than 100 m, no other technique can compete with the angular resolution of interferometers ($\simeq$ 1 mas). However, by using either nulling interferometry or by inserting a coronagraph in the focal plane of an interferometer as described in the previous section, it is possible to increase the accuracy of an interferometer to stellar angular diameter measurements by an order of magnitude or more. Indeed, as presented in Section 3.3.2 for nulling interferometry, the rejection provided by both a phase mask coronagraph and a nuller depends quadratically on the angular size of the target being cancelled:

$$N_a = \frac{1}{R_a} = \frac{\pi^2}{k}\left(\frac{B\theta_\star}{\lambda}\right)^2 \tag{8.4}$$

where B is the interferometric baseline or the telescope diameter D, $\theta_\star$ the angular radius of the star, λ the wavelength of observation and k a constant factor depending on the occulting technique being used. For nulling interferometry, $k = 4$, while for an Annular Groove Phase Mask coronagraph (AGPM) or equivalently a Vectorial Vortex coronagraph (Mawet et al. 2005b; Mawet et al. 2009), this factor is $k = 12$. This relationship between null depth and angular diameter is the same as for visibilities but is however easier to measure because it comes to measure small fluctuations around zero rather than around 1 for visibilities. Moreover, by dimming the on-axis light, the signal coming from the central part of the star which does not contain any information on the angular size of the star is suppressed. Only the off-axis light containing useful information leaks through the optical system. The SNR of the critical information is therefore increased compared to classical interferometers and the accuracy and sensitivity to diameter measurement is improved. However, it comes at the price of an increased instrumental complexity.

8.2.1 Paper: Combining coronagraphy with interferometry as a tool for measuring stellar diameters, *P. Riaud and C. Hanot*

In the following paper (Riaud & Hanot 2010), we present the use of an instrument combining interferometry and coronagraphy in order to measure stellar angular diameters. The principle of the instrument is first presented in the case of a two-telescope Fizeau interferometer combining the beams onto a phase mask coronagraph. The different astrophysical sources and physical phenomena implemented in the simulations are then described. After developing the dependence of the instrumental rejection as a function of the observed astrophysical object and the major error sources, we show how, using the statistical data analysis described in Chapter 4, we can get rid of most of them and improve the accuracy on the measurements. Finally, we use our simulations to give a realistic estimation of the instrument performance to measure the angular diameter of Cepheid stars and discuss the robustness of the method against the presence of circumstellar disks or companions around these stars. For this paper, I developed a rigorous technique for analyzing the data that one would obtain with such an instrument based on the statistical self-calibrated method (Hanot et al. 2011). As it is shown, the combination of such an innovative data reduction technique with the instrumental concept presented here-after can lead to a significant improvement on the precision at which stellar diameters can be measured.

The Astrophysical Journal, 719:749–762, 2010 August 10 doi:10.1088/0004-637X/719/1/749

COMBINING CORONAGRAPHY WITH INTERFEROMETRY AS A TOOL FOR MEASURING STELLAR DIAMETERS

P. Riaud and C. Hanot
IAGL, Université de Liège, 17 Allée du 6 Août, B-4000 Sart Tilman, Belgium; riaud.pierre@gmail.com, hanot@astro.ulg.ac.be

Received 2010 February 18; accepted 2010 June 23; published 2010 July 22

ABSTRACT

The classical approach for determining stellar angular diameters is to use interferometry and to measure fringe visibilities. Indeed, in the case of a source having a diameter larger than typically $\lambda/6B$, B being the interferometer's baseline and λ the wavelength of observation, the fringe contrast decreases. Similarly, it is possible to perform angular diameter determinations by measuring the stellar leakage from a coronagraphic device or a nulling interferometer. However, all coronagraphic devices (including those using nulling interferometry) are very sensitive to pointing errors and to the size of the source, two factors with significant impact on the rejection efficiency. In this work, we present an innovative idea for measuring stellar diameter variations, combining coronagraphy together with interferometry. We demonstrate that, using coronagraphic nulling statistics, it is possible to measure such variations for angular diameters down to $\approx\lambda/40B$ with 1σ error-bars as low as $\approx\lambda/1500B$. For that purpose, we use a coronagraphic implementation on a two-aperture interferometer, a configuration that significantly increases the precision of stellar diameter measurements. Such a design offers large possibilities regarding the stellar diameter measurement of Cepheids or Mira stars, at a 60–80 μas level. We report on a simulation of a measurement applied to a typical Cepheid case, using the VLTI-UT interferometer on Paranal.

Key words: instrumentation: high angular resolution – instrumentation: interferometers – methods: statistical – techniques: photometric

Online-only material: color figure

1. INTRODUCTION

Cepheid variable stars constitute unique standard candles for the determination of extragalactic distance scales (Vilardell et al. 2007; Feast et al. 2008). However, even for the nearby Cepheids, precise distance measurements are extremely challenging due to their small stellar angular diameters (<3 mas). Thanks to the use of optical interferometry, it has been possible, since a decade, to directly measure the angular diameter variations of δ Cep, and to combine them with radial velocity measurements to derive its distance (Mourard et al. 1997). Unfortunately, due to its actual limitation in terms of angular resolution, classical interferometry (i.e., that of visibility measurements) is not sensitive enough to measure the pulsation of more distant Cepheids (Mourard et al. 1994; Armstrong et al. 2001; Kervella et al. 2001). Indeed, with classical stellar interferometry, a stellar angular diameter is measured by fitting the corresponding visibility profile with a Bessel J_1 function. Under good observing conditions, this technique allows a typical precision of 500 ± 200 μas on stellar diameter determinations at 1.65 μm on the VLT-UT largest baseline (UT1–UT4 130 m). Even though such a precision is sufficient in the case of closeby Cepheids, this approach fails to detect fine stellar atmosphere pulsations of more distant Cepheids or Mira stars (>1 Kpc), which have typical angular diameters of 60–80 μas with variations of $\sim$2 μas. As a consequence, the number of available extragalactic distant-scale calibrators is significantly reduced. Obtaining higher accuracy measurements should help setting better constraints on the previous period–radius and period–mass relations, with a direct impact on the extragalactic distance scale studies (Macri et al. 2006; Ferrarese et al. 2007; van Leeuwen et al. 2007; Vilardell et al. 2007; Feast et al. 2008).

In this paper, we suggest the use of an innovative configuration based on the implementation of the coronagraphy principle to a multi-aperture interferometer. Combination of these two techniques (interferometry and coronagraphy, or equivalently, nulling interferometry) is generally used to improve the detection of faint structures or companions around nearby stars (Riaud et al. 2002; Tinetti 2006; Wallner et al. 2006). Given the fact that coronagraphic devices are sensitive to the angular source size, a coronagraphic implementation of a stellar interferometer can further improve the detection variations of stellar sources diameters.

In order to derive distance estimates when using an interferometer in the visibility mode, the Cepheid diameter measurements can be combined with the radii derived from the stellar flux and radial velocity curves. Our technique, based on the statistics of the best rejection factor of the coronagraphic device, directly measures the stellar diameter. The rejection varies with the square of the stellar diameter, with a large variation in the first Airy ring of the coronagraphic image. Indeed, a change in the source diameter has an impact on the intensity of the residual speckles included in the first Airy ring, which is proportional to the square of the angular diameter (see Equation (2)). We use the null depth leakage from a ground-based interferometer, operating in speckle mode (i.e., using short exposure times), to measure the stellar diameter with a sub-resolution precision ($\approx\lambda/40B$ with $\pm 1\sigma$ error-bars as low as $\approx\lambda/1500B$, where λ is the wavelength of observation and B the interferometer baseline). Compared to the classical visibility measurement where $V^2 \approx 1$ for a sub-resolution stellar diameter, a coronagraphic device allows to reject the coherent part of the interferometric pattern and enhances fine photometric variation of the rejection factor due to the angular diameter. The gain in the angular diameter accuracy is directly proportional to the rejection factor of the coronagraphic mask. The proposed technique can be applied to extended envelopes around Cepheids (Mérand et al. 2007) or Mira stars. Compared to continuum observations, it makes possible to detect the fine diameter variations of extended envelopes in Hα (in the visible) or Brγ (in the near-infrared), with the simultaneous use of two channels (differential imaging).

2. NULLING INTERFEROMETRY PRINCIPLE

2.1. Coronagraphic Rejection Function

Considering an image obtained in coronagraphic mode with a vortex coronagraph (Mawet et al. 2005) on a uniform circular aperture, the coronagraphic attenuation $f_{\rm ca}$ can be approximated by

$$f_{\rm ca}(x) \approx 1 - \frac{4J_1^2(\pi x/\sqrt{3})}{(\pi x/\sqrt{3})^2}, \tag{1}$$

where $f_{\rm ca}(x)$ is the function of the coronagraphic attenuation relative to the angular distance (x) measured in λ/d, d being the aperture diameter. These results (Mawet et al. 2005) take into account the full inner working angle (IWA) of the coronagraphic mask. Under such conditions, a limited development of the above expression near the center, $f_{\rm ca}(x)_{\rm LD}$, is given by

$$f_{\rm ca}(x)_{\rm LD} \approx (\pi^2 x^2/6). \tag{2}$$

Defining the rejection as $R_\alpha = 1/f_{\rm ca}$, we conclude that, near the center of a coronagraphic image, R_α is inversely proportional to x^2, the square of the angular size of the source. For the case of a resolved source and a circular pupil coronagraph (Riaud et al. 2002), the total rejection factor is given by

$$R_\alpha = \frac{\int_0^\alpha x \cdot dx}{\int_0^\alpha f_{ac}(x) \cdot x \cdot dx} \tag{3}$$

$$R_\alpha \approx \frac{\alpha^2}{2}\left[\int_0^\alpha f_{ac}(x)_{DL} \cdot x \cdot dx\right]^{-1} = \frac{12}{\pi^2\alpha^2}. \tag{4}$$

In the above calculations, we considered a "top hat" stellar diameter (2α) with no limb darkening. In the case of a two-aperture interferometer, the integration variable x is in units of λ/B. The effect of nulling on stellar diameter measurements is more important at the center of the coronagraphic image, and in nulling interferometry projects such as DARWIN or TPF (Wallner et al. 2006) it is generally referred to as "stellar leakage." This effect has been extensively studied in the nulling mode for TPF-I/DARWIN and in the coronagraphic mode for TPF-C programs.

However, the effect of the atmospheric turbulence imposes strong limitations on the nulling performance of a coronagraph (Riaud et al. 2003; Jenkins 2008). To evaluate these limitations, all interferometric simulations used in this paper have been carried out under realistic atmospheric turbulence conditions. In the next section, we explain the possible coronagraphic configuration that could be used in the VLTI interferometer (UT1–UT4) to perform the best possible stellar diameter retrieval.

2.2. Interferometric Recombination with a Coronagraph

The principle of the instrument we will describe in this paper is somewhat different from usual coronagraphs where the masks are used in the focal plane of a single mirror. Instead, we propose to recombine two or more beams directly on a phase-mask coronagraph (Fizeau Mode). First, the light coming from the telescopes is injected into monomode fiber bundles, therefore filtering the input pupils (see Figure 1). The main advantages of this technique are first that it allows to simplify the interferometric recombination (Riaud et al. 2001b) and second that it apodizes the entrance pupil of the Fizeau recombination which partially removes the effect of the central obscuration of the telescopes. These two advantages help the system (and therefore the rejection factor) to be more robust to the external fluctuations (Strehl, tip-tilt, etc.). The main drawback however is that these injections into monomode fibers decrease the overall throughput of the instrument by about 25%, depending on the design and on the residual tip-tilt on the sub-apertures. At the output of the fiber bundles, the two interferometer arms are focused onto a phase-mask coronagraph, such as the Four Quadrant Phase-Mask (FQPM; Rouan et al. 2000; Riaud et al. 2001a) or the Annular Grove Phase-Mask (AGPM; Mawet et al. 2005) or the vortex phase-mask (Swartzlander et al. 2008; see Figure 1). Inserting such masks at the focal plane of the interferometer allows direct nulling of a source located on the optical axis of the system with no additional step. The problem, however, is that the resulting coronagraphic image is too diluted (over several thousands of speckles) to be usable. A densification stage must therefore be added after the Lyot stops to increase the S/N (see Section 3.2). After the coronagraph, the two beams are collimated so that the Lyot stops can be used (just like in usual coronagraphy designs), the only difference being that we have two coronagraphic pupils instead of one. At this stage, a near-infrared photodiode with an overall quantum efficiency of 25% (Wu et al. 2009; Myers et al. 2006; Hicks et al. 2003) can be placed in front of the entire pupil in order to monitor the photometric variations of the interferometer. This important information can be later used to significantly increase the precision on the measurement by applying some corrections to the measured rejection factor. Finally, the last step before the final interferometric recombination is the densification of the two beams (Labeyrie 1996). As already explained, this important step dramatically increases the S/N in a narrow field of view (Riaud et al. 2001b), allowing one to perform coronagraphic measurements with short integration times, which is mandatory in order to get non-zero probabilities of measuring high rejection ratios. The densification is a very simple two-step process.

1. First, both beams are expanded using two diverging lenses (one for each channel), while the separation between them is kept constant.
2. Then, once there is almost no gap left between them, another set of two converging lenses are used to perform the collimation.[1] In the final image plane (D2; see Figure 1), a densified coronagraphic image is generated in the first lobe of the Airy pattern (corresponding to a field of view of three fringes).

One of the main advantages of this instrument compared to usual long baseline interferometers is that all the optics that come after the pupil injection into the single-mode fibers are fixed. The resulting workbench is therefore much more simple and stable. Despite this fixed optical scheme, one must not forget that the real projected baseline on the sky changes during observation, and so does the rejection factor. This effect must be taken into account during the coronagraphic data analysis.

The main nulling efficiency limitation for all coronagraphic ground-based devices due to the atmospheric turbulence. Indeed, the tip-tilt noise has a major weight as it influences the centering of the central fringe on the coronagraphic device. As

---

[1] On a technical point of view, these lenses (or micro-lenses) could be manufactured in infrasil so that they would be usable from the I band to the K band.

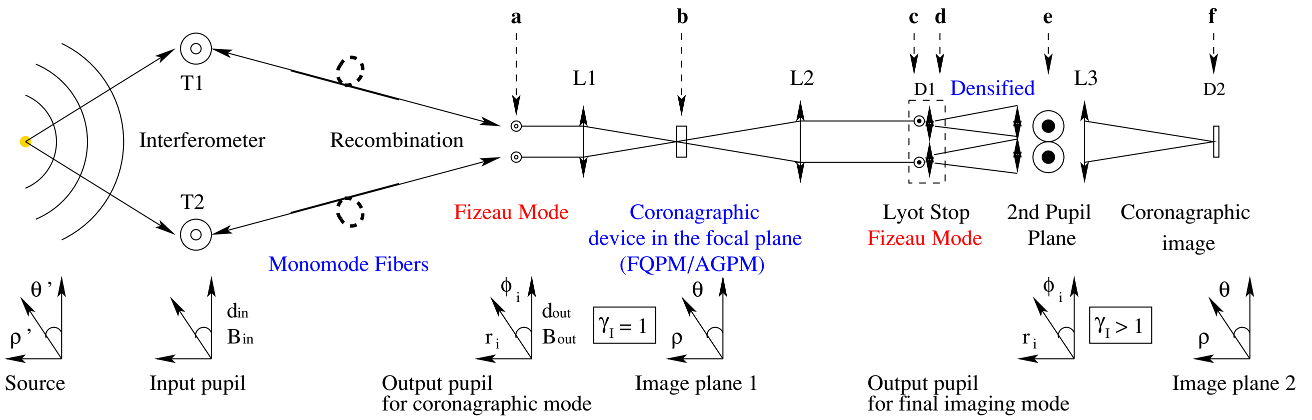

Figure 1. Optical scheme of the proposed implementation of coronagraphy on an interferometer with two apertures. On the left part of the graph, the interferometer (T1, T2) is combined with monomode fiber bundles on a Fizeau mode imaging. The L1 lens forms the interferometric Fizeau image on the FQPM/AGPM coronagraph (first focal plane). The L2 lens images the pupil in the second plane, while the Lyot stop suppresses the diffracted starlight. The photodiodes D1 (in the pupil plane) are monitoring the rejection factor (see Figure 3). After the Lyot stop, the apertures are recombined using a densified pupil in order to increase the signal-to-noise ratio (S/N) in the central fringe. Finally, L3 forms the coronagraphic images (second focal plane) on the high-speed detector D2 in the interferometric field of view (see Figure 2). More details about the optical and numerical implementation of steps a–f can be found in Figure 2. We also present all coordinate systems used in Section 3. Concerning the two pupil planes and the two focal planes, we use the same coordinates (r_i, ϕ_i) and (ρ, θ), respectively, needed in the mathematical considerations. Thus, the Fizeau and densified modes are explained with the same theory.

(A color version of this figure is available in the online journal.)

explained above, in order to have a significant amount of coronagraphic measurement with high contrast ratios, it is mandatory to have high frequency detectors (up to 100 Hz for the *K* band and 1 kHz for the *I* band) in order to follow the lifetime of the speckles (Labeyrie 1970) and prevent any averaging of the nulling measurements. Within a data set, the majority of the frames give an image which is not centered on the coronagraph because of the poor Strehl ratios. They are characterized by weak attenuation factors, while the few ones with a good centering have higher attenuation factors. Therefore, by taking several thousands of short-exposure coronagraphic images ($>10^4$), it is possible to obtain frames with a rejection larger than 20–100 at their center (see Section. 6.1), which is a requirement to emphasize the contribution of the stellar diameter variations.

Another limitation comes from the photometric fluctuations. To prevent this effect, the total flux can be monitored in both the coronagraphic pupil and the image plane during the acquisition process. The relative photometry between the rejected starlight in the pupil plane and the residual image is mandatory in order to properly calibrate the rejection factor of the interferometric system, but an absolute photometry is not necessary for this case. The photometry requirement is similar to the interferometric visibility measurement, for which 1% to 3% accuracy is needed. As the Cepheids undergo intrinsic luminosity variations, an effect that is detectable with a full data analysis, it is possible to study the correlation between the diameter retrieved by our method and the absolute luminosity variations.

The detailed design of the coronagraphic implementation on the two-aperture interferometer proposed in the current work is presented in Figure 1.

3. MATHEMATICAL CONSIDERATIONS

3.1. *Interferometric Configurations*

This section provides the mathematical background needed to understand the coronagraphic effect on an interferometer. The numerical simulations presented in subsequent sections are based on these analytical considerations. Indeed, we propose in the first stage (before the coronagraph) to use direct Fizeau interferometric imaging followed by the densified interferometric mode after the Lyot stop (the second stage). The difference between these two modes is simply given by the densification factor γ_I. All the mathematical developments are common to both densified and non-densified recombinations.

The first recombination method used is the one introduced by Fizeau (1868) and consists in making a direct homodyne combination of the sub-apertures without changing the relative sub-pupil sizes of the system. The pupil transform is strictly homothetic between the input and the output interferometric pupil with $\gamma_I = 1$ (see Equation (7)). The densified recombination case is characterized by $\gamma_I > 1$. We will explain the general case, where the homothetic pupil transformation between the input and the output pupil changes the optical path by a factor γ_I. The case of full densification of only two telescopes is called Michelson recombination (Michelson 1891; Michelson & Pease 1921). For that, we must consider three different planes to calculate the image properties for various interferometers: (1) the input pupil plane (telescopes), (2) the output pupil plane in the optical system, and (3) the plane where the final image is generated (see Figure 1). In the case of a global pupil transform, we can define the ratio coefficient after the pupil remapping as

$$\gamma_d = d_{\rm out}/d_{\rm in}, \tag{5}$$

$$\gamma_b = B_{\rm out}/B_{\rm in}, \tag{6}$$

$$\gamma_I = \gamma_d/\gamma_b, \tag{7}$$

where $d_{\rm out}$, $d_{\rm in}$ are the respective diameters of the sub-aperture in the output and input pupil plane, and $B_{\rm out}$, $B_{\rm in}$ are the baselines of the interferometric array in the two latter planes. The dilution factor of the interferometric scheme becomes $B_{\rm out}/d_{\rm out}$ after the pupil remapping.

The position of the telescopes in the pupil plane of the interferometer can be described by means of Dirac positions (δ) for the ith aperture in the $r_i \cdot e^{i\phi_i}$ polar coordinate system (see Figure 1). It should be noted that even though the coronagraphic mode is that of Fizeau, the final image is in the densified mode. We use the same notation for the new positions of the telescopes after the densified process in the pupil plane to describe the properties of the interferometric images ((r_i, ϕ_i); see Figure 1). The coordinates (ρ', θ') and (ρ, θ) are the position vectors in the source and the image plane, respectively.

It is possible to calculate the optical transfer function (OTF) for a general interferometric scheme in the following way:

$$\mathrm{OTF}(\rho, \theta, \rho', \theta') = \left| T_{(a,\gamma_d)} \cdot I_{(\delta,\gamma_b)} \right|^2, \tag{8}$$

where $T_{(a,\gamma_d)}$ is the envelope function given by the diffraction pattern of a sub-aperture and $I_{(\delta,\gamma_b)}$ is the interferometric pattern given by the position δ of the telescopes in the frequency domain.

The envelope pattern in the case of a circular aperture with central obscuration a with $a < 1$ is a pure radial function. It can be easily calculated in the following way:

$$T_{(a,\gamma_d)} = \frac{2J_1(\pi \cdot d_{\mathrm{out}}(\rho - \rho'/\gamma_d)/\lambda)}{\pi \cdot d_{\mathrm{out}}(\rho - \rho'/\gamma_d)/\lambda} - \frac{2J_1(\pi \cdot a \cdot d_{\mathrm{out}}(\rho - \rho'/\gamma_d)/\lambda)}{\pi \cdot a \cdot d_{\mathrm{out}}(\rho - \rho'/\gamma_d)/\lambda}, \tag{9}$$

where $\rho - \rho'/\gamma_d$ denotes the homothetic pupil transformation effect on the source position in the final image plane. For an off-axis source (radial position ρ' relative to the center), the envelope is shifted to a lower angular position ρ'/γ_d. Note that this envelope solution is generalizable for various shapes of one pupil. In the same manner, we calculate the interferometric pattern function given by the Fourier transform of the Dirac pattern telescope position in the frequency domain:

$$\mathrm{CS}_{\theta,\phi_i} = \cos(\theta) \cdot \cos(\phi_i) + \sin(\theta) \cdot \sin(\phi_i), \tag{10}$$

$$\mathrm{CS}_{\theta',\phi_i} = \cos(\theta') \cdot \cos(\phi_i) + \sin(\theta') \cdot \sin(\phi_i), \tag{11}$$

$$I_{(\delta,\gamma_b)} = \sum_i^n \exp - \frac{2i\pi \cdot r_i}{\lambda} \left(\rho\, \mathrm{CS}_{\theta,\phi_i} - \frac{\rho'}{\gamma_b} \mathrm{CS}_{\theta',\phi_i} \right), \tag{12}$$

where n is the number of sub-apertures and ρ, ρ'/γ_d represents the same homothetic pupil transformation effect on the source position on the final image plane. If we call $O(\rho', \theta')$ the object intensity distribution, we can derive the intensity distribution (Equation (8)):

$$I_{\mathrm{obj}}(\rho, \theta) = \int_\lambda \int_{\rho'} \int_{\theta'} O(\rho', \theta') \cdot \mathrm{OTF}(\rho, \theta, \rho', \theta') \cdot d\rho' \cdot d\theta' \cdot d\lambda. \tag{13}$$

1. The Fizeau case corresponds to $\gamma_I = 1$ where the convolution relationship is kept during this recombination. For off-axis sources, the displacement of the interferometric pattern given by the multiple sub-apertures $I_{(\delta,\gamma_b)}$ follows perfectly the displacement of the telescope diffraction pattern $T_{(a,\gamma_d)}$.
   The result is a real point-spread function (PSF) where the fringe pattern is modulated by a large diffraction disk. For a large dilution factor (small diameter of sub-apertures and long baselines), the focal plane image features one single white fringe and many (hundred or more) dispersed fringes. Only a fraction of the energy is in the white fringe.
2. In the densified mode, where $\gamma_I > 1$, there is no simple convolution relationship anymore between the object and the transfer function of the interferometer. Indeed, the interferometric pattern $I_{(\delta,\gamma_b)}$ moves faster by a factor γ_I than the new telescope diffraction pattern after the pupil remapping.
   The final image of the observed object is in a narrow field of view defined by the new telescope diffraction envelope $T_{(a,\gamma_d)}$. The main property of the densified image is that the astrophysical object observed by the first mirror of the telescope (λ/d_{in}) is compressed in this new narrow field of view (λ/d_{out} called "Zero Order Field" in Labeyrie 1996; Riaud et al. 2001b; Riaud 2003) with a limited number of resolution elements.

3.2. Coronagraphic Configurations

In this section, we present the rejection effect of a phase-mask coronagraph on the Fizeau interferometric configuration. The coronagraph is working in a coupled mode on all apertures (i.e., on the Fizeau PSF) rather than independently on each telescope. Under this condition, the coronagraphic pupil acts on the full amplitude image function and shows a cross-talk effect by mutual contamination of the rejected starlight in each sub-aperture. In the first order, the following calculation shows that the cross-talk effect is of minor importance and that the coronagraphic rejection is mainly driven by the differential piston on each telescope of the interferometric system. We shall now demonstrate these properties by applying the vortex phase-mask on the Fizeau image.

Let us call the coronagraphic phase-mask function, M_c, in the ideal case of vortex coronagraph of order 2 (Mawet et al. 2005):

$$M_c = e^{\pm i2\theta}, \tag{14}$$

where θ is the angular coordinate in the coronagraphic focal plane.

Within a Fizeau recombination, the amplitude image is given directly by the sub-aperture pattern $T_{(a,\gamma_d)}$ modulated by the interferometric fringes $I_{(\delta,\gamma_b)}$. The amplitude of the coronagraphic image, A_{CI}, after the coronagraphic phase-mask effect can be expressed directly in the Fizeau case by

$$A_{\mathrm{CI}} = T_{(a,\gamma_d)} \cdot I_{(\delta,\gamma_b)} \cdot M_c. \tag{15}$$

Mawet et al. (2005) have demonstrated that, in the pupil plane, the diffracted starlight by a vortex coronagraph has the following form:

$$\Pi_c(r, \theta) = \epsilon_{\lambda,i}, \qquad r < d_{\mathrm{out}}/2; \tag{16}$$

$$\Pi_c(r, \theta) = \frac{e^{\pm i2\phi}}{(2r/d_{\mathrm{out}})^2}, \qquad r > d_{\mathrm{out}}/2; \tag{17}$$

where $\epsilon_{\lambda,i}$ is the coronagraphic residual in the ith sub-pupil due to wavefront errors, the telescope central obscuration and the mask chromatism limitation. Under this condition, at the exit pupil plane of the Fizeau interferometer after a vortex coronagraph, the diffracted light possesses two different terms:

$$\Pi_{Fc}(r, \theta) = \sum\nolimits_i^n \left(\epsilon_{\lambda,i} + E_{c,i} \right), \tag{18}$$

where $E_{c,i}$ is the cross-talk energy between the different pupils. The cross-talk energy between pupils i and j is given by

$$E_{c,i} = \frac{d_{\text{out}}^2}{4} \cdot \left| \sum_{j \neq i}^{n} \int_0^{\frac{d_{\text{out}}}{2}} \int_0^{\alpha_m} \frac{e^{\pm i 2\phi} \cdot r \cdot dr \cdot d\phi}{(r - (r_j - r_i))^2} \right|_i^2 \tag{19}$$

with

$$\alpha_m = 2 \cdot \arctan(d_{\text{out}}/(r_j - r_i)). \tag{20}$$

In the case of the Fizeau recombination of the two VLT-UT1/UT4 telescopes, we may calculate the cross-talk term with $r_j - r_i = B_{\text{out}}/d_{\text{out}} = 16.25$, $\gamma_I = 1$, and finally, by considering $E_{c,1} \approx E_{c,2}$.

As a consequence, from Equation (19) we derive

$$E_{c,i} = 9.35 \times 10^{-7} \ll \epsilon_{\lambda,i}.$$

Phase-mask coronagraphs such as the FQPM or the Optical Vectorial Vortex Coronagraph (OVVC) have been tested on optical-benches from the visible (Riaud et al. 2003) to the near-infrared (Mawet et al. 2009) wavelengths, and the obtained attenuation factors obtained are larger than 1000 in full bandpass ($R = 5$) and $>10^5$ in narrow bandpass ($R = 300$). Under such conditions, some manufacturing defects or limitations appear to be negligible in our configuration. Indeed, the main limitation of the coronagraphic rejection in the Fizeau configuration ($\epsilon_{\lambda,i}$) is due to the residual atmospheric piston between the two apertures.

3.3. Differential Piston

In this section, we describe the effect of differential piston on an interferometer. A long baseline interferometer tends to amplify the wavefront tip and tilt in the different sub-apertures introduced by the atmospheric turbulence ($\lambda/d \rightarrow \lambda/B$). Equation (12) gives the differential piston term for different recombination schemes. Concerning the Fizeau configuration ($\gamma_I = 1$), the differential piston effect can be easily seen as the full PSF pattern moving in front of the coronagraphic device. The coronagraph is highly sensitive to tip-tilt errors and the rejection factor is strongly reduced. Under such a condition, it is mandatory to follow the image with a fringe tracker (FT; $<\lambda/2$ rms) in order to keep the rejection high enough. In this paper, we consider a rather pessimistic case with an FT having an error of $\lambda/3$ rms in the H band (500 nm rms). The Finito and Prima instruments on the VLTI, for example, provide a smaller differential piston error (Le Bouquin et al. 2008, 2009; van Belle 2009).

The final configuration after a proper coronagraphic pupil filtering is densified to increase the S/N. This second stage of densification artificially creates wavefront stairs in each sub-pupil with an important tip-tilt, and it can be seen as a high fringe moving in the limited field of view given by the densification process. If the FT residual remains below $<\lambda/2$ rms, the densified image is of zero order (white fringes) in the limited field of view of the "Zero Order Field." In terms of the Fourier frequencies, all high order images (dispersed peaks) present in the Fizeau mode are folded in the zero order to increase the signal.

3.4. The Monomode Fiber Telescope Link

For our Fizeau recombination in the near-infrared, we preferred to use single-mode optical fibers (Shaklan 1990; Coudé Du Foresto 1997; Wallner et al. 2002) rather than bulk optics, as they provide a more flexible and compact solution for a beam combination. The spatial filtering properties of single-mode fibers are used to properly convert random atmospheric phase perturbations into photometric fluctuations. Phase-mask coronagraphy seems to be more robust to photometric fluctuations in the pupil plane than to phase ones (Riaud et al. 2001a). Nevertheless, although in this case the atmospheric jitter decreases, high frequency noise starts to be present in the amplitude measurements. The configuration allows better nulling rejection on the center but increases speckle noise (amplitude fluctuation) at high frequencies.

The fundamental mode field distribution for a single-mode fiber corresponds to the Bessel functions J_1 near the center ($r < 0.5\,\omega_0$) and a K_1 Bessel for $r > 0.5\,\omega_0$, where ω_0 is the radius of the fiber waist (see Equation (23)). We can however approximate with very good accuracy ($\approx$2%) the fundamental mode field distribution in each sub-aperture pupil (Π_{Ai}) using a Gaussian function:

$$\Pi_{Ai} = A_i \cdot \frac{\omega_0}{\omega_z} . e^{-r_i^2/\omega_z^2}, \tag{21}$$

$$\omega_z = \omega_0 \cdot \sqrt{1 + \left(\lambda z/\pi\omega_0^2\right)^2}, \tag{22}$$

$$\omega_0 \approx a \cdot \left(0.65 + \frac{1.619}{V^{1.5}} + \frac{2.879}{V^6}\right), \tag{23}$$

$$V = 2\pi \cdot \text{NA} \cdot a/\lambda, \tag{24}$$

$$\text{NA} = \sqrt{n_c^2 - n_g^2}, \tag{25}$$

where ω_0 is the waist of the fiber corresponding to the minimum size of irradiance in the output fiber ($\approx$3–10 μm), a the radius of the fiber core ($\approx$3–6 μm), V the normalized cutoff frequency (the fiber is monomode if $V < 2.405$), NA the numerical fiber aperture given by the index of refraction of the core material, n_c and n_g the refraction indices of the cladding material (NA = 0.12–0.2), and ω_z the mode field distribution irradiance at a distance z.

Due to an infinite extension of the Gaussian distributions, the mode field distribution must be truncated on each sub-pupil by a diaphragm $\Pi_D = d_{\text{out}}$. The envelope $T_{(a,\gamma_d)}$, previously described by a simple Bessel function in the case of the classical circular aperture ($2J_1(\rho)/\rho$), must be replaced by a new one, obtained from the Hankel transform H of Π_{Ai} in order to include the diaphragm effect. In this case, Π_{Ai} (see Equation (26)) depends on the propagation distance z_{out} within the injection system:

$$d_\omega = \frac{d_{\text{out}}}{2\omega_0 \cdot \sqrt{1 + \left(\lambda z_{\text{out}}/\pi\omega_0^2\right)^2}}, \tag{26}$$

$$\Pi_{Ai} = \frac{A_i \cdot e^{-d_\omega^2 r_i^2/d_{\text{out}}^2}}{\sqrt{1 + \left(\lambda z_{\text{out}}/\pi\omega_0^2\right)^2}}, \tag{27}$$

$$T_{z_{\text{out}}} = H\left[\Pi_{Ai} \cdot \Pi_D\right], \tag{28}$$

$$T_{z_{\text{out}}} = \frac{2A_i \cdot e^{-d_\omega^2 \rho^2/d_{\text{out}}^2}}{\sqrt{1 + \left(\lambda z_{\text{out}}/\pi\omega_0^2\right)^2}} \frac{J_1(\pi \cdot d_{\text{out}}\rho/\lambda)}{\pi \cdot d_{\text{out}}\rho/\lambda}. \tag{29}$$

The final envelope is a Gaussian function modulated by a Bessel J_1 function, due to the presence of the diaphragm in the pupil plane. Compared to the previous mathematical development, the envelope image does not possess the $\rho - \rho'/\gamma_d$ term as the classical diffraction envelope. The advantage of using monomode fibers is that they strongly attenuate the tip-tilt term in each sub-pupil and at the same time there remains only a piston term between all sub-pupils.

If only the center of the fundamental mode is used, the irradiance distribution is almost uniform in each sub-pupil, but the total injection efficiency ($<15\%$) of the beams drops significantly. Now, if a large part of the Gaussian irradiance distribution in each pupil is used, the strong apodization function rejects the flux in the second lobe of the Bessel function and the total efficiency also remains low. Therefore, the optimal size of the diaphragm radius is around 0.8–1.2 $\omega_{z_{\mathrm{out}}}$, with the total efficiency becoming $\approx$20%–25%. This value corresponds to the matching between the fundamental mode of the fiber and the energy in the first λ/d of a perfect telescope PSF (see Section 4).

The polarization maintaining fibers (Delage & Reynaud 2001) seem to be less efficient regarding the nulling rejection of the coronagraph than the classical circular fibers due to a possible mode ellipticity. Indeed, the mode is elliptic and no matching of the azimuthal symmetry of all phase-mask coronagraphs can be used in this experiment. Finally, the dispersion correction of the long monomode fiber links can be done by including a small portion of photonic fused-silica fibers (1–2 m) that create negative dispersion for an optimized central wavelength.

4. NUMERICAL SIMULATIONS

In order to study the effect of coronagraphic nulling on stellar diameters, we have performed numerical simulations. To make our study as realistic as possible, we have considered a single-layer atmospheric turbulence (Von Karman statistics) to which a random tip-tilt (Gaussian statistic) and a piston noise have been added to the pupil plane (Figure 2(a)). We assume a residual tip-tilt of 8 mas rms between the two apertures, a Fried parameter of $r_0 = 15$ cm, and an outer scale of 25 m in the visible band (Paranal atmospheric characteristics). The adaptive optics is a low-order AO with a tip-tilt mirror (5 mas rms) on each Very Large Telescope (VLT; Bonaccini et al. 1997) and with a partial correction of the first-order aberrations (Zernike polynomials 2–9 and Strehl ratio of $\approx$30% in the H band). The FT is simulated as a low-pass filter having a frequency noise distribution following a $1/f$ law and a correction accuracy expressed in terms of a wavelength fraction. Finally, we have added to the simulations of the photometric measurements in full H band: (1) photon and readout noises ($6e^-$), (2) noise due to saturation effects ($10^5\,e^-$), and (3) a residual flat noise ($\pm1\%$ PTV).

The effect of stellar diameter variations on the rejection is calculated as follows: we create a coronagraphic image template using a total of 113 pixels that cover the requested stellar diameter with a uniform statistic. A limb-darkened law for the stellar luminosity decreases the effective diameter by about 5%. On every frame, any possible instrumental limitation, such as residual chromatism on the phase-mask, is included in addition to the turbulence effect. We assume a uniform diameter for the observed star. In this way, this image is a signature of the coronagraphic response of the stellar radius with respect to the interferometric configuration.

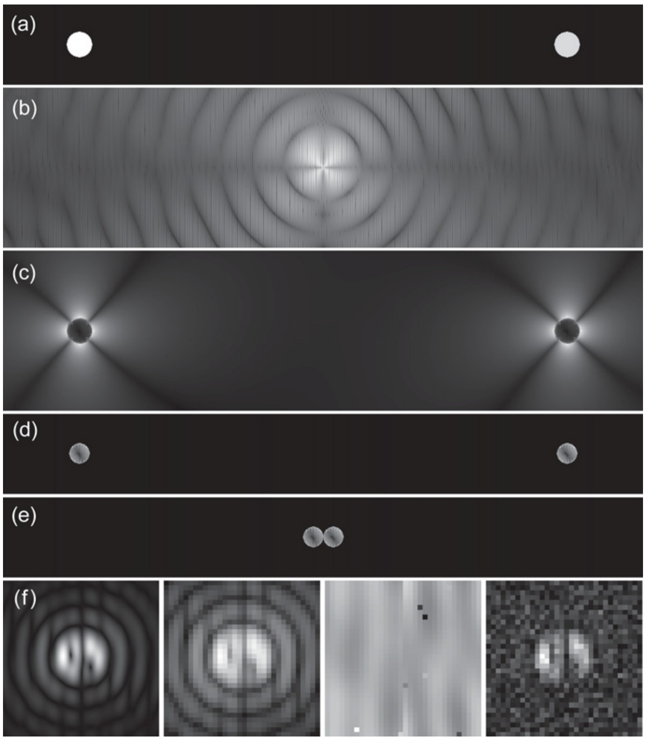

Figure 2. Numerical simulation illustrating the principle of coronagraphy with an interferometer, implemented on a UT 1–UT 4 VLTI configuration, using a 130 m baseline. Panel (a): the two entrance interferometric pupils are shown in the case of low differential piston (1 mas rms here). To make the simulations more realistic, turbulence and tip-tilt noise before a proper monomode filtering have been included. Panel (b): direct Fizeau PSF image obtained on the AGPM coronagraphic mask. This image is seen with the intensity for a circular entrance polarization. We notice a relatively bad centering of the stellar fringes with respect to the coronagraphic mask and the presence of a singularity in the mask center (vortex phase-mask). Panel (c): coronagraphic pupil plane, seen without the use of a diaphragm. Panel (d): coronagraphic pupil plane, seen after the use of a simple diaphragm. Panel (e): coronagraphic pupil plane, after the densification process, where the two pupils are joined. Panel (f): residual coronagraphic images in densified mode. (Left to right) Panel (f1): central part of a densified coronagraphic image calculated by the simulation. Panel (f2): same image as in panel (f1), but with a proper detector sampling (32 × 32 pixels), after pixel averaging. Panel (f3): image of the residual flat ($\pm1\%$ PTV) added on the coronographic image to mimic the data analysis limitation. Panel (f4): the final image, which includes flat, readout ($6e^-$), and photon noises, was considered (during the simulations) to be taken at a low S/N (max $\approx$ 1800 ADU, for a bias of 500 ADU). We notice the difference of the fringe scale in the Fizeau mode (panel (b)) and the final densified mode. The brightness scale in the images is non-linear.

Each short coronagraphic exposure is then calculated using a large sampling (2048 × 2048 pixels), to minimize the aliasing effect due to the interferometric configuration (considering an interferometric baseline of 780 pixels—130 m). Each final image is finally downsampled to 32 × 32 pixels to mimic the sampling of the detector corresponding to a field of view of $\approx 10\lambda/B$ on each side of the detector, with 3 pixels per λ/B. Indeed, in order to allow high-speed frame recording, a smaller detector is needed. A NICMOS technology in the near-infrared with a 32 × 32 pixels detector can allow a 500 Hz frame rate, which is sufficient for the J, H, and K bands. Finally, as in this interferometric mode, the (narrow) central field of view contains all information for a proper visibility retrieval, we suggest to use the densified configuration, combined with a 32 × 32 pixels detector to increase the S/N (Riaud et al. 2001b). In order to perform a "dark speckle" analysis (Labeyrie 1995) and follow the seeing variations, it is essential to obtain a large number of frames. As each frame corresponds to a single speckle realization ($\tau = 3$ ms in the visible, $\tau = 20$ ms in the

K band; see Table 3), the probability to obtain a high starlight coherence in the data set (Strehl ratio $>30\%$) is less than 10% (see Figure 4). To increase the interferometric throughput in the monomode fiber, we only make use of low-order adaptive optics for atmospheric piston and tip-tilt correction.

In order to obtain the best-value of coronagraphic nulling, the stabilization of the Optical Path Difference (OPD) between the two apertures can be achieved using an FT. The rejection factor in the center of the stellar peak is generally small, varying from ≈ 20 when no FT is used, to 40–150 when a fringe stabilizer such as FINITO (Le Bouquin et al. 2009) or PRIMA (van Belle 2009) is used due to the significant seeing variations. Nevertheless, for a high Strehl ratio ($>50\%$), the effect of the resolved source can be seen with the coronagraphic device. The numerical simulation requires 10^3–10^4 different speckle images. To reduce the computation time as much as possible, all programs are written in C language with a fast Fourier transform optimized on the NVIDIA GPU (Govindaraju & Manocha 2007) under a Linux architecture. Under such conditions, 4 hr of computing time are needed to perform 16,384 short coronographic images, including chromatism, turbulence, and photometric noise.

5. NULLING PERFORMANCE FOR A CORONAGRAPHIC DEVICE ON AN INTERFEROMETER

It is possible to recombine an interferometer with either a coronagraphic (Riaud et al. 2001b, 2002) or with a nulling system (Lay 2004, 2005). The final performance, in terms of total rejection, will be limited for any kind of recombinations by two strong effects: (1) the stellar leakage (the case studied in the current work) and (2) the chromatism of the π phase-shift. However, the latter limitation only becomes significant to reach huge rejection ratios ($R_c > 10^5$) that are needed for the search of Earth-like planets with space-borne interferometers (Wallner et al. 2006). In the following sections, we will study some other nulling-related limitations that we describe with the general term "instrumental nulling" issues.

5.1. Instrumental Nulling

1. *Phase-mask transition*. There are still some limitations in the manufacturing of phase-mask coronagraphs, such as the FQPM or the Optical Vectorial Vortex Coronagraph of charge 2 (OVVC2)/AGPM. Using an FQPM coronagraph, it has been demonstrated that $R_c > 10^5$ (Riaud 2003) can be achieved through a narrow band on a visible workbench. On a ground-based telescope facility, $R_c > 4 \times 10^2$ has been achieved with an OVVC2 (Swartzlander et al. 2008; Mawet et al. 2009).
2. *Cross-talk between the sub-apertures in the Fizeau mode*. The starlight rejected by each sub-aperture contaminates the other ones. This effect is very small: for a $B_{\mathrm{out}}/d_{\mathrm{out}} > 16$ ratio, it does not affect the rejection ratios at the 10^6 level (see Equation (19)).
3. *Central obscuration*. Phase-mask coronagraphs, such as AGPM/OVVC2/FQPM, are sensitive to the central obscuration of the telescope. Indeed, for a circular pupil, the rejection is perfect in the theoretical case (Riaud 2003; Mawet et al. 2005). A central obscuration strongly reduces the energy located in the central Airy disk of the telescope's diffraction pattern. This reduction directly affects the coronagraph's rejection. Unlike Jenkins (2008) who develops the amplitude of the PSF using a Bessel series, the residual intensity due to the central obscuration a can be easily calculated via the energy conservation law (Riaud 2003). The residual energy, E_{res}, is given directly by the surface ratio between the central obscuration and the entire pupil, and the result is

$$
\begin{aligned}
E_{\mathrm{res}}(a, r_d) &= 0, && r < a;\\
E_{\mathrm{res}}(a, r_d) &= \pi a^2 \left(1 - \frac{a^2}{r_d^2}\right), && a < r < r_d;\\
E_{\mathrm{res}}(a, r_d) &= \pi \left(1 + \frac{a^4}{r_d^2} - 2a^2\right), && r > r_d; \qquad (30)
\end{aligned}
$$

where r_d is the diaphragm radius. The diaphragm chosen in our VLT simulation with single-mode filtering possesses an outer diameter of 90%, in pupil units. Indeed, single-mode fiber filtering attenuates the impact of the central obscuration. This configuration allows a maximum total rejection factor of ≈ 1000 in full H band because the diaphragm optimization is limited by the coronagraphic diffraction limitation. The latter is mainly due to the presence of manufacturing defects in the center of the phase-mask and to chromaticity issues (Mawet et al. 2009). The impact of the central obscuration is reduced thanks to the use of monomode fibers. Due to the relatively poor FT efficiency (all simulations are given for a conservative $\lambda/3$ rms accuracy), the median rejection factor is generally lower than 40 (see Figure 4).

5.2. Optical Throughput Limitation

The first limitation is due to the coupling efficiency of single-mode filtering, which is 25%. This number is obtained by computing the injection efficiency of a beam having a perfect Strehl ratio into a single-mode fiber. This instrumental configuration allows a high instrumental stability and it must be preserved. In terms of optical throughput, the Fizeau recombination together with the densified mode[2] seems to be more efficient than other systems. Indeed, the Fizeau recombination is a much simpler optical system that allows a low residual wavefront error. The densified pupil is only applicable before the coronagraph if the sub-apertures are off-axis (i.e., no central obscuration) and a pupil-edge continuity is required after the densification process (i.e., square or hexagon sub-apertures). This is not our case, as we are considering two circular VLT-UT pupils. In the context of VLT-UT coronagraphic nulling, the entrance pupil must not be densified, as it would increase the cross-talk between the two pupils. We can notice that the FQPM coronagraph does not suffer from cross-talk effects in the case where four sub-apertures are mapped on a cross configuration with a pupil separation of $2\sqrt{2}$, in pupil radius units.

The classical Bracewell nuller can be used in the same way, but the beam recombination with cascaded beam splitters (depending on the number of sub-apertures) requires a lot of photons and provides a low stability due to the huge optical complexity. This configuration is not considered in our study. Two different optical schemes can be chosen to overcome the aforementioned drawbacks: integrated optics and off-axis single-mode fiber recombination can be efficient ways to increase the throughput and stability for nulling interferometry in the near-infrared. The Palomar Fiber Nuller (Haguenauer & Serabyn

---

[2] In our case, the Fizeau recombination is combined with a phase-mask coronagraph and a pupil densification at the last stage, after a starlight filtering by a Lyot stop.

2006; Martin et al. 2008) and MAII (Buisset et al. 2006) are examples of instruments with a simpler recombination system.

6. STATISTICAL DATA ANALYSIS

In this section, we present a statistical analysis using a large number of short-exposure frames to estimate possible biases in the stellar radius measurements. The principle is to compare the rejection statistics measured in different data sets corresponding to a possible variation of the stellar diameter during the Cepheid period. The mathematical approach is that of a classical, "dark speckles" analysis: we calculate the statistical distribution of the rejection factor $R_{c,\alpha}$ in n different coronagraphic images, obtained during the photometric acquisition including instrumental and stellar diameter effects. If we define $R_{c,\alpha}$ as being the rejection factor in a coronagraphic image, D_1 the photodiode in the pupil plane, and D_2 the high-speed detector in the full field of view (see Figure 1), $R_{c,\alpha}$ is calculated according to the formula:

$$R_{c,\alpha} = \frac{\phi(D_1) + \sum_{\text{pixels}} M_B . [\phi(D_2)]}{\sum_{\text{pixels}} M_B . [\phi(D_2)]}, \qquad (31)$$

where $\phi(D_1)$ and $\phi(D_2)$ are, respectively, the fluxes measured by the photodiode in the pupil plane and the flux measured on the detector, and M_B is the photometric attenuation induced by the coronagraphic mask. To calculate more precisely the rejection ratio, the mask's rejection M_B is assessed using the best frames (see Section 6.1) with an appropriate threshold on the photometric data to enhance the image shape.

6.1. *Nulling Histogram Retrieval*

During an observation, the null depth fluctuates with time as a function of the different error sources. Therefore, it becomes more difficult to recover the astrophysical null R_α. The method we propose here is based on the statistical analysis of the probability distribution function (PDF) of the rejection factor.

6.1.1. *Photon-noise Limitation*

As the majority of the stellar targets are fainter than sixth magnitude in the H band, it is necessary to stack short exposures to generate an improved signal-to-noise image. Indeed, if instead, we increase the exposure time for the individual coronagraphic images, we average the fast fluctuations of the instrumental rejection ratio and reduce the probability to reach very high rejections. S/N considerations indicate that the limiting magnitude for the proposed technique is about 7.5 in the full H band.

6.1.2. *Coronagraphic Data Analysis*

Let us explain the rejection histogram retrieval procedure for a proper stellar diameter estimation. In the case of a pulsating star observed with an interferometric coronagraphic system, the stellar diameter varies between two measurements. If $R_{\tau 1}$ and $R_{\tau 2}$ are two sequences of rejection ratio measurements at different epochs, a simple ratio of their distributions is sufficient to identify the one that contains the smaller number of frames with high rejection ratios ($R_c > 40$ in our case where the FT has $\lambda/3$ rms accuracy) for the largest stellar diameter. Having carefully removed the appropriate bias level (background level), the data are reduced as follows.

1. The rejection ratio of each coronagraphic image with $M_B = 1$ over the whole detector image is first calculated.

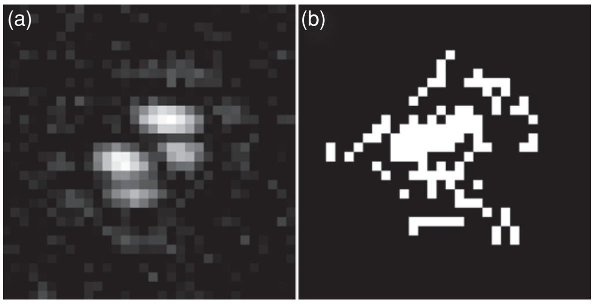

Figure 3. Left panel: H-band image of the Cepheid EN TrA, generated by stacking some 100 individual frames (5 ms exposure time per frame). Right panel: binary mask M_B of the best image used to derive the rejection factor on the central part of all coronagraphic images.

2. The best frame in terms of rejection ratio is taken, in order to create the new binary mask M_B (see Figure 3).
3. The rejection ratio is computed on the remaining images using the new binary mask M_B obtained in the first analysis. In order to enhance the stellar diameter measurement, it is necessary to limit our analysis to rejection ratios R_c larger than the median value (see Figure 4) as this part of the data is more affected by the stellar diameter effect.

Before illustrating our data analysis on a real Cepheid star (EN TrA; see Section 7.1), we must determine the mathematical form of the histogram function. This theoretical step is mandatory in order to obtain an accurate unbiased diameter measurement.

6.1.3. *Rejection Function*

The rejection function is defined as the ratio $R_c = I_+(t)/I_-(t)$ where $I_+(t)$ and $I_-(t)$ are, respectively, the overall incoming intensity of the light feeding the instrument and the nulled output intensity after introduction of the coronagraph. It can be expressed as a function of the different fluctuating sources of noise that influence its value. From this general form of the rejection function, depending on the intensity mismatch $di(t)$, the phase error $\Delta\phi(t)$ and the relative polarization rotation angle ϱ of the interferometric beams, it is straightforward to derive the instrumental rejection function. This analysis in terms of null depth function ($1/R_c$) has been developed in the general case of a nulling interferometer by Hanot et al. (2010).

Indeed, if $\Delta\phi(t)$, $di(t)$, ϱ are small, in the case of a two-aperture interferometer, the rejection, function is

$$R_c = \frac{I(t)}{(\Delta\phi(t)^2/4 + di(t)^2/16 + \varrho^2/4)}. \qquad (32)$$

From Equation (32), the rejection, taking into account the astrophysical contribution, is then simply given by

$$R_{c,\alpha} = R_c + I(t) R_\alpha. \qquad (33)$$

Among the three fluctuating terms in Equation (32), the phase error is a combination of both the FT residuals and turbulence fluctuations. Indeed, FTs are not able to correct for the fastest phase perturbations induced by the atmosphere. As a result, the phase error $\Delta\phi(t)$ is only corrected for frequencies within the FT range. From a probability distribution point of view, it creates two different distributions in the noise analysis: $\Delta\phi(t) = \Delta\phi_{\text{atm}}(t) - \Delta\phi_{\text{ft}}(t)$.[3]

---

[3] If $\Delta\phi_{\text{atm}}(t)$ and $\Delta\phi_{\text{ft}}(t)$ are independent normal variables following the law $\aleph(\mu_{\text{atm}}, \sigma^2_{\text{atm}})$ and $\aleph(\mu_{\text{ft}}, \sigma^2_{\text{ft}})$, then $\Delta\phi(t) = \Delta\phi_{\text{atm}}(t) - \Delta\phi_{\text{ft}}(t)$ is also a normal distribution and follows the law $\aleph(\mu_{\text{atm}} + \mu_{\text{ft}}, \sigma^2_{\text{atm}} + \sigma^2_{\text{ft}})$.

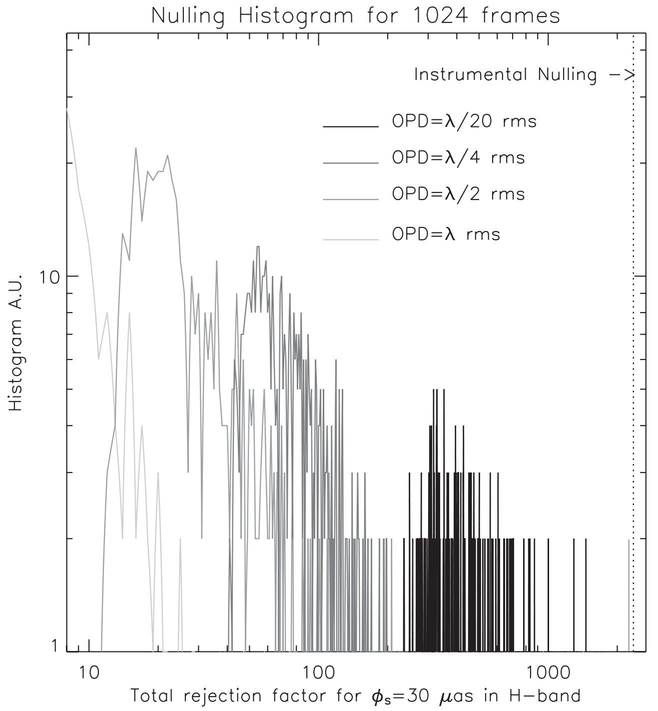

Figure 4. Nulling histogram of 1024 different interferometric coronagraphic frames as a function of the total rejection factor, for four cases of OPD errors between the two apertures. In the simulations, a stellar diameter of 30 μas in the H band ($0.011\lambda/B$) has been considered. The significantly improved behavior in the stabilization regime when using an FT is clearly visible (OPD $< \lambda/2$ rms).

For the sake of simplicity, we will also consider from now on that the polarization effect is static and small compared to the other terms and therefore does not contribute to the statistical distribution ($\varrho = 0$).

6.1.4. Probability Distribution Function

To analyze the PDF of the coronagraphic rejection factor, we must take into account the main statistical errors during the observations. We consider in this analysis that $\Delta\phi(t)$, $di(t)$, and $I(t)$ follow normal distributions, with means μ_i and standard deviations σ_i. To calculate the final PDF of Equation (33), we make use of two theorems.

If two random variables A and B are independent with probability density functions equal to f_a and f_b, respectively (Rohatgi 1976; Pelat 1996):

$$f_{a/b}(C) = \int_{-\infty}^{+\infty} |B|\, f_a(B.C).f_b(B)dB, \tag{34}$$

where the variable substitution $C = A/B$ has been applied.

$$f_{a+b}(C) = \int_{-\infty}^{+\infty} f_a(A).f_b(C-A)dA, \tag{35}$$

where we have used the following variable substitution: $C = A + B$.

Therefore, the density function of a sum of two independent random variables is simply the convolution of the densities of these two variables.

Using these two principles, we can find an analytical solution to the instrumental rejection factor, $R_c = I/(di^2/16 + \Delta\phi^2/4)$ (neglecting the polarization term).

First of all, we know that $I(t)$, $di(t)$, and $\Delta\phi(t)$ are Gaussian distributions, therefore we have

$$f_i(z) = \frac{e^{\frac{-(z-\mu_i)^2}{2\sigma_i^2}}}{\sqrt{2\pi}\sigma_i}, \tag{36}$$

where i corresponds, respectively, to I, di, and $\Delta\phi$ for the three distributions. The expression for both di^2 and $\Delta\phi^2$ densities is given by Pelat (1996) in the case of pure Gaussian distributions:

$$f_i\left(\frac{z^2}{\xi_i}\right) = \frac{e^{-(\xi_i z+\mu_i^2)/2\sigma_i^2}}{\sqrt{2\pi}\sigma_i\sqrt{\xi_i z}} \cosh\left(\frac{\mu_i\sqrt{\xi_i z}}{\sigma_i^2}\right), \tag{37}$$

where the ξ_i are the coefficients multiplying $\Delta\phi^2$ and di^2 in Equation (33) ($\xi_{\Delta\phi} = 4, \xi_{di} = 16$). Now that we have the different expressions for the three random variables I, di^2, and $\Delta\phi^2$, we can first find the expression of $(di^2/16 + \Delta\phi^2/4)$ by substituting Equation (37) into Equation (35):

$$f_{di^2+\Delta\phi^2}(y) = \frac{e^{-\left(\frac{\mu_{\Delta\phi}^2}{\sigma_{\Delta\phi}^2}+\frac{\mu_{di}^2}{\sigma_{di}^2}\right)}}{4\pi\sigma_{\Delta\phi}\sigma_{di}}\, e^{-\left(\frac{y}{2\sigma_{di}^2}\right)} \int_0^{2\pi} \frac{x^{-1/2} e^{-\frac{x}{2}\left(\frac{1}{\sigma_{\Delta\phi}^2}+\frac{1}{\sigma_{di}^2}\right)}}{\sqrt{y-x}}$$
$$\times \cosh\left(\frac{\mu_{\Delta\phi}}{\sigma_{\Delta\phi}^2}\sqrt{x}\right) \cosh\left(\frac{\mu_{di}}{\sigma_{di}^2}\sqrt{y-x}\right) dx. \tag{38}$$

The instrumental rejection ratio R_c is then obtained by using the fundamental statistic relations, Equations (34) and (38):

$$f_{R_c}(z) = \frac{e^{-\left(\frac{\mu_{\Delta\phi}^2}{\sigma_{\Delta\phi}^2}+\frac{\mu_{di}^2}{\sigma_{di}^2}\right)}}{\sqrt{2}\pi^{\frac{3}{2}}\sigma_{\Delta\phi}\sigma_{di}\sigma_I} \int_0^{+\infty} \int_0^{2\pi} \frac{x^{-1/2} e^{-\frac{x}{2}\left(\frac{1}{\sigma_{\Delta\phi}^2}+\frac{1}{\sigma_{di}^2}\right)}}{\sqrt{y-x}}$$
$$\times\ \cosh\left(\frac{\mu_{\Delta\phi}}{\sigma_{\Delta\phi}^2}\sqrt{x}\right) \cosh\left(\frac{\mu_{di}}{\sigma_{di}^2}\sqrt{y-x}\right) dx$$
$$\times\ y\, e^{-\left(\frac{y}{2\sigma_{di}^2}\right)} e^{-\left(\frac{(zy-\mu_I)^2}{2\sigma_I^2}\right)} dy, \tag{39}$$

where x and y are, respectively, the continuous random variables of $f_{\Delta\phi}(x^2)$ and $f_{di}(y^2)$ while z is the result of the variable substitution $z = y\,w$, where w is the variable of $f_I(w)$. Finally, adding the astrophysical rejection ratio to the instrumental one mathematically corresponds to convolve the R_c density with a Dirac distribution $\delta(R_\alpha)$ (see Equation (4)), with R_α being the astrophysical rejection limitation. Therefore, the final rejection ratio probability distribution taking into account both the instrumental and astrophysical limitations, $f_{R_{c,\alpha}}(z)$, is

$$f_{R_{c,\alpha}}(z) = f_{R_c}(z'), \qquad z' = \frac{zR_\alpha}{z+R_\alpha}. \tag{40}$$

If we replace R_α into Equation (4), the new position z' of the full statistic with respect the purely instrumental nulling $f_{R_c}(z)$ becomes

$$2\alpha(\lambda/B) = \frac{4\sqrt{3}}{\pi}\sqrt{\frac{z-z'}{zz'}}. \tag{41}$$

The Equation (40) is very important to recover the astrophysical rejection ratio R_α in the entire statistical distribution $f_{R_{c,\alpha}}$.

Indeed, once the R_α corresponding to the best fit of the rejection distribution $f_{R_{c,\alpha}}$ is found, it is straightforward to derive the stellar angular diameter using Equation (4). The fitting procedure presented hereafter uses the statistical distribution to recover the angular stellar diameter with a sub-resolution precision.

6.1.5. *Fitting Procedure of the Statistical Distribution*

An increase of the stellar diameter will shift the rejection factor histogram toward lower values and will dramatically reduce the number of frames with a rejection factor larger than $R_c \approx 40$ depending on the FT accuracy (see Figure 5). The variation of the peak position of the rejection PDF is highly correlated with the stellar diameter if the intensity fluctuation is less than 10%, due to the photometric monitoring in the pupil plane.

The PDF fitting is performed using the non-linear Levenberg–Marquardt method. We use a modified "mpfit" procedure provided by Markwardt (2008) and Moré (1977) with the GSL library (Galassi et al. 2009; Piessens et al. 1983) that provides the numerical integration needed to fit the final rejection PDF. In order to accelerate the convergence of the Levenberg–Marquardt algorithm, we must restrict the different fitting parameters to the most probable ranges of values. For the means and standard deviations of the intensity mismatch and phase errors, we have defined the following ranges:

$$0 < \mu_{\Delta\phi} < 0.5, \quad 0 < \mu_{di} < 15\%, \quad \sigma_{\Delta\phi} > 0, \quad \sigma_{di} > 0.$$

6.2. *Presence of a Faint Companion or a Circumstellar Disk*

Coronagraphic techniques are generally used to enhance the sensitivity to faint companions or circumstellar structures around a star. We study here the effect of the presence of a faint companion or a circumstellar disk around the target on the determination of its angular diameter. Indeed, this detection can contaminate our data and, consequently, the analysis of the stellar leakage to retrieve the radius of the target. The observed field of view corresponds to the diameter of the Airy pattern of the sub-aperture (≈50 mas in the H band for an 8 m class telescope) and the whole information is "compressed" in the densified field of view (three fringes) due to the poor (u,v) coverage obtained by only two apertures. It is possible to increase the number of resolution elements used to reconstruct the source by rotating the interferometer's baseline during the observations. For that, we consider that either the companion or the circumstellar disk signals are under the detection limit (3σ) of the instrument. If either a companion or a disk is clearly visible (signal $>3\sigma$), two different situations are possible.

1. If it is a companion or any point-like off-axis source, it is possible to properly modify the mask M_B to remove the off-axis contribution and achieve an improved rejection analysis.
2. In the case of extended features, it is not possible to modify the mask. However, if these faint features are below the direct detection confidence, it becomes easier to prove that the faint features around the star are constant in terms of photometric result, and appear as an offset in the data. This photometric "excess" is generally constant with respect to the photon noise and a proper bias calibration of the flux becomes the key to retrieve the stellar diameter information. In this case, the system possesses two free parameters (the stellar radius and the photometric "excess").

Table 1
Example of Distant Galactic Cepheids (Berdnikov et al. 2000)

Name	EN TrA	VZ Pup	AD Pup	AQ Pup
Stellar type	F2Ib	F7.5	F8	F5Ib
Distance in kpc	7.04	4.62	4.09	2.89
Diameter in μas	75	142	170	200
I_c mag	7.8	8.3	8.7	7.1
J mag	7.1	7.1	7.7	5.9
H mag	6.6	6.6	7.2	5.3
K mag	5.9	6.5	7.1	5.1

7. APPLICATION: CEPHEID PULSATION MEASUREMENTS AT THE VLTI

The problem of measuring stellar pulsations of Cepheids is twofold: (1) they are only marginally resolved using the existing baselines and (2) the pulsation of their amplitudes is rather weak (≈10%–15%). However, using the Palomar Testbed Interferometer, it has been possible to detect the pulsation of ζ Gem (Lane et al. 2000), one of the most distant galactic Cepheids ever discovered. Still, the level of significance remains weak and more observations are needed to improve these first results. Our technique can increase this significance of the detection for relatively close Cepheid variables that have been already observed (e.g., δ Cep, ζ Gem: Kervella et al. 2001, and η Aql: Lane et al. 2002) but can also allow us to observe more distant targets (see Table 1).

Using our method, there are several factors that can increase the significance of a diameter variation in Cepheids. One of the most critical ones is the accuracy to which the photometric calibration and reduction is performed. For example, the spectral response of the photodiode has to be carefully calibrated, to minimize observational biases. Additionally, Cepheid observations can be optimized by choosing an "unresolved" reference star, close to the principal target, that will act as a nulling calibrator. Finally, it is still feasible to observe stars with known diameter information, obtained with "classical" interferometric visibility measurements (see Section 8.1). These observations can serve to set an absolute stellar calibrator for our statistical method used on the coronagraphic images.

7.1. *Simulation Results with the EN TrA Star*

We have performed a nulling mode simulation for the most distant Cepheid of our sample: EN TrA (see Table 1). Throughout our study, we considered a uniform diameter varying from 68–78 μas (see Table 2) and a VLTI-UT configuration using a 130 m baseline. The star has an H-band magnitude of 6.6. Without coronagraphic attenuation, it corresponds to an incoming total signal of 15,800 photons for 0.5 s of exposure time and a spectral resolution of 10 (the total overall transmission is 3%). Its properties, together with those of some better candidates for using our method, are presented in Table 1.

Because the number of photons arriving to the detector per exposure time is low, it is necessary to stack a large number of frames (typically 100 for this example) in order to increase the S/N. The quality of our data depends on the number of measurements having higher rejection factor. To increase this number, it is necessary to stabilize the fringes that move rapidly because of the atmospheric turbulence. On the UTs, the fringe stabilization depends on both the low-order corrections of the individual telescopes adaptive optics (Strehl ratio lower than

Table 2
Limitation of the Rejection Factor R_α due to the Finite Extent of the EN TrA Stellar Diameters During the Cepheid Cycle

Diameter in μas	68	72	75	78
Diameter (α) in λ/B	0.0259	0.0275	0.0286	0.0298
R_α (Equation (3))	1810	1600	1480	1370

Note. This limitation is computed in the *H* band for different values of the stellar angular diameter (α).

Table 3
Some Key Numbers and Properties of the Interferometer

Filter	*I*	*J*	*H*	*K*
Wavelength in μm	0.8	1.2	1.65	2.2
λ/B in mas	1.26	1.9	2.6	3.5
τ in ms	3	6	12	20
Detector frequency in kHz	1	0.4	0.2	0.1
Readout noise (e^-)	5	6	6	6

Note. Table summarizes some key numbers and properties of the interferometer such as (1) the different filter wavebands, (2) the central wavelength corresponding to these filters, (3) the angular separation between two interferometric fringes, (4) the speckle lifetime τ in ms, (5) the detector frequencies in the different bands, and (6) the readout noise of these detectors in electrons.

30% at 1.65 μm) and of the VLTI FT ($\lambda/3$ rms at 1.65 μm). When used with the ATs, this AO system is replaced by simpler tip/tilt mirrors (STRAP). In both cases, such systems improve the detectability due to the partial correction of the tip-tilt errors in each sub-aperture, since it decreases the number of bad frames due to poor centering (see Figure 4). The frequency of the photodiodes and the NICMOS detector is 200 Hz and must be compared to the supposed speckle lifetime which is ~12 ms in the *H* band (see Table 3). For each observational simulation, we generate 4096 individual average exposures (2048 s of total exposure time per fixed stellar diameter). Five diameter measurements, obtained during the pulsating period of the Cepheid, resulted on five values spanning from 68 to 78 μas depending on the pulsation phase. The influence of the atmospheric conditions has been taken into account by modifying the amplitude of the turbulence between each data set (we assume a Taylor turbulence, with a layer displacement having a speed of 8 m s^{-1}). The detector's response has also been modified during the five data sets. The influence of the stellar diameter on the global statistics of the coronagraphic nulling is clearly visible in Figure 5. Although the size of the star's diameter does not seem to play an important role on the histogram shape for low rejection factors, its importance becomes more prominent for the measurement at larger rejections factors.

7.1.1. Fitting the Rejection Histograms

Such a fitting example is presented in Figure 6 for a value of the EN TrA stellar diameter of 68 μas. During our statistical analysis of the rejection factor histogram, we fit the full statistic with the phase and the intensity mismatch error distributions ($\Delta\phi, di$). The phase and intensity mismatch distributions corresponding to the least square of the fitting procedure for the four different stellar diameters (see Figure 5) are 0.385 ± 0.072 wave rms for ($\mu_{\Delta\phi}, \sigma_{\Delta\phi}$) and 8.3% ± 5.4% rms for the amplitude mismatch error (μ_{di}, σ_{di}). The intensity fluctuation $I(t)$ during the stellar diameter retrieval is directly monitored by the photodiode's system ($\sigma_I = 2\%$ rms) and is therefore considered as known during the fitting process. The values of the phase errors retrieved by the histogram fitting method (see Table 4) seem to be efficient as they are very close to the input parameters of the Monté Carlo numerical simulation.

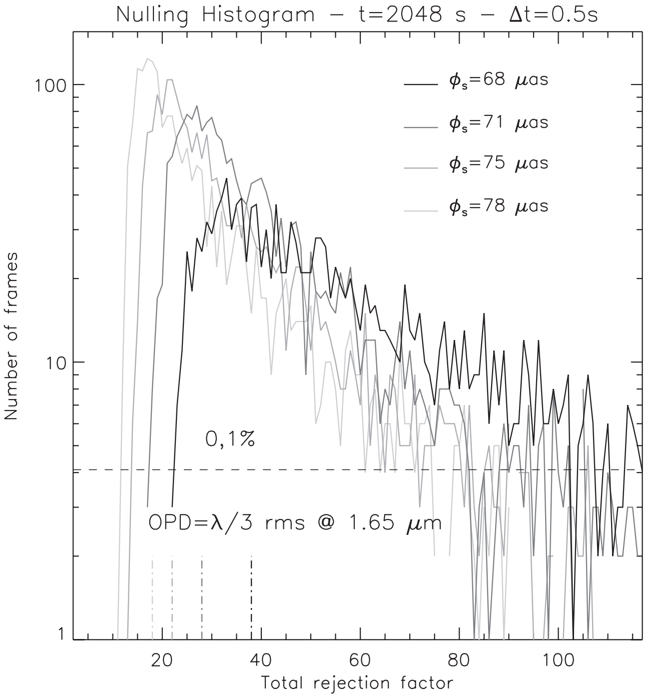

Figure 5. Nulling histogram for 4096 different interferometric coronagraphic nulling *H*-band images on the Cepheid star EN TrA. During the simulations, five stellar diameters with values between 68 and 78 μas were measured. The figure shows the histogram of the total rejection factor as a function of the stellar diameter. In this figure, only the data with a rejection larger than the median of the histogram are shown (50% of initial frame number).

Table 4
Retrieved Fitting Parameters for the EN TrA Star

Stel. diam. (μas)	68	72	75	78
$\mu_{\Delta\phi}$ in wave	0.308	0.365	0.41	0.46
$\sigma_{\Delta\phi}$ in wave rms	0.076	0.064	0.071	0.08
μ_{di} in %	8	9	10	6.5
σ_{di} in % rms	2	3	10	6.5
σ_I in % rms	2	2	2	2
Retrieved diam. (μas)	68.4	71.6	75	78

Once the astrophysical rejection corresponding to the optimal fit of the data set distribution is found, they are converted into stellar angular diameters using Equation (4). Table 4 shows a summary of the stellar diameters that are measured compared to the one simulated in the model. For all cases, the error on the measured diameter is small and always $<0.6\,\mu$as. The rms error on the angular diameter for the four simulations is 0.41 μas which corresponds, in terms of λ/B to accuracies better than $\lambda/1000B$.

Note that for on-sky measurements, the observation of a calibrator star of well-known diameter (of ~300 μas) can increase the accuracy of the method. Indeed, by doing so, it is possible to get rid of possible systematic biases that are not corrected by the statistical reduction method.

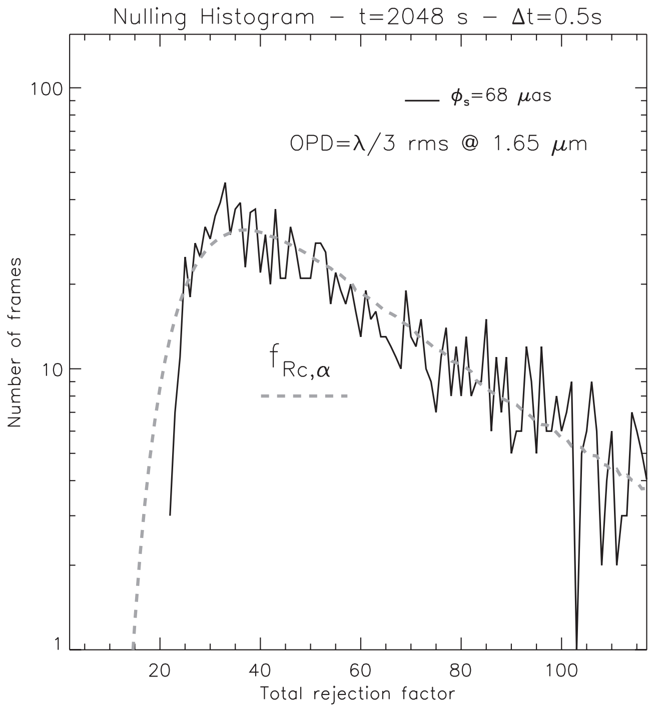

Figure 6. Nulling histogram of 4096 different interferometric coronagraphic nulling H-band images for a stellar diameter of 68 μas. The figure shows the histogram of the total rejection factor for data with a rejection factor larger than the median value. The dashed line gives the fitting function $f_{R_{c,\alpha}}$ that characterizes the global rejection statistic.

7.2. *Simulations with a Circumstellar Companion or Disk*

In this section, we perform the simulation for the same Cepheid in the presence of a faint companion or a disk around the star. We test the stellar diameter retrieval quality with respect to the magnitude difference, Δm, between the star and the faint companion/disk, where $5 \leqslant \Delta m \leqslant 9$. A $\Delta m = 5$ corresponds to the detection limit of the disk or companion at the 3σ level with our technique. The accuracy of the proposed method remains good, with an error of 6 μas PTV for the brightness companion/disk and less than 1 μas PTV for the fainter case. The simulation results are presented in Figures 7 and 8.

8. DISCUSSION

This paper demonstrates the possibility of improving the accuracy of stellar diameter measurements with a coronagraphic device by means of a statistical data analysis. However, despite the advantages proposed with this configuration, interferometry, in general, still suffers from two limitations.

1. The detection noise is significant due to the very short exposure times.
2. The fringe tracking accuracy is rather low (typically ∼λ/3 rms).

The example presented in Section 7 was based on a simulation of 4096 exposures, with 68 minutes of total integration time (equally distributed between the target and the reference star). The results presented in the previous paragraph can be further improved by observing a calibrator star of well-known diameter. Doing so, it is possible to get rid of the possible instrumental biases that are not taken into account by the statistical data reduction (e.g., the rotation of polarization). It is

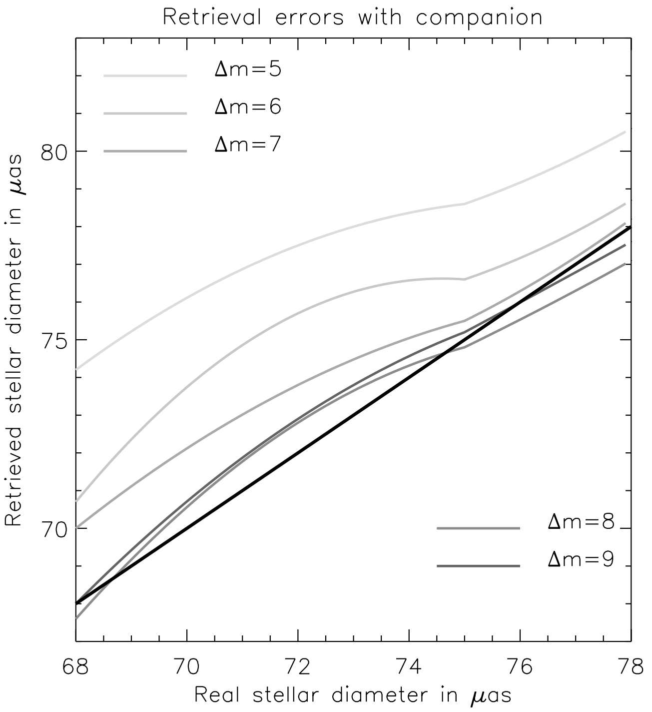

Figure 7. Retrieval errors obtained on the 4096 different interferometric coronagraphic nulling H-band images for the Cepheid variable EN TrA with a low-mass star as a companion. The magnitude difference between the primary star and the companion ranges between 5 and 9. A $\Delta m = 5$ corresponds to the instrument detection limit at the 3σ level. The figure shows the five retrieved angular stellar diameters as a function of the real value, for different luminosity ratios. The black line corresponds to the exact solution.

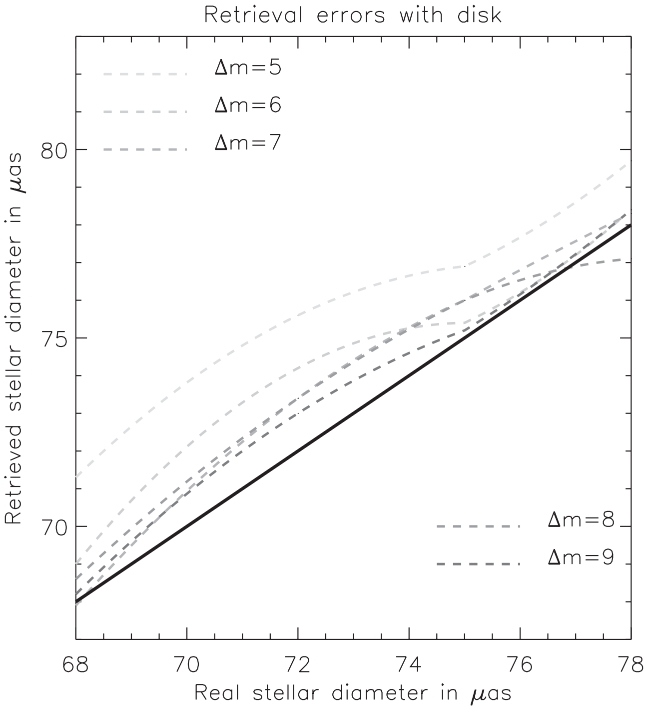

Figure 8. Retrieval errors obtained for the Cepheid variable EN TrA with a circumstellar disk (face-on). The difference in the magnitude of the disk is 5–9 for the flux total. The figure shows the five retrieved angular stellar diameters with respect to its actual value for different luminosity ratios.

worth mentioning that only reference stars with a diameter in the range 200–400 μas are usable in the coronagraphic mode. Indeed, large stellar diameters strongly limit the rejection factor ($R_c < 5$) of the coronagraphic mode. In this case, classical visibility measurements can be more efficient than the nulling mode.

8.1. *Classical Visibility versus Coronagraphic Retrieval*

We can compare the gain of our technique with the sub-resolution visibility fitting procedure used in classical interferometry (Lachaume 2003). A classical long baseline interferometer, such as CHARA (Baines et al. 2008), uses a fitting procedure to retrieve the Uniform and Limb-darkened stellar diameter (UD, LD). The data obtained with this interferometer for the case of a 330 m baseline in H and K bands on 46 stars (reference and science) lead to the following results (in λ/B unit): uniform angular diameters have been measured down to $\lambda/6B$. The error on these measurement is on average of $\lambda/43B$ and goes down to $\lambda/172B$ in the best case. The gain with a coronagraphic system remains important for small stellar diameters (typically $\sim\lambda/40B$). Indeed, for EN TrA, we have been able with our method to measure an angular diameter of $\sim\lambda/35B$ with a precision of $\lambda/1310B$. With the VLTI and the UTs, the limiting magnitude of $I = 9$ opens wide possibilities of studying distant Cepheids (2–7 Kpc) in the Milky Way.

8.2. *Nulling Interferometry*

The technique proposed in this work is also applicable to the case of nulling interferometer experiments such as GENIE on the VLTI (Gondoin et al. 2003) or the fiber nuller (Haguenauer & Serabyn 2006; Martin et al. 2008). The main difference with the configuration proposed in the current paper is that the field of view of GENIE is limited by one resolution element (while in our configuration it is three resolution elements). Some studies by Hanot et al. (2010) on the fiber nuller point to a better stellar diameter calibration using this technique than with classical methods.

9. CONCLUSIONS

The present article introduces a new approach to tackle the problem of measuring stellar diameters, using a coronagraphic interferometer. Such a configuration is far more accurate (by a factor of 100 in the speckle mode) compared to the “classical” visibility measurements, and potentially even more accurate if an FT is used. Direct measurements of angular diameter variations of Cepheids avoid the problem of color versus surface brightness calibration in the distance determination (Fouqué et al. 2007; Marengo et al. 2003). The suggested configuration is also applicable to previous Cepheid measurements, to obtain more precise measurements of their pulsations. Additionally, our technique can also be implemented for more distant Cepheid (∼2–7 kpc); interferometric measurements of more distant Cepheid diameter can improve our knowledge of the period–luminosity relation, which has a direct impact on the extragalactic distance scale measurements.

This work received the support of the University of Liège. The authors are grateful to T. Nakos (Ghent University), J. Surdej, Jean-Pierre Swings, and O. Absil (IAGL) for manuscript corrections. The authors also acknowledge support from the Communauté française de Belgique–Actions de recherche concertées–Académie universitaire Wallonie-Europe.

REFERENCES

Armstrong, J. T., Nordgren, T. E., Germain, M. E., Hajian, A. R., Hindsley, R. B., Hummel, C. A., Mozurkewich, D., & Thessin, R. N. 2001, AJ, 121, 476
Baines, E. K., McAlister, H. A., ten Brummelaar, T. A., Turner, N. H., Sturmann, J., Sturmann, L., Goldfinger, P. J., & Ridgway, S. T. 2008, ApJ, 680, 728
Berdnikov, L. N., Dambis, A. K., & Vozyakova, O. V. 2000, A&AS, 143, 211
Bonaccini, D., Gallieni, D., Biasi, R., Gori, F., Ghioni, M., Trottier, C., & Hubin, N. 1997, Proc. SPIE, 3126, 580
Buisset, C., Rejeaunier, X., Rabbia, Y., Ruilier, C., Barillot, M., & Karlsson, A. 2006, in IAU Coll. 200, Direct Imaging of Exoplanets: Science & Techniques, ed. C. Aime & F. Vakili (Cambridge: Cambridge Univ. Press), 309
Coudé Du Foresto, V. 1997, C. R. Acad. Sci., 325, 177
Delage, L., & Reynaud, F. 2001, Opt. Express, 9, 267
Feast, M. W., Laney, C. D., Kinman, T. D., van Leeuwen, F., & Whitelock, P. A. 2008, MNRAS, 386, 2115
Ferrarese, L., Mould, J. R., Stetson, P. B., Tonry, J. L., Blakeslee, J. P., & Ajhar, E. A. 2007, ApJ, 654, 186
Fizeau, H. 1868, C. R. Acad. Sci. Paris, 68, 932
Fouqué, P., et al. 2007, A&A, 476, 73
Galassi, M., Davies, J., Theiler, J., Gough, B., Jungman, G., Alken, P., Booth, M., & Rossi, F. 2009, GNU Scientific Library Reference Manual (3rd ed.; Network Theory Ltd)
Gondoin, P., et al. 2003, Proc. SPIE, 4838, 700
Govindaraju, N. K., & Manocha, D. 2007, Parallel Comput., 33, 663
Haguenauer, P., & Serabyn, E. 2006, Appl. Opt., 45, 2749
Hanot, C., et al. 2010, ApJ, submitted
Hicks, C., Kalatsky, M., Metzler, R. A., & Goushcha, A. O. 2003, Appl. Opt., 42, 4415
Jenkins, C. 2008, MNRAS, 384, 515
Kervella, P., Coudé du Foresto, V., Perrin, G., Schöller, M., Traub, W. A., & Lacasse, M. G. 2001, A&A, 367, 876
Labeyrie, A. 1970, A&A, 6, 85
Labeyrie, A. 1995, A&A, 298, 544
Labeyrie, A. 1996, A&AS, 118, 517
Lachaume, R. 2003, A&A, 400, 795
Lane, B. F., Creech-Eakman, M. J., & Nordgren, T. E. 2002, ApJ, 573, 330
Lane, B. F., Kuchner, M. J., Boden, A. F., Creech-Eakman, M., & Kulkarni, S. R. 2000, Nature, 407, 485
Lay, O. P. 2004, Appl. Opt., 43, 6100
Lay, O. P. 2005, Appl. Opt., 44, 5859
Le Bouquin, J.-B., Abuter, R., Haguenauer, P., Bauvir, B., Popovic, D., & Pozna, E. 2009, A&A, 493, 747
Le Bouquin, J.-B., et al. 2008, Proc. SPIE, 7013, 701318.1
Macri, L. M., Stanek, K. Z., Bersier, D., Greenhill, L. J., & Reid, M. J. 2006, ApJ, 652, 1133
Marengo, M., Karovska, M., Sasselov, D. D., Papaliolios, C., Armstrong, J. T., & Nordgren, T. E. 2003, ApJ, 589, 968
Markwardt, C. B. 2008, in ASP Conf. Ser. 411, Astronomical Data Analysis Software and Systems XVIII, ed. D. Bohlender, P. Dowler, & D. Durand (San Francisco, CA: ASP), 251
Martin, S., Serabyn, E., Liewer, K., Loya, F., Mennesson, B., Hanot, C., & Mawet, D. 2008, Proc. SPIE, 7013, 70131Y
Mawet, D., Riaud, P., Absil, O., & Surdej, J. 2005, ApJ, 633, 1191
Mawet, D., Serabyn, E., Liewer, K., Hanot, C., McEldowney, S., Shemo, D., & O’Brien, N. 2009, Opt. Express, 17, 1902
Mérand, A., et al. 2007, ApJ, 664, 1093
Michelson, A. 1891, Nature, 45, 160
Michelson, A., & Pease, F. 1921, ApJ, 53, 249
Moré, J. 1977, in The Levenberg–Marquardt Algorithm: Implementation and Theory, Vol. 630, ed. G. A. Watson (Berlin: Springer), 105
Mourard, D., Bonneau, D., Koechlin, L., Labeyrie, A., Morand, F., Stee, P., Tallon-Bosc, I., & Vakili, F. 1997, A&A, 317, 789
Mourard, D., Tallon-Bosc, I., Rigal, F., Vakili, F., Bonneau, D., Morand, F., & Stee, P. 1994, A&A, 288, 675
Myers, R. A., Farrell, R., Karger, A. M., Carey, J. E., & Mazur, E. 2006, Appl. Opt., 45, 8825
Pelat, D. 1996, Bruits et Signaux (Ecole Doctorale de Paris), 351, (http://cel.archives-ouvertes.fr/docs/00/09/29/37/PDF/pelat.pdf)
Piessens, R., deDoncker Kapenga, E., & Uberhuber, C. D. K. 1983, Quadpack: a Subroutine Package for Automatic Integration (New York: Springer)
Riaud, P. 2003, PhD thesis, Université Paris VI
Riaud, P., Boccaletti, A., Baudrand, J., & Rouan, D. 2003, PASP, 115, 712

Riaud, P., Boccaletti, A., Rouan, D., Lemarquis, F., & Labeyrie, A. 2001a, PASP, 113, 1145

Riaud, P., et al. 2001b, in Liége Int. Astrophys. Coll. 36, From Optical to Millimetric Interferometry: Scientific and Technological Challenges, ed. J. Surdej et al. (Liége: Université de Liége, Institut d'Astrophysique et de Géophysique), 85

Riaud, P., et al. 2002, A&A, 396, 345

Rohatgi, V. 1976, An Introduction to Probability Theory Mathematical Statistics (New York: Wiley), 141

Rouan, D., Riaud, P., Boccaletti, A., Clénet, Y., & Labeyrie, A. 2000, PASP, 112, 1479

Shaklan, S. 1990, Opt. Eng., 29, 684

Swartzlander, G. A., Jr., Ford, E. L., Abdul-Malik, R. S., Close, L. M., Peters, M. A., Palacios, D. M., & Wilson, D. W. 2008, Opt. Express, 16, 10200

Tinetti, G. 2006, Orig. Life Evol. Biosph., 36, 541

van Belle, G. 2009, American Astronomical Society Meeting Abstracts, 214, 411.01

van Leeuwen, F., Feast, M. W., Whitelock, P. A., & Laney, C. D. 2007, MNRAS, 379, 723

Vilardell, F., Jordi, C., & Ribas, I. 2007, A&A, 473, 847

Wallner, O., Ergenzinger, K., Flatscher, R., & Johann, U. 2006, Proc. SPIE, 6268, 626827

Wallner, O., Winzer, P. J., & Leeb, W. R. 2002, Appl. Opt., 41, 637

Wu, G., Jian, Y., Wu, E., & Zeng, H. 2009, Opt. Express, 17, 18782

Conclusions

Objectives and results

The detection and characterization of extra-solar planets is an extremely fast growing field. In 2011 only, several hundreds planets have already be announced by the Kepler team, and for the first time, a significant amount of them will be located in the habitable zone of their star (Borucki et al. 2011). Detections based on indirect methods have still many bright years ahead but today, scientists want more than just finding exoplanets. They also desire to characterize their properties. To do so, collecting photons from them is mandatory and direct detection methods are required. A first step will be made with the advent of new ground-based planet imagers, of the JWST, and maybe in the near future of a space-based mission dedicated to the characterization of extra-solar planets. Indeed, in the context of his Cosmic Vision program, ESA has recently preselected the ECHO (Exoplanet Characterisation Observatory) mission, a space-based telescope aiming at characterizing extra-solar planets using photometric transits. This mission will undoubtedly represent a major step forward in our understanding of planetary atmospheres but will be restricted to the observation of super-Earth size planets around dwarf stars. The spectral analysis of Earth twins, located in the habitable zone of F- and G- type main sequence stars will necessarily pass by the construction of dedicated high-angular and extremely high-contrast imagers. The purpose of this work was to contribute to the development of these future instruments, especially using interferometry, and to use current facilities to observe (sub)-stellar companions around nearby stars.

In the first part, we have demonstrated the capabilities of future ground- and space-based planet imagers and compared their performances. Using coronagraphic simulations provided by A. Boccaletti and C. Vérinaud together with planet evolutionary models, we have then shown that performing large surveys among young main-sequence dwarf stars located in nearby moving groups had many interests (Hanot et al. 2010a). First, it increases the sensitivity of the instrument toward lower mass planets down to a few Neptune masses. Second, it can bring decisive information to constrain the various evolutionary models which differ significantly during the first million years of a sub-stellar object. Future XAO systems will play a decisive role in the success of such surveys. Using a well corrected sub-aperture of the Hale telescope, we have demonstrated that extreme AO systems, even on small (1.5 m) apertures, could compete with larger less-corrected telescopes. We have used this facility to observe multiple compact systems at blue wavelengths with angular separations as small as $0\farcs15$ and have obtained two new orbital solutions.

But detecting extrasolar planets in the habitable zone of their stars requires a huge resolving power which is impossible to achieve with 10-m class telescopes at infrared wavelengths. In the second part of this work, we have therefore focused on the development of new techniques for interferometry. Ground-based (nulling) interferometers are strongly limited by atmospheric-induced perturbations, which introduce fast fluctuating noise and is difficult to correct. Therefore, we have first worked on the development of a new data reduction technique using the null depth and fast intensity fluctuations rather than their average values (Hanot et al. 2011). By doing so, we have demonstrated that it is possible to retrieve the astrophysical information with a much better accuracy than is possible with standard data reduction methods. Using the Palomar Fiber Nuller, we have shown that such a method (which is not instrument specific) could lead to dynamic ranges up to 10,000:1 from the ground. We have then applied this technique to a new instrumental concept mixing coronagraphy and interferometry. Using simulations, we have finally demonstrated that such a technique could allow the measurement of stellar angular diameters with an extremely high accuracy ($\sim 10^{-6}$ arcsec) using existing long baseline interferometers (Riaud & Hanot 2010).

In Chapter 5, we have used the AMBER instrument to perform a survey among the brightest and youngest M- and K- stars inside moving groups with the hope of finding (sub-)stellar companions. Thanks to its resolving power, AMBER is indeed able to probe the innermost regions (0.1 to 10 AU) around those stars where no other imaging techniques can be used, with a sensitivity of 15 $M_{\rm Jup}$ for the best targets. Our first three observing runs have unfortunately not been successful but similar programs led by close collaborators have allowed us to derive strong contrast limits for the instrument close to the 1% level.

Reaching deeper contrasts with classical stellar interferometers is possible but is expected to be limited to $\sim 10^{-3}$ in the case of non-resolved host stars. Such contrasts are not sufficient to detect rocky planets around main sequence stars and nulling interferometry must therefore be used to further enhance the dynamic range. In Chapters 6 and 7, we have presented our contribution to the development of two nulling interferometers that are the CELINE testbed (Hanot et al. 2010b) and the PFN. With the first one, we have demonstrated encouraging preliminary results with monochromatic null depths at the 10^{-4} level. The second one can be deployed on the Hale telescope at Palomar observatory and has demonstrated on-sky null depths of 10^{-3}. Thanks to this efficient instrument, we have managed to measure stellar angular diameters and to constrain the presence of dust and companions in the innermost region around Vega with an unprecedented precision (Mennesson et al. 2011a,b).

Perspectives

Numerous perspectives will follow this work. One of the most promising is probably related to the development of our statistical data reduction method for interferometry. Indeed, recent results in different fields of high-contrast imaging have emphasized the importance of data post-processing for enhancing the performance of instruments (e.g. the LOCI algorithm for AO observations, Lafrenière et al. 2007b). Our result obtained with the Palomar Fiber Nuller is an additional illustration of this fact, and current or future interferometric facilities could also greatly benefit from this technique. We are therefore planning on adapting our data reduction to some of them, such as CHARA/FLUOR or the Keck Interferometer Nuller. Furthermore, since the statistical approach allows the detection of astrophysical signals well below the mean contrast level and its rms fluctuations, we anticipate that the instrumental stability requirements could be strongly relaxed. This implies that the constraints on intensity and phase fluctuations may be significantly reduced. This is a most attractive prospect for deep nulling interferometry from space.

Our on-going survey looking for sub-stellar companions in both hemispheres will be pursued in the future with two different instruments. For the stars located in the southern hemisphere, the AMBER instrument at VLTI that we have used until now will be replaced by PIONIER. This instrument will provide a better *uv* coverage thanks to the simultaneous combination of four telescopes, and a better sensitivity, with possible detections down to $7 M_{\rm Jup}$. In the northern hemisphere, the survey will be complemented with the upgraded PFN. The main limitation of the instrument, which is its sensitivity, will soon be improved with the installation of a new camera. Moreover, the next generation of AO at Palomar (currently being commissioned), will bring a much better stability to the instrument and will decrease the phase error fluctuations down to about 80 nm. These upgrades will allow us to reach null depths of 10^{-4} and detect giant exoplanets around young and bright stars. For the near- to mid-term future, the installation of the PFN on larger facilities such as the Keck telescope or the LBT is under study. It would provide a better angular resolution but also an increased sensitivity thanks to the use of 4-8 m apertures instead of 1.5 m. Initial testing of a fibered nulling interferometer has already been conducted at Keck but further developments are needed.

Finally our developments and researches to develop improved technologies for nulling interferometry will continue, in particular with the CELINE testbench, which is still in its infancy. Significant efforts will be put on the optical testing of our Fresnel rhomb-based phase shifters and on photonic fibers. The broadband capabilities of the instrument will be studied in details. The long-term goal of the testbench will be the development of a visitor infrared nulling instrument for a ground-based facility.

Appendix

A

Paper: Fresnel rhombs as achromatic phase shifters for infrared nulling interferometry

In the following paper (Mawet et al. 2007), published in Optics Express, we present a new technological solution for introducing a relative half-wave phase shift between the beam of an infrared nulling interferometer. My main contribution to this paper has been to perform a polarimetric test of the rhombs. The purpose of this test was to assess the performances of the $ZnSe$ fresnel rhombs as phase shifters before their final test on the Nulltimate test-bench (Labèque et al. 2004). It allowed us to prove the capability of this technology to lead to very deep broadband rejection ratios.

Fresnel rhombs as achromatic phase shifters for infrared nulling interferometry

Dimitri Mawet[1], **Charles Hanot**[1], **Cédric Lenaerts**[1], **Pierre Riaud**[3],
Denis Defrère[1], **Denis Vandormael**[2], **Jérôme Loicq**[2], **Karl Fleury**[2],
Jean-Yves Plesseria[2], **Jean Surdej**[1] **and Serge Habraken**[1,2]

[1]*University of Liège, 17 allée du 6 Août, B-4000, Sart Tilman, Belgium*
[2]*Centre Spatial de Liège, Avenue du Pré-Aily, B-4031, Liège-Angleur, Belgium*
[3]*Observatoire de Paris-Meudon, 5 place Jules Janssen, 92190 Meudon, France*
mawet@astro.ulg.ac.be

Abstract: We propose a new family of achromatic phase shifters for infrared nulling interferometry. These key optical components can be seen as optimized Fresnel rhombs, using the total internal reflection phenomenon, modulated or not. The total internal reflection indeed comes with a phase shift between the polarization components of the incident light. We propose a solution to implement this vectorial phase shift between interferometer arms to provide the destructive interference process needed to disentangle highly contrasted objects from one another. We also show that, modulating the index transition at the total internal reflection interface allows compensating for the intrinsic material dispersion in order to make the subsequent phase shift achromatic over especially broad bands. The modulation can be induced by a thin film of a well-chosen material or a subwavelength grating whose structural parameters are thoroughly optimized. We present results from theoretical simulations together with preliminary fabrication outcomes and measurements for a prototype in Zinc Selenide.

OCIS codes: (120.3180) Interferometry; (050.5080) Phase Shift.

References and links

1. R.N. Bracewell, "Detecting Non Solar Planets by Spinning Infrared Interferometer," Nature **274**, 780–781 (1978).
2. A. Léger, J.M. Mariotti, B. Mennesson, M. Ollivier, J.L. Puget, D. Rouan, J. Schneider, "Could We Search for Primitive Life on Extrasolar Planets in the Near Future," Icarus **123**, 249–255 (1996).
3. A.L. Mieremet, J.J. Braat, H. Bokhove, K. Ravel, "Achromatic phase shifting using adjustable dispersive elements," Proc. SPIE **4006**, 1035–1041 (2000).
4. J. Gay, Y. Rabbia, "Principe d'un coronographe interférentiel," C. R. Acad. Sci. Paris **322**, 265–271 (1996).
5. E. Serabyn, M.M. Colavita, "Fully Symmetric Nulling Beam Combiners," Appl. Opt. **40**, 1668–1671 (2001).
6. B. Chazelas, F. Brachet, P. Bordé, B. Mennesson, M. Ollivier, O. Absil, A. Labèque, C. Valette, A. LégerA., "Instrumental stability requirements for exoplanet detection with a nulling interferometer: variability noise as a central issue," Appl. Opt. **45**, 984–992 (2006).
7. F. Hénault, "Design of achromatic phase shifters for spaceborne nulling interferometry," Opt. Lett. **31**, 3635–3637 (2006).
8. C. Hanot et al., Proc. SPIE **6693-62**, in press (2007).
9. A.L. Karlsson, O. Wallner, J.M. Perdigues Armengol, O. Absil,"Three telescope nuller based on multibeam injection into single-mode waveguide," Proc. SPIE **5491**, 831–841 (2004).
10. D. Mawet, C. Lenaerts, P. Riaud, J. Surdej, S. Habraken, D. Vandormael, "Use of subwavelength gratings in TIR incidence as achromatic phase shifters," Opt. Express **13**, 8686–8691 (2005).

#84445 - $15.00 USD Received 25 Jun 2007; revised 24 Aug 2007; accepted 25 Aug 2007; published 21 Sep 2007

11. M.G. Moharam and T.K Gaylord, "Rigourous Coupled-Wave Analysis of planar grating diffraction," J. Opt. Soc. Am. **71**, 811–818 (1981).
12. M. Born & E. Wolf, "Reflection and refraction of a plane wave," in *Principles of Optics* eds. (Cambridge University press, seventh edition, 1997), 49–53.
13. K. B. Rochford, A. H. Rose, P. A. Williams, C. M. Wang, I. G. Clarke, P. D. Hale, G. W. Day, "Design and performance of a stable linear retarder," Appl. Opt. **36**, 6458–6465 (1997).
14. R. Anderson, "Quarterwaveplate and Fresnel rhomb compared in the 10-Mum CO2 laser emission region," Appl. Opt. **27**, 2746–2747 (1988).
15. P. Clapham, M. Downs, R. King, "Some applications of thin films to polarization devices," Appl. Opt. **8**, 1965–1974 (1969).
16. J.C. Lagarias, J. A. Reeds, M. H. Wright, and P. E. Wright, "Convergence Properties of the Nelder-Mead Simplex Method in Low Dimensions," SIAM Journal of Optimization **9** (1), 112–147 (1998).
17. Gary J. Hawkins, *Spectral Characterisation of Infrared Optical Materials and Filters* (PhD Thesis - The University of Reading UK, 1998).
18. F. Peter, Z Phys **15**, 358-368 (1923).
19. W. J. Tropf, "Temperature-dependent refractive index models for BaF2, CaF2, MgF2, SrF2, LiF, NaF, KCl, ZnS and ZnSe," Opt. Eng. **34**, 1369–1373 (1995).
20. W. J. Tropf, M.E. Thomas, M.J. Linevsky, "Infrared refractive indices and thermo-optic coefficients for several materials," Proc. SPIE **3425**, 160–171 (1998).
21. A. Labèque, B. Chazelas, F. Brachet, C. Commeaux, P. Blache, A. Léger, M. Ollivier, T. Lepine, C. Valette, "The Nulltimate project: building and testing, at low temperature, achromatic phase shifters to prepare the Darwin mission," Proc. SPIE **5491**, 999–1010 (2004).
22. P. Lalanne, P. Pichon, P. Chavel, E. Cambril, H. Launois, "Interferometric Characterization of Subwavelength Lamellar Gratings," Appl. Opt. **38**, 4980–4984 (1999).
23. W. R. Chen, S. J. Chang, Y. K. Su et al., "Refractive Ion Etching of ZnSe, ZnSSe, ZnCdSe and ZnMgSSe by H2/Ar and CH4/H2/AR," Jpn. J. Appl. Phys. **39**, 3308–3313 (2000).
24. K. Kurisu, T. Hirai, K. Fuse et al., "Development of a Diffractive Optical Element for Laser Processing," SEI Technical Review **53**, 86–91 (2002).
25. G.R. Mariner and K. Vedam, "Stress-optic coefficient of ZnSe at 10.6 microns," Appl. Opt. **20**, 2878–2879 (1981).
26. C. Yang and P. Yeh, "Artificial uniaxial and biaxial dielectrics with the use of photoinduced gratings," J. Appl. Phys. **81**, 23–29 (1997).

1. Introduction

Despite the tremendous progress in the indirect detection techniques and the increasing number of detected extrasolar planetary objects, exoplanet hunters are still struggling with the technical challenges hampering the conception of an observatory that will allow the direct imaging and characterization of Earth-like planets. Indeed, even our best telescopes can't see them directly because of the large flux ratio between the planet and its parent star. For example, an Earth-like exoplanet is typically $\sim 10^9$ times fainter than its host star in the visible spectrum, $\sim 10^6$ in the thermal infrared. Among all raised ideas to reach the needed very high dynamic range, such as visible coronagraphy, infrared nulling interferometry proposed by R. Bracewell in 1978 [1] appears to be a most promising technique. The nulling interferometry consists in adjusting the phases (with a π phase shift in the two-telescope case) of the beams coming from various telescopes (two or more) to produce a fully destructive interference on the optical axis, nulling the starlight while letting the planetary signal pass through.

One of the most critical units of a nulling interferometer is the phase shifter. The difficulty is to conceive it to perform well enough over the whole operational bandpass. Remotely characterizing exoplanet atmospheres, which is our ultimate goal, requires spectroscopic analysis over large spectral bands. For example, the Darwin Infrared Space Interferometer [2] considered by the European Space Agency (ESA), or the Terrestrial Planet Finder-Interferometer (TPF-I) considered by NASA, will operate in the infrared wavelength range spanning from 6 to 18 (or 20) μm. Several studies have been initiated by both agencies, with the purpose of selecting the best achromatic phase shifter (APS). Exhaustive listing or detailed trade-off between different existing APS is beyond the scope of this paper. However, let us cite the four most promising

#84445 - $15.00 USD Received 25 Jun 2007; revised 24 Aug 2007; accepted 25 Aug 2007; published 21 Sep 2007

concepts that are currently being examined:

- the dispersive plate APS [3], directly inspired by the techniques used by optical designers to minimize lens chromatic aberrations, uses a given number of glass or dielectric plates, whose materials and thicknesses are optimized together with the free-air optical path difference (OPD), mutually neutralizing the various dispersion gradients to produce a given phase shift over the desired bandpass;
- the focus-crossing APS [4], where an achromatic phase shift of π is produced by making the beam cross a focus along one of the interferometer arm;
- the field-reversal APS [5], which is based on the achromatic reversal of the electric-field vector on one of the two interfering waves, by means of a rotational shearing interferometer with a fixed shear of 180 degrees;
- the vectorial APS, subject of this paper, which consists in spatially distributing a phase retardance that is primarily affecting the orthogonal polarization components.

According to [6], for an interferometer with stellar leakages similar to those of a Bracewell two-telescope interferometer, a sensible value for the mean instrumental leakage contribution to the null depth would be

$$N(\lambda) = 10^{-5}\left(\frac{\lambda}{7\,\mu m}\right)^{3.37} \tag{1}$$

In addition to the APS imperfections there are many systematic sources of deterioration of the null depth: e.g., telescope pointing errors, photometric unbalance, OPD errors, etc. Consequently, the requirement for the limitation on the null depth due to the APS alone, must be significantly lower than expressed in Eq. 1, i.e., $N = 10^{-6}$ or better. In practice, we will always apply a reasonable security by requiring a few 10^{-7}.

As we will show, the vectorial APS family is a promising alternative to the three first mentioned APS. Indeed, as compared to the difficulty of finding the dispersive plate APS working point(s), the vectorial APS implementation is straightforward. Moreover, unlike the focus-crossing and field-reversal APS, vectorial APS do not come with a subsequent pupil flip. The pupil inversion, creating a pair of images for one single planet, induces several limitative consequences. First, the spatial coherence γ of the interfering beams must be of the order of the null specification on the APS, i.e. $\gamma \leq 10^{-6}$. Second, Hénault [7] recently stressed out that the pupil-flip APS could be less favorable because the pupil inversion seems to substantially impact extinction maps, implying S/N losses and weakening the detection capacity of the instrument [8]. These problems can only be mitigated with monomode spatial filtering. Third, contrary to the mirror APS which only provides a π phase shift (some interferometer configurations require other phase shift values), the vectorial APS is theoretically able to satisfy any requirements in this respect. For instance, it could provide the 90°, 120° and 240° phase shifts required by the three telescope nuller [9] (TTN), either in the planar or non-planar configuration.

We recently proposed the idea of using subwavelength gratings in total internal reflection (TIR) incidence as achromatic phase shifters [10]. Theoretical calculations using the Rigorous Coupled Wave Analysis [11] (RCWA) pointed to interesting results. The purpose of the present paper is fourfold:

- put the subwavelength grating in TIR incidence APS in the more general context of modulated Fresnel rhomb APS for infrared nulling interferometry;
- presenting a general tolerance study of Fresnel rhomb-based vectorial APS;

- introducing some manufacturing and design considerations for the actual prototype under fabrication at CSL (“Centre Spatial de Liège”) to be tested at room (298 K) and cryogenic (100 K) temperatures at IAS (“Institut d’Astrophysique Spatiale”, Orsay, France);
- presenting some preliminary retardance measurement results obtained at 632.8 nm.

2. Principles

The TIR phenomenon comes with a phase shift between the vectorial *s* and *p* polarization components. This vectorial phase shift takes the following general form [12]

$$\Delta\phi_{s-p} = 2\arctan\left[\frac{\sqrt{\sin^2\theta - n_{ti}^2}}{n_{ti}^2\cos\theta}\right] - 2\arctan\left[\frac{\sqrt{\sin^2\theta - n_{ti}^2}}{\cos\theta}\right] \qquad (2)$$

where θ is the angle of incidence, greater or equal to θ_c, the critical angle defined as $\sin\theta_c = n_{ti} = n_t/n_i$ and where n_i and n_t are the refractive indices of the incident and emergent media, respectively. This property is exploited in the well-known Fresnel rhombs, which are retarders to be used alone as polarization optics.

2.1. *Double rhomb configuration*

Single Fresnel rhombs are known to be very sensitive to incidence angle variations (at the sub-arcmin level). This drawback would be penalizing in our application since the thermal infrared interferometric beam is likely to slightly diverge because of diffraction while somewhat wandering around because of vibrations. For this reason, we chose the double rhomb configuration for its known insensitivity to incidence variations [13]. Indeed, the pairs of reflections in the two rhombs are complementary (see Fig. 1 and Fig. 2); an increase in the first two TIR angles due to departure from nominal incidence leads to a decrease in the last two angles. Thus if the phase shift varies linearly with the TIR angle, the retardance changes are cancelled. Therefore a wider range of incidence angle variations can be tolerated: up to several degrees.

2.2. *Modulated total internal reflection achromatic phase shifter*

Classical Fresnel rhombs are limited by the intrinsic index dispersion of the rhomb bulk material [14]. Engraving a subwavelength grating on the TIR interface or simply depositing a single thin layer of a well chosen material leads to a significant improvement. Indeed, the electromagnetic field evanescent interaction with the optimized micro-structure or thin film allows us to tune the index ratio n_{ti} of Eq. 2. It is to be noted that in the double rhomb configuration, the number of subwavelength gratings to be imprinted (resp. thin film to be deposited) on the TIR

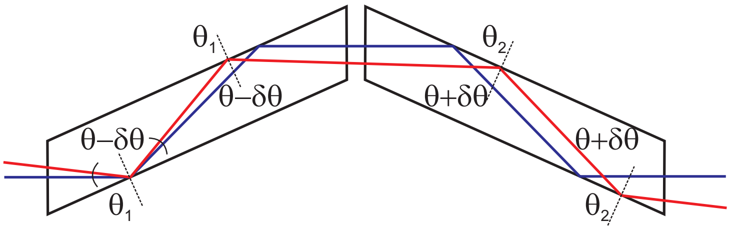

Fig. 1. This scheme shows the double-rhomb configuration. θ_1 (resp. θ_2) is the angle of incidence upon the TIR interfaces of the first (resp. second) rhomb.

#84445 - $15.00 USD Received 25 Jun 2007; revised 24 Aug 2007; accepted 25 Aug 2007; published 21 Sep 2007

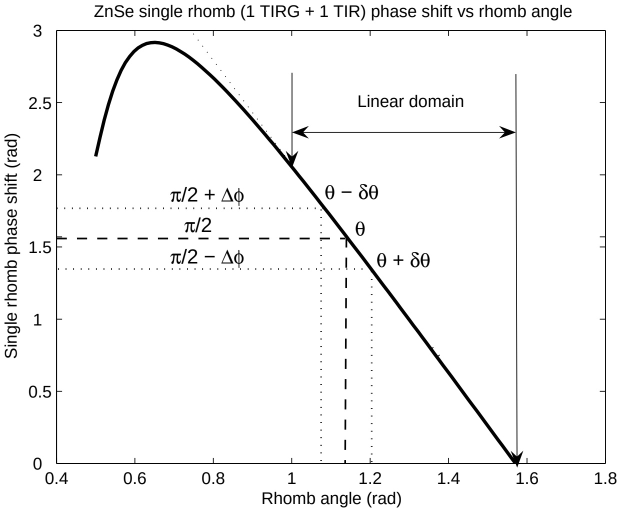

Fig. 2. The double-rhomb geometry allows incidence-angle variations $\delta\theta$ to be compensated by the angle complementarity between the two rhombs and the linearity of the phase shift with respect to the rhomb angle. The linearity is present in the bare Fresnel rhomb or the TIR modulated one.

interface may be limited to only two out of four. Indeed, the dispersion compensation artificially introduced by the modulated interface can already and substantially improve the global behavior of the component in terms of phase shift achromaticity.

2.2.1. Total internal reflection grating

The principle of the total internal reflection grating achromatic phase shifter (TIRG APS) is to use a subwavelength grating in the TIR incidence condition [10]. One dimensional subwavelength gratings turn out to be artificially anisotropic [10]. It means that the structure can be associated with two synthetic effective indices, one for each polarization component: TE (transverse electric, vibrating parallel to the grating grooves, or s) and TM (transverse magnetic, vibrating perpendicular to the grooves, or p). These effective indices, n_{TE} and n_{TM} are totally dependent on the grating and incidence geometries (see Fig. 5), which can be wisely engineered to compensate for the natural material dispersion.

2.2.2. Total internal reflection thin film

Instead of engraving a subwavelength grating onto the TIR interface, one can deposit a layer of a well-chosen foreign material. The principle of the so-called total internal reflection thin film achromatic phase shifter (TIRTF APS) is to make use of such a thin film coated with an appropriate thickness on the TIR interface. This principle has been known for quite a long time in the optical where MgF_2 thin films are commonly deposited on $BK7$ or Silica rhombs to improve the angular and chromatic behavior of commercial Fresnel rhombs [15].

2.3. Implementation

Implementing two strictly identical π retarders into the two interferometer arms and rotating them by ninety degrees with respect to each other around the interferometer optical axis, is

#84445 - $15.00 USD Received 25 Jun 2007; revised 24 Aug 2007; accepted 25 Aug 2007; published 21 Sep 2007

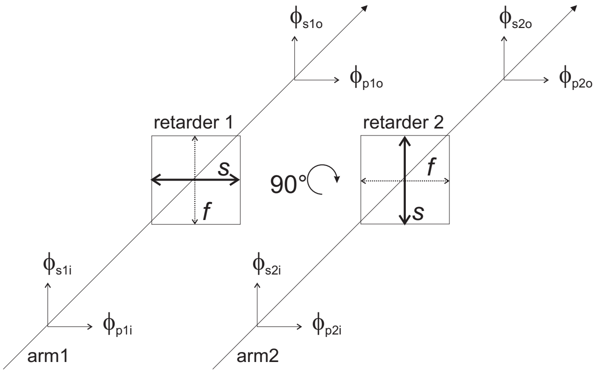

Fig. 3. Implementation of a vectorial phase shifter (retarder) in a two-telescope nulling interferometer (Bracewell). The π retardance between the orthogonal polarizations s and p induced by the light differential optical delay between the slow (s) and fast axis (f) of the vectorial phase shifters 1 and 2 ($\phi_{s1o} - \phi_{p1o} = \phi_{s2o} - \phi_{p2o} = \pi$) can be spatially distributed between the interferometer arms. Indeed, a rotation of 90° of the retarders around the optical axis permutes the role of the polarizations so that at the output, the potentially interfering polarization states, i.e. the parallel ones are in phase opposition, $\phi_{s1o} - \phi_{s2o} = \phi_{p1o} - \phi_{p2o} = \pm\pi$.

a practical solution to spatially distribute the initial vectorial phase shift (see Fig. 3); “vectorial” meaning between the polarization components. The ninety degree rotation between the retarders around the optical axis must be respected at ± 2 arcmin to reach the 10^{-7} secure null depth level.

3. Theoretical analysis

This section is devoted to the theoretical analysis of the TIRG and TIRTF APS. The purpose of this analysis was to optimize (with the “simplex-search” optimization method [16], highly robust when the parameter space is highly discontinuous) the APS component in order to “achromatize” the Darwin/TPF-I working wavelength range: 6-18 μm. However, due to practical constraints like wavefront filtering or dichroic limitations, the latter is expected to be divided into two or three sub-bands. In the two-band case, the first one ranges from 6 to 11 microns while the second one ranges from 11 to 18 microns. Before going into the details of the theoretical analysis, one had to choose the materials according to the bandwidth specifications mentioned here above. Regarding this matter, we immediately had to discard common infrared materials like Silicon (*Si*) and Gallium Arsenide (*GaAs*) for their strong multi-phonon absorption features beginning between 8 and 12 microns [17]. For the same reason, we also had to discard Zinc Sulphide (*ZnS*) and Germanium (*Ge*), other widespread infrared materials.

The choice for the bulk material constituting the rhomb in fact revealed to be very difficult and severely limited since the material has to be perfectly transparent up to 18 microns (20 if possible) and of course available in large ingots of very good optical quality (good homogeneity, low impurity, etc.). For this reason, we focussed on common long-wave infrared materials such as Zinc Selenide (*ZnSe*), Cadmium Telluride (*CdTe*), and KRS-5. Although *ZnSe* is in general used in the 11-18 μm range, *CdTe* and KRS-5 are the only ones perfectly clear up to 18 microns. Note that *ZnSe*, *ZnS* or even CVD (Chemical Vapor Deposition) Diamond can be used as the TIRTF APS layer materials in their phonon absorption ranges since their working thicknesses are very thin and the subsequent absorptions therefore negligible. These selected materials are

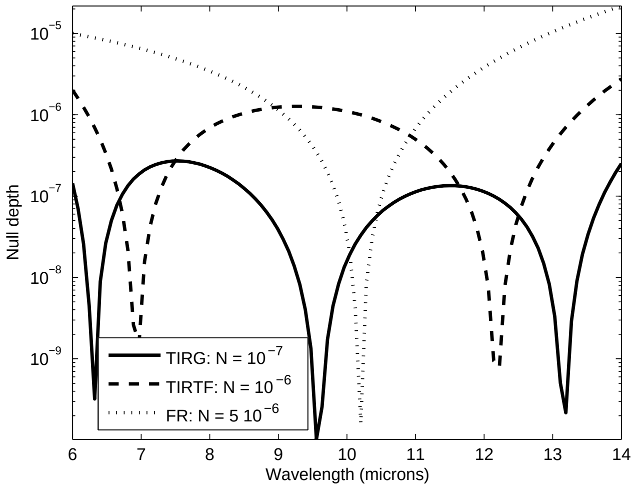

Fig. 4. *ZnSe* double-rhomb APS: comparison between Fresnel Rhomb (FR) with non-treated TIR interfaces, TIR thin film (TIRTF) and TIR grating (TIRG). More than substantially improving the global (mean) null depth over the considered wavelength range, the TIRTF and the TIRG solutions significantly decrease the strong leakage at its edges, inevitable with the FR solution.

common in infrared applications, they cover a large refractive index spectrum ($n = 2-4$) and their processing (polishing, etching, sputtering, etc.) is in general well known for most of them. The refractive index dispersions will be taken from [18] for Diamond, from [19] for *ZnSe*, from [20] for KRS-5 and from [17] for *ZnS*, *CdTe*.

To simulate grating responses in the subwavelength domain, we used an algorithm based on the RCWA, which is also called the Fourier modal method because it is based on Fourier decompositions of the physical characteristics of the grating and fields so that the resolution takes place in the frequency space.

3.1. ZnSe Rhomb

In its polycrystalline form, *ZnSe* is available in large quantities and volumes at a reasonable cost. It is also relatively convenient to polish with very good surface qualities. Moreover, its thermal properties are very attractive, with a low thermal expansion coefficient (7.1×10^{-6}/K) and a rather good thermal conductivity (0.18 W/cm/K). Unfortunately, the chosen double-rhomb configuration inevitably lengthens the optical path in the material. For instance, in the present case, a working angle of about 65.03° would lead to a physical path of about 17 cm inside the material for an entrance beam diameter of 15 mm. In the second Darwin sub-band ($11-18$ μm), such a long path is penalizing since *ZnSe* begins its phonon absorption around 14 microns. Indeed, the absorption coefficient [17] k is equal to 4.24×10^{-6} at 14 μm and 298 K, leading to absorption of about 50%. This value reduces to 2.52×10^{-6} at 100 K, giving an absorption of 30%, which remains acceptable for demonstration purposes. For this reason, a *ZnSe* TIRG APS in the double-rhomb configuration will be practically limited to the $6-14\,\mu$m wavelength range. One of the main outcomes of the theoretical results presented in Table 1 is that the *ZnSe* bare Fresnel rhomb (without any modulation of the TIR interfaces) is not perform-

Table 1. Average null depths for the optimized Fresnel double rhomb, TIRG, TIRTF configurations for the selected infrared materials. D stands for Diamond (CVD).

Rhomb material / band	**Fresnel rhomb**	***TIRG APS***	***TIRTF APS***
ZnSe / $6-11\ \mu$m	2×10^{-6}	1×10^{-8}	D/*ZnS* layer: 1×10^{-7}
ZnSe / $6-14\ \mu$m	6×10^{-6}	1×10^{-7}	D/*ZnS* layer: 1×10^{-6}
CdTe / $6-11\ \mu$m	2×10^{-7}	5×10^{-9}	D/*ZnSe*/*ZnS* layer: 1×10^{-8}
CdTe / $11-18\ \mu$m	8×10^{-7}	1×10^{-8}	D/*ZnSe*/*ZnS* layer: 5×10^{-8}
CdTe / $6-18\ \mu$m	2×10^{-6}	1×10^{-7}	D/*ZnSe*/*ZnS* layer: 5×10^{-7}
KRS-5 / $6-11\ \mu$m	2×10^{-7}	NA	NA
KRS-5 / $11-18\ \mu$m	1×10^{-6}	NA	NA
KRS-5 / $6-18\ \mu$m	2×10^{-6}	NA	NA

ing well enough for the Darwin baseline 10^{-6} specification (see Fig. 4, dotted line). However, depositing a foreign material at the TIR interface or imprinting a subwavelength grating onto it allows overcoming this limitation in the $6-11\,\mu$m wavelength range. In the larger $6-14\,\mu$m range, only the subwavelength grating solution is able to meet the specification (Fig. 4, continuous line) while the thin film one just misses it by a small factor (Fig. 4, dashed line).

3.2. CdTe Rhomb

Availability of *CdTe* ingots is more limited than *ZnSe* ones. Polishing of *CdTe* is quite delicate but currently under evaluation for improvement by several manufacturers. *CdTe*, which also possesses rather good thermal characteristics (expansion coefficient of 5.9×10^{-6}/K and conductivity of 0.062 W/cm/K), nevertheless appears to be a viable potential solution. Indeed, as already stated, *CdTe* is one of the selected rhomb materials perfectly clear up to 18 microns. Moreover, theoretical RCWA results are excellent, showing better performance than *ZnSe* (see Table 1). First of all, the *CdTe* bare Fresnel rhomb solution is worth considering since it is theoretically performing well enough, at least for the Darwin first sub-band but unfortunately not for the second one. Depositing a thin film of a foreign material (e.g., Diamond, *ZnSe* or *ZnS*) overcomes this limitation. As far as the subwavelength grating solution is concerned, results are comfortably in the specifications for both bands. Let us emphasize that there exists a most interesting theoretical solution which would "achromatize" the full Darwin wavelength range from 6 to 18 microns with a single APS consisting of an optimized double *CdTe* rhomb modulated with a subwavelength grating (Table 1).

3.3. KRS-5 Rhomb

KRS-5 infrared dispersion is extremely low [20], making it an ideal material for a Fresnel rhomb. Indeed, results displayed in Table 1 confirm its very good potential. Unfortunately, KRS-5 is a very difficult material to handle. It is toxic, brittle and is not easily polished (to our knowledge its polishing was never demonstrated at qualities better than $\lambda/4$ rms, $\lambda = 632.8$ nm). It is to be emphasized that KRS-5 is common in infrared applications despite its bad thermal conductivity (5.4×10^{-3} W/cm/K) and expansion coefficient (5.8×10^{-5}/K). KRS-5 was also considered since it is one of the rare materials perfectly transparent above 15 microns. Finally, KRS-5 cannot be micro-structured nor easily treated with foreign materials because of its chemical reactivity.

#84445 - $15.00 USD Received 25 Jun 2007; revised 24 Aug 2007; accepted 25 Aug 2007; published 21 Sep 2007

4. Design and tolerancing of a modulated Fresnel rhomb prototype

In this section, we will discuss the design of a modulated Fresnel rhomb prototype intended at being one of the APS selected for study, fabrication and test in the framework of one of ESA's Darwin R&D preparatory activities: Nulltimate [21], which is a project of infrared cryogenic (100 K) nulling testbed. This section will be devoted to the tolerancing of the subwavelength grating and the macroscopic rhomb. The choice of the material for the prototype has been made thanks to a trade-off matrix. Even if *CdTe* shows the best theoretical characteristics in terms of transparency and performances, *ZnSe* was the retained material to make the prototype in the $6-14\,\mu$m Nulltimate wavelength range for the following reasons:

- in its polycrystalline state, *ZnSe* is a priori easy to source, and a convenient material to handle and polish (surface qualities of $\lambda/30$ rms with $\lambda = 632.8$ nm are routinely obtained);
- it is compatible with the thickness-adjustable beam splitters of the Nulltimate test bench which are planned to be in *ZnSe*;
- it is transparent in the optical, letting the *HeNe* 632.8-nm interferometric metrology beam pass through.

4.1. TIRG tolerancing

The fabrication of the TIRG APS will be based on micro-electronic technologies. The first classical step consists in imprinting a photomask of the grating in a photoresist coated on the chosen substrate material. The precision of this step is critical because it defines once and for all the lateral dimensions of the grating (Fig. 5): its period Λ and the so-called feature line, i.e., the period multiplied by the filling factor f. This pattern will then uniformly be transferred into the substrate by an appropriate reactive plasma-beam etching down to the desired depth (h). The fabrication has to be interactive to properly compensate for process errors. In situ monitoring is a possible solution [22] but not the only one as we will discuss.

4.1.1. Manufacturing scenario

Let us now consider the *ZnSe* TIRG APS designed for the 6-14 μm wavelength range. A rough optimization for this range leads to a 900-nm period. Then, assuming this fixed period, best

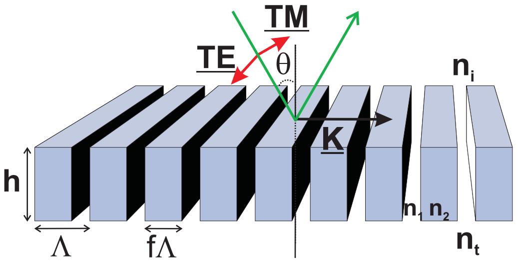

Fig. 5. Schematic of a subwavelength grating. The structure parameters are: the grating vector $|\underline{K}| = 2\pi/\Lambda$, perpendicular to the grating lines, with Λ the spatial period, the thickness h and the filling factor f, such that $f\Lambda$ is the feature line. $\underline{TE}$ and $\underline{TM}$ are the orthogonal polarization components of the θ-incident light. n_i and n_t are the refractive indices of the incident and emergent (transmitting) media, respectively. n_1 and n_2 are the refractive indices of the grating itself (in this case, $n_2 = n_i$ and $n_1 = n_t$).

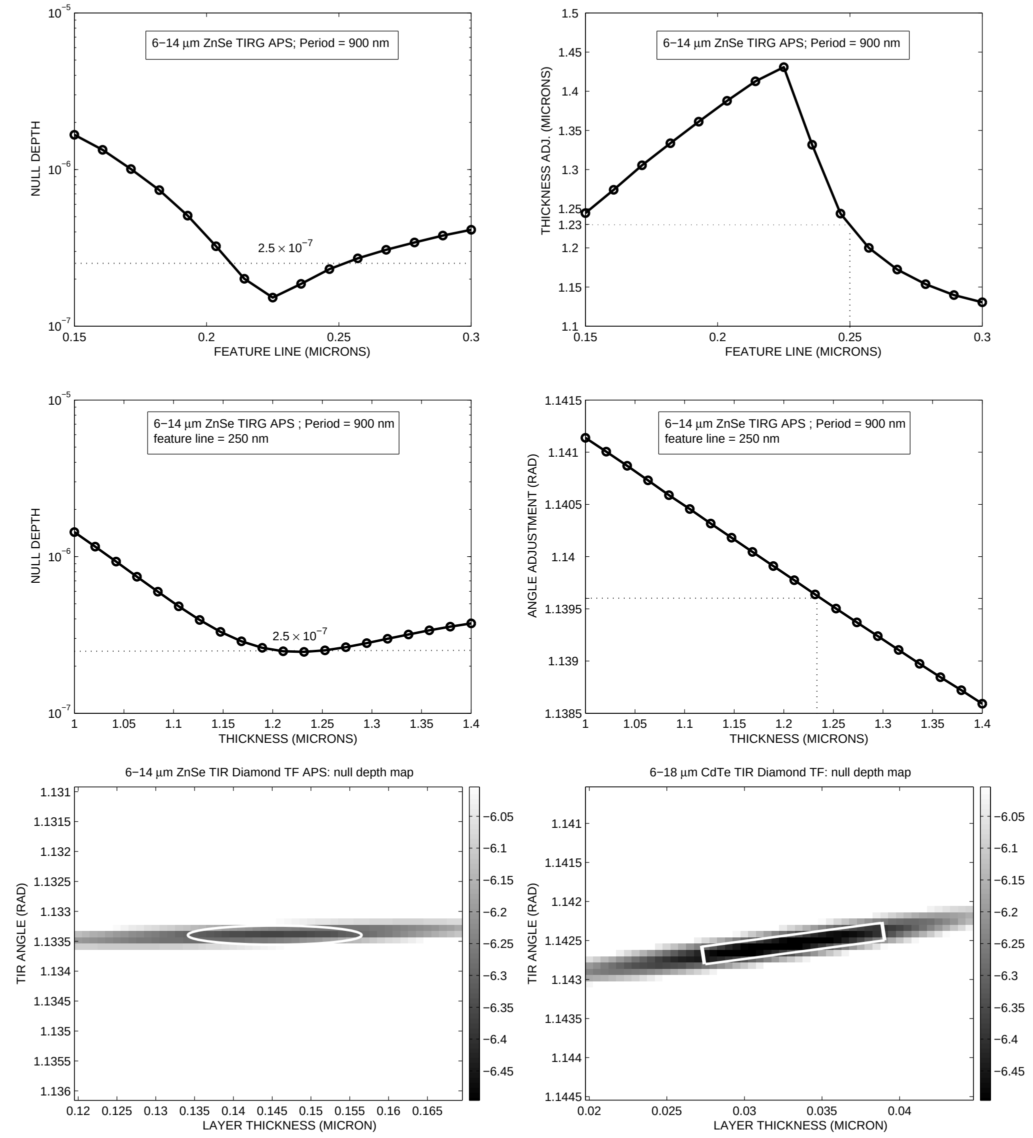

Fig. 6. 6-14 μm *ZnSe* double rhomb APS with 900 nm period. Top left: optimized null depth vs feature line. Top right: thickness adjustment (optimized) vs feature line. Middle left: angle optimized null depth vs thickness for a fixed feature line of 250 nm. Middle right: corresponding angle adjustment (optimized) vs thickness. Bottom: two-dimensional maps of the null depth (log scale, $10^{-\alpha}$) according to the variables “thickness of the layer” and “incidence angle”. Left: *ZnSe* TIRTF APS coated with Diamond for the 6 to 14 micron band. Right: *CdTe* TIRTF APS coated with Diamond for the 6 to 18 micron band.

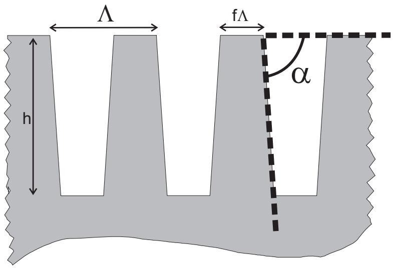

Fig. 7. Trapezoidal profile likely to emerge from the plasma-etching process. The new parameter to be taken into account is the grating slope angle α.

solutions are searched using the “simplex” optimization method [16] coupled to the RCWA algorithm with the filling factor f, the grating thickness h and the incidence angle θ left as free parameters. Results of this optimization are displayed in Fig. 6 (top left), where the optimal null depth is plotted versus the feature line, i.e., the product of the 900-nm fixed period and the varying filling factor. Continuous variations are now imposed to the feature line while letting the optimization algorithm find the corresponding adjustment of the thickness that minimizes the null depth (see 6, top right). The best null depth, in this case the minimum one, is about 1.5×10^{-7}. This optimal value is obtained for the 220-nm feature line. The corresponding adjusted thickness is 1.43 μm. If we calculate the grating aspect ratio, we find 6.5 which is demanding given the nature of the material to be subsequently etched. To relax this difficulty, we chose the conservative width of 250 nm for the feature line which corresponds to an adjusted thickness of 1.23 μm and a subsequently reduced aspect ratio of about 5. Let us now fix the feature line to 250 nm, keep the period at 900 nm and vary the thickness artificially, letting the optimization algorithm find the corresponding incidence polar angle θ adjustment that minimizes the null depth. Results of this analysis are shown in Fig. 6, middle left and right. Provided that the polar angle can be adjusted with a sub-arcmin precision, the $N \approx 2.5 \times 10^{-7}$ tolerance on the thickness definition is 1.23 ± 25 nm, i.e., about 2%, which is feasible.

The conclusion of this tolerance analysis is that, provided that there are interactions between measurements and manufacturing at each key step, the tolerances on the parameter definitions are rather comfortable, up to a few tens of nanometers for the feature line and the thickness. A posteriori correction is reported on the incidence angle which is very convenient since the double-rhomb geometry still ensures the insensitivity to the entrance beam incidence configuration (input angle and beam divergence, for instance) at the macroscopic level.

4.1.2. Grating slope angle

Departure from the nominal assumed grating profile, i.e. a perfectly rectangular one, is likely to naturally emerge from the plasma-beam etching process (Fig. 7). The calculated tolerance on the grating slope angle α is 5°, which is very tight and necessitates very directional and anisotropic plasma etching processes.

4.2. TIRTF tolerancing

As far as an eventual TIRTF APS component is concerned, tolerancing can be envisaged in another way. Since the parameter space is limited to two variables, i.e. the thickness of the layer and the angle of incidence, the working points can be traced in two-dimensional maps. From Fig. 6 bottom, we can conclude that the tolerance on the thickness is of $\sim 10\%$. It is to be

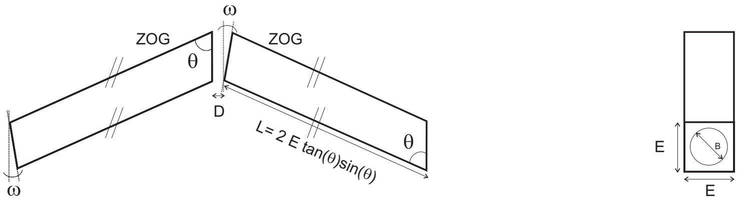

Fig. 8. Double-rhomb geometrical scheme and definition of the wedge angle *w*.

noted that coatings are routinely deposited with a precision of $\sim 1\%$ on the thicknesses.

4.3. *Surface roughness and material homogeneity*

We have conducted a complete tolerancing study of roughness and homogeneity effects using a Monte-Carlo method coupled with rigorous diffraction analysis. The conclusion is that the surface roughness and grating thickness variability should not exceed 10 nm rms. Concerning linewidth roughness (feature line uniformity), it should not depart from 25 nm rms. As far as material refractive index homogeneity (δn) is concerned, the conclusion is that the current *ZnSe* synthesizing method (CVD) provides an excellent optical quality ($\delta n \approx 3 \times 10^{-6}$) that should not affect the nulling performance of the interferometer [8]. Small defects should moreover be filtered out by the planned spatial filters.

4.4. *Rhomb geometry and ghosts*

The geometry of the rhomb (Fig. 8) is well constrained by the TIR optimal angle ($\theta' \approx 65^\circ$) and the dimension of the incoming interferometric beam, i.e. B= 15 mm in diameter (the input face size E will be 20 by 20 mm). Each of the four rhombs must be strictly identical with arcsec precision for the angles and micrometric precision for the dimensions, which can be ensured to a certain degree by polishing them together in a same batch. Slight departure from nominal dimension will impact OPD, but can be compensated thanks to the thickness-adjustable beam splitters of the testbed which are also in *ZnSe*. In order to dump stray light originating from spurious reflections at the *ZnSe*/air interfaces, we chose to apply anti-reflective treatments ($R \approx 1.5\%$). Unfortunately, given the stringent constraints of nulling interferometry, we also had to apply well-chosen wedges between rhomb interfaces. In order to further mitigate ghosts, we have used ray-tracing analysis which led to an optimal wedge value of $w = 1^\circ$. Both rhombs of the double-rhomb configuration possess the same but opposed wedge angle so that deviation and dispersion are annihilated and therefore do not impact the nulling process (Fig. 9). Let us also mention that the rhomb spacing D must be identical at the 0.1 mm-level between both interferometer arms in order to avoid differential dispersion of the OPD.

5. **Manufacturing**

In this section, we will present some manufacturing details for the *ZnSe* Fresnel rhomb APS.

5.1. *ZnSe Rhomb cutting and polishing*

We have conducted cutting and polishing trials of *ZnSe* rhombs with the appropriate global geometry and dimensions (Fig. 10). Results of ZYGO interferometric measurements in terms of surface quality comfortably fall in the specifications, and beyond our expectations with surface figures of $\lambda/100$ rms ($\lambda = 632.8$ nm). Concerning the roughness, WYKO profilometer measurements give a rather good 3 nm rms.

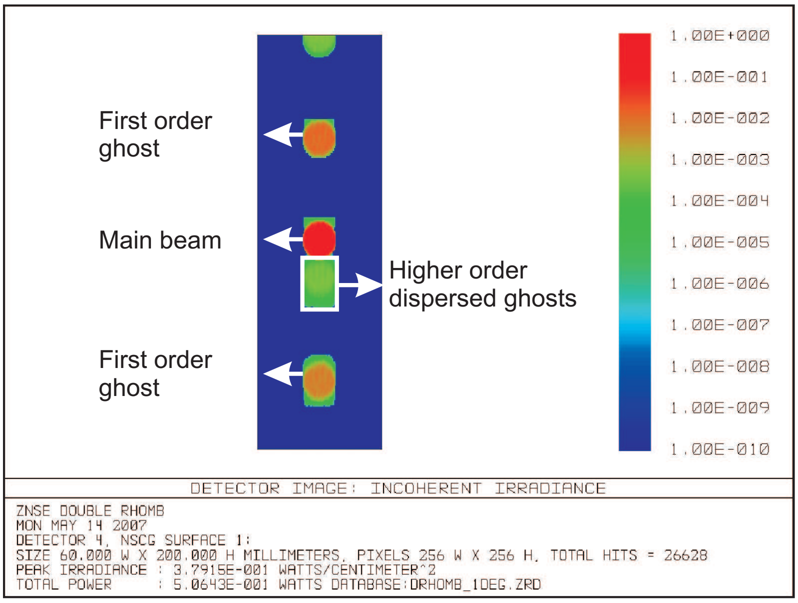

```
DETECTOR IMAGE: INCOHERENT IRRADIANCE
ZNSE DOUBLE RHOMB
MON MAY 14 2007
DETECTOR 4, NSCG SURFACE 1:
SIZE 60.000 W X 200.000 H MILLIMETERS, PIXELS 256 W X 256 H, TOTAL HITS = 26628
PEAK IRRADIANCE : 3.7915E-001 WATTS/CENTIMETER^2
TOTAL POWER     : 5.0643E-001 WATTS DATABASE:DRHOMB_1DEG.ZRD
```

Fig. 9. ZEMAX ray-tracing analysis of a *ZnSe* double wedged (1°) rhomb.

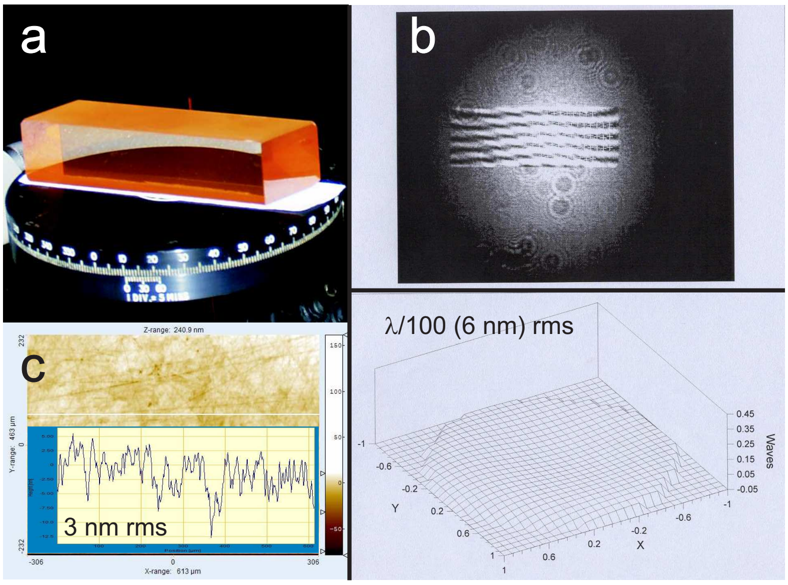

Fig. 10. a. Picture of a *ZnSe* Fresnel rhomb. b. ZYGO interferograms. c. WYKO profiles.

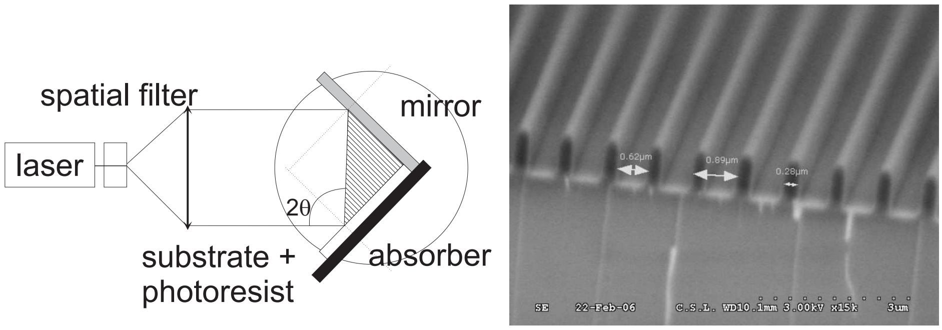

Fig. 11. Left: principle of holographic lithography (Lloyd mirror mounting). The grating period is inversely proportional to the angle between the two interferometer beams. Right: Micro-pattern on photoresist to be transferred by reactive plasma beam etching into the *ZnSe* substrate. The period and filling factor correspond to the design specifications.

5.2. TIR Grating manufacturing

We chose to manufacture the micro-pattern using holographic lithography and dry etching. The first one is necessary for masking the parts of the substrates to be protected during the etching step (Fig. 11, right). Direct laser writing or classical mask exposure techniques are not applicable onto the rhomb facets since they are designed to accommodate thin and flat substrates such as wafers for micro electronics. The holographic recording allows us to overcome this limitation by imprinting the photoresist mask thanks to a two-wave sinusoidal interference fringe pattern (Lloyd mirror mounting, Fig. 11, left). A good understanding and control of the recording and developing parameters (as energy dose, development duration, resist thickness, resist optical contrast, etc.) have produced reproducible rectangular binary profiles with a controlled filling factor (at the 10-nm level) instead of the natural sine profile. After its processing, the remaining photoresist pattern serves as a lithographic mask for the subsequent reactive plasma beam etching (RPBE) process, which makes use of both the ballistic effect and chemical reactivity of a beam of reactive ions to transfer structures into a substrate. The various parameters (gas melanges, beam energy, beam incidence, etc.) characterizing the etching process are optimized for the transfer into various materials. The interest of such a technique comes particularly from its high selectivity, the potential to efficiently etch one material and not another coexisting one, used as a mask. The infrared material (*ZnSe* or *CdTe*) is engraved using a selective chemistry (CH_4/H_2 [23] or chlorine-based [24] compounds), depending on the crystal phase of the material which leaves intact the photoresist mask but etches the infrared substrate. Validation trials are currently under progress. They aim at identifying the best process conditions ensuring the most efficient transfer of the diffractive structure from the mask into the material. Highest selectivity, homogeneity and reproducibility are the key factors under optimization.

5.3. Mechanical mount

The two mechanical mounts (one per interferometer arm) of the two *ZnSe* double rhombs must be thoroughly optimized to account for thermo-mechanical effects. Indeed, the component shall be measured at room (298 K) and cryogenic (100 K) temperatures. It will thus be cooled down and the mount must allow for an efficient heat transfer while compensating differential contractions. The alignment of the two rhombs must be controlled around 3 axes with an arcmin precision. The double rhomb spacing difference between both arms, and thus between the two corresponding mechanical mounts must be below 0.1 mm. The mounts must also account for

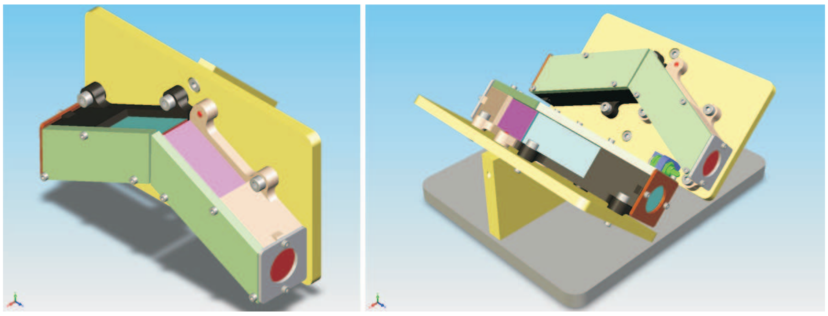

Fig. 12. Design of the *ZnSe* double Fresnel rhomb APS mechanical mounts. Right illustrates the practical implementation of the components in the interferometer at 45° from the test bench table, rotated of 90° from each other.

the *ZnSe* sensitivity to stress birefringence. In order to quantify the latter to help the mount design, a finite element analysis was conducted and resulted in the conclusion that the rhombs must lay freely at 45° in their mounts (Fig. 12). Indeed, given the stress-optics coefficient of *ZnSe*, $C_{\lambda=10.6\mu m} \approx -12$ brewsters [25], even its own weight constraint σ can induce a substantial birefringence $\Delta n = C_{\lambda=10.6\mu m}\sigma$ which is just within the specifications.

6. Measurement of a ZnSe Fresnel rhomb retardance at 632.8 nm

We conducted preliminary measurements of the performance of a *ZnSe* Fresnel rhomb at 632.8 nm with a simple polarimeter arrangement [26](Fig.13). A governing equation relates the ratio of the intensities $I^{\frac{\pi}{2}}$ (corresponding to $P2^{\frac{\pi}{2}}$) and I^0 (corresponding to $P2^0$) of the two orthogonal polarization states to the orientations of the input/output polarizer with respect to the retarder (α), and the retardance (Γ)

$$\frac{I^0}{I^{\frac{\pi}{2}}} = \frac{\sin^2 2\alpha \, \sin^2(\Gamma/2)}{1 - \sin^2 2\alpha \, \sin^2(\Gamma/2)} \tag{3}$$

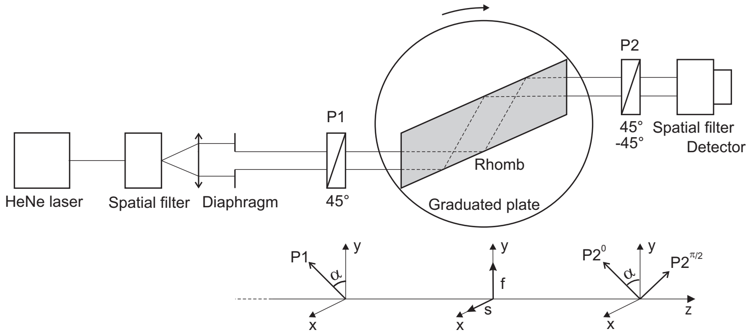

Fig. 13. Optical setup used to perform the *ZnSe* rhomb retardance measurement. Linearly polarized light (P1) is incident upon the rhomb, and the light emerges with an elliptical polarization. The intensities of the two orthogonal polarization states are measured by rotating the output polarizer (P2). *s* and *f* are respectively the slow and fast rhomb axis.

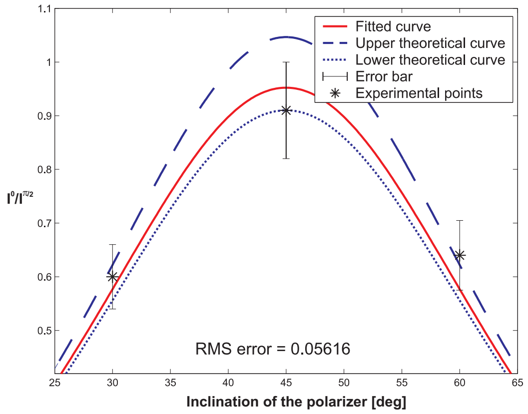

Fig. 14. *ZnSe* single rhomb retardance measurement. In blue: limits of the expected retardance vs polarizer inclinations. In red: fitted curve corresponding to a retardance of 88.8°±1.5°. The RMS error of the fit is 0.05616 and corresponds to a phase error of 1.5°, which is fully compliant with our setup precision.

In addition to the retardance measurement, the experiment allowed us to disentangle several parasitic effects that could prevent the rhomb to reach its theoretical phase shifting potential. The rhomb TIR angle of 65°±0.1° should theoretically provide a 91°±0.5° phase shift at 632.8 nm. The primary source of perturbation was identified as the surface and bulk scattering ($\sim 1\%$). Fortunately, we have demonstrated that it can be mitigated at least at the 10^{-5} level (accuracy of our optical setup) by inserting a spatial filter at the rhomb output, as planned for Nulltimate too. The secondary identified source was the spurious parasitic reflections. Tilting the rhomb by $\sim 1°$ was necessary to get rid of the ghost, in agreement with our ray-tracing analysis that concluded to the necessity of wedging the final rhombs (Sect. 4.4). We have then measured a phase shift of 88.8°±1.5° [Fig.14] (uncertainty of the optical setup) which is consistent with the tilt-corrected theoretical value of 90.2°±0.5°(uncertainty of the measured rhomb angle). Given the different systematics in our experiment at 632.8 nm, we can extrapolate an upper boundary for the expectable null depth at 6 μm: $N < 10^{-4}$. Moreover, this experiment allowed us to identify the way to mitigate every potential sources of disturbance imputable to the sole rhomb APS so that its final performance should comply to the Darwin specifications.

7. Conclusion

To summarize, we have presented a new family of APS for thermal infrared radiations relying on the TIR phenomenon, modulated or not. The modulation can be induced either by an integrated subwavelength grating or a deposited thin film. Theoretical results show remarkable improvements over the classical Fresnel rhomb technique, which is always limited by the intrinsic dispersion of the bulk material used. We have also presented some design key points and encouraging preliminary measurements for the *ZnSe* prototype under manufacturing. In the framework of R&D activities for the Darwin mission, this prototype will be tested on the Nulltimate test bench at IAS. Results will be the subject of a forthcoming paper.

Acknowledgments

The authors acknowledge the financial support of ESA.

Bibliography

Absil, O., 2006, *Astrophysical studies of extrasolar planetary systems using infrared interferometric techniques*, Ph.D. thesis, University of Liège.

Absil, O., Coudé du Foresto, V., Barillot, M. & Swain, M. R., 2007, Nulling interferometry: performance comparison between Antarctica and other ground-based sites, *Astron. & Astrophys.* **475**, 1185–1194.

Absil, O., den Hartog, R., Gondoin, P. et al., 2006a, Performance study of ground-based infrared Bracewell interferometers. Application to the detection of exozodiacal dust disks with GENIE, *Astron. & Astrophys.* **448**, 787–800.

Absil, O., di Folco, E., Mérand, A. et al., 2006b, Circumstellar material in the Vega inner system revealed by CHARA/FLUOR, *Astron. & Astrophys.* in press.

Absil, O., di Folco, E., Mérand, A. et al., 2008, A near-infrared interferometric survey of debris disc stars. II. CHARA/FLUOR observations of six early-type dwarfs, *Astron. & Astrophys.* **487**, 1041–1054.

Absil, O., Le Bouquin, J., Lebreton, J. et al., 2010, Deep near-infrared interferometric search for low-mass companions around β Pictoris, *Astron. & Astrophys.* **520**, L2+.

Absil, O. & Mawet, D., 2010, Formation and evolution of planetary systems: the impact of high-angular resolution optical techniques, *A&A Rev.* **18**, 317–382.

Alibert, Y., Mordasini, C., Benz, W. & Winisdoerffer, C., 2005, Models of giant planet formation with migration and disc evolution, *Astron. & Astrophys.* **434**, 343–353.

Anderson, R., 1988, Quarterwaveplate and Fresnel rhomb compared in the 10-Mum CO2 laser emission region, *Applied Optics* **27**, 2746–2747.

Aristidi, E., Carbillet, M., Lyon, J. & Aime, C., 1997a, Imaging binary stars by the cross-correlation technique, *Astron. & Astrophys., Suppl.* **125**, 139–148.

Aristidi, E., Carbillet, M., Prieur, J. et al., 1997b, ICCD speckle observations of binary stars: Measurements during 1994-1995, *Astron. & Astrophys., Suppl.* **126**, 555–561.

Arsenault, R., Donaldson, R., Dupuy, C. et al., 2004, MACAO-VLTI adaptive optics systems performance, in *Advancements in Adaptive Optics* (D. B. Calia, B. L. Ellerbroek & R. Ragazzoni, eds.), *Proc. SPIE*, vol. 5490, 47–58.

Aumann, H., Beichman, C., Gillett, F. et al., 1984, Discovery of a shell around Alpha Lyrae, *Astrophysical Journal, Letters* **278**, L23–L27.

Babcock, H. W., 1953, The Possibility of Compensating Astronomical Seeing, *Publ. of the Astron. Soc. Pac.* **65**, 229–+.

Baraffe, I., Chabrier, G., Allard, F. & Hauschildt, P. H., 1995, New Evolutionary Tracks for Very Low Mass Stars, *Astrophysical Journal, Letters* **446**, L35+.

Baraffe, I., Chabrier, G., Allard, F. & Hauschildt, P. H., 1997, Evolutionary models for metal-poor low-mass stars. Lower main sequence of globular clusters and halo field stars, *Astron. & Astrophys.* **327**, 1054–1069.

Baraffe, I., Chabrier, G., Allard, F. & Hauschildt, P. H., 1998, Evolutionary models for solar metallicity low-mass stars: mass-magnitude relationships and color-magnitude diagrams, *Astron. & Astrophys.* **337**, 403–412.

Baraffe, I., Chabrier, G., Allard, F. & Hauschildt, P. H., 2002, Evolutionary models for low-mass stars and brown dwarfs: Uncertainties and limits at very young ages, *Astron. & Astrophys.* **382**, 563–572.

Baraffe, I., Chabrier, G. & Barman, T., 2008, Structure and evolution of super-Earth to super-Jupiter exoplanets. I. Heavy element enrichment in the interior, *Astron. & Astrophys.* **482**, 315–332.

Baraffe, I., Chabrier, G., Barman, T. S. et al., 2003, Evolutionary models for cool brown dwarfs and extrasolar giant planets. The case of HD 209458, *Astron. & Astrophys.* **402**, 701–712.

Barnes, R., Greenberg, R., Quinn, T. R. et al., 2011, Origin and Dynamics of the Mutually Inclined Orbits of υ Andromedae c and d, *Astrophysical Journal* **726**, 71–+.

Basri, G., Borucki, W. J. & Koch, D., 2005, The Kepler Mission: A wide-field transit search for terrestrial planets [review article], *New A Rev.* **49**, 478–485.

Baudoz, P., Boccaletti, A., Riaud, P. et al., 2006, Feasibility of the Four-Quadrant Phase Mask in the Mid-Infrared on the James Webb Space Telescope, *Publ. of the Astron. Soc. Pac.* **118**, 765–773.

Baudoz, P., Rabbia, Y. & Gay, J., 2000, Study and test of a hybrid coronagraph, in *Proc. SPIE Vol. 4007, Adaptive Optical Systems Technology, Peter L. Wizinowich; Ed.*, 971–979.

Bean, J. L., Seifahrt, A., Hartman, H. et al., 2010, The CRIRES Search for Planets Around the Lowest-mass Stars. I. High-precision Near-infrared Radial Velocities with an Ammonia Gas Cell, *Astrophysical Journal* **713**, 410–422.

Beichman, C. A., Krist, J., Trauger, J. T. et al., 2010, Imaging Young Giant Planets From Ground and Space, *Publ. of the Astron. Soc. Pac.* **122**, 162–200.

Berger, J., Zins, G., Lazareff, B. et al., 2010, PIONIER: a visitor instrument for VLTI, in *Society of Photo-Optical Instrumentation Engineers (SPIE) Conference Series*, *Presented at the Society of Photo-Optical Instrumentation Engineers (SPIE) Conference*, vol. 7734.

Beuzit, J., Feldt, M., Dohlen, K. et al., 2008, SPHERE: a planet finder instrument for the VLT, in *Society of Photo-Optical Instrumentation Engineers (SPIE) Conference Series*, *Presented at the Society of Photo-Optical Instrumentation Engineers (SPIE) Conference*, vol. 7014.

Boccaletti, A., Abe, L., Baudrand, J. et al., 2008, Prototyping coronagraphs for exoplanet characterization with SPHERE, in *Society of Photo-Optical Instrumentation Engineers (SPIE) Conference Series*, *Society of Photo-Optical Instrumentation Engineers (SPIE) Conference Series*, vol. 7015.

Boccaletti, A., Augereau, J., Baudoz, P. et al., 2009, VLT/NACO coronagraphic observations of fine structures in the disk of β Pictoris, *Astron. & Astrophys.* **495**, 523–535.

Boccaletti, A., Baudoz, P., Baudrand, J. et al., 2005, Imaging exoplanets with the coronagraph of JWST/MIRI, *Advances in Space Research* **36**, 1099–1106.

Boccaletti, A., Riaud, P., Baudoz, P. et al., 2004, The Four-Quadrant Phase Mask Coronagraph. IV. First Light at the Very Large Telescope, *Publ. of the Astron. Soc. Pac.* **116**, 1061–1071.

Boccaletti, A., Riaud, P., Moutou, C. & Labeyrie, A., 2000, Snapshot coronagraphy with an interferometer in space, *Icarus* **145**, 628–636.

Boden, A. F., 2000, Elementary Theroy of Interferometry, in *Principles of Long Baseline Stellar Interferometry* (P. R. Lawson, ed.), 9–29, JPL Publications, Pasadena.

Boden, A. F., Sargent, A. I., Akeson, R. L. et al., 2005, Dynamical Masses for Low-Mass Pre-Main-Sequence Stars: A Preliminary Physical Orbit for HD 98800 B, *Astrophysical Journal* **635**, 442–451.

Bonnefoy, M., Lagrange, A., Boccaletti, A. et al., 2011, High angular resolution detection of β Pictoris b at 2.18 μm, *Astron. & Astrophys.* **528**, L15+.

Borucki, W. J., Koch, D. G., Basri, G. et al., 2011, Characteristics of planetary candidates observed by Kepler, II: Analysis of the first four months of data, *ArXiv e-prints* .

Boss, A. P., 1998, Evolution of the Solar Nebula. IV. Giant Gaseous Protoplanet Formation, *Astrophysical Journal* **503**, 923–937.

Boss, A. P., 2002, Stellar Metallicity and the Formation of Extrasolar Gas Giant Planets, *Astrophysical Journal, Letters* **567**, L149–L153.

Bouchez, A. H., Dekany, R. G., Angione, J. R. et al., 2008, The PALM-3000 high-order adaptive optics system for Palomar Observatory, in *Society of Photo-Optical Instrumentation Engineers (SPIE) Conference Series*, *Society of Photo-Optical Instrumentation Engineers (SPIE) Conference Series*, vol. 7015.

Bouchez, A. H., Dekany, R. G., Roberts, J. E. et al., 2010, Status of the PALM-3000 high-order adaptive optics system, in *Society of Photo-Optical Instrumentation Engineers (SPIE) Conference Series*, *Presented at the Society of Photo-Optical Instrumentation Engineers (SPIE) Conference*, vol. 7736.

Bracewell, R. N., 1978, Detecting nonsolar planets by spinning infrared interferometer, *Nature* **274**, 780–781.

Buisset, C., Rejeaunier, X., Rabbia, Y. & Barillot, M., 2007, Stable deep nulling in polychromatic unpolarized light with multiaxial beam combination, *Appl. Opt.* **46**(32), 7817–7822.

Burrows, A., Hubbard, W. B., Saumon, D. & Lunine, J. I., 1993, An expanded set of brown dwarf and very low mass star models, *Astrophysical Journal* **406**, 158–171.

Burrows, A., Marley, M., Hubbard, W. B. et al., 1997, A Nongray Theory of Extrasolar Giant Planets and Brown Dwarfs, *Astrophysical Journal* **491**, 856–875.

Carbillet, M., Boccaletti, A., Thalmann, C. et al., 2008, The Software Package SPHERE: a CAOS-based numerical tool for end-to-end simulations of SPHERE/VLT, in *Society of Photo-Optical Instrumentation Engineers (SPIE) Conference Series*, *Society of Photo-Optical Instrumentation Engineers (SPIE) Conference Series*, vol. 7015.

Carson, J. C., Eikenberry, S. S., Brandl, B. R. et al., 2005, The Cornell High-Order Adaptive Optics Survey for Brown Dwarfs in Stellar Systems. I. Observations, Data Reduction, and Detection Analyses, *Astronomical Journal* **130**, 1212–1220.

Chabrier, G. & Baraffe, I., 1997, Structure and evolution of low-mass stars, *Astron. & Astrophys.* **327**, 1039–1053.

Charbonneau, D., Allen, L. E., Megeath, S. T. et al., 2005, Detection of Thermal Emission from an Extrasolar Planet, *Astrophysical Journal* **626**, 523–529.

Charbonneau, D., Brown, T. M., Noyes, R. W. & Gilliland, R. L., 2002, Detection of an Extrasolar Planet Atmosphere, *Astrophysical Journal* **568**, 377–384.

Chauvin, G., Lagrange, A.-M., Zuckerman, B. et al., 2005, A companion to AB Pic at the planet/brown dwarf boundary, *Astron. & Astrophys.* **438**, L29–L32.

Chiu, K., Fan, X., Leggett, S. K. et al., 2006, Seventy-One New L and T Dwarfs from the Sloan Digital Sky Survey, *Astronomical Journal* **131**, 2722–2736.

Colavita, M. M., 1994, Measurement of the Atmospheric Limit to Narrow Angle Interferometric Astrometry Using the Mark-Iii Stellar Interferometer, *Astron. & Astrophys.* **283**, 1027–+.

Colavita, M. M., Serabyn, E., Millan-Gabet, R. et al., 2009, Keck Interferometer Nuller Data Reduction and On-Sky Performance, *Publ. of the Astron. Soc. Pac.* **121**, 1120–1138.

Coudé du Foresto, V., Ridgway, S. & Mariotti, J.-M., 1997, Deriving object visibilities from interferograms obtained with a fiber stellar interferometer, *Astron. & Astrophys., Suppl.* **121**, 379–392.

Crampton, D., Simard, L. & Silva, D., 2009, TMT Science and Instruments, in *Science with the VLT in the ELT Era* (A. Moorwood, ed.), 279–+.

Cuby, J., 2010, The European ELT: status report, in *SF2A-2010: Proceedings of the Annual meeting of the French Society of Astronomy and Astrophysics. Eds.: S. Boissier, M. Heydari-Malayeri, R. Samadi and D. Valls-Gabaud, p.3* (S. Boissier, M. Heydari-Malayeri, R. Samadi, & D. Valls-Gabaud , ed.), 3–+.

Defrère, D., Absil, O., Coudé Du Foresto, V. et al., 2008, Nulling interferometry: performance comparison between space and ground-based sites for exozodiacal disc detection, *Astron. & Astrophys.* **490**, 435–445.

Defrère, D., Absil, O., den Hartog, R. et al., 2010, Nulling interferometry: impact of exozodiacal clouds on the performance of future life-finding space missions, *Astron. & Astrophys.* **509**, A9+.

Dekany, R., Bouchez, A., Britton, M. et al., 2006, PALM-3000: visible light AO on the 5.1-meter Telescope, in *Society of Photo-Optical Instrumentation Engineers (SPIE) Conference Series*, *Presented at the Society of Photo-Optical Instrumentation Engineers (SPIE) Conference*, vol. 6272.

Delplancke, F., Leveque, S. A., Kervella, P. et al., 2000, Phase-referenced imaging and micro-arcsecond astrometry with the VLTI, in *Society of Photo-Optical Instrumentation Engineers (SPIE) Conference Series* (P. Léna & A. Quirrenbach, ed.), *Society of Photo-Optical Instrumentation Engineers (SPIE) Conference Series*, vol. 4006, 365–376.

Deming, D., Seager, S., Richardson, L. J. & Harrington, J., 2005, Infrared radiation from an extrasolar planet, *Nature* **434**, 740–743.

Demory, B., Ségransan, D., Forveille, T. et al., 2009, Mass-radius relation of low and very low-mass stars revisited with the VLTI, *Astron. & Astrophys.* **505**, 205–215.

di Folco, E., Thévenin, F., Kervella, P. et al., 2004, VLTI near-IR interferometric observations of Vega-like stars, *Astron. & Astrophys.* **426**, 601–617.

Duquennoy, A. & Mayor, M., 1991, Multiplicity among solar-type stars in the solar neighbourhood. II - Distribution of the orbital elements in an unbiased sample, *Astron. & Astrophys.* **248**, 485–524.

Eggleton, P. P. & Tokovinin, A. A., 2008, A catalogue of multiplicity among bright stellar systems, *Mon. Not. of the Royal Astron. Soc.* **389**, 869–879.

Ehrenreich, D., Lagrange, A., Montagnier, G. et al., 2010, Deep infrared imaging of close companions to austral A- and F-type stars, *Astron. & Astrophys.* **523**, A73+.

Foo, G., Palacios, D. M. & Swartzlander, G. A., Jr., 2005, Optical vortex coronagraph, *Optics Letters* **30**, 3308–3310.

Ford, E. B., Lystad, V. & Rasio, F. A., 2005, Planet-planet scattering in the upsilon Andromedae system, *Nature* **434**, 873–876.

Fortney, J. J., Marley, M. S., Saumon, D. & Lodders, K., 2008, Synthetic Spectra and Colors of Young Giant Planet Atmospheres: Effects of Initial Conditions and Atmospheric Metallicity, *Astrophysical Journal* **683**, 1104–1116.

Ftaclas, C., Martín, E. L. & Toomey, D., 2003, Searching for Ultracool Companions with NICI, in *Brown Dwarfs* (E. Martín, ed.), *IAU Symposium*, vol. 211, 521–+.

Funk, B., Libert, A., Süli, Á. & Pilat-Lohinger, E., 2011, On the influence of the Kozai mechanism in habitable zones of extrasolar planetary systems, *Astron. & Astrophys.* **526**, A98+.

Gai, M., Menardi, S., Cesare, S. et al., 2004, The VLTI fringe sensors: FINITO and PRIMA FSU, in *New Frontiers in Stellar Interferometry* (W. Traub, ed.), *Proc. SPIE*, vol. 5491, 528–539.

Galland, F., Lagrange, A., Udry, S. et al., 2006, Extrasolar planets and brown dwarfs around A-F type stars. III. β Pictoris: looking for planets, finding pulsations, *Astron. & Astrophys.* **447**, 355–359.

Germain, M. E., Douglass, G. G. & Worley, C. E., 1999, Speckle Interferometry at the US Naval Observatory. II., *Astronomical Journal* **117**, 1905–1920.

Gibson, N. P., Pont, F. & Aigrain, S., 2010, A new look at NICMOS transmission spectroscopy: no conclusive evidence for molecular features, *ArXiv e-prints* .

Goldreich, P. & Tremaine, S., 1979, The excitation of density waves at the Lindblad and corotation resonances by an external potential, *Astrophysical Journal* **233**, 857–871.

Goldreich, P. & Tremaine, S., 1980, Disk-satellite interactions, *Astrophysical Journal* **241**, 425–441.

Grether, D. & Lineweaver, C. H., 2006, How Dry is the Brown Dwarf Desert? Quantifying the Relative Number of Planets, Brown Dwarfs, and Stellar Companions around Nearby Sun-like Stars, *Astrophysical Journal* **640**, 1051–1062.

Griffin, R. F., 1992, Spectroscopic binary orbits from photoelectric radial velocities. Paper 104: 47 Cygni, *The Observatory* **112**, 111–120.

Guillot, T., 2005, THE INTERIORS OF GIANT PLANETS: Models and Outstanding Questions, *Annual Review of Earth and Planetary Sciences* **33**, 493–530.

Guyon, O., Pluzhnik, E. A., Kuchner, M. J. et al., 2006, Theoretical Limits on Extrasolar Terrestrial Planet Detection with Coronagraphs, *Astrophysical Journal, Suppl.* **167**, 81–99.

Haguenauer, P. & Serabyn, E., 2006, Deep nulling of laser light with a single-mode-fiber beam combiner, *Appl. Opt.* **45**, 2749–2754.

Haguenauer, P., Serabyn, E., Bloemhof, E. E. et al., 2005, An off-axis four-quadrant phase-mask coronagraph for Palomar: high contrast near bright stars imager, in *Society of Photo-Optical Instrumentation Engineers (SPIE) Conference Series* (D. R. Coulter, ed.), *Society of Photo-Optical Instrumentation Engineers (SPIE) Conference Series*, vol. 5905, 261–271.

Haisch, K. E., Lada, E. A. & Lada, C. J., 2001, Disk frequencies and lifetimes in yong clusters, *Astrophysical Journal, Letters* **553**, L153–L156.

Halbwachs, J. L., 1981, List of Estimated Angular Separations of Spectroscopic Binaries, *Astron. & Astrophys., Suppl.* **44**, 47–+.

Hanot, C., Absil, O., Surdej, J. et al., 2010a, Compared sensitivities of VLT, JWST and ELT for direct exoplanet detection in nearby stellar moving groups, in *Society of Photo-Optical Instrumentation Engineers (SPIE) Conference Series*, *Society of Photo-Optical Instrumentation Engineers (SPIE) Conference Series*, vol. 7731.

Hanot, C., Mawet, D., Loicq, J. et al., 2007, Fresnel rhombs as achromatic phase shifters for infrared nulling interferometry: first experimental results, in *Society of Photo-Optical Instrumentation Engineers (SPIE) Conference Series*, *Presented at the Society of Photo-Optical Instrumentation Engineers (SPIE) Conference*, vol. 6693, 51–+.

Hanot, C., Mennesson, B., Martin, S. et al., 2011, Improving Interferometric Null Depth Measurements using Statistical Distributions: Theory and First Results with the Palomar Fiber Nuller, *Astrophysical Journal* **729**, 110–+.

Hanot, C., Riaud, P., Mawet, D. et al., 2010b, Development of a CELestial Infrared Nuller Experiment (CELINE) for broadband nulling and new single-mode fiber testing, in *Society of Photo-Optical Instrumentation Engineers (SPIE) Conference Series*, *Society of Photo-Optical Instrumentation Engineers (SPIE) Conference Series*, vol. 7734.

Hartkopf, W. I., 1999, New orbits for WDS 19307+2758, WDS 19336+3846, WDS 22383+4511., *IAU Commission on Double Stars* **139**, 2–2.

Hartkopf, W. I., Mason, B. D., McAlister, H. A. et al., 2000, ICCD Speckle Observations of Binary Stars. XXIII. Measurements during 1982-1997 from Six Telescopes, with 14 New Orbits, *Astronomical Journal* **119**, 3084–3111.

Hartkopf, W. I., McAlister, H. A. & Franz, O. G., 1989, Binary star orbits from speckle interferometry. II - Combined visual-speckle orbits of 28 close systems, *Astronomical Journal* **98**, 1014–1039.

Hartkopf, W. I., McAlister, H. A., Mason, B. D. et al., 1994, ICCD speckle observations of binary stars. 11: Measurements during 1991-1993 from the Kitt Peak 4 M telescope, *Astronomical Journal* **108**, 2299–2311.

Hayward, T. L., Brandl, B., Pirger, B. et al., 2001, PHARO: A Near-Infrared Camera for the Palomar Adaptive Optics System, *Publ. of the Astron. Soc. Pac.* **113**, 105–118.

Heap, S. R., Lindler, D. J., Lanz, T. M. et al., 2000, Space Telescope Imaging Spectrograph Coronagraphic Observations of β Pictoris, *Astrophysical Journal* **539**, 435–444.

Heintz, W. D., 1978, *Double stars*, vol. 15, Reidel Publishing Company.

Heinze, A. N., Hinz, P. M., Kenworthy, M. et al., 2010, Constraints on Long-period Planets from an L'- and M-band Survey of Nearby Sun-like Stars: Modeling Results, *Astrophysical Journal* **714**, 1570–1581.

Hinkley, S., Oppenheimer, B. R., Brenner, D. R. et al., 2010, Early Data from Project 1640: A New High Contrast Imaging Program at Palomar Observatory, in *American Astronomical Society Meeting Abstracts*, *American Astronomical Society Meeting Abstracts*, vol. 215, 601.05.

Hinz, P. M., Angel, J. R. P., Woolf, N. J. et al., 2000, BLINC: a testbed for nulling interferometry in the thermal infrared, in *Interferometry in Optical Astronomy* (P. Léna & A. Quirrenbach, eds.), *Proc. SPIE*, vol. 4006, 349–353.

Hinz, P. M., Connors, T., McMahon, T. et al., 2004, Large Binocular Telescope Interferometer: the universal beam combiner, in *Society of Photo-Optical Instrumentation Engineers (SPIE) Conference Series* (W. A. Traub, ed.), *Presented at the Society of Photo-Optical Instrumentation Engineers (SPIE) Conference*, vol. 5491, 787–+.

Hinz, P. M., Hoffmann, W. F. & Hora, J. L., 2001a, Constraints on Disk Sizes around Young Intermediate-Mass Stars: Nulling Interferometric Observations of Herbig Ae Objects, *Astrophysical Journal, Letters* **561**, L131–L134.

Hinz, P. M., Meyer, M. R., Mamajek, E. E. et al., 2001b, Detection of an Extended Dust Disk Around HD 100546 Using Nulling Interferometry, in *Bulletin of the American Astronomical Society*, *Bulletin of the American Astronomical Society*, vol. 33, 1395–+.

Horch, E. P., Robinson, S. E., Meyer, R. D. et al., 2002, Speckle Observations of Binary Stars with the WIYN Telescope. II. Relative Astrometry Measures during 1998-2000, *Astronomical Journal* **123**, 3442–3459.

Hubbard, W. B., Burrows, A. & Lunine, J. I., 2002, Theory of Giant Planets, *Annual Review of Astron. & Astrophys.* **40**, 103–136.

Hubickyj, O., Bodenheimer, P. & Lissauer, J. J., 2005, Accretion of the gaseous envelope of Jupiter around a 5 10 Earth-mass core, *Icarus* **179**, 415–431.

Huélamo, N., Figueira, P., Bonfils, X. et al., 2008, TW ;Hydrae: evidence of stellar spots instead of a Hot Jupiter, *Astron. & Astrophys.* **489**, L9–L13.

Janson, M., Bergfors, C., Goto, M. et al., 2010, Spatially Resolved Spectroscopy of the Exoplanet HR 8799 c, *Astrophysical Journal, Letters* **710**, L35–L38.

Jenkins, C., 2008, Optical vortex coronagraphs on ground-based telescopes, *Mon. Not. of the Royal Astron. Soc.* **384**, 515–524.

Jennison, R. C., 1958, A phase sensitive interferometer technique for the measurement of the Fourier transforms of spatial brightness distributions of small angular extent, *Mon. Not. of the Royal Astron. Soc.* **118**, 276–+.

Johns, M., 2008, Progress on the GMT, in *Society of Photo-Optical Instrumentation Engineers (SPIE) Conference Series*, *Presented at the Society of Photo-Optical Instrumentation Engineers (SPIE) Conference*, vol. 7012.

Johnson, J. A., Aller, K. M., Howard, A. W. & Crepp, J. R., 2010, Giant Planet Occurrence in the Stellar Mass-Metallicity Plane, *Publ. of the Astron. Soc. Pac.* **122**, 905–915.

Jorgensen, A. M., Mozurkewich, D., Armstrong, J. T. et al., 2007, Improved Coherent Integration through Fringe Model Fitting, *Astronomical Journal* **134**, 1544–1550.

Jura, M., Kahane, C., Fischer, D. & Grady, C., 1997, Circumstellar Gas in the Wide Binary HD 188037, *Astrophysical Journal* **485**, 341–+.

Kaeufl, H., Ballester, P., Biereichel, P. et al., 2004, CRIRES: a high-resolution infrared spectrograph for ESO's VLT, in *Society of Photo-Optical Instrumentation Engineers (SPIE) Conference Series* (A. F. M. Moorwood & M. Iye, ed.), *Society of Photo-Optical Instrumentation Engineers (SPIE) Conference Series*, vol. 5492, 1218–1227.

Kalas, P., Graham, J. R., Chiang, E. et al., 2008, Optical Images of an Exosolar Planet 25 Light-Years from Earth, *Science* **322**, 1345–.

Karovska, M., Schlegel, E., Hack, W. et al., 2005, A Large X-Ray Outburst in Mira A, *Astrophysical Journal, Letters* **623**, L137–L140.

Kasper, M., Apai, D., Janson, M. & Brandner, W., 2007, A novel L-band imaging search for giant planets in the Tucana and β Pictoris moving groups, *Astron. & Astrophys.* **472**, 321–327.

Kasper, M. E., Beuzit, J., Verinaud, C. et al., 2008, EPICS: the exoplanet imager for the E-ELT, in *Society of Photo-Optical Instrumentation Engineers (SPIE) Conference Series*, *Society of Photo-Optical Instrumentation Engineers (SPIE) Conference Series*, vol. 7015.

Kasting, J. F. & Catling, D., 2003, Evolution of a Habitable Planet, *Annual Review of Astron. & Astrophys.* **41**, 429–463.

Kervella, P., Bersier, D., Mourard, D. et al., 2004a, Cepheid distances from infrared long-baseline interferometry. II. Calibration of the period-radius and period-luminosity relations, *Astron. & Astrophys.* **423**, 327–333.

Kervella, P., Ségransan, D. & Coudé du Foresto, V., 2004b, Data reduction methods for single-mode optical interferometry. Application to the VLTI two-telescopes beam combiner VINCI, *Astron. & Astrophys.* **425**, 1161–1174.

Kirkpatrick, J. D., Reid, I. N., Liebert, J. et al., 2000, 67 Additional L Dwarfs Discovered by the Two Micron All Sky Survey, *Astronomical Journal* **120**, 447–472.

Kloppenborg, B., Stencel, R., Monnier, J. D. et al., 2010, Infrared images of the transiting disk in the ϵ Aurigae system, *Nature* **464**, 870–872.

Kraus, A. L., Ireland, M. J., Martinache, F. & Lloyd, J. P., 2008, Mapping the Shores of the Brown Dwarf Desert. I. Upper Scorpius, *Astrophysical Journal* **679**, 762–782.

Kroupa, P., 1995, Unification of the nearby and photometric stellar luminosity functions, *Astrophysical Journal* **453**, 358–+.

Kuchner, M. J. & Traub, W. A., 2002, A Coronagraph with a Band-limited Mask for Finding Terrestrial Planets, *Astrophysical Journal* **570**, 900–908.

Kuhn, J. R., Potter, D. & Parise, B., 2001, Imaging Polarimetric Observations of a New Circumstellar Disk System, *Astrophysical Journal, Letters* **553**, L189–L191.

Labèque, A., Chazelas, B., Brachet, F. et al., 2004, Nulltimate project: building and testing, at low temperature, achromatic phase shifters to prepare the darwin mission, in *Proc. SPIE* (SPIE, ed.), vol. 5491, 999–1010.

Labeyrie, A., 1970, Attainment of Diffraction Limited Resolution in Large Telescopes by Fourier Analysing Speckle Patterns in Star Images, *Astron. & Astrophys.* **6**, 85–+.

Labeyrie, A., 1975, Interference fringes obtained on VEGA with two optical telescopes, *Astrophysical Journal, Letters* **196**, L71–L75.

Labeyrie, A., 1995, Images of exo-planets obtainable from dark speckles in adaptive telescopes, *Astron. & Astrophys.* **298**, 544–548.

Labeyrie, A., 1996, Resolved imaging of extra-solar planets with future 10-100km optical interferometric arrays, *Astron. & Astrophys., Suppl.* **118**, 517–524.

Lafrenière, D., Doyon, R., Nadeau, D. et al., 2007a, Improving the Speckle Noise Attenuation of Simultaneous Spectral Differential Imaging with a Focal Plane Holographic Diffuser, *Astrophysical Journal* **661**, 1208–1217.

Lafrenière, D., Marois, C., Doyon, R. et al., 2007b, A New Algorithm for Point-Spread Function Subtraction in High-Contrast Imaging: A Demonstration with Angular Differential Imaging, *Astrophysical Journal* **660**, 770–780.

Lagrange, A., Bonnefoy, M., Chauvin, G. et al., 2010, A Giant Planet Imaged in the Disk of the Young Star β Pictoris, *Science* **329**, 57–.

Lagrange, A., Desort, M., Galland, F. et al., 2009a, Extrasolar planets and brown dwarfs around A-F type stars. VI. High precision RV survey of early type dwarfs with HARPS, *Astron. & Astrophys.* **495**, 335–352.

Lagrange, A., Gratadour, D., Chauvin, G. et al., 2009b, A probable giant planet imaged in the β Pictoris disk. VLT/NaCo deep L'-band imaging, *Astron. & Astrophys.* **493**, L21–L25.

Lagrange, A., Kasper, M., Boccaletti, A. et al., 2009c, Constraining the orbit of the possible companion to β Pictoris. New deep imaging observations, *Astron. & Astrophys.* **506**, 927–934.

Le Bouquin, J., Abuter, R., Haguenauer, P. et al., 2009a, Post-processing the VLTI fringe-tracking data: first measurements of stars, *Astron. & Astrophys.* **493**, 747–752.

Le Bouquin, J., Lacour, S., Renard, S. et al., 2009b, Pre-maximum spectro-imaging of the Mira star T Leporis with AMBER/VLTI, *Astron. & Astrophys.* **496**, L1–L4.

Léger, A., Ollivier, M., Altwegg, K. & Woolf, N. J., 1999, Is the presence of H_2O and O_3 in an exoplanet a reliable signature of a biological activity?, *Astron. & Astrophys.* **341**, 304–311.

Lenzen, R., Close, L., Brandner, W. et al., 2005, NACO-SDI: A Novel Simultaneous Differential Imager for the Direct Imaging of Giant Extra-Solar Planets, in *Science with Adaptive Optics* (W. Brandner & M. E. Kasper, eds.), 46.

Lenzen, R., Hartung, M., Brandner, W. et al., 2003, NAOS-CONICA first on sky results in a variety of observing modes, in *Society of Photo-Optical Instrumentation Engineers (SPIE) Conference Series* (M. Iye & A. F. M. Moorwood, ed.), *Presented at the Society of Photo-Optical Instrumentation Engineers (SPIE) Conference*, vol. 4841, 944–952.

Lépine, S. & Simon, M., 2009, Nearby Young Stars Selected by Proper Motion. I. Four New Members of the β Pictoris Moving Group From The Tycho-2 Catalog, *Astronomical Journal* **137**, 3632–3645.

Leveque, S. A., Wilhelm, R., Salvade, Y. et al., 2003, Toward nanometer accuracy laser metrology for phase-referenced interferometry with the vlti, vol. 4838, 983–994, SPIE.

Libert, A. & Tsiganis, K., 2009, Kozai resonance in extrasolar systems, *Astron. & Astrophys.* **493**, 677–686.

Lin, D. N. C., Bodenheimer, P. & Richardson, D. C., 1996, Orbital migration of the planetary companion of 51 Pegasi to its present location., *Nature* **380**, 606–607.

Lin, D. N. C. & Papaloizou, J., 1986, On the tidal interaction between protoplanets and the protoplanetary disk. III - Orbital migration of protoplanets, *Astrophysical Journal* **309**, 846–857.

Liu, W. M., Hinz, P. M., Hoffmann, W. F. et al., 2009, Observations of Main-Sequence Stars and Limits on Exozodical Dust with Nulling Interferometry, *Astrophysical Journal* **693**, 1500–1507.

Luhman, K. L., Briceño, C., Stauffer, J. R. et al., 2003, New Low-Mass Members of the Taurus Star-forming Region, *Astrophysical Journal* **590**, 348–356.

Lyot, B., 1939, The study of the solar corona and prominences without eclipses (George Darwin Lecture, 1939), *Mon. Not. of the Royal Astron. Soc.* **99**, 580–594.

Macintosh, B. A., Graham, J. R., Palmer, D. W. et al., 2008, The Gemini Planet Imager: from science to design to construction, in *Society of Photo-Optical Instrumentation Engineers (SPIE) Conference Series*, *Presented at the Society of Photo-Optical Instrumentation Engineers (SPIE) Conference*, vol. 7015.

Madhusudhan, N. & Seager, S., 2009, A Temperature and Abundance Retrieval Method for Exoplanet Atmospheres, *Astrophysical Journal* **707**, 24–39.

Mannings, V. & Barlow, M. J., 1998, Candidate Main-Sequence Stars with Debris Disks: A New Sample of Vega-like Sources, *Astrophysical Journal* **497**, 330–341.

Marcy, G. W. & Butler, R. P., 2000, Planets Orbiting Other Suns, *Publ. of the Astron. Soc. Pac.* **112**, 137–140.

Markus, K., 2010, Overall science goals and top level AO requirements for the E-ELT, in *Adaptative Optics for Extremely Large Telescopes*.

Markwardt, C. B., 2009, Non-linear Least-squares Fitting in IDL with MPFIT, in *Astronomical Society of the Pacific Conference Series* (D. A. Bohlender, D. Durand, & P. Dowler, ed.), *Astronomical Society of the Pacific Conference Series*, vol. 411, 251–+.

Marley, M. S., Fortney, J. J., Hubickyj, O. et al., 2007, On the Luminosity of Young Jupiters, *Astrophysical Journal* **655**, 541–549.

Marois, C., Doyon, R., Nadeau, D. et al., 2003, Effects of Quasi-Static Aberrations in Faint Companion Searches, in *EAS Publications Series* (C. Aime & R. Soummer, ed.), *EAS Publications Series*, vol. 8, 233–243.

Marois, C., Doyon, R., Nadeau, D. et al., 2005, TRIDENT: An Infrared Differential Imaging Camera Optimized for the Detection of Methanated Substellar Companions, *Publ. of the Astron. Soc. Pac.* **117**, 745–756.

Marois, C., Doyon, R., Racine, R. & Nadeau, D., 2000, Efficient Speckle Noise Attenuation in Faint Companion Imaging, *Publ. of the Astron. Soc. Pac.* **112**, 91–96.

Marois, C., Lafrenière, D., Doyon, R. et al., 2006, Angular Differential Imaging: A Powerful High-Contrast Imaging Technique, *Astrophysical Journal* **641**, 556–564.

Marois, C., Macintosh, B., Barman, T. et al., 2008, Direct Imaging of Multiple Planets Orbiting the Star HR 8799, *Science* **322**, 1348–.

Martin, S., Serabyn, E., Liewer, K. et al., 2008, The development and applications of a ground-based fiber nulling coronagraph, in *Society of Photo-Optical Instrumentation Engineers (SPIE) Conference Series*, *Society of Photo-Optical Instrumentation Engineers (SPIE) Conference Series*, vol. 7013.

Marzari, F. & Weidenschilling, S. J., 2002, Eccentric Extrasolar Planets: The Jumping Jupiter Model, *Icarus* **156**, 570–579.

Masciadri, E., Mundt, R., Henning, T. et al., 2005, A Search for Hot Massive Extrasolar Planets around Nearby Young Stars with the Adaptive Optics System NACO, *Astrophysical Journal* **625**, 1004–1018.

Matsuo, T., Shibai, H., Ootsubo, T. & Tamura, M., 2007, Planetary Formation Scenarios Revisited: Core-Accretion versus Disk Instability, *Astrophysical Journal* **662**, 1282–1292.

Mawet, D., Hanot, C., Lenaers, C. et al., 2007, Fresnel rhombs as achromatic phase shifters for infrared nulling interferometry, *Optics Express* **15**, 12850–+.

Mawet, D., Lenaerts, C., Riaud, P. et al., 2005a, Use of subwavelength gratings in TIR incidence as achromatic phase shifters, *æ* **13**, 8686–8692.

Mawet, D., Lenaerts, C., Riaud, P. et al., 2006, Infrared achromatic phase shifters using modulated total internal reflection, in *Advances in Stellar Interferometry. Edited by Monnier, John D.; Schöller, Markus; Danchi, William C.. Proceedings of the SPIE, Volume 6268, pp. 62682J (2006).* (SPIE, ed.), vol. 6268.

Mawet, D., Riaud, P., Absil, O. & Surdej, J., 2005b, Annular Groove Phase Mask Coronagraph, *Astrophysical Journal* **633**, 1191–1200.

Mawet, D., Riaud, P., Surdej, J. & Baudrand, J., 2005c, Subwavelength surface-relief gratings for stellar coronagraphy, *Applied Optics* **44**, 7313–7321.

Mawet, D., Serabyn, E., Liewer, K. et al., 2009, Optical vectorial vortex coronagraphs using liquid crystal polymers: theory, manufacturing and laboratory demonstration, *Opt. Express* **17**(3), 1902–1918.

Mawet, D., Serabyn, E., Liewer, K. et al., 2010, The Vector Vortex Coronagraph: Laboratory Results and First Light at Palomar Observatory, *Astrophysical Journal* **709**, 53–57.

Mawet, D., Serabyn, E., Stapelfeldt, K. & Crepp, J., 2009, Imaging the Debris Disk of HD 32297 with a Phase-Mask Coronagraph at High Strehl Ratio, *Astrophysical Journal, Letters* **702**, L47–L50.

Mayor, M., Bonfils, X., Forveille, T. et al., 2009, The HARPS search for southern extra-solar planets. XVIII. An Earth-mass planet in the GJ 581 planetary system, *Astron. & Astrophys.* **507**, 487–494.

Mayor, M. & Queloz, D., 1995, A Jupiter-Mass Companion to a Solar-Type Star, *Nature* **378**, 355–+.

McAlister, H., Hartkopf, W. I. & Franz, O. G., 1990, ICCD speckle observations of binary stars. V - Measurements during 1988-1989 from the Kitt Peak and the Cerro Tololo 4 M telescopes, *Astronomical Journal* **99**, 965–978.

McAlister, H. A. & Fekel, F. C., 1980, Speckle interferometric measurements of binary stars. V, *Astrophysical Journal, Suppl.* **43**, 327–337.

McAlister, H. A., Hartkopf, W. I., Gaston, B. J. et al., 1984, Speckle interferometric measurements of binary stars. IX, *Astrophysical Journal, Suppl.* **54**, 251–257.

McAlister, H. A., Hartkopf, W. I., Hendry, E. M. et al., 1983, Speckle interferometric measurements of binary stars. VIII, *Astrophysical Journal, Suppl.* **51**, 309–320.

McAlister, H. A., Hartkopf, W. I., Hutter, D. J. & Franz, O. G., 1987, ICCD speckle observations of binary stars. II - Measurements during 1982-1985 from the Kitt Peak 4 M telescope, *Astronomical Journal* **93**, 688–723.

McAlister, H. A., Hartkopf, W. I., Sowell, J. R. et al., 1989, ICCD speckle observations of binary stars. IV - Measurements during 1986-1988 from the Kitt Peak 4 M telescope, *Astronomical Journal* **97**, 510–531.

McAlister, H. A. & Hendry, E. M., 1982a, Speckle interferometric measurements of binary stars. VI, *Astrophysical Journal, Suppl.* **48**, 273–278.

McAlister, H. A. & Hendry, E. M., 1982b, Speckle interferometric measurements of binary stars. VII, *Astrophysical Journal, Suppl.* **49**, 267–272.

McCarthy, C. & Zuckerman, B., 2004, The Brown Dwarf Desert at 75-1200 AU, *Astronomical Journal* **127**, 2871–2884.

McLean, I. S. & Adkins, S., 2004, Instrumentation at the Keck Observatory, in *Society of Photo-Optical Instrumentation Engineers (SPIE) Conference Series* (A. F. M. Moorwood & M. Iye, ed.), *Presented at the Society of Photo-Optical Instrumentation Engineers (SPIE) Conference*, vol. 5492, 1–12.

Mennesson, B., 2007, A Single-Mode Nulling Rotating Coronagraph for High Contrast Ground Based Imaging, in *In the Spirit of Bernard Lyot: The Direct Detection of Planets and Circumstellar Disks in the 21st Century*.

Mennesson, B., Haguenauer, P., Serabyn, E. & Liewer, K., 2006, Deep broad-band infrared nulling using a single-mode fiber beam combiner and baseline rotation, in *Society of Photo-Optical Instrumentation Engineers (SPIE) Conference Series*, *Society of Photo-Optical Instrumentation Engineers (SPIE) Conference Series*, vol. 6268.

Mennesson, B., Hanot, C., Serabyn, E. et al., 2011a, High contrast stellar observations within the diffraction limit at the palomar hale telescope, *Astrophysical Journal* **Submitted**.

Mennesson, B., Hanot, C., Serabyn, E. et al., 2011b, New constraints on companions and dust within a few au of vega, *Astrophysical Journal* **Submitted**.

Mennesson, B., M., O. & C., R., 2002, Use of single-mode waveguides to correct the optical defects of a nulling interferometer, *JOSA A* **19**, 596–602.

Mérand, A., 2008, Determining Accurate Distances to Cepheids Using the Interferometric Baade-Wesselink Method: Possible Interferometric Biases, in *EAS Publications Series* (S. Wolf, F. Allard, & P. Stee, ed.), *EAS Publications Series*, vol. 28, 53–59.

Metchev, S. A., Kirkpatrick, J. D., Berriman, G. B. & Looper, D., 2008, A Cross-Match of 2MASS and SDSS: Newly Found L and T Dwarfs and an Estimate of the Space Density of T Dwarfs, *Astrophysical Journal* **676**, 1281–1306.

Michelson, A. A., 1920, On the Application of Interference Methods to Astronomical Measurements, *Astrophysical Journal* **51**, 257–262.

Michelson, A. A. & Pease, F. G., 1921, Measurement of the diameter of alpha Orionis with the interferometer, *Astrophysical Journal* **53**, 249–259.

Miura, N., Iribe, T., Kubo, T. et al., 1995, Speckle observations of visual and spectroscopic binaries. VI., *Publications of the National Astronomical Observatory of Japan* **4**, 67–73.

Monnier, J. D., Zhao, M., Pedretti, E. et al., 2007, Imaging the Surface of Altair, *Science* **317**, 342–.

Mordasini, C., Alibert, Y. & Benz, W., 2009a, Extrasolar planet population synthesis. I. Method, formation tracks, and mass-distance distribution, *Astron. & Astrophys.* **501**, 1139–1160.

Mordasini, C., Alibert, Y., Benz, W. & Naef, D., 2009b, Extrasolar planet population synthesis. II. Statistical comparison with observations, *Astron. & Astrophys.* **501**, 1161–1184.

Murakawa, K., Suto, H., Tamura, M. et al., 2004, CIAO: Coronagraphic Imager with Adaptive Optics on the Subaru Telescope, *PASJ* **56**, 509–519.

Muterspaugh, M. W., Lane, B. F., Konacki, M. et al., 2005, PHASES High-Precision Differential Astrometry of δ Equulei, *Astronomical Journal* **130**, 2866–2875.

Muterspaugh, M. W., Lane, B. F., Kulkarni, S. R. et al., 2006, Limits to Tertiary Astrometric Companions in Binary Systems, *Astrophysical Journal* **653**, 1469–1479.

Nagasawa, M., Ida, S. & Bessho, T., 2008, Formation of Hot Planets by a Combination of Planet Scattering, Tidal Circularization, and the Kozai Mechanism, *Astrophysical Journal* **678**, 498–508.

Nelson, J. & Sanders, G. H., 2006, TMT status report, in *Society of Photo-Optical Instrumentation Engineers (SPIE) Conference Series*, *Presented at the Society of Photo-Optical Instrumentation Engineers (SPIE) Conference*, vol. 6267.

Neuhäuser, R., Guenther, E. W., Alves, J. et al., 2003, An infrared imaging search for low-mass companions to members of the young nearby β Pic and Tucana/Horologium associations, *Astronomische Nachrichten* **324**, 535–542.

Ollivier, M. & Mariotti, J.-M., 1997, Improvement in the rejection rate of a nulling interferometer by spatial filtering, *Applied Optics* **36**(22), 5340–5346.

Parsons, S. B., 2004, New and Confirmed Triple Systems with Luminous Cool Primaries and Hot Companions, *Astronomical Journal* **127**, 2915–2930.

Parsons, S. B. & Ake, T. B., 1998, Ultraviolet and Optical Studies of Binaries with Luminous Cool Primaries and Hot Companions. V. The Entire IUE Sample, *Astrophysical Journal, Suppl.* **119**, 83–104.

Paulson, D. B. & Yelda, S., 2006, Differential Radial Velocities and Stellar Parameters of Nearby Young Stars, *Publ. of the Astron. Soc. Pac.* **118**, 706–715.

Perets, H. B. & Naoz, S., 2009, Kozai Cycles, Tidal Friction, and the Dynamical Evolution of Binary Minor Planets, *Astrophysical Journal, Letters* **699**, L17–L21.

Perrin, G., 2003, The calibration of interferometric visibilities obtained with single-mode optical interferometers. Computation of error bars and correlations, *Astron. & Astrophys.* **400**, 1173–1181.

Peters, R. D., Lay, O. P. & Lawson, P. R., 2010, Mid-Infrared Adaptive Nulling for the Detection of Earthlike Exoplanets, *Publ. of the Astron. Soc. Pac.* **122**, 85–92.

Petrov, R. G., Malbet, F., Weigelt, G. et al., 2007, Amber, the near-infrared spectro-interferometric three-telescope vlti instrument, *Astron. & Astrophys.* **464**, 1–12.

Pollack, J. B., 1984, Origin and History of the Outer Planets: Theoretical Models and Observational Contraints, *Annual Review of Astron. & Astrophys.* **22**, 389–424.

Pollack, J. B., Hubickyj, O., Bodenheimer, P. et al., 1996, Formation of the Giant Planets by Concurrent Accretion of Solids and Gas, *Icarus* **124**, 62–85.

Press, W., Teukolsky, S., Vetterling, W. & Flannery, B., 2007, *Numerical Recipes 3rd Edition: The Art of Scientific Computing*, Cambridge University Press.

Prieur, J., Oblak, E., Lampens, P. et al., 2001, Speckle observations of binary systems measured by Hipparcos, *Astron. & Astrophys.* **367**, 865–875.

Prieur, J., Scardia, M., Pansecchi, L. et al., 2008, Speckle observations with PISCO in Merate - V. Astrometric measurements of visual binaries in 2006, *Mon. Not. of the Royal Astron. Soc.* **387**, 772–782.

Primmerman, C. A., Murphy, D. V., Page, D. A. et al., 1991, Compensation of atmospheric optical distortion using a synthetic beacon, *Nature* **353**, 141–143.

Proust, D., Ochsenbein, F. & Pettersen, B. R., 1981, A catalogue of variable-visual binary stars, *Astron. & Astrophys., Suppl.* **44**, 179–187.

Queloz, D., Anderson, D., Collier Cameron, A. et al., 2010, WASP-8b: a retrograde transiting planet in a multiple system, *Astron. & Astrophys.* **517**, L1+.

Quirrenbach, A., Coudé du Foresto, V., Daigne, G. et al., 1998, PRIMA: study for a dual-beam instrument for the VLT Interferometer, in *Society of Photo-Optical Instrumentation Engineers (SPIE) Conference Series* (R. D. Reasenberg, ed.), *Presented at the Society of Photo-Optical Instrumentation Engineers (SPIE) Conference*, vol. 3350, 807–817.

Quirrenbach, A., Mozurkewich, D., Buscher, D. F. et al., 1994, Phase-referenced visibility averaging in optical long-baseline interferometry, *Astron. & Astrophys.* **286**, 1019–1027.

Racine, R., Walker, G. A. H., Nadeau, D. et al., 1999, Speckle Noise and the Detection of Faint Companions, *Publ. of the Astron. Soc. Pac.* **111**, 587–594.

Rebull, L. M., Stapelfeldt, K. R., Werner, M. W. et al., 2008, Spitzer MIPS Observations of Stars in the β Pictoris Moving Group, *Astrophysical Journal* **681**, 1484–1504.

Redfield, S., Endl, M., Cochran, W. D. & Koesterke, L., 2008, Sodium Absorption from the Exoplanetary Atmosphere of HD 189733b Detected in the Optical Transmission Spectrum, *Astrophysical Journal, Letters* **673**, L87–L90.

Riaud, P., Boccaletti, A., Baudrand, J. & Rouan, D., 2003, The Four-Quadrant Phase Mask Coronagraph. III. Laboratory Performance, *Publ. of the Astron. Soc. Pac.* **115**, 712–719.

Riaud, P., Boccaletti, A., Gillet, S. et al., 2002, Coronagraphic search for exo-planets with a hypertelescope. I. In the thermal IR, *Astron. & Astrophys.* **396**, 345–352.

Riaud, P., Boccaletti, A., Rouan, D. et al., 2001, The Four-Quadrant Phase-Mask Coronagraph. II. Simulations, *Publ. of the Astron. Soc. Pac.* **113**, 1145–1154.

Riaud, P. & Hanot, C., 2010, Combining Coronagraphy with Interferometry as a Tool for Measuring Stellar Diameters, *Astrophysical Journal* **719**, 749–762.

Riaud, P., Mawet, D., Absil, O. et al., 2006, Coronagraphic imaging of three Weak-line T-Tauri stars: evidence of planetary formation around PDS70, *accepted in A&A* .

Rieke, G. H., Su, K. Y. L., Stansberry, J. A. et al., 2005a, Decay of Planetary Debris Disks, *Astrophysical Journal* **620**, 1010–1026.

Rieke, M., Kelly, D., Horner, S. & NIRCam Team, 2005b, The Near Infrared Camera (NIRCam) for the James Webb Space Telescope (JWST), in *Bulletin of the American Astronomical Society*, *Bulletin of the American Astronomical Society*, vol. 37, 1351–+.

Roberts, L. C., Shao, M., Vasisht, G. et al., 2009, Exoplanet imaging at the palomar 5-m: Enhancing the contrast of the project 1640 coronagraph, in *American Astronomical Society Meeting Abstracts*, *American Astronomical Society Meeting Abstracts*, vol. 214.

Roberts, L. C., Jr., Turner, N. H. & ten Brummelaar, T. A., 2007, Adaptive Optics Photometry and Astrometry of Binary Stars. II. A Multiplicity Survey of B Stars, *Astronomical Journal* **133**, 545–552.

Rouan, D., Riaud, P., Boccaletti, A. et al., 2000, The Four-Quadrant Phase-Mask Coronagraph. I. Principle, *Publ. of the Astron. Soc. Pac.* **112**, 1479–1486.

Rousset, G., 1997, Adaptive optics developmens in astronomy., *Academie des Science Paris Comptes Rendus Serie B Sciences Physiques* **325**, 173–176.

Rousset, G., Lacombe, F., Puget, P. et al., 2003, NAOS, the first AO system of the VLT: on-sky performance, in *Society of Photo-Optical Instrumentation Engineers (SPIE) Conference Series* (P. L. Wizinowich & D. Bonaccini, ed.), *Presented at the Society of Photo-Optical Instrumentation Engineers (SPIE) Conference*, vol. 4839, 140–149.

Ruilier, C. & Cassaing, F., 2001, Coupling of large telescopes and single-mode waveguides: application to stellar interferometry, *J. Opt. Soc. Am. A.* **18**(1), 143.

Sasselov, D. D. & Lecar, M., 2000, On the Snow Line in Dusty Protoplanetary Disks, *Astrophysical Journal* **528**, 995–998.

Scardia, M., Prieur, J., Sala, M. et al., 2005, Speckle observations with PISCO in Merate - I. Astrometric measurements of visual binaries in 2004, *Mon. Not. of the Royal Astron. Soc.* **357**, 1255–1266.

Schultz, A. B., Fraquelli, D., Calzetti, D. et al., 2000, NICMOS Coronagraphy, in *Bulletin of the American Astronomical Society*, *Bulletin of the American Astronomical Society*, vol. 32, 1419–+.

Scuderi, L. J., Dittmann, J. A., Males, J. R. et al., 2010, On the Apparent Orbital Inclination Change of the Extrasolar Transiting Planet TrES-2b, *Astrophysical Journal* **714**, 462–468.

Seifahrt, A. & Käufl, H. U., 2008, High precision radial velocity measurements in the infrared. A first assessment of the RV stability of CRIRES, *Astron. & Astrophys.* **491**, 929–939.

Selsis, F., Despois, D. & Parisot, J.-P., 2002, Signature of life on exoplanets: Can Darwin produce false positive detections?, *Astron. & Astrophys.* **388**, 985–1003.

Serabyn, E., 2000, Nulling interferometry: symmetry requirements and experimental results, in *Interferometry in Optical Astronomy* (P. Léna & A. Quirrenbach, eds.), *Proc. SPIE*, vol. 4006, 328–339.

Serabyn, E., Booth, A. J., Colavita, M. M. et al., 2004, The Keck interferometer nuller: system architecture and laboratory performance, in *New Frontiers in Stellar Interferometry* (W. Traub, ed.), *Proc. SPIE*, vol. 5491, 806–815.

Serabyn, E., Mawet, D., Bloemhof, E. et al., 2009, Imaging Faint Brown Dwarf Companions Close to Bright Stars with a Small, Well-corrected Telescope Aperture, *Astrophysical Journal* **696**, 40–46.

Serabyn, E., Mawet, D. & Burruss, R., 2010, An image of an exoplanet separated by two diffraction beamwidths from a star, *Nature* **464**, 1018–1020.

Serabyn, E. & Mennesson, B., 2006, Accessing Small Inner Working Angles with a Rotating Subaperture Nuller, in *IAU Colloq. 200: Direct Imaging of Exoplanets: Science and Techniques* (C. Aime & F. Vakili, ed.), 379–384.

Serabyn, E., Wallace, J. K., Troy, M. et al., 2006, Extreme adaptive optics using an off-axis subaperture on a ground-based telescope, in *Society of Photo-Optical Instrumentation Engineers (SPIE) Conference Series*, *Society of Photo-Optical Instrumentation Engineers (SPIE) Conference Series*, vol. 6272.

Serabyn, E., Wallace, K., Troy, M. et al., 2007, Extreme Adaptive Optics Imaging with a Clear and Well-Corrected Off-Axis Telescope Subaperture, *Astrophysical Journal* **658**, 1386–1391.

Setiawan, J., Henning, T., Launhardt, R. et al., 2008, A young massive planet in a star-disk system, *Nature* **451**, 38–41.

Shao, M. & Colavita, M. M., 1992a, Long-baseline optical and infrared stellar interferometry, *Annual Review of Astron. & Astrophys.* **30**, 457–498.

Shao, M. & Colavita, M. M., 1992b, Potential of long-baseline infrared interferometry for narrow-angle astrometry, *Astron. & Astrophys.* **262**, 353–358.

Shectman, S. & Johns, M., 2010, GMT overview, in *Society of Photo-Optical Instrumentation Engineers (SPIE) Conference Series*, *Presented at the Society of Photo-Optical Instrumentation Engineers (SPIE) Conference*, vol. 7733.

Simard, L., Crampton, D., Ellerbroek, B. & Boyer, C., 2010, The TMT instrumentation program, in *Society of Photo-Optical Instrumentation Engineers (SPIE) Conference Series*, *Presented at the Society of Photo-Optical Instrumentation Engineers (SPIE) Conference*, vol. 7735.

Slesnick, C. L., Carpenter, J. M. & Hillenbrand, L. A., 2006, A Large-Area Search for Low-Mass Objects in Upper Scorpius. I. The Photometric Campaign and New Brown Dwarfs, *Astronomical Journal* **131**, 3016–3027.

Smith, B. A. & Terrile, R. J., 1984, A circumstellar disk around Beta Pictoris, *Science* **226**, 1421–1424.

Smith, W. H., 1987, Spectral differential imaging detection of planets about nearby stars, *Publ. of the Astron. Soc. Pac.* **99**, 1344–1353.

Soummer, R., 2005, Apodized Pupil Lyot Coronagraphs for Arbitrary Telescope Apertures, *Astrophysical Journal, Letters* **618**, L161–L164.

Soummer, R., Valenti, J., Brown, R. A. et al., 2010, Direct imaging and spectroscopy of habitable planets using jwst and a starshade, vol. 7731, 77312I, SPIE.

Stevenson, D. J., 1982, Interiors of the giant planets, *Annual Review of Earth and Planetary Sciences* **10**, 257–295.

Su, K. Y. L., Rieke, G. H., Misselt, K. A. et al., 2005, The Vega Debris Disk: A Surprise from Spitzer, *Astrophysical Journal* **628**, 487–500.

Sudarsky, D., Burrows, A. & Hubeny, I., 2003, Theoretical Spectra and Atmospheres of Extrasolar Giant Planets, *Astrophysical Journal* **588**, 1121–1148.

Swain, M., Vasisht, G., Akeson, R. et al., 2003, Interferometer Observations of Subparsec-Scale Infrared Emission in the Nucleus of NGC 4151, *Astrophysical Journal, Letters* **596**, L163–L166.

Swain, M. R., Tinetti, G., Vasisht, G. et al., 2009a, Water, Methane, and Carbon Dioxide Present in the Dayside Spectrum of the Exoplanet HD 209458b, *Astrophysical Journal* **704**, 1616–1621.

Swain, M. R., Vasisht, G., Henning, T. et al., 2010, THESIS: the terrestrial habitable-zone exoplanet spectroscopy infrared spacecraft, in *Society of Photo-Optical Instrumentation Engineers (SPIE) Conference Series*, *Society of Photo-Optical Instrumentation Engineers (SPIE) Conference Series*, vol. 7731.

Swain, M. R., Vasisht, G. & Tinetti, G., 2008, The presence of methane in the atmosphere of an extrasolar planet, *Nature* **452**, 329–331.

Swain, M. R., Vasisht, G., Tinetti, G. et al., 2009b, Molecular Signatures in the Near-Infrared Dayside Spectrum of HD 189733b, *Astrophysical Journal, Letters* **690**, L114–L117.

Swartzlander, G. A., Jr., Ford, E. L., Abdul-Malik, R. S. et al., 2008, Astronomical demonstration of an optical vortex coronagraph, *Optics Express* **16**, 10200–+.

Szeto, K., Roberts, S., Gedig, M. et al., 2008, TMT telescope structure system: design and development progress report, in *Society of Photo-Optical Instrumentation Engineers (SPIE) Conference Series*, *Presented at the Society of Photo-Optical Instrumentation Engineers (SPIE) Conference*, vol. 7012.

Takeda, G. & Rasio, F. A., 2005, High Orbital Eccentricities of Extrasolar Planets Induced by the Kozai Mechanism, *Astrophysical Journal* **627**, 1001–1010.

Tamura, M., Hodapp, K., Takami, H. et al., 2006, Concept and science of HiCIAO: high contrast instrument for the Subaru next generation adaptive optics, in *Society of Photo-Optical Instrumentation Engineers (SPIE) Conference Series*, *Society of Photo-Optical Instrumentation Engineers (SPIE) Conference Series*, vol. 6269.

Tango, W. J., Davis, J., Jacob, A. P. et al., 2009, A new determination of the orbit and masses of the Be binary system δ Scorpii, *Mon. Not. of the Royal Astron. Soc.* **396**, 842–848.

ten Brummelaar, T., Mason, B. D., McAlister, H. A. et al., 2000, Binary Star Differential Photometry Using the Adaptive Optics System at Mount Wilson Observatory, *Astronomical Journal* **119**, 2403–2414.

Thompson, A. R., Moran, J. M. & Swenson, G. W., 2001, *Interferometry and Synthesis in Radio Astronomy*, Wiley, New-York.

Tokovinin, A. & Cantarutti, R., 2008, First Speckle Interferometry at SOAR Telescope with Electron-Multiplication CCD, *Publ. of the Astron. Soc. Pac.* **120**, 170–177.

Torres, C. A. O., Quast, G. R., Melo, C. H. F. & Sterzik, M. F., 2008, *Young Nearby Loose Associations*, 757.

Tremaine, S. & Zakamska, N. L., 2004, Extrasolar Planet Orbits and Eccentricities, in *The Search for Other Worlds* (S. S. Holt & D. Deming, ed.), *American Institute of Physics Conference Series*, vol. 713, 243–252.

van Belle, G., 2011, Commissioning Results From The VLTI PRIMA Facility, in *American Astronomical Society Meeting Abstracts*, *American Astronomical Society Meeting Abstracts*, vol. 217, 302.06.

Vérinaud, C., Korkiakoski, V., Yaitskova, N. et al., 2008, System design and analysis of the exo-planet imaging camera and spectrograph (EPICS) for the European ELT, in *Society of Photo-Optical Instrumentation Engineers (SPIE) Conference Series*, *Society of Photo-Optical Instrumentation Engineers (SPIE) Conference Series*, vol. 7014.

Ward, W. R., 1997, Survival of Planetary Systems, *Astrophysical Journal, Letters* **482**, L211–L214.

Winn, J. N., Howard, A. W., Johnson, J. A. et al., 2011, Orbital Orientations of Exoplanets: HAT-P-4b is Prograde and HAT-P-14b is Retrograde, *Astronomical Journal* **141**, 63–+.

Wizinowich, P. L., Le Mignant, D., Bouchez, A. H. et al., 2006, The W. M. Keck Observatory Laser Guide Star Adaptive Optics System: Overview, *Publ. of the Astron. Soc. Pac.* **118**, 297–309.

Wolfe-Simon, F., Blum, J. S., Kulp, T. R. et al., 2010, A bacterium that can grow by using arsenic instead of phosphorus, *Science* .

Wolszczan, A. & Frail, D. A., 1992, A planetary system around the millisecond pulsar PSR1257 + 12, *Nature* **355**, 145–147.

Worley, C. E. & Mason, B. D., 1998, Micrometer Measures of Double Stars, *Astronomical Journal* **116**, 917–930.

Wright, G. S., Rieke, G. H., Colina, L. et al., 2004, The JWST MIRI instrument concept, in *Society of Photo-Optical Instrumentation Engineers (SPIE) Conference Series* (J. C. Mather, ed.), *Presented at the Society of Photo-Optical Instrumentation Engineers (SPIE) Conference*, vol. 5487, 653–663.

Zapolsky, H. S. & Salpeter, E. E., 1969, The Mass-Radius Relation for Cold Spheres of Low Mass, *Astrophysical Journal* **158**, 809–+.

Zhao, M., Monnier, J. D., ten Brummelaar, T. et al., 2008, Exoplanet studies with CHARA-MIRC, in *Society of Photo-Optical Instrumentation Engineers (SPIE) Conference Series*, *Society of Photo-Optical Instrumentation Engineers (SPIE) Conference Series*, vol. 7013.

Zuckerman, B. & Song, I., 2004, Young Stars Near the Sun, *Annual Review of Astron. & Astrophys.* **42**, 685–721.

Zuckerman, B., Song, I., Bessell, M. S. & Webb, R. A., 2001, The β Pictoris Moving Group, *Astrophysical Journal, Letters* **562**, L87–L90.